Quantum Efficiency Lifetime Studies using the Photocathode Preparation Experimental Facility Developed for the ALICE Accelerator

A thesis submitted to The University of Manchester for the degree of
Doctor of Philosophy
in the faculty of Engineering and Physical Sciences

2011

Narong Chanlek

Accelerator Physics Group
School of Physics and Astronomy

Contents

List of Tables

List of Figures

Abstract

This thesis describes the development of a gallium arsenide (GaAs) photocathode preparation facility (PPF) with a load-lock interface as part of an upgrade to the ALICE photo-injector electron gun. The PPF has the capacity to prepare up to six negative electron affinity (NEA) GaAs photocathodes, and permits the rapid and reliable replacement of the degraded photocathode in the gun, while maintaining the integrity of the gun vacuum system. The photocathode preparation has been studied and developed using a custum-built surface characterisation system which permits the preparation of NEA GaAs photocathode in conjunction with the application of several surface science characterisation techniques within the same vacuum system. With GaAs/AlGaAs hetero-structure photocathodes designed and developed in collaboration with the Institute of Semiconductor Physics (ISP/Novosibirsk), quantum efficiencies (QE) of 15 - 19% at 635 nm and long lifetimes of the order of 6,800 hours are achieved in a reproducible way.

Using the PPF, I have investigated the degradation in the QE of NEA GaAs photocathodes under exposures to gases typically present in the gun vacuum, namely O_2, CO_2, CO, H_2, CH_4 and N_2. The effects of these gases on the NEA GaAs photocathodes have been demonstrated for the first time in a vacuum set-up with a base pressure in 10^{-11} mbar range. It was found that H_2, CH_4 and N_2 have no effect on the photocathodes lifetime, whilst substantial reductions of the QE have been observed during the exposures to O_2, CO_2 and CO. It was also demonstrated for the first time that the NEA GaAs photocathode activated with Cs and NF_3 is more stable during CO_2 and CO exposures than the photocathode activated with Cs and O_2.

Declaration

That no portion of the work referred to in the thesis has been submitted in support of an application for another degree or qualification of this or any other university or other institute of learning.

Copyright Statement

Acknowledgements

I would like to express my sincere gratitude to all those who have helped and made this thesis possible. First, I would like to thank my supervisor Dr. Roger M. Jones for his patient guidance and suggestions throughout this work. I also would like to thank:

- my co-supervisors: Dr. Keith Middleman and Dr. Lee Jones, Senior vacuum scientist and Accelerator physicist, Accelerator Science and Technology Centre (ASTeC), for their support, advice, assistance and encouragement which were essential for the successful completion of this thesis.

- Dr. Boris Militsyn, Senior accelerator physicist, ASTeC, for giving me an opportunity to work with such a unique and challenging machine, the ALICE PPF and his very useful suggestions and comments throughout this work.

- Joe Herbert, Head of vacuum group, ASTeC, for giving me the opportunity to work in their research group.

- Adrian Hannah and Mark Pendleton, Vacuum engineer, ASTeC. Without their continuous vacuum technical support, none of my work would have been possible, especially, Adrian Hannah who has given me useful knowledge about vacuum techniques.

- Dr. Reza Valizadeh, Surface scientist, ASTeC, for his suggestions, comments and discussion about surface science and vacuum techniques.

- Prof. Alexandr Terekhov and Dr. Heinrich Scheibler, Head of laboratory and Senior scientist, Institute of Semiconductor Physics, Novosibirsk, for their

comments and suggestions when they visited Daresbury Laboratory. I am very appreciative of them.

Other people who deserve special thanks are:

- my advisor, Prof. Fred Loebinger
- Dr. Ian Shinton
- Dr. Oleg Malyshev, ASTeC
- Julian McKenzie, ASTeC
- Ian Burrows, Ryan Cash and Barry Fell, Daresbury Laboratory.
- Rebecca Jones

Since there are a great number of people who have contributed to this thesis, it is difficult for me to remember all of you. I would like to do apologise if your name has not been mentioned above and wish to thank all of you.

Finally, I would like to thank the Royal Thai Government for their funding and a PhD opportunity. I also thank to ASTeC and the Cockcroft Institute for giving me the opportunity to undertake this research project.

Chapter 1

Introduction

Current and proposed linear colliders, energy recovery linacs (ERLs), free-electron lasers (FELs) and next generation light sources require high brightness electron sources. In particular, electron sources that can produce high current with short, intense and low transverse emittance electron bunches are essential. For example, the ideal electron source for the International Linear Collider (ILC) [1] would be able to produce a bunch of 6.4 nC with a normalised root mean square (rms) transverse emittance of 70 mm·mrad and a bunch length of 2 ns at a bunch repetition rate of 3 MHz, filling one in every 434 radio frequency (RF) buckets, equivalent to an average current of 3.2 A at the source. To meet these requirements, a direct current (DC) photo-electron gun operating with a strained GaAs/GaAsP superlattice structures photocathode has been proposed to used as an electron source for the ILC.

The Accelerators and Lasers in Combined Experiments (ALICE) ERL is currently undergoing commissioning at Daresbury Laboratory [2]. Unlike accelerators based on storage ring technology, its performance strongly depends upon the characteristics of the electron source. Electron bunches of 80 pC which are approximately 60 - 80 ps long and a normalised rms emittance as low as 6 mm·mrad at the maximum repetition rate of 81.25 MHz, filling one in every 16 RF buckets [3], is required from the electron source in operation. Currently, the DC photo-electron gun operating with a GaAs photocathode has been used as an electron source for ALICE.

For another example, consider the Linac Coherent Light Source (LCLS), an X-ray FEL at SLAC National Accelerator Laboratory [4]. To obtain short wavelength lasing, the design requires an electron source that can deliver a single bunch of 1 nC with 10 ps length equivalent to a peak current of 100 A at a repetition rate of 79.33 MHz, filling one in every 36 RF buckets with a normalized rms transverse emittance of 1.0 mm·mrad [5]. To generate an electron bunch with such a short time duration and low transverse emittance, a gun based on a normal-conducting radio frequency (NRF) cavity with a copper (Cu) photocathode has been chosen.

From these examples, it is clear that the electron source is a critical part of a modern accelerator, and it is the electron source that determines the ultimate achievable performance of the machine.

1.1 Electron sources

In principle, a number of processes can be used to generate electrons, including field emission, thermionic emission and photoemission [6]. Of these processes, only thermionic emission and photoemission are currently considered to be an effective electron source for accelerator application.

1.1.1 Thermionic emission sources

Thermionic sources have been widely used in the past for conventional electron accelerators for decades, and still remain in use at many laboratories.

In these sources, a heated cathode emits low energy electrons in a gated field which are then longitudinally compressed in sub-harmonic bunching cavities before being accelerated to relativistic energies. The emission current from the heated cathode is given by the Richardson-Dushman equation [7]:

$$J_0 = A_0 T^2 e^{\frac{-e\phi}{kT}} \tag{1.1}$$

Where J_0 is the saturated thermal emission current density (A·mm^{-2}), A_0 is Dushman's constant, the theoretical value is 120.4 A·cm^{-2}·K^{-2}, k is Boltzmann's constant

(8.6×10^5 eV·K^{-1}), e is the charge of an electron (1.602×10^{-19} C), ϕ is the work function of the material (eV) and T is the cathode temperature (K). The current is dependent on both the temperature and the emitting area of the cathode. A high operating temperature and large emitting area will produce a high emission current, with a similarly large thermal emittance, this being a measure of the electron beam quality. However, a well-prepared cathode should produce a high current with low thermal emittance, so there is a trade-off to be made. Commonly-used cathode materials for thermionic sources are LaB_6 operating at a temperature of 1600 °C, and dispenser cathodes (a tungsten matrix with work-function-lowering compounds such as caesium added) operating at a temperature of 950 °C. Both types of cathode can support a typical current density in the 10 - 30 A·cm^{-2} range [8].

Thermionic sources are robust and simple, and avoid the need for complex and sensitive drive laser systems found in photoemission sources. A thermionic source with a dispenser cathode assembly manufactured by EIMAC has been used for JAERI FEL with DC acceleration to 230 kV [9], and is proposed for the Spring-8 Compact SASE Source (SCSS) with DC acceleration to 500 kV [10]. However, the main problem for a thermionic electron source is that electrons are continuously emitted throughout the accelerating phase of the RF. It is difficult to produce the short bunch length with flexible bunch/macro bunch structure required for several modern accelerators.

1.1.2 Photoemission sources

A photoemission source, usually referred to as a photocathode electron gun or photo-injector, is based on the photoelectric effect. Electrons are emitted from the cathode material as a consequence of the absorbtion of photons. The energy of photons ($h\nu$; h is Plank's constant and ν is the frequency of photon) must be greater than the work function of the material. Any additional energy from the photons over the work function will become the kinetic energy of the emitted electrons as in Equation 1.2:

$$E_k = h\nu - \phi \tag{1.2}$$

To a first approximation, the number of emitted electrons depends on the number of the absorbed photons. The higher the intensity of the photon source, the greater number of emitted electrons.

The basic principle of this electron source is that a cathode (called a photocathode) is illuminated by a pulse of laser light which is synchronised with the phase of an RF accelerating field. Consequently, electrons are emitted from the cathode and quickly accelerated to relativistic energies by a high gradient electric field. In this way, it is possible to control the charge distribution, current density and electron bunch length through manipulation of the drive laser pulse.

The photoemission source has been proven to be an efficient source. Commonly-used photocathode materials such as GaAs, CsK_2Sb, Cu and Cs_2Te have been reported to generate current densities of at least 500 A·cm^{-2} [11], 800 A·cm^{-2} [12], 3,000 A·cm^{-2} [13] and 6,900 A·cm^{-2} [14], respectively. This technology is presently used by many laboratories such as Daresbury (GaAs photocathode) [2], Thomas Jefferson National Accelerator Facility (TJNAF) (GaAs photocathode) [15], TESLA Test Facility (TTF) linac at DESY (Cs_2Te photocathode) [16] and the Japan Atomic Energy Research Institute (JAERI) (GaAs photocathode) [17].

1.2 Types of photocathode electron guns

Photocathode electron guns or photo-injectors can be categorised into two main types: direct current (DC) and radio frequency (RF) gun.

1.2.1 Direct current (DC) guns

DC guns are the most mature technology which can deliver a bunch charge up to several hundred pico-Coulombs at high duty cycle or long pulse, including continuous wave (CW) operational mode [18]. A schematic diagram of an accelerator injector including a DC photo-injector gun is shown in Figure 1.1. The gun consists of an earthed anode and a negatively-biased photocathode which is operated at high voltage, up to several hundred kilo-Volts. When the photocathode is illuminated with a pulse of laser light which is synchronised with the RF accelerating field in

the booster cavity, electrons are emitted and accelerated through the large potential difference between the anode and cathode, then compressed longitudinally by a bunching system to produce a tightly-bunched beam for subsequent acceleration by the booster cavity. Solenoid magnet arrangements provide beam focusing and compensation for emittance dilution due to linear space charge forces before the electron beam undergoes acceleration to relativistic energies [19]. Examples of machines operating with DC guns are the ALICE at Daresbury [2], the Infrared Free Electron Laser (IR-FEL) and Continuous Electron Beam Accelerator Facility (CEBAF) at TJNAF [18, 20] , the ERL FEL at JAERI [17] and the ERL test injector at Cornell University (GaAs photocathode) [21].

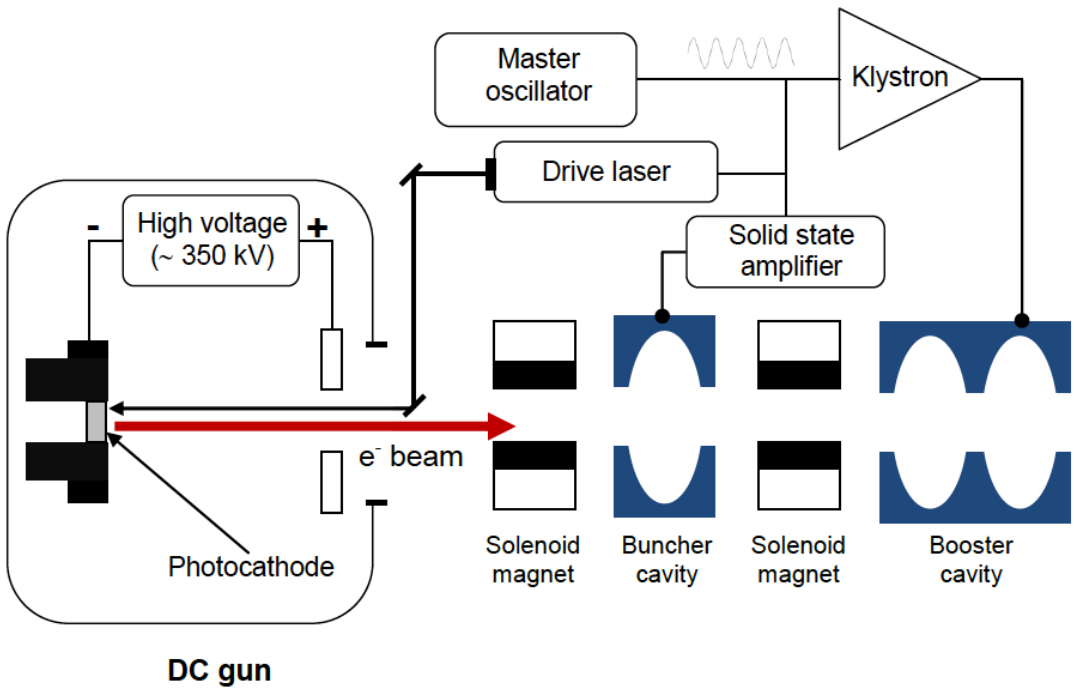

Figure 1.1: Schematic diagram of an electron injector with a DC photocathode gun.

The main technological limitation of this gun type is the failure of the dielectric insulators (usually ceramic) used to separate the high voltage components which limits the maximum achievable gradient to 350 kV with approximately 8 MV·m^{-1} in CW mode [21]. In addition, the bunching and compression process degrades the initial beam quality because nonlinear forces arising from space-charge and bunching fields lead to emittance growth.

1.2.2 Radio frequency (RF) guns

To increase the maximum electric field and decrease the emittance degradation due to the bunching system, several groups have developed and focused on RF guns. The RF gun principle is rather simple and elegant. A photocathode mounted in the end wall of an RF cavity, as shown in Figure 1.2, is illuminated by a pulse of laser which is synchronised with accelerating frequency. Electrons are emitted and immediately accelerated by the sinusoidal electric fields inside the cavity, the peak of which is higher than the static DC field. Bunching, beam focusing and emittance compensation are accomplished using the radial RF electric fields. Rapid acceleration of the electrons to the relativistic regime preserves the beam quality. Emittance growth associated with space charge effect is reduced since space charges forces within the electron bunch are inversely proportional to the mass of the electrons; the bunch quickly becomes relativistic, thus alleviating adverse space charge effects [22].

Normal-conducting radio frequency (NRF) guns

NRF guns in particular are historically the first and most common type of RF guns. They are relatively easy to construct and produce the highest quality beams on a per bunch basis. However, the maximum achievable accelerating gradient is limited to 10 MV·m^{-1} in CW mode due to thermal stress limits [21]. However, in pulsed operation, NRF guns are able to attain 140 MV·m^{-1} or more [4]. The impedance and ohmic losses cause a large amount of RF power to be dissipated in the cavity walls as heat which limits their operation in CW mode. To-date, a high-average-current RF photocathode gun operating continuously at 100% duty factor is yet to be demonstrated [23].

There are several such guns in operation including the Boeing gun at Los Alamos National Laboratory (LANL) operating at a frequency of 700 MHz with a CsKSb photocathode [18, 21], the Linac/Laser-Based Ultrafast X-ray Facility (LUX) at Lawrence Berkley National Laboratory (LBNL) operating at a frequency of 1.3 GHz with a multi-alkali photocathode [18, 21], the FEL FLASH at Deutsches Elektronen-

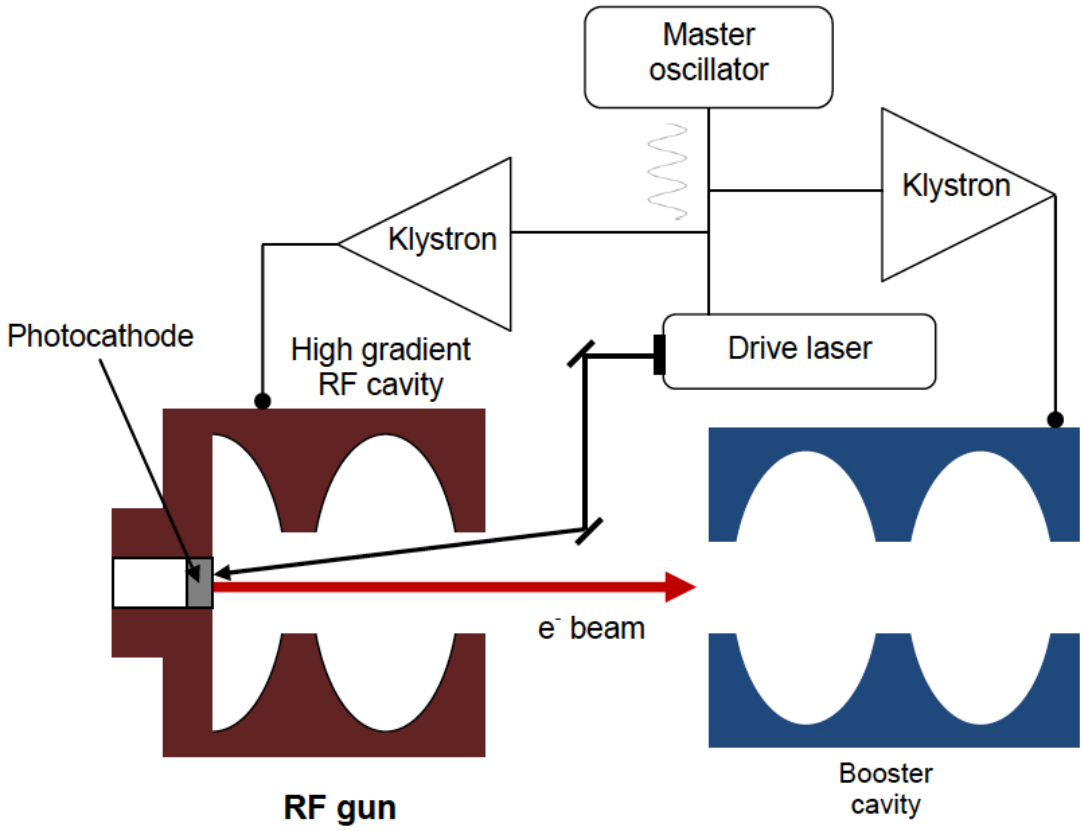

Figure 1.2: Schematic diagram of an electron injector with an RF photocathode gun.

Synchrotron (DESY) operating at a frequency of 1.3 GHz with a Cs_2Te photocathode [24], the Compact Linear Collider (CLIC)/ CLIC Test Facility (CTF2) at the European Organization for Nuclear Research (CERN) operating at a frequency of 3 GHz with a Cs_2Te photocathode [25] and the LCLS at SLAC operating at a frequency of 2.85 GHz with a Cu photocathode [5].

Superconducting radio frequency (SRF) guns

SRF guns are an advanced type of electron sources. In principle, this gun can deliver high average current, low emittance, and short bunch length in CW mode due to the low RF losses in the cavity [26, 27]. The maximum achievable accelerating gradient is around 20 MV·m^{-1} with respect to peak gun fields in CW mode [21]. However, these guns have their own technological challenges driven by their super-

conducting condition such as cathode thermal management and contamination of SRF cavity [21]. SRF guns have been successfully tested recently at Forschungszentrum Rossendorf (FZR) operating at a frequency of 1.3 GHz with a Cs_2Te photocathode [28] and have been under development by Advanced Energy Systems (AES) in collaboration with Brookhaven National Laboratory (BNL), TJNAF and FZR, operating at a frequency of 703.75 MHz with a CsK_2Sb photocathode [18, 27].

1.3 Photocathode characteristics

All photo-injector schemes share drive laser and photocathode materials technologies, and their ultimate performance is strongly determined by cathode material properties. The optimum photocathode material has to be carefully selected depending on the application and the corresponding electron beam requirements. Some crucial characteristics of a photocathode to be considered and optimised are summarised in this section.

1.3.1 Quantum efficiency

Quantum efficiency (QE) is defined as the ratio of the number of electrons emitted by the photocathode to the number of incident (rather than absorbed) photons. This quantity gives an indication of the photocurrent which can be obtained from the cathode. The QE varies significantly with photocathode material and laser wavelength. In practice, the actual QE achieved is a sensitive function of the cathode fabrication and preparation process. The QE as a function of laser wavelength for several photocathode materials are shown in Figure 1.3.

In practice, QE (%) is determined by drive laser power, P (mW) and measured photocurrent, I (μA) by using the relation [30]:

$$QE = \frac{Ihc}{\lambda eP} \times 100\% \tag{1.3}$$

where λ is the laser wavelength (nm), h is Plank's constant (6.626×10^{-34} J·s), e is the electron charge (1.6×10^{-19} C), and c is the velocity of light (2.998×10^{8} m·s^{-1}).

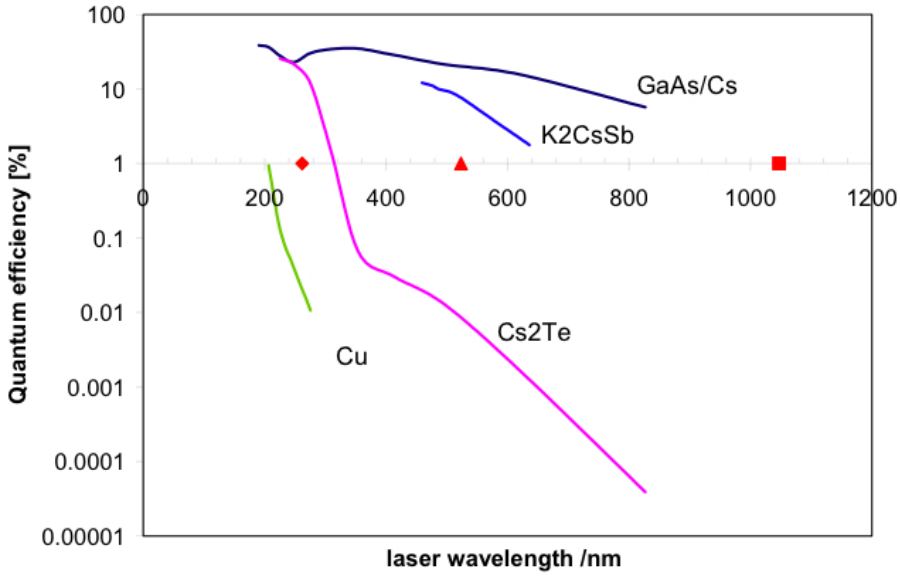

Figure 1.3: QE as a function of laser wavelength for the four materials most commonly used in photo-injectors taken from [29]. The symbols on the horizontal axis mark the wavelength of the fundamental (■, square), first harmonic (▲, triangle) and second harmonic (♦, diamond) of a Nd:YLF laser. The QE is expressed as a percentage.

Note that the definition above assumes that the emission is not space-charge limited, in other words, the photocurrent increases linearly with the laser power.

1.3.2 Thermal emittance

A beam is a collection of electrons travelling together, all with approximately the same energy and direction. In general, its motion can be described by six-degrees of freedom in phase space, namely the position (x, y, z) and momentum (p_x, p_y, p_z) in Cartesian coordinates. The coordinate system used in defining electron beams is shown in Figure 1.4. Phase space is the space in which all possible states of a system are represented. Provided that all forces are conservative in an accelerator, Liouville's theorem is applicable. It states that the six-dimensional phase space volume occupied by the beam is invariant as it travels in an accelerator; its shape may change around the accelerator, but its volume will not change.

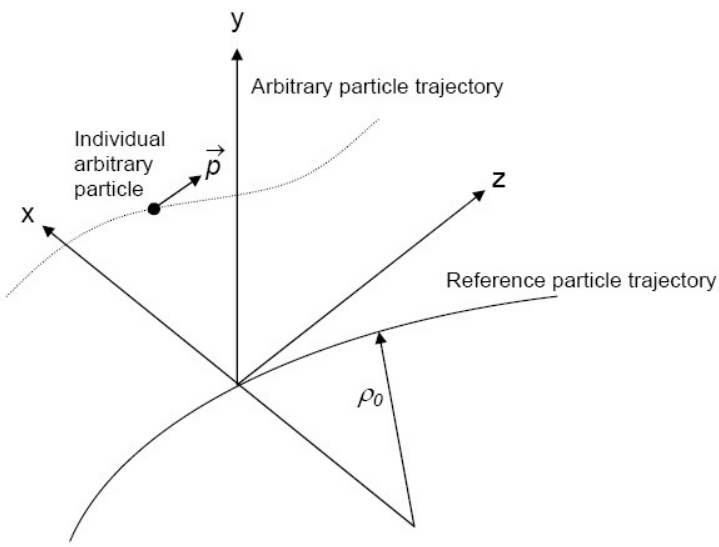

Figure 1.4: The electron beam coordinate system.

To characterise the beam properties, it is convenient to consider projections of the six-dimensional volume onto two transverse phase planes; (x, p_x) and (y, p_y) and one longitudinal phase plane; (z, p_z), where z is assumed as the average particle motion. Provided that there is no coupling between these planes, Liouville's theorem is still valid and states that the areas of each phase space plane are also invariant. These areas are a good measure of electron beam quality, and are expressed in terms of the *emittance*. There are a number of different definitions for emittance used in an accelerator. One useful definition is the *normalised rms emittance*, ε_n defined in the x-plane as [8]:

$$\varepsilon_{n,x} = \pi\sqrt{< x^2 >< x'^2 > - < x'x >^2}, \tag{1.4}$$

where $x' = p_x/p_z$ and:

$$\begin{aligned} < x^2 > &= \frac{\int\int_{beam} \rho(xx')x^2\, dx\, dx'}{\int\int_{beam} \rho(xx')\, dx\, dx'} \\ < x'^2 > &= \frac{\int\int_{beam} \rho(xx')x'^2\, dx\, dx'}{\int\int_{beam} \rho(xx')\, dx\, dx'} \\ < xx' > &= \frac{\int\int_{beam} \rho(xx')xx'\, dx\, dx'}{\int\int_{beam} \rho(xx')\, dx\, dx'} \end{aligned} \tag{1.5}$$

with the charge density in the x-plane given by $\rho(xx')$.

The emittance is a useful figure-of-merit for electron beam quality in accelerator applications, reflecting the size of the beam and its divergence. Low emittance refers to a beam which is essentially small in diameter and in which all particles have nearly the same momentum. This is desirable for an accelerator.

In a real system the total emittance, ε_{total}, can be resolved into a space charge emittance, ε_{sc}, and a thermal emittance, ε_{th}, component [29] as:

$$\varepsilon_{total} = \sqrt{\varepsilon_{sc}^2 + \varepsilon_{th}^2} \tag{1.6}$$

Thermal emittance is a fundamental property of the source which sets the lower limit of emittance that can be achieved. Thermal emittance is often referred to as intrinsic emittance. For the photocathode the intrinsic emittance can be calculated by:

$$\varepsilon_{th} = \frac{r}{2\sqrt{3}}\sqrt{\frac{E_{thermal}}{m_0 c^2}} \tag{1.7}$$

where r is the hard wall radius of the laser beam and $E_{thermal}$ is the electron energy at the photocathode surface [3]. $E_{thermal}$ depends on the photocathode materials. Actual values for $E_{thermal}$ range from 34 meV for GaAs (at room temperature) to 550 meV for $CsTe_2$ [3].

1.3.3 Threshold for photoemission

Photoemission in photocathodes can be explained with a three-step model proposed by Prof. W.E. Spicer [31, 32, 33]. According to the model, the photoemission process consists of three steps: an electron absorbs a photon, transports to the surface, and finally escapes across a surface potential barrier into the vacuum (this process will be discussed in detail in Chapter 2). The energy of the absorbed photon must be greater than the threshold for photoemission. This threshold determines the lowest drive laser photon energy required for the photocathode, and is an inherent property of material.

Figure 1.5 shows the typical energy band diagrams for metal and semiconductor photocathodes. In the case of a metal photocathode, electrons are excited in the

conduction band below the Fermi energy, E_F to a point above the the vacuum level, E_{VAC}. Therefore, the minimum photon energy required is equivalent to the work function, ϕ. The threshold for photoemission can range typically from 3.8 eV to 4.5 eV, corresponding to wavelengths in the range 326 nm to 276 nm (violet to ultra-violet). In the case of a semiconductor photocathode, electrons are promoted from the valance band to a point in the conduction band above the vacuum level. The photoemission threshold is thus imposed by the sum of the band gap energy, E_G, and the electron affinity, E_A. This can be as low as 1.5 eV, or 827 nm, allowing operation in the visible or infrared regions [29].

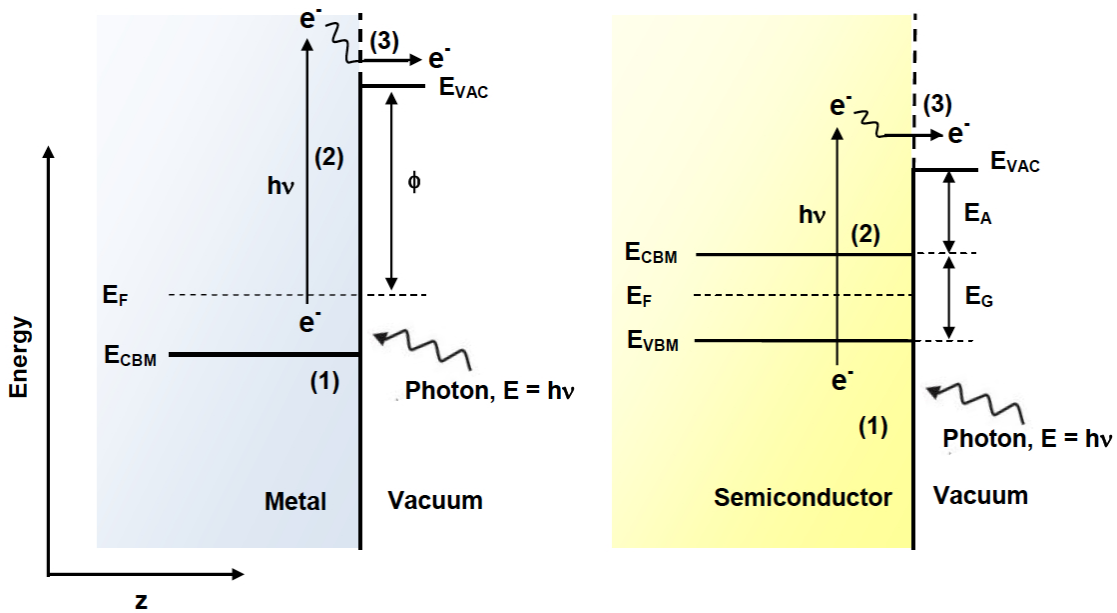

Figure 1.5: Energy band diagrams for metal and semiconductor photocathodes. The diagram illustrates the energy, E, in vertical axis and the space coordinate, z, which is perpendicular to the photocathode surface in the horizontal axis. E_{CBM} is the conduction band minimum energy level, E_F is the Fermi energy level, E_{VBM} is the valence band minimum energy level, E_{VAC} is the energy of vacuum potential barrier, E_G is the energy gap of the semiconductor, E_A is the electron affinity. According to the three-step model, **(1)** an electron absorbs a photon, **(2)** transports to the surface, and **(3)** escapes across the surface potential barrier into the vacuum.

1.3.4 Response time

The response time is determined by the time distribution between the absorbtion of photons and the emission of electrons. It is one important parameter to consider since, in the case of photo-injectors, the electron bunch structure is controlled through the drive laser pulse structure. To preserve this structure, a fast response time is required from the photocathode. A slow response time leads to the temporal length of emitted electron bunches being greater than that of the drive laser.

The response time depends on the photocathode material. This again can be explained with the three step model. Metal photocathodes tend to have very fast response times in the order of sub-picosecond/femtosecond. This is because metals have a short optical penetration depth of the order of tens of nanometers. Photoelectrons can only be created very near the surface, therefore they have a short distance to travel to the surface. As a consequence the response time is very fast. Semiconductor photocathodes, on the other hand, have a long optical penetration depth of the order of a hundred nanometers. Photoelectrons will be created deep within the bulk and their transit time to the surface leads to a delay in emission. Therefore, typical response times are of the order of several picoseconds.

1.3.5 Photocathode lifetime

In operation, the QE of the photocathode decays with time. The photocathode lifetime is defined as the time taken for the QE to fall to $1/e$ of its initial value. Long photocathode lifetime benefits accelerator operations because the extracted electron bunches from the source are stable and users are not interrupted to replace or revive depleted photocathodes.

The photocathode lifetime can be charactrerised in two different modes of operation, namely *dark lifetime* and *operational lifetime*. The dark lifetime is measured when the photocathode is not illuminated, or is illuminated at a very low laser intensity. It depends mainly on the photocathode material and the vacuum system in the gun. In contrast to the dark life time, the operational lifetime is measured from the photocathode during its operation, in the gun. It is significantly shorter

than the dark lifetime since several additional factors such as high power illumination and high electric field appear to play a role. The operational lifetime varies hugely from the order of thousands of hours to several minutes depending on the photocathode material and, most importantly, the operating conditions, as can be seen in Figure 1.6, for example.

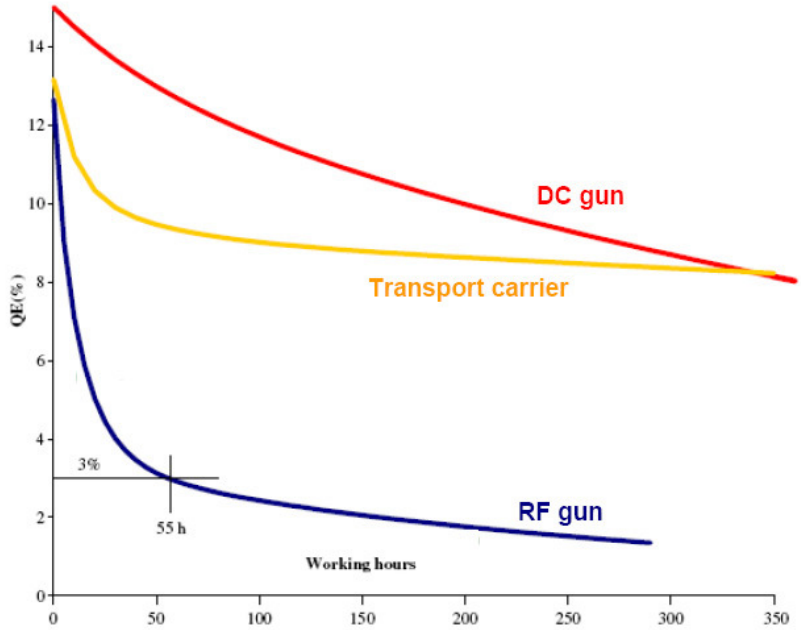

Figure 1.6: Decay of QE for a Cs_2Te photocathode under different operating conditions taken from [34]. **Transport carrier** (*dark lifetime*): measured from 5 photocathodes stored in the transport carrier at pressure $P \approx 3{\times}10^{-11}$ mbar. **DC gun** (*operational lifetime*): measured from 4 photocathodes in the DC gun operating at 8 MV·m^{-1} and pressure $P \leq 10^{-10}$ mbar. **RF gun** (*operational lifetime*): measured from 9 photocathodes in the RF gun operating at 100 MV·m^{-1} and pressure of $2{\times}10^{-10} \leq P \leq 7{\times}10^{-10}$ mbar.

1.3.6 Dark current

Another photocathode characteristic is the dark current. Under a strong accelerating field, electrons can be emitted parasitically between drive laser pulses or from outside of the laser beam by the field emission process. This so-called dark current

can limit the purity of the electron bunches used in timing experiments and thus degrade machine performance [3]. The dark current depends on the cathode material (cathodes with high QE have a lower work function so emit more than low QE cathodes), the preparation process and the accelerating field.

1.4 Overview of photocathode materials

An overview of several photocathode materials and their characteristics is presented in Table 1.4. In general, photocathode materials can be broadly classified into the metal and semiconductor varieties.

1.4.1 Metal photocathodes

Metal photocathodes such as Cu, Mg, Nb, Pb and Ba have a very low QE of 0.001% to 0.2% even at ultra-violet (UV) wavelengths. This is because of their high reflectivity and work function. At these low levels of efficiency, a significant amount of drive laser power is required in operation. With current laser technology, the maximum routinely obtainable UV average power is around 2 W, thus limiting the maximum obtainable average current with a metal photocathode to hundreds of microamperes [49]. This makes them impractical choices to generate a high current electron beam for some applications such as ERLs. The advantage of metal photocathodes is their robustness. They can withstand degradation from contaminants, heating and high electric fields. Consequently, they have a very long lifetime and are simple to prepare and operate. Metals also have a fast response time (sub-picosecond) as mentioned in the previous section. This is hugely advantageous for applications where very short electron bunches and/or complicated temporal profiles are required. Cu and Mg are stable photocathode materials, but have low QE, in the order of 0.0014% and 0.06% at 266 nm, respectively. They are usually used in an NRF injector because they can be installed continuously with the RF cavity wall without significant degradation of RF performance [34]. Cu has been used in the LCLS at SLAC, the SPARC project at Frascati and the Neptune photoinjector at University of California, Los Angeles (UCLA) [4, 29]. Ba has the best spectral

Table 1.1: Overview of photocathode materials and their typical characteristics.

Photocathode material	**QE (%)**	**Laser wavelength (nm)**	**Response time**	**Operational lifetime**	**Laboratories /References**
Cu	0.0014	266	<< ps	very long	SLAC [4], ARGONNE [35], BNL [36], MIT [37]
Mg	0.06	266	<< ps	very long	LCLS [4], ARGONNE [35], BNL [38] University of Tokyo [39]
Ba	0.100	337	<< ps	long	[40]
Y	0.050	266	<< ps	very long	ARGONNE [35], BNL [36]
Ca	0.004	248	<< ps	very long	ARGONNE [35]
Sm	0.007	266	<< ps	very long	BNL [36]
Nb	0.001	266	<< ps	very long	BNL [41]
Pb	0.17	266	<< ps	very long	SLAC [4], BNL [36]
Cs_2Te	4 - 20	266	$\sim$ ps	10 - 100 hours	DESY (TTF) [42], LANL [40], Fermi lab [43] CERN [40], University of Twente [40], KEK-ATF [44]
CsKTe	22.5	259	-	< 12 hours	University of Twente [45]
K_2Te	1	259	-	< 20 hours	University of Twente [46]
K_2CsSb	8	537	$\sim$ ps	< 4 hours	Bruyères-Le-Châtel [52], Milano [47], LANL [47] KEK [47], University of Twente [47],
Cs_3Sb	0.4 - 4	527	$\sim$ ps	< 4 hours	Bruyères-Le-Châtel [47]
GaAs (Cs-O)	10 - 30	532	< ns	$\sim$ 400 hours	ALICE [2], TJNAF [15], ILC [1], JAERI [9] Max-Planck Institute [48]

response in metals, can be operated at the longest wavelength 337 nm, but is less robust and cannot withstand high electric fields [34]. Nb is a promising photocathode for SRF photoinjector technology because of its inherent superconducting property. The use of Nb cavity wall as the photocathode for SRF guns will avoid the complexities of a cathode insertion and loading system. The possibility to use Nb as the photocathode has been tested at BNL and SLAC [50, 51]. Recently, Pb also has been considered as the photocathode in SRF guns since its QE of 0.17% at 266 nm is higher than Nb [50].

1.4.2 Semiconductor photocathodes

Semiconductor photocathodes are being widely used in accelerators because of their relatively high QE for excitation at visible wavelengths, reaching values in the order of 10% or more. Most semiconductors have a good response in the visible wavelength, permitting operation with practical, reliable and affordable drive laser systems. However, the major disadvantage in the use of semiconductor photocathodes is their short lifetime. Their lifetime is limited for various reasons, mainly because of their extreme sensitivity to contamination from residual gas species in the vacuum system. Ultra-high vacuum (UHV) conditions of at least 10^{-10} mbar are required for their operation, ideally though extreme-high vacuum (XHV) in the order of 10^{-12} mbar is needed. Another disadvantage is their long response time in the range of tens of picoseconds, making them unsuitable for femtosecond electron bunch generation.

There are several types of semiconductor photocathodes: alkali-antimonide, alkali-telluride and type III-V semiconductors. Cs_3Sb and K_2CsSb have a long history of use in photo-injectors [52] because of their high QE (several percent in the visible wavelength regime) and their relative ease of preparation. The main problem when using these materials is their limited lifetime due to their sensitivity to residual gases in the vacuum system. In a photo-injector which has the pressure of 8×10^{-9} mbar, the cathode lifetime can be limited to only 1 hour [29], making its use in RF guns impractical. K_2CsSb has been used at the ELSA linac at Bruyères-Le-Châtel, KEK

and is the part of the SRF photo-injector R&D programme at BNL [28, 40, 47, 52]. Cs_2Te with a QE of 10% at 263 nm has been proved to withstand a poisoning from residual gases and has been successfully operated in the NRF gun [3]. However, as in the case of metal, the sensitivity to UV wavelength requires a lot of power from the drive laser at longer wavelengths to generate the UV light. The use of Cs_2Te photocathode has been proposed and developed at LANL and CERN [42, 47].

GaAs is also used as a polarised electron source [40, 53]. With advances in semiconductor technology, GaAs can be grown on a different substrate such as GaAsP, creating the lattice mismatch between the active photocathode layer and the substrate. The lattice mismatch creates degeneracy at the top of the valence energy bands. When excited by circularly-polarised resonant photons, the electrons emitted from any one of these levels have a preferred spin polarisation [34, 54]. GaAs has become very attractive for high average current accelerators since its QE can be enhanced by activation to a negative electron affinity (NEA) state. This state is achieved when depositing Cs and oxidant (either O_2 or NF_3) layers onto its atomically-clean surface [55, 56, 57], in doing so QE's as high as 25 - 30% at 532 nm have been demonstrated [48]. Although NEA GaAs has a very short lifetime, its QE can be recovered by re-depositing Cs on the surface, making it practical for use. More details of this photocathode will be discussed in the next chapter. GaAs is being used currently in several accelerators such as ALICE at the Daresbury Laboratory [2], the IR-FEL and CEBAF (polarised electrons) at TJNAF [15], and its use has been proposed for the ILC [1].

1.4.3 Summary

Selection of the optimal photocathode material depends on the application. For example, Cu has been chosen for the LCLS since it can form a single piece with the end plate of the half cell cavity allowing RF gun operation at the highest possible field values. Its QE is relatively low, but its fast response time at the sub-picosecond level allows the production of electron bunches whose temporal structure closely match that of the drive laser. The metal photocathode is also sufficiently rugged to

operate in an RF gun [5, 58]. In contrast with the LCLS RF gun, GaAs has been selected for the ALICE DC gun because its high QE can fulfill the requirement of high peak and average current for the ERL based light source. It responds to green laser light (532 nm), thus making the drive laser practical and affordable. The aim of this thesis is to study the GaAs photocathode for the ALICE accelerator. An overview of the ALICE accelerator and its photocathode electron gun is given in the following section.

1.5 ALICE and its electron gun

ALICE (Accelerators and Lasers In Combined Experiments) is a test facility for a fourth generation accelerator which has been designed and built at Daresbury Laboratory [2]. It is a 35 MeV ERL test facility based on 1.3 GHz SRF technology with a photo-injector electron source. The electron beam is used to drive a FEL. A schematic layout of the ALICE facility is shown in Figure 1.7.

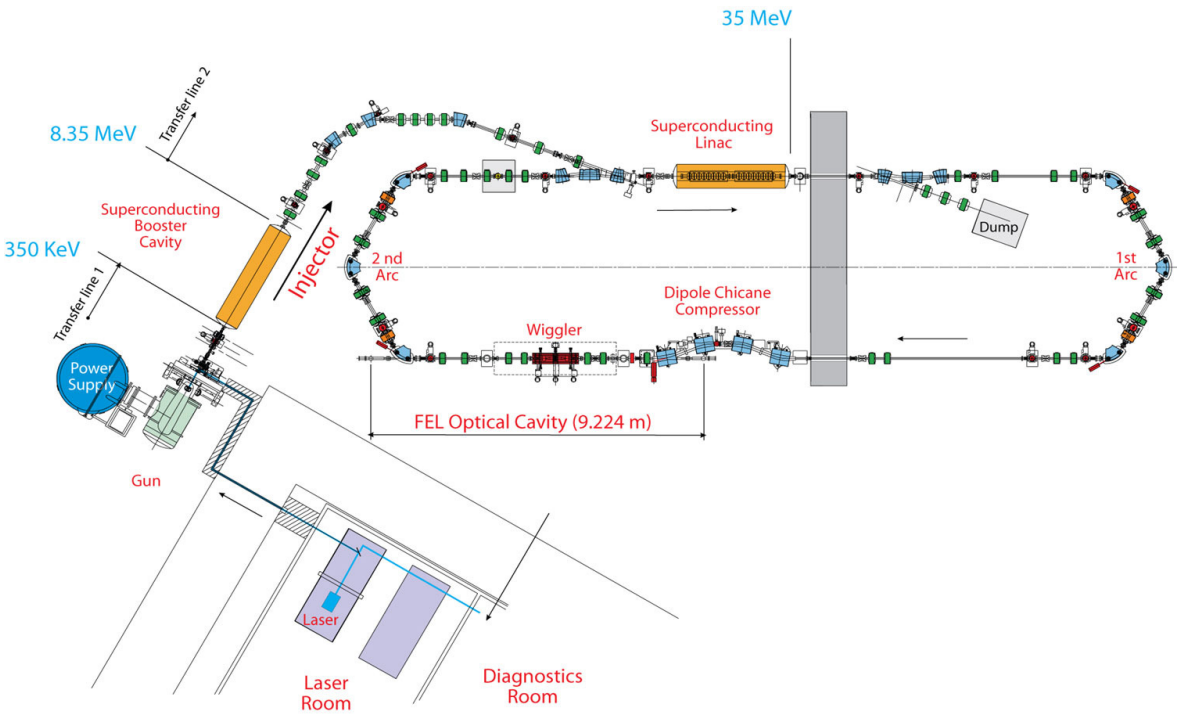

Figure 1.7: Schematic layout of the ALICE facility at Daresbury Laboratory [2].

The machine comprises a 350 keV DC photocathode gun with 2 solenoids for emittance compensation. Following the gun is a 1.3 GHz normal conducting single cell buncher cavity for reducing the energy spread in the beam to tolerable levels for the FEL to lase successfully. The gun generates bunches of up to 80 pC at a bunch repetition frequency of 81.25 MHz, equivalent to CW current of 6.5 mA. However, the gun does not operate CW, instead producing macro pulses at a repetition rate of 1 - 20 Hz, with each macro-pulse variable in length from a single electron bunch to a 100 μs window containing 8,125 electron bunches. There is then a superconducting booster module which consists of two 9-cell, 1.3 GHz TESLA-type cavities. These structures have accelerating gradients of 4.8 and 2.9 MV$\cdot$m^{-1} for the 1st and 2nd cavity, respectively, which can accelerate the beam to an energy of 8.35 MeV, this being the injection beam into the recirculating section.

The main accelerating module consists of a pair of 9-cell TESLA-type superconducting cavities operated at 1.3 GHz, and have accelerating gradients of 12.9 MV$\cdot$m^{-1} per cavity. This module accelerates the beam to a final energy of 35 MeV. Both superconducting linacs are cooled down to approximately 2 K with liquid helium. After being turned by 180° in the first arc, the electron beam reaches a dipole magnetic chicane (bunch compressor) where it is compressed longitudinally to sub-picosecond bunch lengths. Then the beam enters the wiggler magnet which drives the mid IR-FEL. With tunable beam energy and variable undulator gap, the FEL generates IR radiation in the 4 - 12 μm wavelength range. After the FEL, the beam is returned to the main linac via a second 180° arc, arriving when the RF phase is exactly opposite to that of the initial accelerating phase. The beam is thus decelerated and gives energy back to the electromagnetic field inside the linac RF cavities (energy recovery) emerging at the injection energy of 8.35 meV. The energy-recovered beam is then diverted to the beam dump, ending its short but useful life.

In contrast to other light sources based on storage ring technologies, the performance of the ERL strongly depends on the electron source. The DC gun is seen to be the most mature technology, and is therefore suitable for an ERL. The ALICE electron gun is a replica of the IR-FEL DC electron gun design at TJNAF, as shown in Figure 1.8. The gun consists of an earthed Pierce-type anode and GaAs

photocathode mounted on the face of a spherical cathode ball. The gun is designed to operate at 350 kV, generating electric fields at the level of ∼8 MV·m^{-1} at the cathode ball surface and ∼12 MV·m^{-1} at the cathode stem. The power supply is rated to 500 kV and the gun was conditioned to 485 kV, however, it is normally operated at 350 kV to reduce the field emission current and outgassing within the vacuum vessel. The photocathode is illuminated by green laser light from a CW mode-locked[1], frequency-doubled Nd:YVO_4. This laser system provides a 532 nm beam with a transverse size on the cathode of ∼4 mm full-width-half-maximum (FWHM) at a repetition rate of 81.25 MHz. The intrinsic laser pulses are Gaussian in profile with a 7 ps FWHM length, though a pair of pulse-stacking crystals increase this to a 28 ps pulse with a broadly flat top. The gun is kept under XHV in the middle 10^{-12} mbar range without operation and in the low 10^{-11} during the operation to protect the photocathode from contamination, and thus prolong its lifetime.

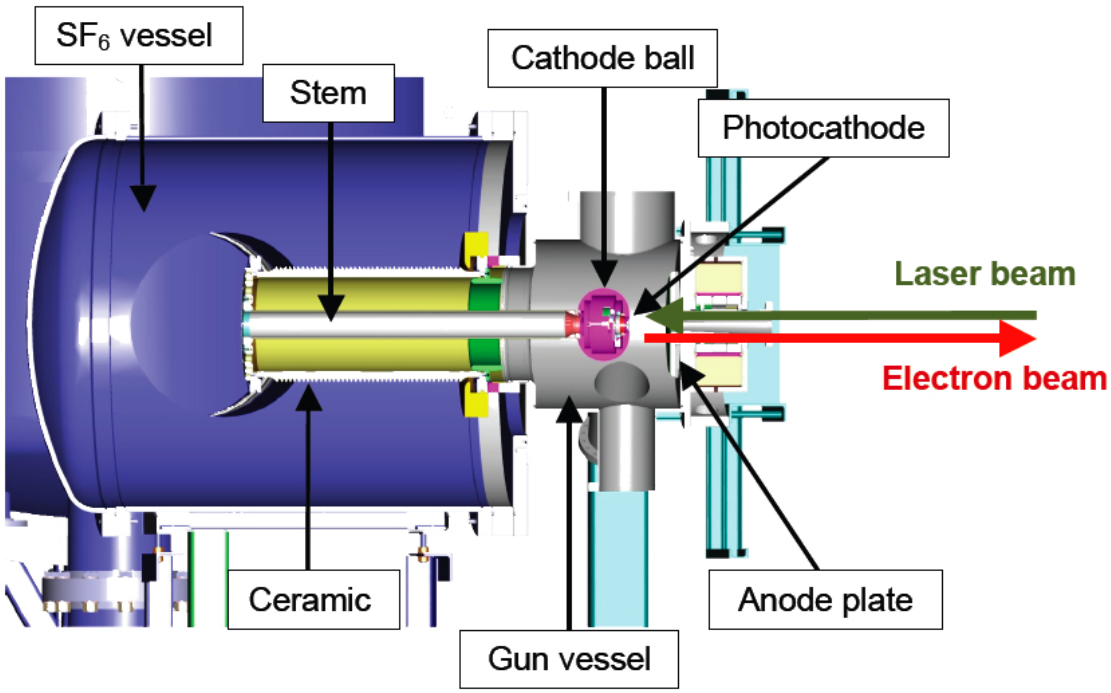

Figure 1.8: Schematic diagram of the ALICE DC photo-electron gun.

[1]A pulse laser beam

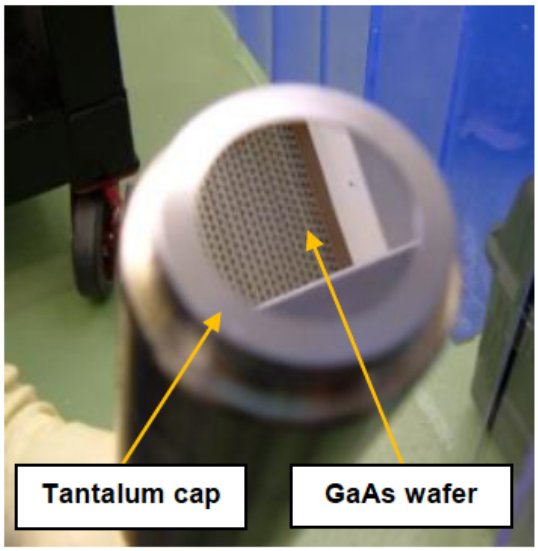

Figure 1.9: Photograph of the GaAs photocathode during assembly into the ALICE photo-electron gun. The bulk GaAs wafer with a diameter of 31 mm is mounted on the molybdenum plug and positioned with a tantalum cap with circular cutout in the centre, leaving the centre portion of the wafer exposed to approximately 25 mm in diameter.

A photograph of the GaAs photocathode is shown in Figure 1.9. To enhance the QE, the GaAs photocathode is activated to the low electron affinity (LEA) state by depositing Cs and oxidant (O_2 or NF_3) layers onto its atomically-clean surface, performed inside the gun under XHV conditions. The QE of the freshly-activated photocathode is normally about 3%, as shown in Figure 1.10 (a), although this decays with operational time as shown in Figure 1.10 (b). In the ALICE gun, the photocathode typically has an operational lifetime of between 200 - 400 hours, as shown in Figure 1.11 (a). The cathode lifetime is limited by several mechanisms, but the main one is the ion-back-bombardment. These mechanisms will be discussed in detail in Chapter 2. One of the other mechanisms responsible is the contamination of the GaAs photocathode from residual gases inside the gun vessel. As it is shown in Figure 1.11 (b), the QE of the cathode still gradually degrades with time even when the cathode is not operated under high laser power illumination and high electric field.

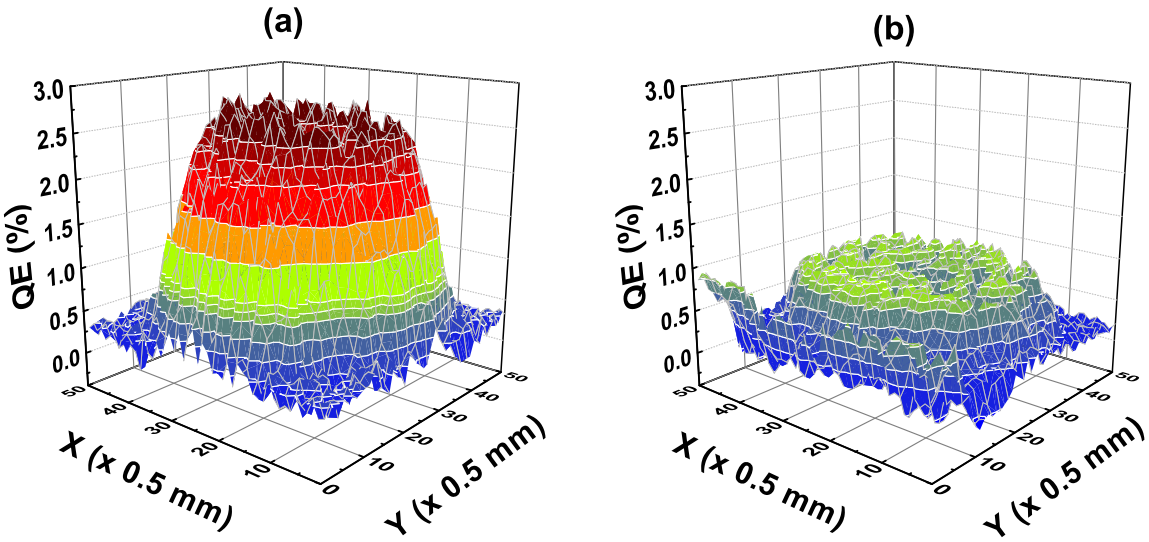

Figure 1.10: QE scan map for a freshly-activated (a) and degraded (b) GaAs photocathode in the ALICE photo-electron gun [2]. The scan area consists of 50×50 data points with a resolution of 0.5×0.5 mm^2.

When the QE decreases to the point where the required bunch charge can no longer be obtained, the QE can be partially recovered by re-depositing Cs on the photocathode surface. This is known as re-caesiation, and typically occurs every 14 days. After several cycles, the QE of the photocathode will degrade until it is not possible to recover the QE simply through the re-caesiation. The photocathode needs to be cleaned and deposited with the Cs and oxidant layers on the surface again. Since there is no photocathode exchange system, this QE recovery process is currently performed inside the gun which disturbs the gun performance and stability, and also interrupts the operation.

An upgrade to the ALICE photoinjector electron gun is currently underway. A plan view of the upgraded gun is shown in Figure 1.12. As part of the gun upgrade program, a GaAs photocathode preparation facility (PPF) with a "load-lock" interface has been designed and built. The main benefits of the PPF facility can be summarised as follows:

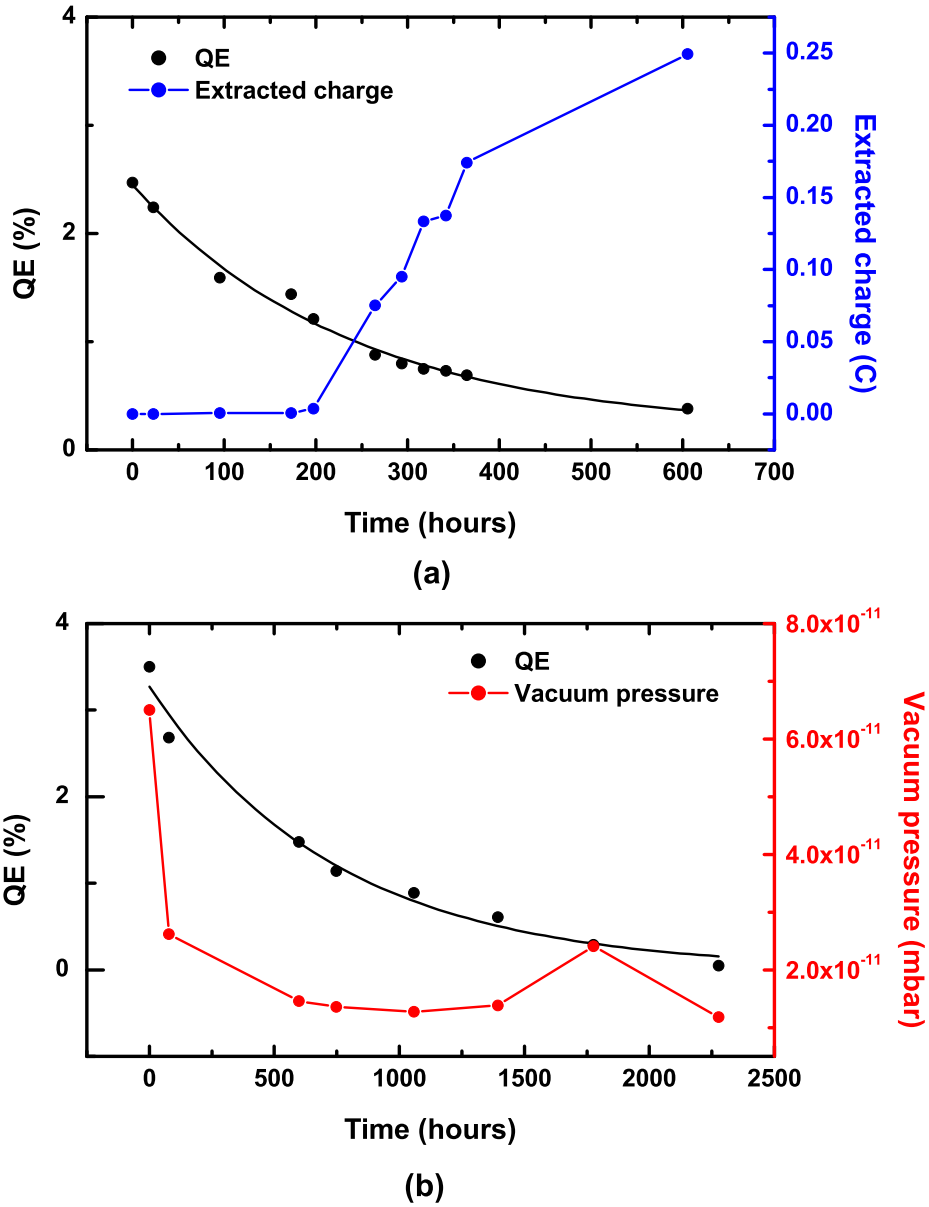

Figure 1.11: (a) The QE operational lifetime and charge extracted from the ALICE photocathode in the ALICE DC gun measured between 25 May 2010 to 7 June 2010. The 1/e lifetime is estimated to be 404 hours. (b) The QE dark lifetime (without laser illumination and high applied voltage) of the ALICE photocathode and the vacuum pressure in the ALICE DC gun measured between 21 February 2009 to 27 May 2009. The 1/e lifetime is estimated to be 892 hours.

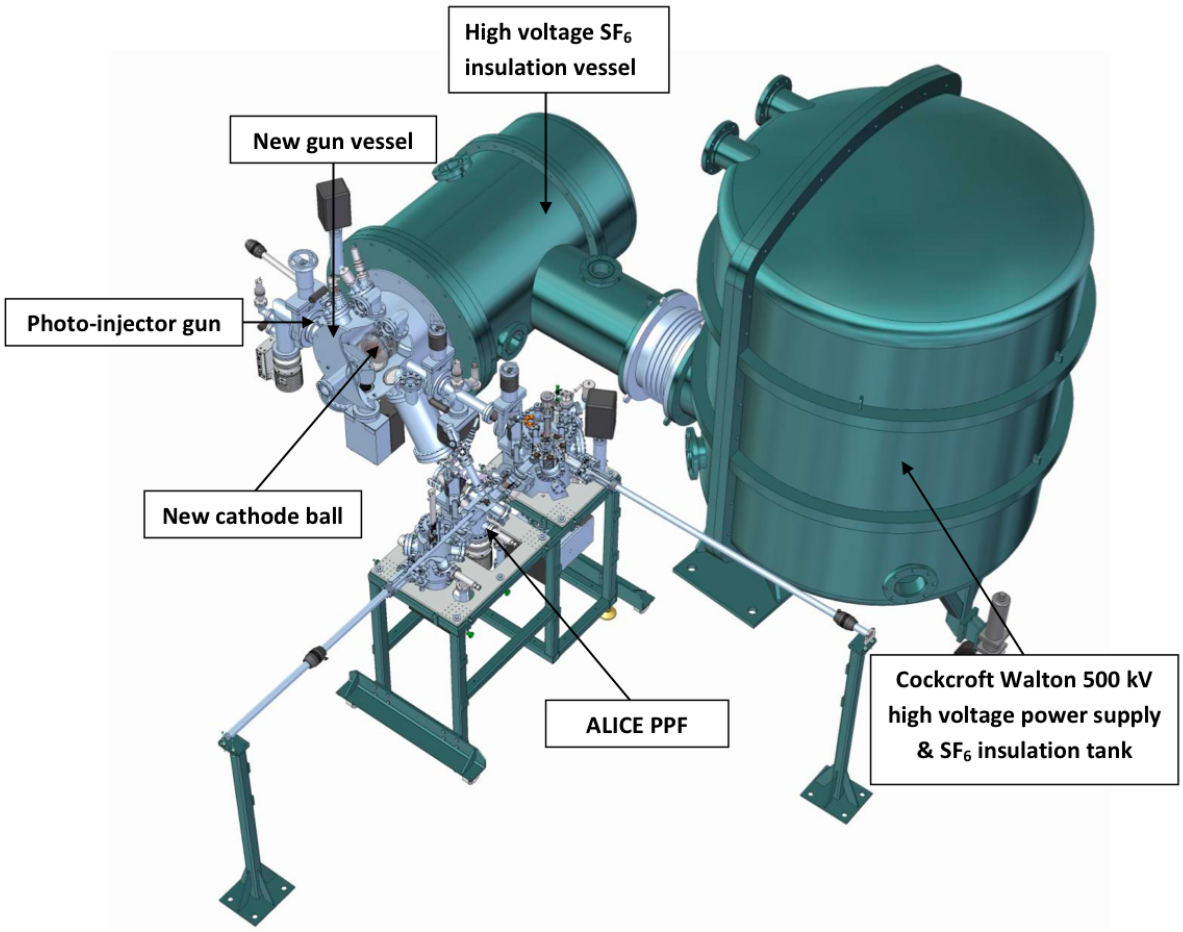

Figure 1.12: A plan view of the ALICE photo-electron gun upgrade showing the photocathode preparation facility.

- It provides a much more rapid and reliable way to exchange the photocathode. The facility accommodates up to six photocathodes, and serves as the transition point for photocathodes between the laboratory at atmospheric pressure and the photo-injector gun at XHV. The PPF avoids the need to break the gun vacuum and then re-establish the XHV operating conditions following a photocathode change from several weeks to a few hours, avoiding all of the risks associated with bake-out such as leaks or ceramic failure. This is essential for guns delivering average currents of 10 mA or more when the operational lifetime of a photocathode does not exceed a few days because a long delay for a photocathode change is unacceptable at a user facility.

- The PPF has a capability to prepare GaAs photocathodes, i.e., clean and activate to the NEA state, in a controllable and reproducible way, as in semiconductor physics experiments, thus significantly increasing the quantum efficiency and lifetime. Currently, the ALICE gun is not equipped with separated loading and photocathode preparation chambers, so the gun has to be opened and exposed to the atmosphere every time the photocathode is replaced. After photocathode loading, the gun chamber should be baked at 250 °C for several weeks. During the baking process, the photocathode is contaminated by residual gases, leading to low QE of photocathode and an activation procedure is not reproducible.

- When the activation process is moved out of the gun, risks arising from the photocathode preparation process such as gun electrode exposure to Cs is also removed, and consequently, this improves the overall high voltage performance.

- It will provide opportunities and the flexibility for the gun to operate with new different types of the photocathode. One of the possible options under our consideration is the use of alkali antimonide-based photocathodes, which may operate at a wavelength of 532 nm with reasonably high levels of quantum efficiency and fast response time.

Presently, the PPF has been constructed and successfully commissioned in the "stand-alone" mode, i.e., not connected to the gun, at the Cockcroft Institute, Daresbury Laboratory. I made a major contribution at the commissioning stage. New GaAs/AlGaAs hetero-structure photocathodes have been designed and developed in collaboration with the Institute of Semiconductor Physics (ISP/Novosibirsk). A QE as high as 15% from the new photocathodes has been demonstrated at a wavelength of 635 nm in the first operation [59, 60]. A test gun vessel and cathode ball have been built and connected to the PPF in order to prove the design and fully test the transfer mechanism for the movement of photocathodes between the gun vessel and the PPF. These mechanisms have already demonstrated acceptable performance and are functioning well at both atmospheric pressure and XHV test regimes. The PPF

system and the photocathode preparation procedure for ALICE will be discussed in greater detail in Chapter 5.

1.6 Overview of this thesis

This thesis describes the development and exploitation of the ALICE PPF. This unique facility has shown many great advantages for the development of an electron source for the accelerator technology and will provide new opportunities for new physics experiments. The aim is to use this facility to investigate the degradation in the QE of GaAs photocathodes under exposures to gases typically present in the gun vacuum. This knowledge will be of great benefit in the development of GaAs photocathodes and photo-injector technologies.

This thesis is oganised as follows. Chapter 2 reviews the physics of GaAs photocathodes and explores the present understanding of the NEA state and photoemission process. The limitations of GaAs as a photocathode are also discussed in this chapter. In spite of the performance achieved with a GaAs photocathode in the ALICE PPF, significant effort has been expended in this research to develop optimised procedures for the preparation of NEA GaAs photocathodes. I have also developed a photocathode preparation and surface characterisation system which permits the preparation of NEA GaAs photocathode in conjunction with the application of several surface science characterisation techniques within the same vacuum system. This system has lead us to a better understanding of the individual preparation processes through information on surface properties such as surface chemistry and bulk crystallinity, allowing optimisation of cathode processing and supporting work in the PPF. Chapter 3 describes this surface science characterisation system and experimental techniques in detail. Chapter 4 is dedicated to the study of several photocathode preparation techniques in the surface characterisation system. Chapter 5 describes the ALICE photocathode preparation facility, and the commissioning of the system, including the new photocathode designs and operation of the facility. The results obtained from the different type photocathodes with their preparation procedure detail are presented in Chapter 6. Using the PPF, I have

investigated the degradation in the QE of NEA GaAs photocathodes under exposures to gases typically present in the gun vacuum, namely O_2, CO_2, CO, H_2, CH_4 and N_2. The effects of these gases on the NEA GaAs photocathodes are presented and discussed in Chapter 7. In closing this thesis, Chapter 8 summarises the work undertaken and results obtained, and suggests further experiments that will help in the future development of GaAs photocathodes.

Chapter 2

The physics of GaAs photocathodes

This chapter contains the fundamental physics of GaAs photocathodes. It is organised as follows. Some of the fundamental properties of GaAs are reviewed in section 2.1. The creation of the NEA state in GaAs is discussed in section 2.2, followed in section 2.3 by the basic physics involved in the photoemission process. Finally, the practical limitations of the NEA GaAs photocathode as an electron source for accelerators are discussed in section 2.4.

2.1 GaAs material properties

GaAs is a type III-V semiconductor, with gallium (Ga) from group III of the periodic table and arsenic (As) from group V. It was first created by Goldschmidt in 1929 [61], and some reference properties for GaAs are provided in Table 2.1. GaAs has a zinc-blende structure, so its structure consists of two interpenetrating face-centred cubic (fcc) lattices; the basic unit of which consists of one Ga atom and one As atom. One atom is at (0, 0, 0) and the another atom is at ($\frac{1}{4}$, $\frac{1}{4}$, $\frac{1}{4}$)a [62]. This structure contains four units of GaAs in a volume a^3 as illustrated in Figure 2.1.

The Ga bonds to four As neighbours with the nearest neighbour bond length $r_0 = \frac{\sqrt{3}a}{4}$. The structure has three main symmetry planes defined by the Miller indices *(hkl)* which are (100), (110) and (111). The most readily-cleaved plane is the

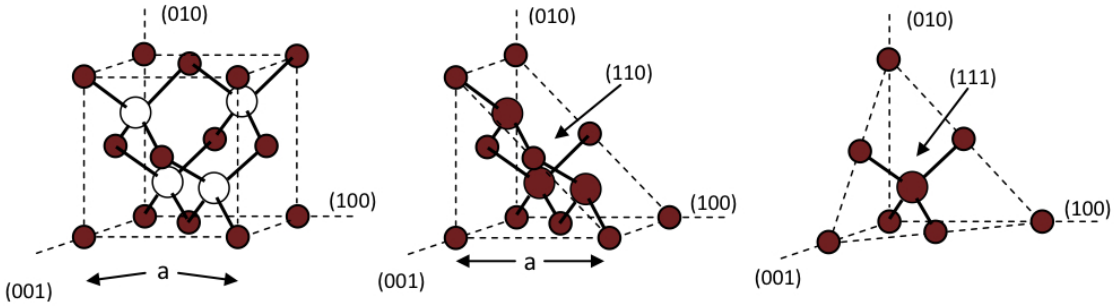

Figure 2.1: The zinc-blende structure and bi sections of GaAs showing the main symmetry planes: (100), (110) and (111).

(110) plane, while the most commonly used surface plane in the photocathode application is the (100) because this orientation provides the best cosmetic quality of the epitaxial layers and multilayer heterostructures [63].

Table 2.1: Material reference properties for bulk GaAs [64].

Property	Parameter
Molecular weight	144.645 amu
Crystal structure	Zinc-blende (Cubic)
Lattice constant (a)	5.65330 Å
Nearest neighbor distance (d)	2.44795 Å
Unit cube volume (a^3)	1.80678×10^{-22} cm^3
Molecular density (d_m)	2.2139×10^{22} cm^{-3}
Melting point (T_m)	1513±2 K
Specific heat	0.327 J·g^{-1}·K^{-1}

The energy band diagram for GaAs is shown in Figure 2.2. GaAs is a direct band gap semiconductor, so the valence band maximum (VBM) lies directly above with the conduction band minimum (CBM) at the Γ point in the first Brillouin zone (reduced wave vector, $q = 0$). The VBM is separated from the CBM by the energy gap (E_G) which varies with temperature from 1.42 eV at 300 K to 1.50 eV at 120 K. The top of the valence band has three degeneracies arising from angular momentum symmetry $L = 1$. The top two degeneracies are known as the heavy

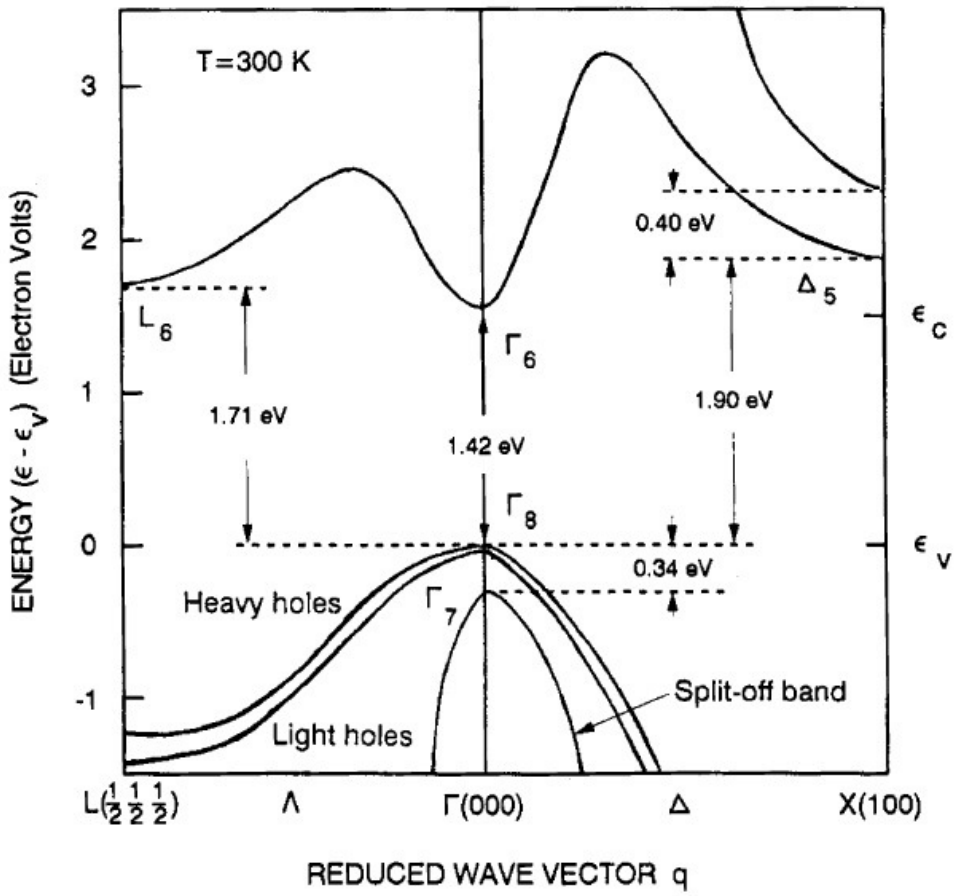

Figure 2.2: Energy band diagram for a bulk GaAs at 300 K [65].

hole (HH) and light hole (LH) respectively. The third degeneracy is the split off hole (SO) which is separated by the spin-orbit splitting energy (ΔE =0.34 eV at 300 K) and therefore, it does not play any role in bulk electronic properties for most purposes [66]. Above the CBM at Γ, the other minima in the conduction band lie in the (111) direction (L), and the (100) direction (X), and are separated from the CBM by 0.29 eV and 0.48 eV, respectively.

Photo-excitation from the valence band to states in the conduction band requires the conservation of both the k-vector and energy. In a direct bangap semiconductor, because the CBM lies directly above the VBM, electrons can move into the CB with no phonon absorption or emission involved in the process. Therefore the photon absorption rate of GaAs is high, making it a highly effective photo-emitter material [102], and an excellent photocathode choice.

2.2 Formation of the negative electron affinity (NEA) GaAs photocathode

GaAs is currently one of the most efficient photocathode materials which naturally has a positive electron affinity (PEA). The energy band diagram for a typical GaAs photocathode surface is illustrated in Figure 2.3 (a). The diagram illustrates the energy, E, in vertical axis and the space coordinate, z, which is perpendicular to the GaAs surface in the horizontal axis. In the diagram, E_{CBM} denotes the conduction band minimum which are separated from the valence band maximum, E_{VBM}, by the energy gap, E_G. With good approximation one can say that there are no electron states within E_G [102]. E_F denotes the Fermi energy level which is close to the middle band gap for the GaAs photocathode surface and an intrinsic semiconductor. Note that in semiconductor physics, the Fermi energy is used to denote the chemical potential of the electrons at non-zero temperature rather than the highest occupied energy level at the absolute zero of temperature. It is dependent on carrier concentration and on temperature.

At the absolute zero temperature, electron states in the conduction band are totally empty, while those in the valence band are completely filled. As the temperature increases, some of the electrons in the valence band are promoted into the conduction band, leaving holes (empty states) in the valence band. Electrons in the conduction band are normally prevented from escaping from the surface by the surface potential called the vacuum level, E_{VAC}. The **electron affinity** (EA, denoted by χ in this thesis) is defined as the difference in energy between the conduction band minimum, E_{CBM}, and the vacuum level, E_{VAC}, and is of the order of 4 eV for GaAs with an energy gap of 1.4 eV [102]. In a PEA photocathode the vacuum level lies above the bottom of the conduction band, preventing the escape of excited electrons in the conduction band from the surface.

However, GaAs has an ability to attain the negative electron affinity (NEA) state whereby the vacuum level is located below the conduction band minimum. Thus electrons with all energies excited to the conduction band can escape to the vacuum, giving a high QE at all photon energies greater than the band gap. The NEA state

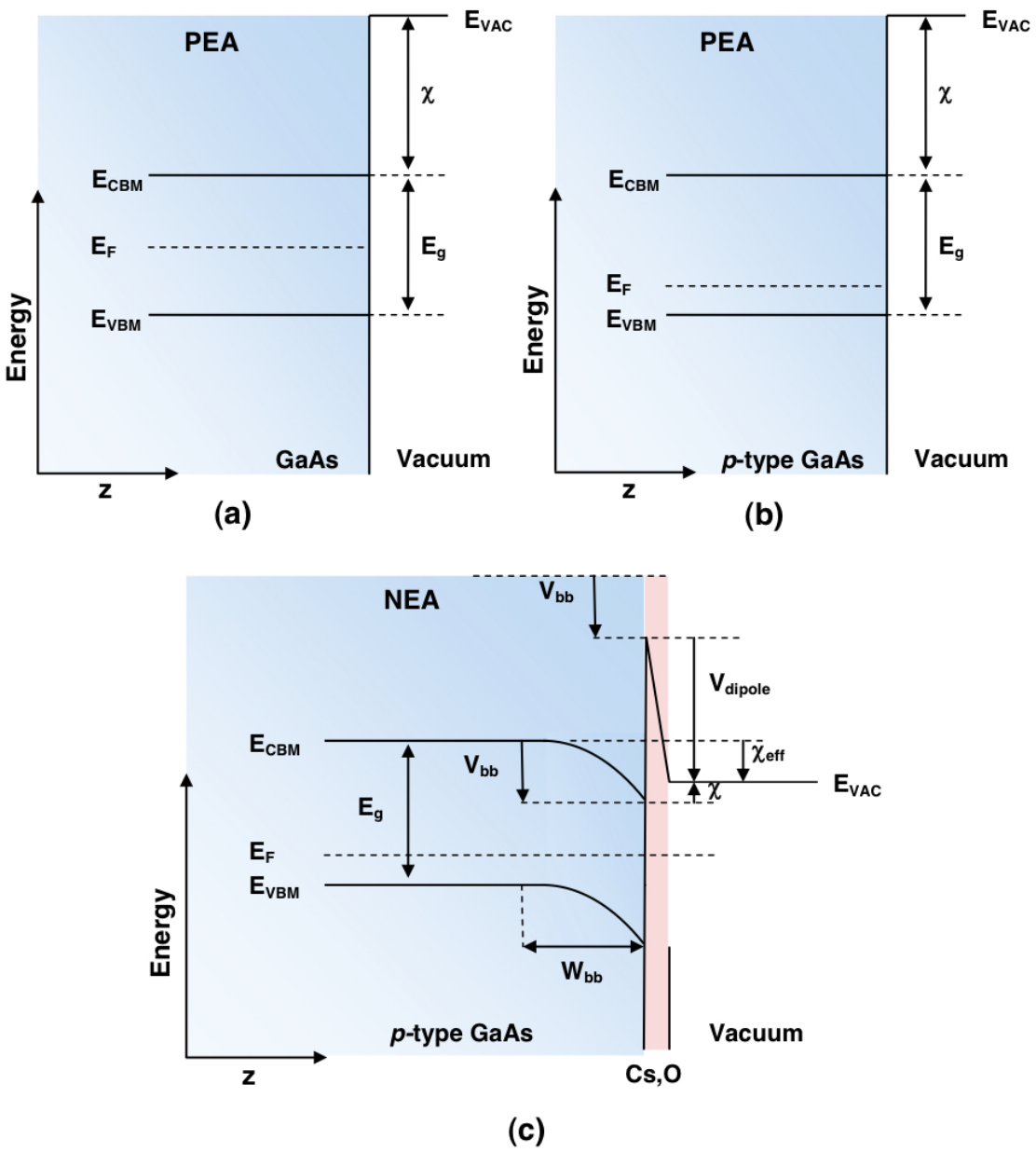

Figure 2.3: Schematic energy diagram for an intrinsic GaAs surface (a), p-type GaAs surface (b) and p-type GaAs surface deposited with Cs and O layers (c). Both the intrinsic GaAs and p-type GaAs surface exhibit a positive electron affinity (PEA) state, while a p-type GaAs surface deposited with Cs and O layers shows a negative electron affinity (NEA) state.

can be formed by alternately applying Cs and oxidant (either O or F) layers onto this highly-doped p-type surface [102].

When the GaAs photocathode is doped p-type, the acceptor impurity leads to additional energy levels in the band gap, close to the E_{VBM}. The most commonly-used acceptor impurity for a GaAs photocathode is zinc (Zn) with a typical concentration level in the range of 10^{18} - 10^{19} cm^{-3}. This energy level of acceptor (Zn) is of approximately 3.1 eV higher than E_{VBM} [68]. At room temperature most of the Zn atoms are ionised, having captured electrons from the valence band and become negatively-charged. Thus holes are created in the valence band and these holes are counted in the concentration of holes in the bulk GaAs. The concentration of holes is approximately equal to the concentration of acceptors. The Fermi level will adjust itself by moving to the vicinity of the E_{VBM} in the bulk, as shown in Figure 2.3 (b), to keep the number of holes equal to the number of electrons.

Further deposition of Cs and oxidant layers onto this highly-doped p-type surface causes the energy bands at the surface to bend *downward* and the vacuum level is strongly reduced, as shown in Figure 2.3 (c). One approach for explaining this formation is the *dipole layer model* [69, 70, 71, 72], which can be described in the following way. The adsorption of Cs induces donor-like surface states in the p-type GaAs surface. These surface states, which may also be found prior to the deposition of Cs on the surface in the form of defect-induced states, give up their electrons to the bulk and become positively-charged [73, 74]. The bulk region in the vicinity of the surface will thus become negatively-charged, and a depletion region is formed over a distance W_{bb}. To maintain equilibrium, the energy bands at the surface are bent downward by the amount V_{bb} as shown in Figure 2.3 (c). The width of band bending, W_{bb} (cm) and the band bending potential can be controlled by the doping concentration as:

$$W_{bb} = (\frac{2\epsilon V_{bb}}{eN_A})^{1/2} \tag{2.1}$$

where ϵ is the dielectric constant (F·cm^{-1}), e is the electron charge and N_A is the doping concentration (cm^{-3}) [68]. In the case of high level of p-doping in the range 10^{19} cm^{-3}, the width of the band-bending is typically of the order of ∼10 nm with

V_{bb} of 0.3 - 0.5 eV [75]. If we define the *effective electron affinity* as the difference in energy between the conduction band minimum in the bulk and the vacuum level, the *effective* EA is reduced by amount of V_{bb}. Since the width of the band-bending is comparable to the optical absorption depth, $1/\alpha(h\nu)$ which is normally on the order of 1 μm for near-threshold excitation (photon energy just greater than the E_G, ~1.4 eV) [76]. Photon absorption can take place in the bulk beyond the band bending region and electrons are excited at distances up to the material escape length. Thus, it can be assumed that there is no significant distinction between the *effective* EA and the *actual* EA.

The Cs atoms also contribute *their* electrons to the semiconductor bulk, forming a dipole layer on the surface. The resulting electric field decreases the vacuum level, and drives the reduction of the EA. This can be considered simply as a parallel-plate capacitor. Co-deposition of oxidant (O or F) layers enhances this effect, leading to a strong decrease of the vacuum level by the level of V_{dipole}. Alternate application of Cs and oxidant layers leads to the formation of the NEA state on the surface [71, 72]. The Cs and oxidant layers also have their own potential energy which is at a higher level than the vacuum level. Therefore, there exists a finite barrier (see Figure 2.3 (c) within the dipole layer which is commonly treated as being completely electron transparent in the model and, hence, we can ignore its presence [69]. The Cs and oxidant layers gives the main contribution to the most important parameters of NEA GaAs photocathode, such as QE, longitudinal and transverse energy spreads of emitted photoelectrons, the photocathode dark current, the maximum value of emitted photocurrent, degradation rate of photocathode, etc. However, the precise nature of the Cs and oxidant layer is not fully understood at the present, so the dipole model is yet to be validated [71, 72]. Controversial issues remain which assign varying degrees of confidence to the models such as the nature and chemical state of the adsorbed Cs and oxidant layer. This is the ongoing focus of research [73, 74, 77, 78].

2.3 The photoemission process

This section discusses the photoemission process in the NEA GaAs photocathode following an explanation given by Prof. A.S. Terekhov [79]. This explanation is based on the Spicer's three-step model in which the diffusion processes of different groups of emitted electrons is taken into account to the model. A schematic energy band diagram illustrating the photoemission process in the NEA GaAs photocathode is shown in Figure 2.4. The photoemission consists of three steps:

1. the absorption of photons by a photocathode and the following photoexcitation of electrons
2. the transportation of the photoexited electrons from the bulk to the photocathode-vacuum interface
3. the emission into the vacuum

2.3.1 Absorption

In the first step, electrons absorb photons, and are excited from the valence band into higher energy states in the conduction band. If the photocathode is illuminated by an incident light perpendicular to its surface, the light intensity $I(z, h\nu)$ after it transverses a thickness z of the photocathode is given by the Buger's law [80]:

$$I(z, h\nu) = (1 - R(h\nu))e^{-\alpha(h\nu)z} \tag{2.2}$$

where $R(h\nu)$ is the reflectivity coefficient of the surface, and $\alpha(h\nu)$ is the absorption coefficient. Equation 2.2 shows that the intensity of the incident light decreases exponentially with thickness of the photocathode, z, which, in turn, implies the probability for a photon to be absorbed at the distance z from the photocathode surface. Both absorption and reflection coefficients of GaAs depend on photon energy. The spectrum of absorption coefficient for GaAs is shown in Figure 2.5. It can be seen in Figure 2.5 that the absorption coefficient increases dramatically, reaching to approximately 10^4 cm^{-1} when the incident photon energy is close to

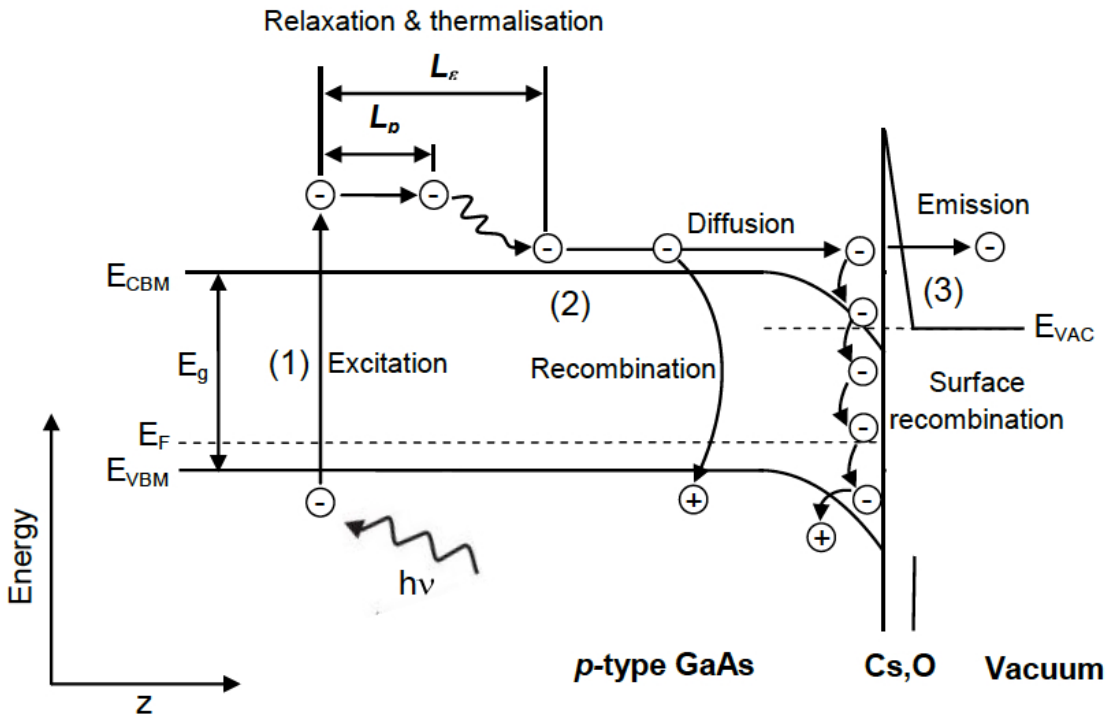

Figure 2.4: Schematic energy band diagram illustrating the photoemission process for the NEA GaAs photocathode. The diagram shows the electron energy, E, along with vertical scale versus space coordinate, z, perpendicular to the photocathode surface. The photoemission process consists of three steps: **(1)** electron absorbs a photon, **(2)** the excited electron diffuses to the surface, and then **(3)** escapes across the surface barrier into the vacuum.

the energy gap of GaAs (approximately 1.4 eV), and then it strongly increases with photon energy. The spectrum of reflection coefficient for GaAs measured at a normal incidence angle to the surface is shown in Figure 2.6. It is clearly seen that the reflection coefficient strongly depends on the incident photon energy, it increases from 0.322 at the photon energy of 1.40 eV up to 0.372 at the photon energy of 2.3 eV.

When the electrons absorb photons with an energy exceeding the energy gap, E_g, of the photocathode, they can be excited into the conduction band and generate holes in the valence band. The energy of the absorbed photon, $h\nu$, is distributed

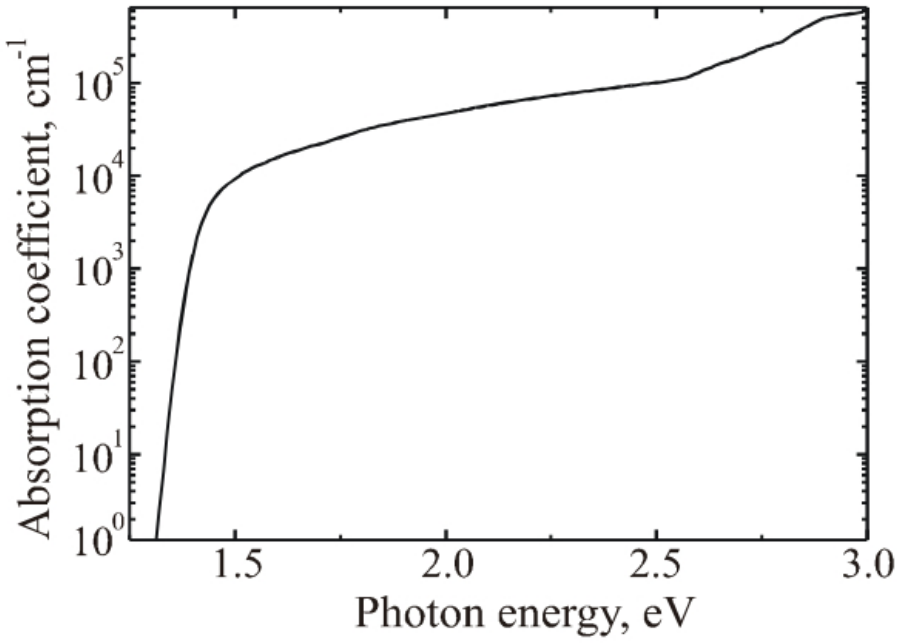

Figure 2.5: Spectrum of absorption coefficient for GaAs taken from [79].

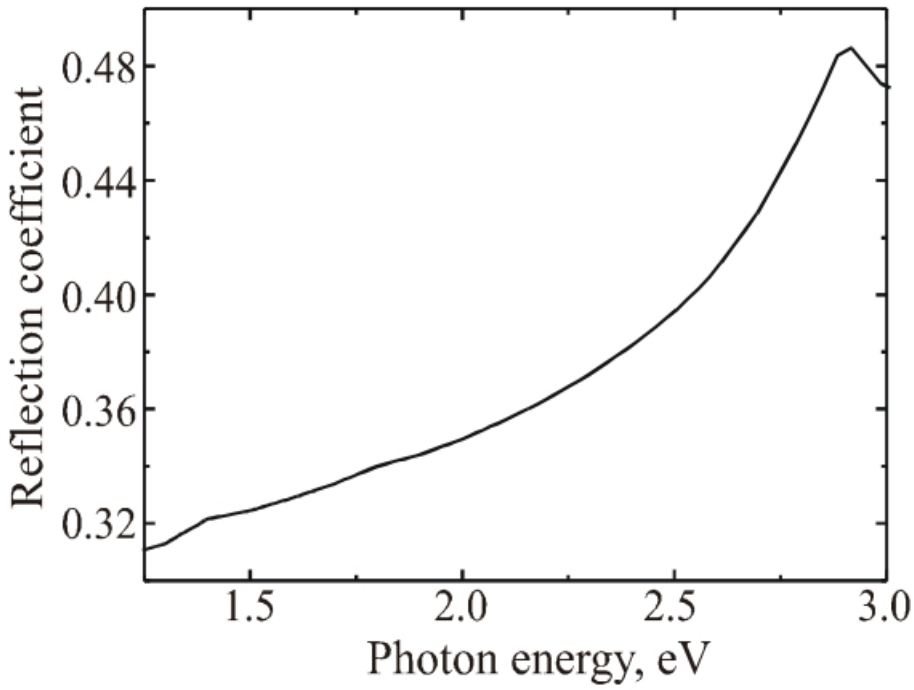

Figure 2.6: Spectrum of reflection coefficient for GaAs taken from [79].

between the electron and hole following the rules [79]:

$$E_{ie} = \frac{(h\nu - E_g) \times m_h}{m_e + m_h} \tag{2.3}$$

$$E_{ih} = \frac{(h\nu - E_g) \times m_e}{m_e + m_h} \tag{2.4}$$

where E_{ie} is the initial energy of electron, E_{ih} the initial energy of hole, and m_e and m_h are the effective masses of electron and of hole, respectively. It is noted that the initial energy, E_{ie}, is calculated with reference to the conduction band minimum, E_{CBM}.

2.3.2 Transportation/thermalisation

After the absorption and photo-excitation to the conduction band, the electrons move ballistically and are transported to the surface of the photocathode. These electrons are called "hot" photoelectrons and their velocity, v_e, can be calculated from their kinetic energy which is directly changed from their initial energy, E_{ie}, using the equation [79]:

$$v_e = \sqrt{\frac{2E_{ie}}{m_e}} \tag{2.5}$$

During transportation to the surface, these electrons can undergo scattering from other excited electrons, holes and phonons, and thus exchanging energy. A distance that the excited electron can travel before its first scattering, is called the momentum relaxation length, L_p, which can be estimated from [79]:

$$L_p = v_e \times \tau_p \tag{2.6}$$

where τ_p is the photoelectron momentum relaxation time and v_e is the velocity of the excited electron. The value of τ_p depends on the energy E_{ie} and the electron scattering processes presenting in the conduction band.

For a heavily p-doped GaAs with a hole concentration of 1×10^{19} cm^{-3}, the electron-holes collision is dominant in the scattering process [79] and the τ_p can have the value of approximately 10^{-13} s [75]. If we assume that the excited electron

with an effective mass, $m_e = 0.067\,m_0$, has an initial energy, E_{ie}, of approximately 0.3 eV (when the photocathode is illuminated with red laser), v_e can be estimated to be of 10^6 m·s^{-1}, using the Equation 2.5. Therefore, the L_p can be calculated to be ∼100 nm from the Equation 2.6. This means that the electrons which are excited within distances of less than 100 nm from the photocathode surface and are directed toward the surface, can be emitted ballistically into vacuum without losing their initial energy. However, the amount of electrons which can escape ballistically with their initial energy is very low and can be neglected in most cases. This is because the excited electrons have to cross the Cs and oxidant layers before their escape into vacuum. This layer is amorphous and thus the momentum scattering probability is very high. The momentum relaxation length can be as small as ∼1 nm within this layer [79].

Most the excited electrons are not emitted ballistically and undergo further scattering. After the multiple scattering, the electrons will lose their energy and move down the energy scale from their initial energy to the bottom of the conduction band minimum, as shown in Figure 2.4. This process is called "thermalisation" of hot electrons. A mean distance that the excited electron can travel before thermalisation to the bottom of the conduction band minimum is called the thermalisation length, L_ε. The value of L_ε cannot be correctly measured, but it can be roughly estimated to be approximately 300 nm for a heavily p-doped GaAs.

After the thermalisation, the energy of the electrons are "concentrated" in the energy scale within $\sim k_B T$ energy interval above the conduction band minimum [71, 72, 79]. Since they are close to the conduction band minimum, the thermalised electrons can live typically for nanoseconds before they recombine with holes in the valence band, corresponding to the diffusion length amounts to 4 - 5 μm [72]. It is seen that the diffusion length of the thermalised electron is much longer than the momentum relaxation length, L_p, and the thermalisation length, L_ε. Therefore, the thermalised electrons are the main contribution to the photoemission from the NEA GaAs photocathodes in most cases, especially a thick active layer photocathode.

2.3.3 Emission

The electrons which can transport to the surface are emitted into the vacuum. Even in the case of the electrons which move ballistically and are directed toward the surface without scattering, the probability for these electrons to actually escape from the surface is still low because there is a finite probability of quantum mechanical reflection at the surface providing an electron reflection coefficient at the surface of approximately 95% [31, 79].

In the case of thermalised electrons, when they approach to the surface, they can be trapped within empty surface electron states within the band-bending region and localised very near to the surface. At this point, the electrons are involved in two competitive processes:

- escape of the electron from the surface state into the vacuum
- electron transition from one state to another state with simultaneous emission of phonons (lattice vibrations) [79].

The probability of an electron escaping from the surface state is proportional to the overlapping integral of the wave functions of the trapped photoelectron and the free electron states in a vacuum. This integral depends on the nature and on the energy position of the emissive surface state [79]. The electron transition from one state to another depends on the electron surface states density and the electron-phonon interaction. When the electron emits one phonon which does not exceed ∼37 meV (the maximum energy of phonons in GaAs [79]), it moves down to the lower energy state. After a few emissions, the electron is moved down to the surface state which is below the vacuum level and can no longer be emitted into the vacuum. This electron will continue to move down and eventually recombine with the holes in the valence band. This recombination is called the surface recombination.

2.4 Practical limitations of the NEA GaAs photocathode

In spite of it being highly efficient in photoemission, a GaAs photocathode activated to the NEA state is not without limitations and drawbacks. Many practical limitations in the usage of this type of photocathode material are known and must be taken into account when it is used as an electron source.

2.4.1 Photocathode lifetime

The major limitation of the NEA GaAs surface is their very short lifetime. This is because the Cs and oxidant layer is extremely sensitive to contamination. Changes in this layer lead to an instability of the NEA state, and a degradation of photocathode performance over time, the symptom being a fall in QE. As defined in the previous chapter, the gradual reduction of QE defines the cathode lifetime which itself has two different modes: dark lifetime and operational lifetime.

The dark lifetime is measured when the photocathode is not illuminated, or is illuminated at a very low laser intensity. Under a vacuum which includes partial pressures of O_2 below $\sim 10^{-13}$ mbar, the dark lifetime of a well-prepared NEA GaAs photocathode may exceed 10^3 - 10^4 hours [79]. The dark lifetime for GaAs is mainly limited because of:

- chemical adsorption of residual gas species in the system, particularly H_2O, O_2, CO_2 and CO.
- instability of the Cs and oxidant layer because it is not well-prepared.
- intrinsic rearrangements of the Cs and oxidant layer and desorption of Cs atoms from the surface.

The operational lifetime is measured from the photocathode during its operation, i.e., when significant levels of charge are being extracted. The dominant mechanisms which limit the operational lifetime for NEA GaAs photocathode are:

- ion-back-bombardment where the extracted electron beam ionises residual gas molecules within the vacuum system. The positive ions generated are then accelerated back towards the photocathode, causing damage to the Cs and oxidant layer.

- operation at high voltage. High voltage discharge and some leakage current that can damage the photocathode surface. The high voltage field also causes desorption of gas from chamber walls.

- photocathode heat load generated by the high power illumination.

2.4.2 Response time

Typically, a very short response time in the few picosecond range is desirable for applications in a photo-electron gun [81]. However, the response time of the NEA GaAs photocathode is relatively slow because of the time taken for the photo-excited electron to travel into the surface. For the GaAs photocathode which has an active layer of approximately 800 nm, the response time is typically 50 - 100 ps [81]. The response time of the NEA GaAs photocathode, τ, is mainly determined by the diffusion time of photoelectrons thermalised at the bottom of conduction band and can be roughly estimated from the formula [82]:

$$\tau = \frac{d^2}{D} \tag{2.7}$$

where d is the minimum of two values: absorption length of photons and photocathode thickness, and D is the diffusion coefficient for photoelectrons in the conduction band. There are at least two ways to reduce the response time [82]. One is to operate the GaAs photocathode in the small positive electron affinity (PEA) state. In this case, non-thermalised electrons dominate the photoemission from the photocathode. Therefore, the response time of the photocathode depends mainly on the relaxation or thermalisation time which can be in a range of a few picoseconds [60, 82]. Another way is decreasing the photocathode thickness. It has been recently shown by the experimental study in Mainz [83] that the fast response time below 2 ps, which

is the limit of the experimental resolution, can be obtained from the photocathode with the layer thickness below 200 nm.

2.4.3 Surface charge limit (SCL)

At a moderate intensity level of laser illumination, the photocurrent is linearly proportional to the incident laser power, corresponding to a constant QE. However, when the photocathode is illuminated with a high intensity laser whose energy is slightly above the band gap energy of the photocathode, the photocurrent output saturates or even in some cases decreases as the intensity of laser illumination increases [84]. This phenomenon is known as the *surface charge limit* (SCL) effect [85, 86]. This effect arises because the slow emission and surface recombination process of thermalised electrons leads to accumulation of trapped electrons within the band-bending region. This accumulation reduces the level of band-bending, resulting in an increase of the EA. If this surface charge does not dissipate immediately, it will prevent the escape of later electrons from the surface. Consequently, the charge extracted by the next laser pulse is considerably reduced compared to that of the previous pulse [85, 87]. However, this effect is not observed in clean and well prepared photocathodes up to illumination power densities of several $W \cdot cm^{-2}$ [71].

Chapter 3

The surface characterisation system and experimental techniques

This chapter describes the construction of the surface characterisation system (SCS) and includes a basic discussion of the experimental techniques used during the course of this thesis. The SCS combines a photocathode preparation capability with surface characterisation techniques such as X-ray photoelectron spectroscopy (XPS), ultraviolet photoelectron spectroscopy (UPS), low energy electron diffraction (LEED) and auger electron spectroscopy (AES) within the same vacuum system. The application of the surface characterisation techniques makes it possible to examine the change of the surface elemental compositions and atomic arrangement during the preparation process. This analysis provides a great deal of experimental data which help in understanding the formation of the NEA state, supporting the development and optimisation of the photocathode preparation process. This study will also support and complete the research program for the ALICE photocathode preparation facility (PPF).

The surface characterisation system has been assembled and developed by myself with support from the vacuum science group, Accelerator Science and Technology Centre (ASTeC) at the Cockcroft Institute (CI). The development of this system was

challenging and complex, and accounts for a large proportion of the time taken to complete the research associated with this thesis. A description of the experimental set-up will now be given.

3.1 Experimental set-up

Preparation of the NEA GaAs photocathode and surface characterisation techniques must be performed in UHV in the range 10^{-10} mbar or less. This level of vacuum is necessary to control the rate of surface contamination over the duration of an experiment by reducing the number of molecules absorbed on the sample surface. By assuming that the sticking coefficient of a gas molecule (i.e. the probability of a gaseous molecule sticking to a surface) is unity following an impact to the surface, the time taken in seconds, τ, for a particular gaseous species to form a monolayer is given by [88]:

$$\tau = 4 \times 10^{-8} \frac{\sqrt{TM}}{P} \tag{3.1}$$

where T is the ambient absolute temperature (K), M is the molecular weight of the gaseous species in atomic mass units, and P is the pressure in the experimental chamber (mbar). For example, at a pressure of 10^{-6} mbar, it takes only 4 s for O_2 ($M = 32$) to form a monolayer on a clean surface. At a pressure of 10^{-10} mbar, the pressure at which most of our experiments were carried out, τ increases to approximately 40,000 s (11 hours) for O_2, falling to approximately 9,000 s (2.5 hours) for CO or N_2 ($M = 28$).

To attain such UHV for the experiment, special care must be taken from the design and assembly to routine operation. The basic rule to achieve UHV is to minimise the gas load and to maximise the available pumping speed. In practice, it is possible to reduce the gas load, which arises from outgassing, diffusion and leaks by orders of magnitude, whereas it is difficult to increase pumping speed more than a factor of 1 - 2 orders of magnitude [89]. The gas load can be minimised by careful selection of materials and processes, whilst paying attention to detail in design, constructional methods, handling and processing.

In this experiment set-up, all chambers were constructed from type-304 stainless steel and utilise standard UHV components. The type-304 stainless steel was chosen because it is nearly non-magnetic field, relatively-low cost, strong, easy to be machined and cleaned after fabrication. All vacuum seals were welded and all conflat-flanges (CF) have standard knife-edges using silver-plated or copper gaskets as a sealing medium. Care with a high degree cleanliness was taken during assembly of all vacuum components to provide as low outgassing rate as possible. The most important outgassing in a clean man-made vacuum system is water absorbed on the internal wall of vacuum chamber or on the surface of vacuum components. This outgassing rate can be reduced by a process called bake-out after the assembly. In this process, the chamber and all vacuum components are heated to a temperature between 150 - 400 °C, more typically 150 to 250 °C which accelerates the desorption of gas molecules (mainly water) absorbed in the body or surface of the metal in the vacuum system.

A schematic diagram and photographs of the surface characterisation system is shown in Figure 3.1 and Figure 3.2, respectively. The surface characterisation system consists of four integrated vacuum chambers: the loading chamber, the preparation chamber, the atomic hydrogen cleaning chamber and the surface characterisation chamber. The loading chamber is used to transfer the GaAs sample from the laboratory environment into the vacuum system while maintaining the other chambers at UHV. Since the GaAs sample used in this experiment is a thin wafer and prone to fracture, it must be clamped onto a stainless steel sample holder using two stainless steel clips, one located at each end of the sample, as shown in Figure 3.3. This sample holder can be picked up and transfered between the chambers using two magnetic linear transfer arms, as shown in Figure 3.4. The preparation chamber is where the sample is activated to the NEA state, and the QE measurement is performed. It is isolated from the loading chamber by a 2.75 inch o-ring seal gate valve (VAT), and from the surface characterisation chamber by a 4.5 inch o-ring seal gate valve (VAT). The surface characterisation chamber is equiped with several surface characterisation techniques to analyse the surface properties of the sample. To develop the cleaning process for GaAs photocathode, atomic hydrogen cleaning

(AHC) was introduced into the system. This technique is applied in a separated chamber known as the atomic hydrogen cleaning chamber. This chamber is isolated from the preparation chamber by another 2.75 inch o-ring seal gate valve (VAT).

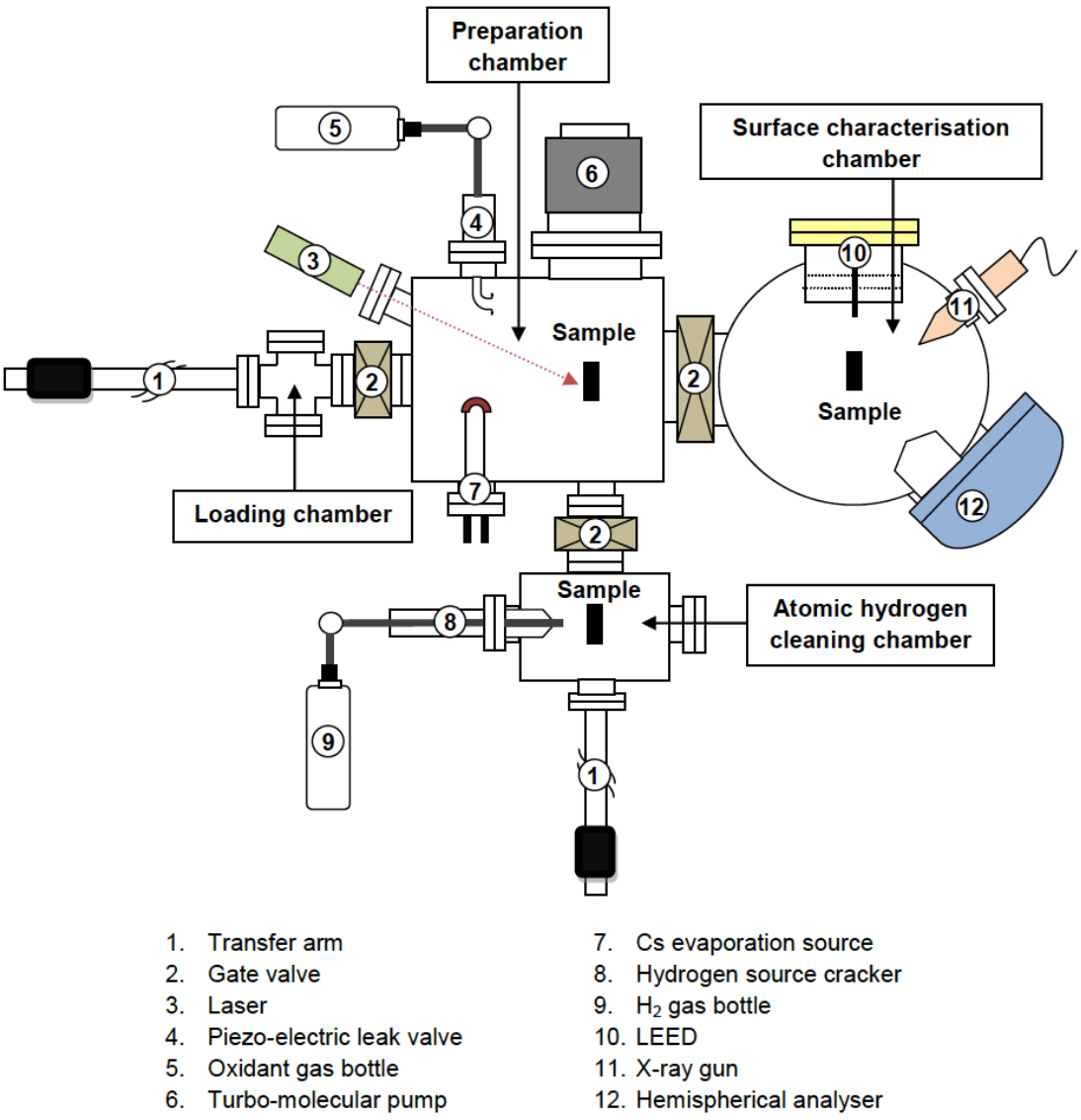

Figure 3.1: Schematic diagram of the surface characterisation system (SCS).

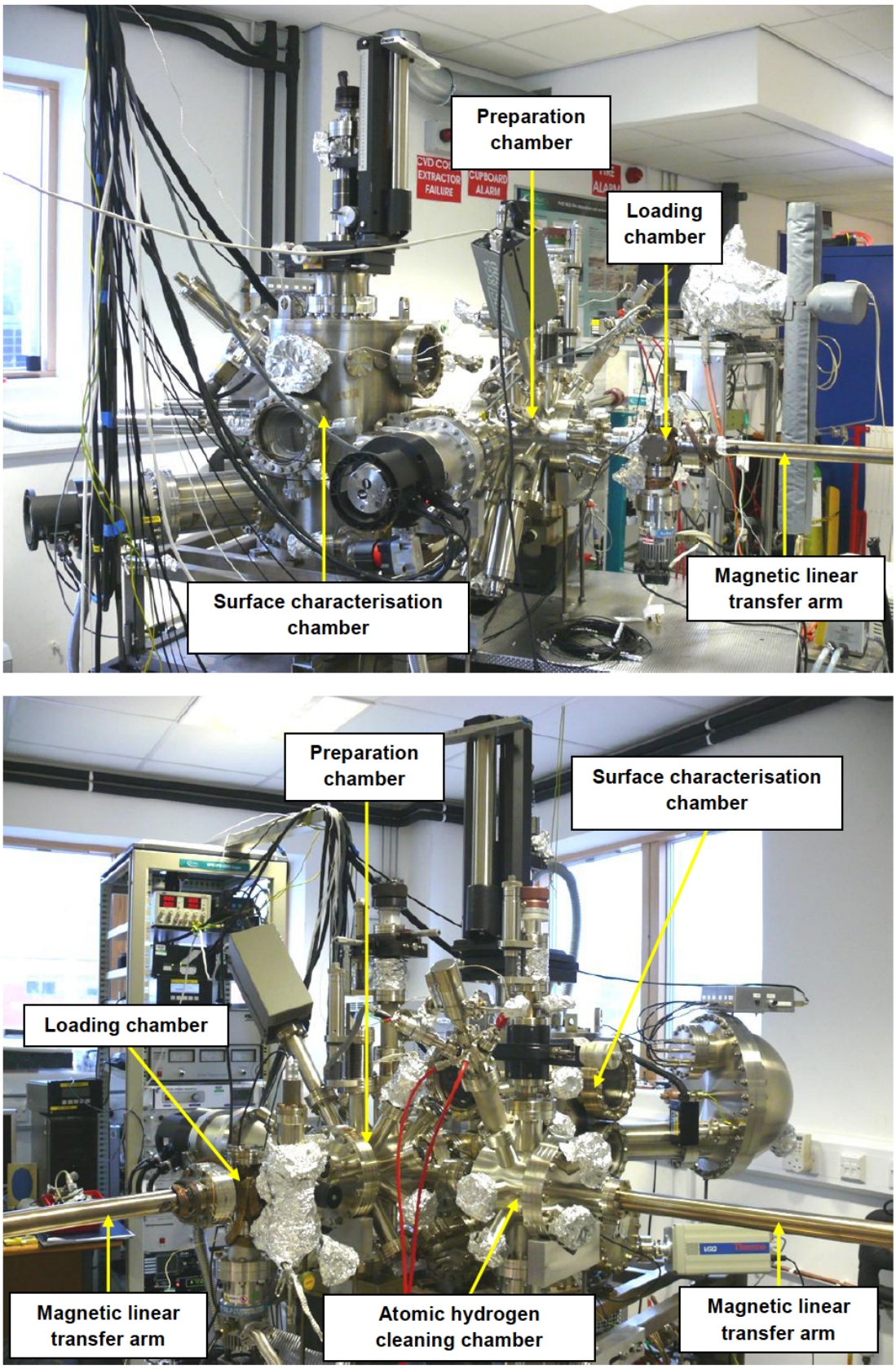

Figure 3.2: Photographs of the surface characterisation system (SCS).

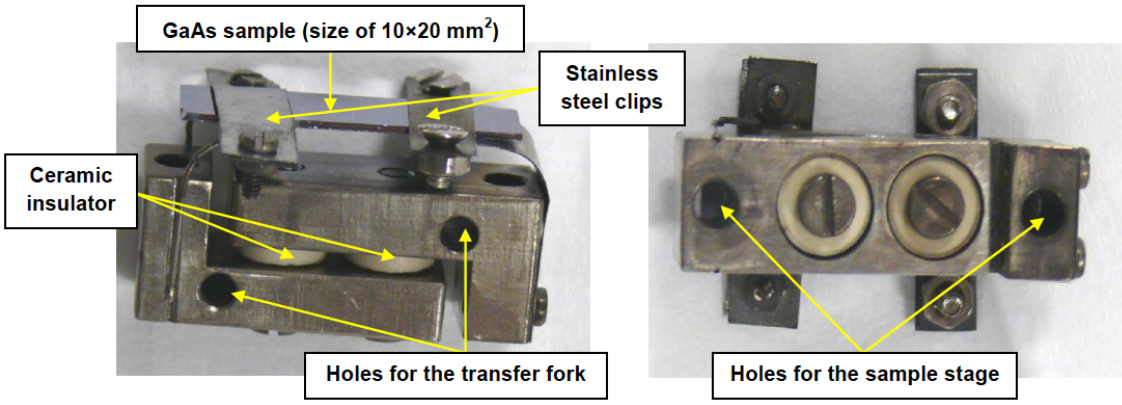

Figure 3.3: Photographs of the stainless steel sample holder mounting with the GaAs sample size of 10×20 mm^2.

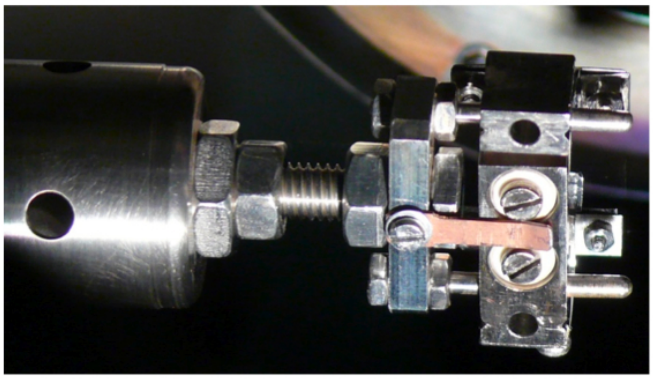

Figure 3.4: Photograph of the transfer arm attaching with the pins located in a sample during transfer.

3.2 Loading chamber

The loading chamber is a 6-way stainless steel cross with standard 2.75 inch CF ports placed around its circumference as shown in Figure 3.5. The chamber houses a 48 inch long magnetic linear transfer arm for moving samples to the preparation and surface characterisation chambers. One port is used as an insertion port to load the sample into the system. The chamber can be vented to the atmospheric pressure by connecting a dry nitrogen feed through a Nupro valve (Swagelok) mounted on one of the 2.75 inch CF ports.

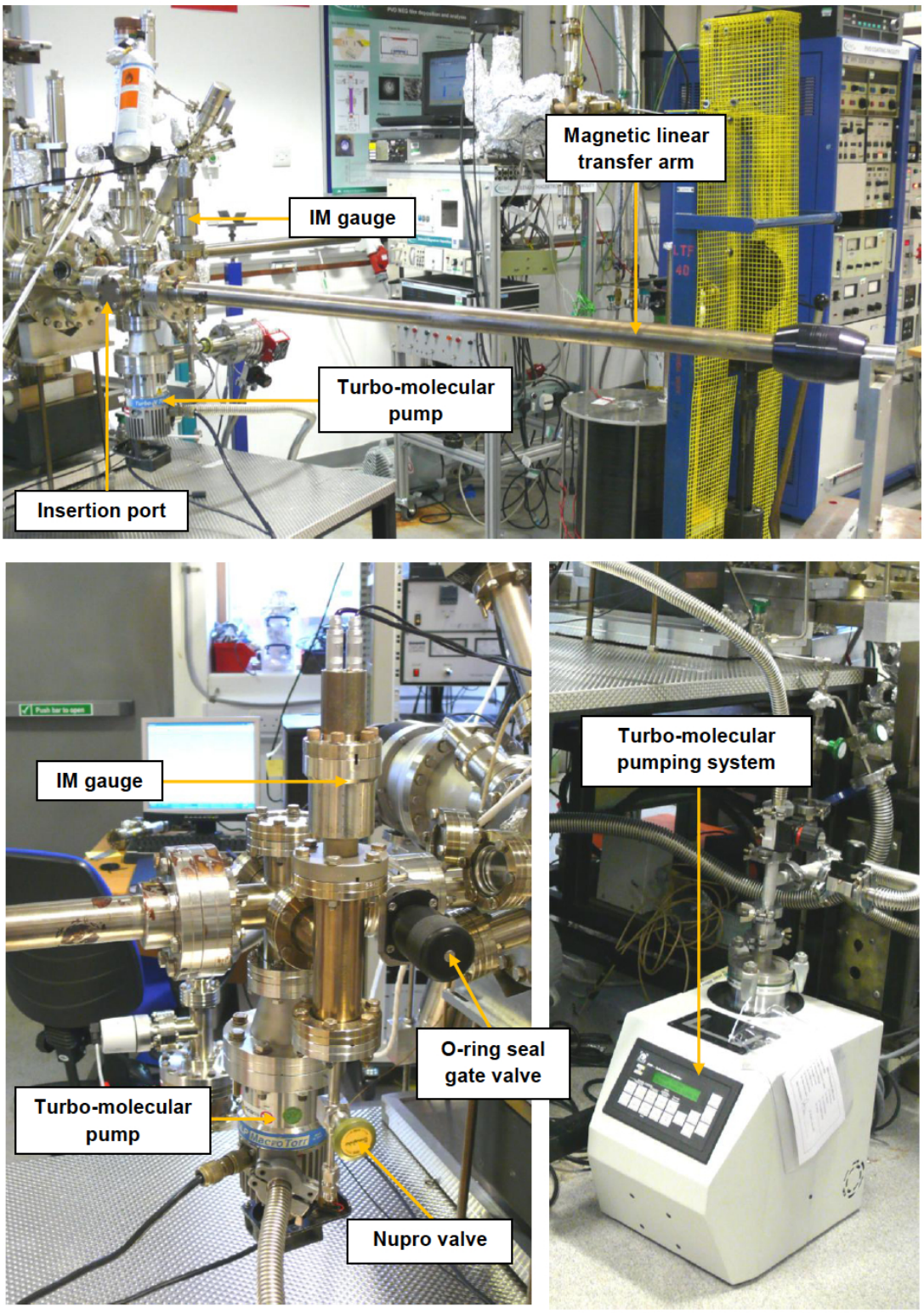

Figure 3.5: Photographs of the loading chamber.

The chamber is pumped down and maintained in the vacuum by using a 70 $l \cdot s^{-1}$ turbo-molecular pump (Turbo-V70LP from Varian Vacuum Technology) connected through a 4.5 inch to 2.75 inch conical reducer under neath the chamber. The turbo-molecular pump consists of rotor and slater blades spinning at a high angular velocity of several thousand Hertz. The rotating blades impart a momentum to gas molecules that collide them in the same direction, so the gas molecules can be removed from the inlet of the pump towards the exhaust. As a result, a vacuum is created. Since this pump can only be operated at low pressure, below 10^{-2} mbar at best, it is backed up by a dry turbo-molecular pumping system (PT 70 F from Oerlikon Leybold Vacuum). This pumping system is an integrated unit that features a turbo-molecular pump and diaphragm backing pump which has a pumping speed of 68 $l \cdot s^{-1}$ and can operate from the atmosphere pressure to 10^{-8} mbar. Since the loading chamber is designed to be relatively small, the pump-down time is fast. It usually takes approximately 2 - 3 hours to pump from atmospheric pressure to 10^{-8} mbar, ultimately reaching a base pressure of 10^{-9} mbar with more time. The pressure can be further improved by a thermal bake-out of the chamber. For the loading chamber, the bake-out temperature is limited to 185 °C by the o-ring seal material in the 2.75 inch gate valve. After baking for 25 hours, a vacuum level in the low 10^{-10} mbar range can be achieved in this chamber. However, it should be noted that baking is avoided when a sample is already inside the chamber since it has been found that the sample becomes contaminated from the gas load present in the chamber during the process [53].

Total pressure in the chamber is monitored using an inverted magnetron (IM) cold cathode gauge (MKS). This gauge operates over the range 10^{-2} to 10^{-11} mbar. The interior of the IM cold cathode gauge is open to the vacuum system, and contains a rod anode surrounded by a cylindrical cathode. A magnetic field is maintained in the gauge head by externally-mounted permanent magnets. The combination of this strong magnetic field and the potential difference between the anode and cathode due to the application of a high voltage causes an ionisation (gas discharge) current between these electrodes. This ionisation (gas discharge) current varies with pressure, and thus it is a measurable quantity that represents pressure.

3.3 Preparation chamber

Photographs of the preparation chamber are shown in Figure 3.6. The preparation chamber is a stainless steel cylinder with 23 CF ports: 19 standard 2.75 inch CF ports and 4 standard 4.5 inch CF ports. The chamber houses a manipulator which can be translated in the x, y and z direction and rotate about a vertical axis. This manipulator is fitted with a sample stage, on which the sample holder can be fixed to it by means of two pins, see Figure 3.7. These two pins are electrically insulated from the sample stage, and are connected to a UHV electrical feedthrough through flexible vacuum-compatible polytetrafluoroethylene (PTFE) electrical cables, providing electrical connection to the sample. The sample can be heated by passing a current through it (Ohmic heating) via the electrical feedthrough. This heating method was chosen in this experiment since it is simple and generates uniform temperature in the sample. To monitor the sample temperature during heating, an IRCON Modline 5 infrared optical pyrometer is used in conjunction with the emissivity calibration data from TJNAF [90]. This device can accurately monitor temperature without physical contact which is highly beneficial for this experiment. It works by sensing the infrared energy radiated by the sample, and converts this into the source temperature. The IRCON Modline 5 pyrometer is sensitive to radiation at 1.6 μm wavelength, and operates in the temperature range between 250 - 1000 °C, and it is thus compatible with the photocathode heat cleaning process (between 400 - 675 °C).

3.3.1 Pumping system

The chamber is pumped down by three integrated pumping systems:

- A 270 l·s^{-1} turbo-molecular pump with a magnetic bearing (Turbovac 340 M from Oerlikon Leybold Vacuum) connected to the chamber through an 8 inch to 4.5 inch conical reducer. This pump is backed by a 210 l·s^{-1} turbo-molecular drag pumping station (TSU 261 from Pfeiffer Vacuum) which combines a turbo-molecular pump with an integrated controller and a diaphragm pump, operating between atmospheric pressure to 10^{-8} mbar. This pumping system

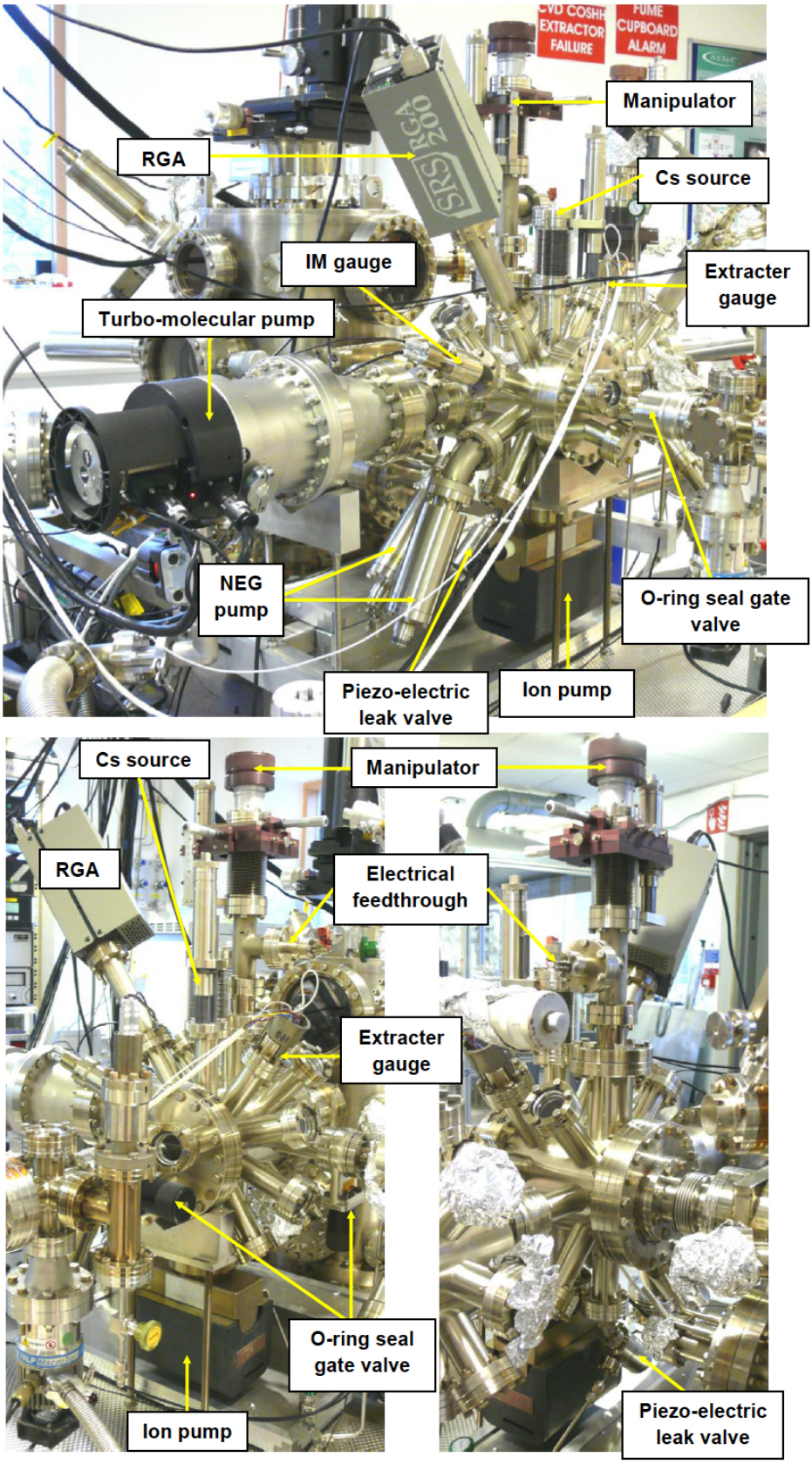

Figure 3.6: Photographs of the preparation chamber.

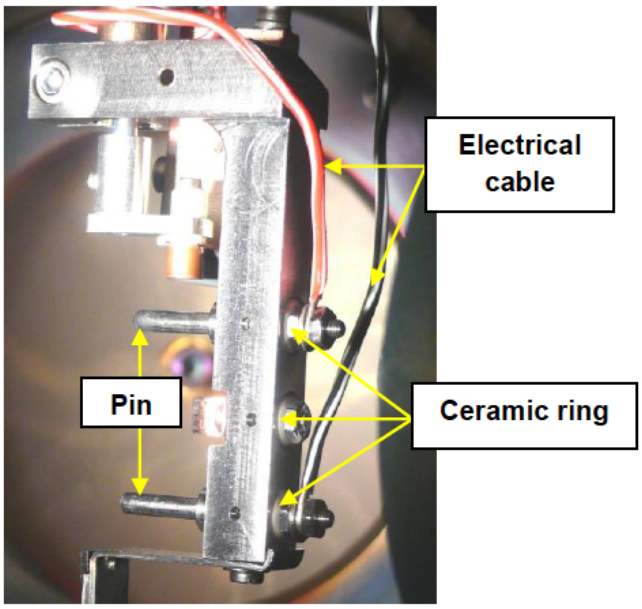

Figure 3.7: Photograph of the sample stage attached to the manipulator. The pins are used to hold the sample, and to provide electrical connection to the sample. Ceramic rings are used to electrically isolate the sample holder from the chamber. The electrical cables connect the pins to the electrical feedthrough on the vacuum chamber.

is used to evacuate the majority of gas from the chamber, and can pump down to a pressure below 10^{-8} mbar without baking.

- A 40 l·s^{-1} ion pump (Differential ion (DI) pump from Physical Electronic) connects directly to a 4.5 inch CF port underneath the chamber. It can start pumping at 10^{-3} mbar, but for longevity it is only operated from 10^{-5} mbar to XHV. The ion pump works by ionising residual gases, and then electrostatically accelerating them toward a titanium surface where they are permanently embedded and trapped. Therefore it is effective at pumping most common atmospheric gases, but is very slow with H_2 and inert gases, such as Ar and Ne.

- Two non-evaporative getter (NEG) pumps (Capaci-Torr MK5 from SAES Getters) connect to two 2.75 inch CF ports. This pump operates by adsorbing

active gas molecules onto the surface of getter material contained in the pump cartridge by chemical reactions.

To achieve the best practical vacuum condition, the preparation chamber was pumped initially by the turbo-molecular pumping system. After reaching a pressure below 10^{-7} mbar, the chamber was baked to 185 °C for 50 hours. At the end of the bake, the temperature was ramped down to 100 °C, then the ion-pump was switched on and allowed to outgas for several minutes. The NEG pumps were activated and all filaments were degassed with the system still at 100 °C to limit re-adsorption of the gas species liberated during degassing. Finally, the chamber was cooled to room temperature, and the system was ready for operation. After a completed bake-out process, a base pressure of 1.5×10^{-10} mbar was achieved in this chamber.

3.3.2 Pressure measurement

The total pressure in the preparation chamber is measured by an IM cold cathode gauge (MKS) and an extractor gauge (Ionivac IE 514 from Oerlikon Leybold Vacuum). The extractor gauge consists of three electrodes. A hot cathode emits electrons which ionise gas molecules inside the chamber before impinging on an anode. The resulting positive ion current is collected through the third electrode called the ion detector and this current is the basis of the measurement. In this manner, it can reliably measure the pressure in the range from 10^{-4} to 1×10^{-12} mbar. In addition to these gauges, a quadrupole residual gas analyser (RGA) (SRS RGA 200 from Stanford Research Systems) is installed to measure the total pressure lower than 10^{-4} mbar, and to monitor the gas composition at various stages of the experiment, and also allow leak testing of the chamber.

An RGA is essentially a mass spectrometer which consists of three main parts: an ion source, mass filter and ion collector, as schematically shown in Figure 3.8. Gas molecules are positively ionised using a hot filament in the ion source. The positive ions are focused into the mass filter where they are separated according their mass/charge ratio. The mass filter consists of four long rods aligned parallel to the extraction axis of the ion source. The rods are connected together electrically

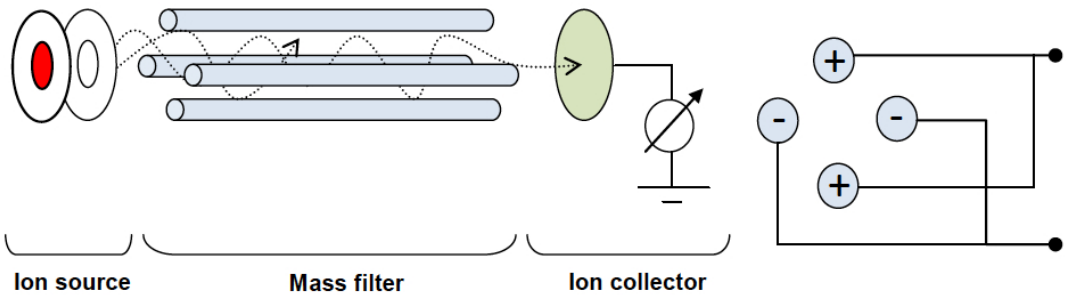

Figure 3.8: Schematic diagram of the working principle of a quadrupole residual gas analyser (RGA).

in diametrically opposite pairs to form a quadrupole field between the four rods. An electrical potential comprising a DC potential and a superimposed RF potential is applied to these pairs. For a given DC and RF potential ratio, only ions with a finite range of mass/charge can pass through the rod and reach the ion collector. By sweeping the amplitudes of the DC and RF potential, ions of successively greater mass/charge will pass through the filter, and can be collected to form the mass spectrum.

The partial pressures of the residual gas species in the preparation chamber as measured by the RGA are shown in Figure 3.9. The spectrum shows that after baking, the dominant residual gas is H_2 in the 10^{-10} mbar range because it is absorbed into the stainless steel during the manufacturing process and then slowly outgasses into the vacuum system. Other gases including more reactive gases such as water vapour, O_2 and CO_2 have partial pressures lower than 10^{-10} mbar.

3.3.3 Cs evaporation source

To deposit Cs layers onto the sample surface, Cs atoms are emitted from a pair of commercially-available Cs dispensers (Alkali Metal Dispensers (AMDs) from SAES). The dispensers are mounted on a 2.75 inch standard electrical feedthrough, as shown in Figure 3.10. This Cs source is installed approximately 15 cm away from the sample. Each Cs dispenser contains a mixture of a caesium chromate salt (Cs_2CrO_4),

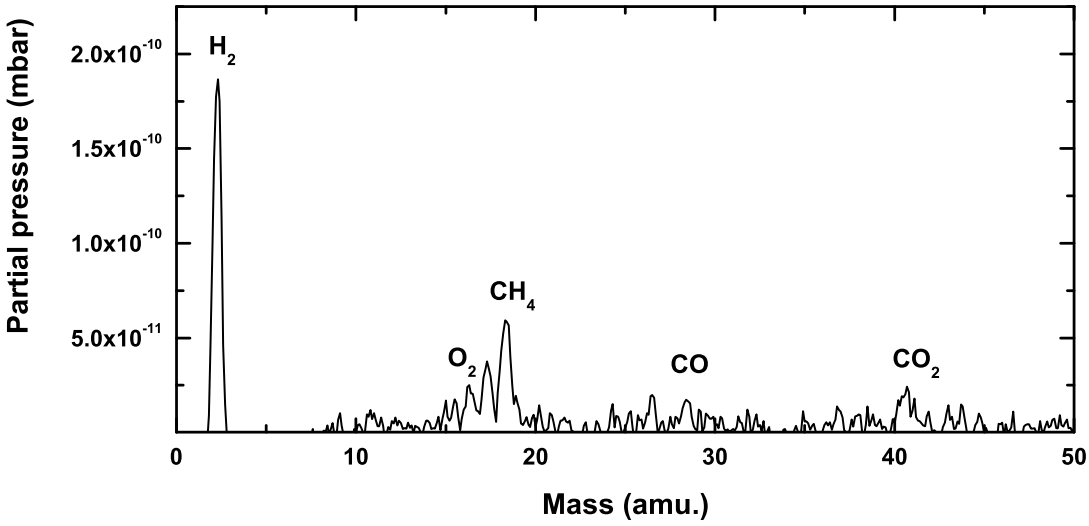

Figure 3.9: A spectrum of the the residual gas composition measured with a quadrupole residual gas analyser.

titanium (Ti) and a reducing agent Zr 84% - Al 16% (St101) getter material. When heated to a suitable temperature under vacuum by passing a DC electrical current through the dispenser, Cs atoms are liberated in the following chemical reaction:

$$2Cs_2CrO_4 + Ti \rightarrow 4Cs + Ti(CrO_4)_2 \tag{3.2}$$

Ti donates four electrons and forms titanium chromate, $Ti(CrO_4)_2$, and remains as an inert solid inside the dispenser whilst four Cs atoms are released. The reducing agent irreversibly absorbs almost all of the chemically-active gases which are pro-

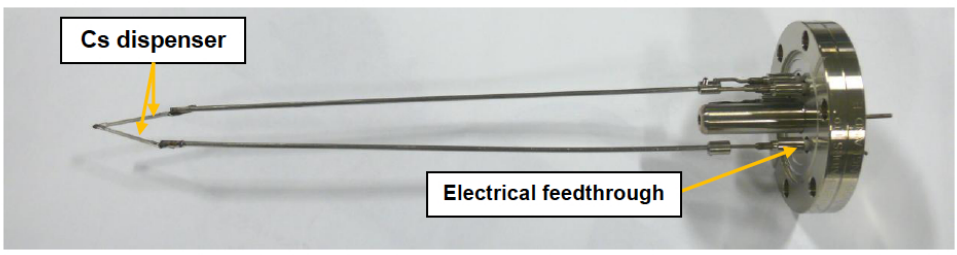

Figure 3.10: Photograph of the Cs evaporation source.

duced during the above chemical reaction, thus preventing them from contaminating the Cs vapour. The release rate of Cs vapour is dependent on temperature which, in turn, can be simply controlled by adjusting the level of electrical current. The typical operating current for this experiment is from 2.5 to 5 A.

3.3.4 Gas handling

To control introduction of gases at various stages of the experiments, a piezo-electric leak valve (PLV 1000 from Oxford Applied Research) is installed on a 2.75 inch port underneath the chamber. This valve accurately controls the leak rate between 6.65×10^{-10} - 6.65×10^{-2} mbar·l·s^{-1} by means of an internal piezo-electric crystal stack. A voltage applied to the stack causes it to mechanically distort and change in shape, according to the piezo-electric effect. In this way, the seal of the valve can be controlled precisely by the applied voltage to the stack. To deliver multiple gas species to the piezo-electric leak valve, the gas handling system was constructed as shown in a diagram in Figure 3.11. The gas system was made from stainless steel tubes (OD 0.5 inch) connected by Swagelok fitting. Multiple gas species including O_2, NF_3, N_2, H_2, CH_4, CO and CO_2 are provided by gas cylinders containing research grade gas (99.998 % pure by volume) with each gas bottle isolated by a Nupro valve. The entire gas line system is evacuated by a oil free dry scroll pump (XDS 10 from BOC Edwards) and a turbo-molecular drag pumping station (TSU 261 from Pfeiffer Vacuum). This allows the gas line to be cleaned prior to alternating gas species, thus maintaining species purity.

3.3.5 Quantum efficiency measurement

The QE is determined by measuring the photocurrent from the cathode and applying to the QE by using Equation 1.3 on page 27. A schematic diagram of the measurement circuit used in this experiment is shown in Figure 3.12. The sample is held at a negative potential of 18 V relative to the chamber via a battery bias box inserted between the electrical feedthrough and a picoammeter (Keithley type 485). A HeNe laser (Melles Griot), maximum power 1 mW at 632.8 nm, is

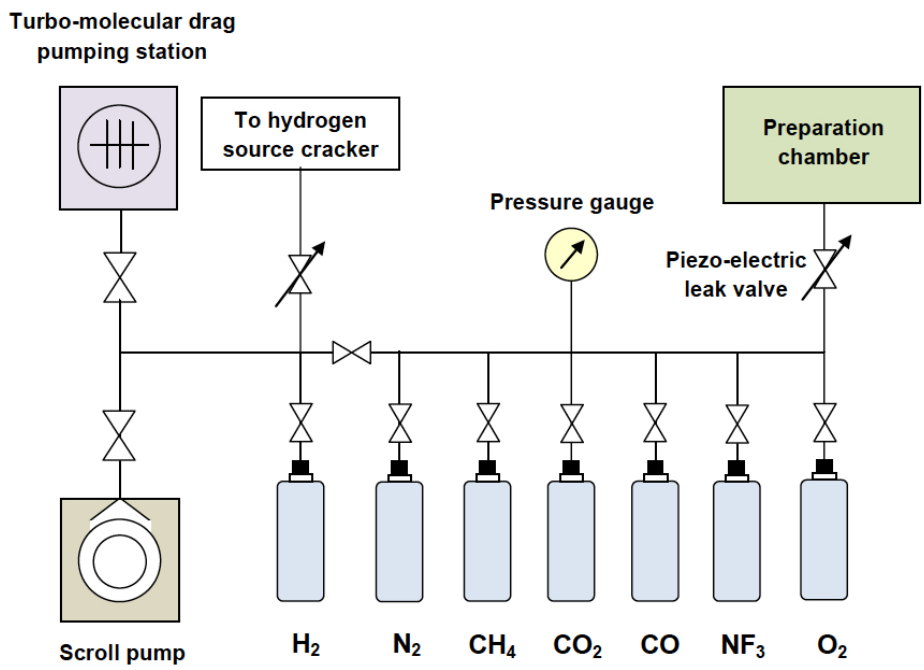

Figure 3.11: Schematic diagram of the gas line configuration of the preparation chamber.

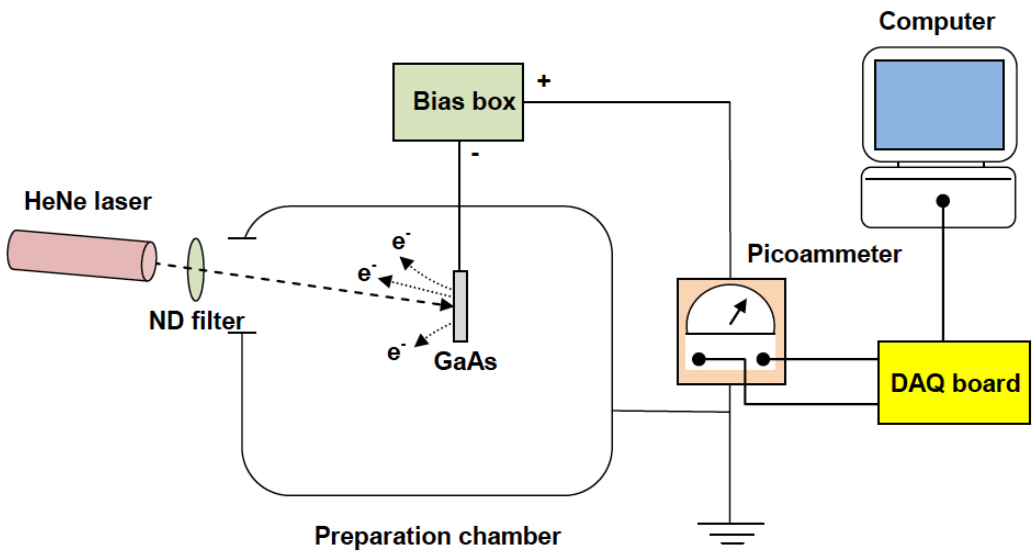

Figure 3.12: Schematic diagram of the total yield QE measurement circuit with analogue data acquisition by computer.

used to irradiate the sample through a neutral density (ND) bandpass filter and sapphire viewport, stimulating the emission of photoelectrons from the sample. The ND filter is used to lower the delivered laser intensity into the micro-watt range in order to avoid pressure rise due to electron-induced desorption from the surrounding metal surfaces due to a high intensity laser. Due to the negative bias, the resulting photoelectrons are accelerated toward the chamber wall and are measured as a total yield photocurrent by the picoammeter. The 0-10 V analogue output of the picoammeter is fed to a National Instruments (NI) DAQ board which facilitates data acquisition with a computer. The photocurrent signals from the DAQ board are processed, displayed and recorded by a software package developed using LabVIEW (Laboratory Virtual Instrumentation Engineering Workbench)[1]. I developed this software package based on that written for the ALICE PPF by H.E. Scheibler [60]. A screenshot of our developed software is shown in Figure 3.13. This software also supports the monitoring and recording of the chamber pressure which is very useful during the activation process and test measurements.

According to Equation 1.3, the measured QE depends mainly on the laser power and the resulting photocurrent. Since these two are uncorrelated, the uncertainty of the QE measurement, $\triangle QE$, in this experiment set-up is estimated following the relation:

$$\triangle QE = QE\sqrt{(\frac{\triangle P_{laser}}{P_{laser}})^2 + (\frac{\triangle I_{photocurrent}}{I_{photocurrent}})^2} \tag{3.3}$$

where $\triangle P_{laser}$ and $\triangle I_{photocurrent}$ is the uncertainty of the laser power and the photocurrent measurement, respectively.

[1]LabVIEW is a commercially available, widely used graphical programming interface for the control and automation of processes and for the acquisition and display of data.

Figure 3.13: Screenshort of the software developed in LabVIEW used for monitoring and recording the photocurrent and pressure during preparation process.

3.4 Atomic hydrogen cleaning chamber

3.4.1 Atomic hydrogen cleaning (AHC) technique and sources

Atomic hydrogen cleaning (AHC) is a well-known technique for the preparation of a clean III-V semiconductor surface [91, 92, 93]. This technique is applied by exposing the sample surface to a thermally-generated atomic hydrogen (H·) beam in a vacuum system. Highly reactive hydrogen atoms (radicals) chemically bond with surface contaminants which are subsequently desorbed from the surface by annealing at relatively low temperatures. Recently, this technique has been introduced for the preparation of NEA GaAs photocathodes [94, 95]. There are many reports in the scientific literature that main contaminants such as oxides and carbon compounds can be removed from the GaAs surface at temperatures below 400 °C [95, 96, 97]. The ability to remove the contaminants at low temperature is a major advantage

of the AHC technique since high temperatures can cause formation of dislocations and defects such as arsenic vacancies, surface roughening and dopant diffusion, decreasing the performance of the photocathode [94, 98].

In practice, H· beam can be generated by sources based on a hot filament, RF plasma discharge and capillary cracking. The working principles for these sources are illustrated in Figure 3.14. The hot filament source is simply operated by placing a hot tungsten filament in a vacuum chamber backfilled with hydrogen gas. As a result, H· are generated by the filament and diffuse in all directions, delivering a very low isotropic flux of H· which is the disadvantage of this source. The hot tungsten filament also produces a high level of gas load into the system that might itself contaminate the sample and damage the vacuum system in the chamber.

The RF plasma discharge source works by feeding hydrogen gas through a tube where a plasma is created in an inductively-coupled RF excitation. The plasma dissociates the hydrogen gas into H·. The H· exit the discharge region through a small aperture and are conducted to the sample. This source can generate a high efficient and well-directed H· flux with a relatively low vacuum deterioration. However, the H· beam may contain a large number of energetic impurity ions from the hydrogen plasma which can damage the sample surface [93]. The H· beam itself may also be aggressive for GaAs surface as there were reported that this technique

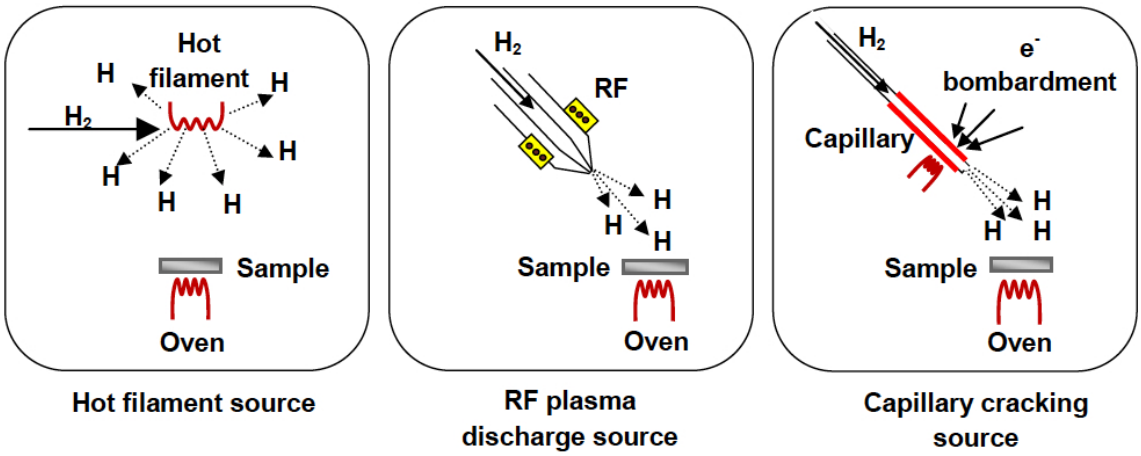

Figure 3.14: Principle of the atomic hydrogen sources.

can degrade the GaAs photocathode performance: quantum efficiency of the GaAs photocathode decreases rapidly together with the increase of H· exposure [94, 98].

The capillary cracking source is considered to have several advantages over the hot filament and RF plasma discharge sources. This source consists of a tungsten capillary which is heated to approximately 1800 - 2000 K. Following multiple collisions with the hot wall, hydrogen gas passing through the capillary is cracked into H· with an efficiency governed by the capillary temperature and the gas pressure. The H· escape from the capillary within a narrow angular distribution, generating a high flux of H· beam. In this way, it can generate a high purity beam with kinetic energy less than 1 eV (as the tungsten capillary can be outgassed very efficiently), avoiding a damaged surface by contaminating energetic particles. However, results of the AHC process depend on the degree of exposure to the H· flux, as well as the surface temperature during the process. Excessive temperature or H· exposure can have drastic consequences for the surface structure. These parameters need to be carefully controlled and optimised.

3.4.2 Vacuum chamber

The atomic hydrogen cleaning chamber is a stainless steel cylinder with 10 CF ports: 8 standard 2.75 inch CF ports and 2 standard 4.5 inch CF ports. It is shown in Figure 3.15. The chamber houses a manipulator with a sample stage which has almost identical design to that in the preparation chamber, allowing sample translation in x, y and z directions and rotatation about a vertical axis. It also houses a 23 inch long magnetic linear transfer arm for moving samples to the preparation chamber. The sample can be heated by passing a DC current through it via the electrical feedthrough. During heating, the surface temperature is monitored using an IRCON Modline 5 infrared optical pyrometer. The H· source used in these experiments is a commercial ion-free cracking source (TGC-H Thermal gas cracker from SPECS Scientific Instruments, Inc). This source is similar to the one used by the Heidelberg group which was successfully operated for the cleaning of the GaAs photocathode surface [72]. In this source, the capillary can be heated to a

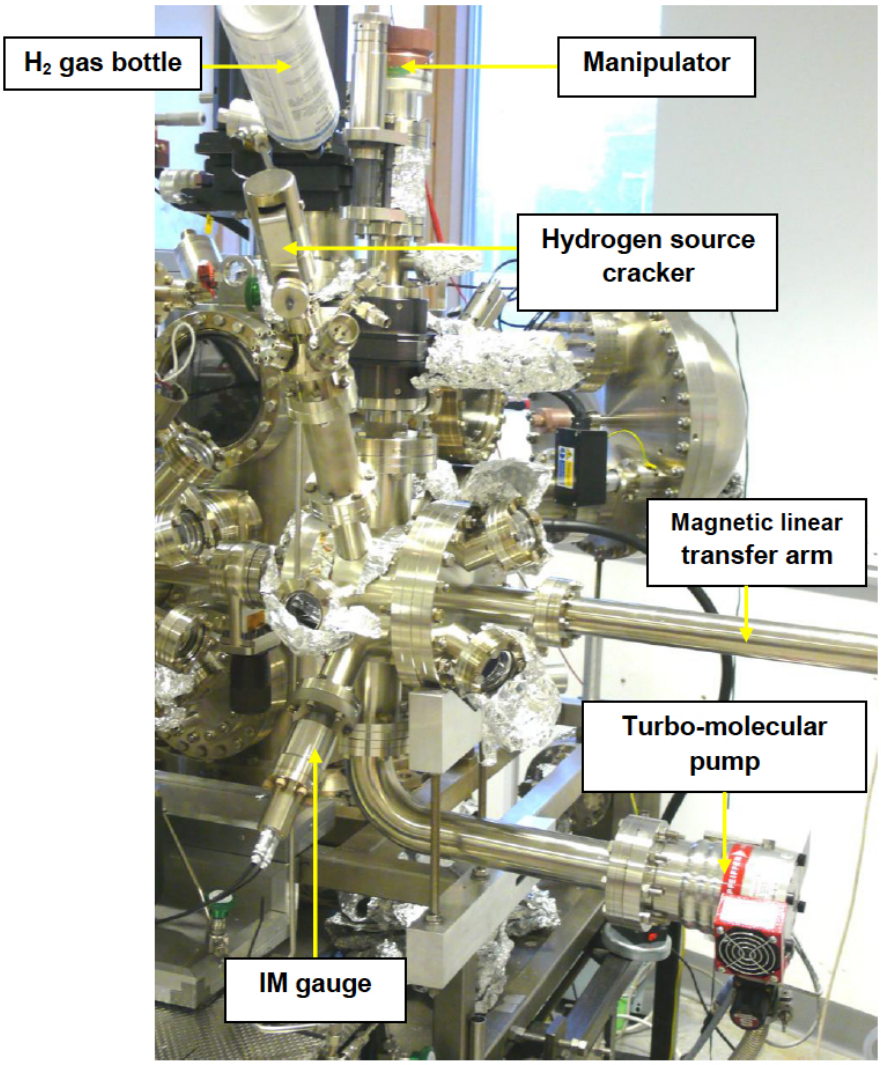

Figure 3.15: Photograph of the atomic hydrogen cleaning chamber.

temperature in excess of 2,000 K via an electron bombardment. The dissociation efficiency is nearly 100% for capillary temperature of 1,400 K or more and pressures below 10^{-8} mbar. The thermal shield between the capillary and the sample is water cooled, reducing the heat load into the system. Hydrogen gas with a purity of 99.996% is supplied to the source and is accurately controlled through a vacuum fine leak valve. The source is mounted on a 2.75 inch CF such that the H· beam travels approximately 10 cm to reach the sample surface. The chamber is pumped down by a 67 $l{\cdot}s^{-1}$ turbo-molecular pump (Hi-Pace 80 from Pfeiffer) backed by a dry turbo-molecular pumping system (PT 70 F from Oerlikon Leybold Vacuum). After

completing bake-out to 150 °C for 2 days, a typical base pressure of 4×10^{-10} mbar is obtained in the chamber. The chamber pressure is monitored using an IM cold cathode gauge (MKS).

3.5 Surface characterisation chamber

The surface characterisation chamber itself was formerly installed on Beamline 4.2 of the Synchrotron Radiation Source (SRS[2]) at Daresbury Laboratory. When the Daresbury SRS was decommissioned, the chamber was loaned to the vacuum science group, ASTeC and was re-configured to be a part of this experimental set-up. A photograph of the original chamber is shown in Figure 3.16. The chamber supports two primary surface characterisation techniques which were both used during the course of this research program. They were X-ray photoemission spectroscopy (XPS) and low energy electron diffraction (LEED), and the techniques will now be described.

Figure 3.16: Photograph of the original surface characterisation chamber.

[2]SRS: A 2 GeV electron synchrotron operated at Daresbury Laboratory between 1981 and 2008.

3.5.1 X-ray photoelectron spectroscopy (XPS)

X-ray photoelectronl spectroscopy (XPS) is a standard technique that is used to investigate the chemical composition of a material surface. In the XPS technique, a sample surface is illuminated with a monoenergetic soft X-ray beam, such as Mg Kα (1253.6 eV) and Al Kα (1486.6 eV). The X-rays are absorbed by surface atoms, resulting in emission of core level electrons. This process is shown schematically in Figure 3.17, where an electron from the K shell is emitted from the atom.

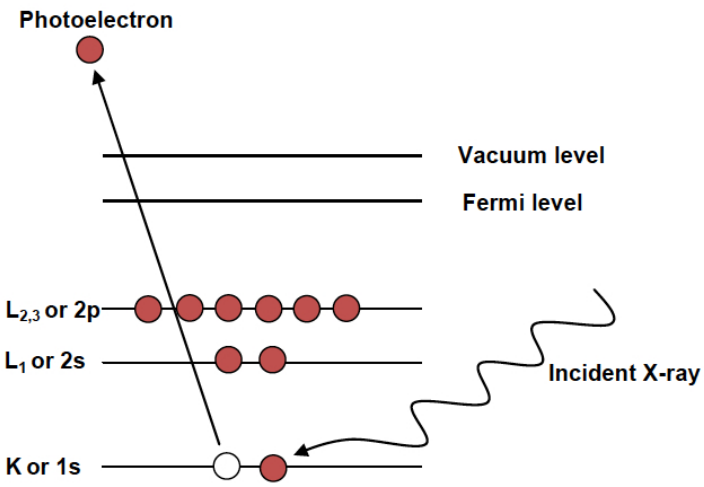

Figure 3.17: Schematic of the XPS process, showing photoemission of a K-shell electron.

The photoelectrons emitted from the sample are detected and their energies measured using an energy analyser. The kinetic energy of the emitted photoelectrons, E_k, is related to the binding energy of electrons, E_b, in the following manner:

$$E_k = h\nu - E_b - \phi_s \tag{3.4}$$

where $h\nu$ is the energy of the X-ray photon and ϕ_s is the spectrometer work function. As the energy of the X-ray photons and the spectrometer work function are known, the binding energy of the emitted electrons can be simply calculated. The binding energies for core level electrons are unique for each chemical species. By counting

the number of photoelectrons as a function of their binding energy, a spectrum representing the surface composition is obtained.

An example of XPS spectrum is given in Figure 3.18. The energy corresponding to each peak is characteristic of a particular electronic state in the sample. The peak shape and precise position provides chemical state information since the binding energy is dependent on the chemical environment. The peak areas can be used, with appropriate sensitivity factors, to determine the relative amount of the element represented by that peak present in the sample. In addition to the core-level electron peaks, peaks originated from Auger electrons may also be observed in the spectrum. When a core-level electron is emitted, the resulting core hole can be subsequently filled by an electron making a transition from a higher level. A photon emitted in this transition may escape into the vacuum, manifesting itself as X-ray fluorescence,

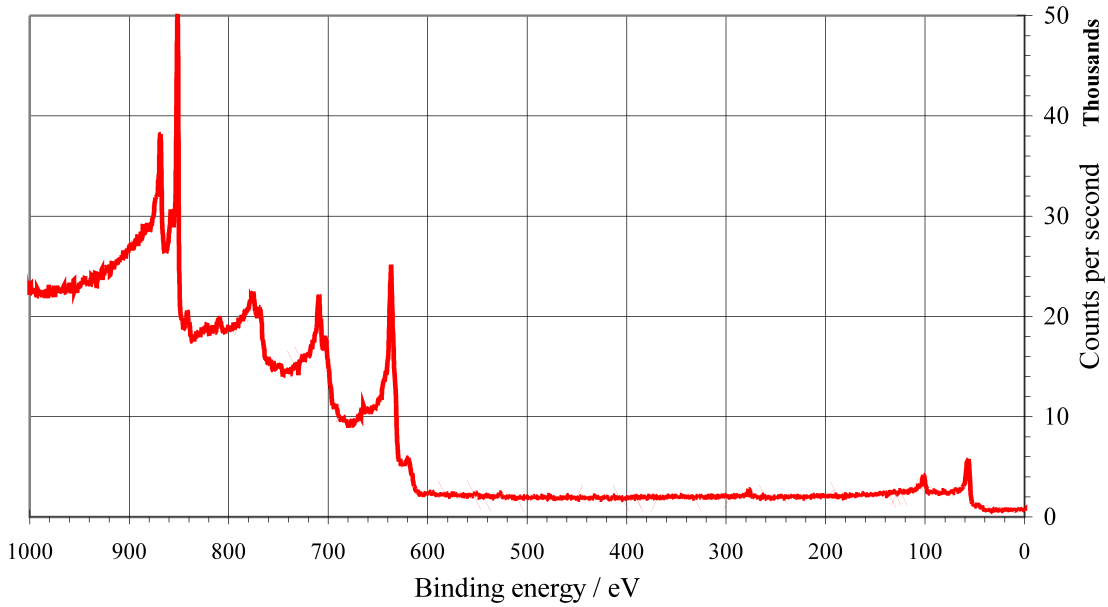

Figure 3.18: Broad XPS spectrum for a clean Ni(110) surface taken from [88]. The photoelectron peaks relate to the following electronic states: 1004 eV - $2s_{1/2}$; 867 eV - $2p_{1/2}$; 852 eV - $2p_{3/2}$; 98 eV - $3s_{1/2}$ and 56 eV - $3p_{1/2}$. The Auger peaks at 774 eV, 708 eV and 635 eV relate to the $L_3M_{23}M_{23}$, $L_3M_{23}V$ and L_3VV transitions, respectively.

or may interact with a bound electron within the atom. In the latter instance, the photon energy is transferred to the bound electron which is subsequently photoemitted as the Auger electron [88]. This process is schematically shown in Figure 3.19. Although it is often not practical, the Auger peak can also be used and provide chemical information for XPS analysis.

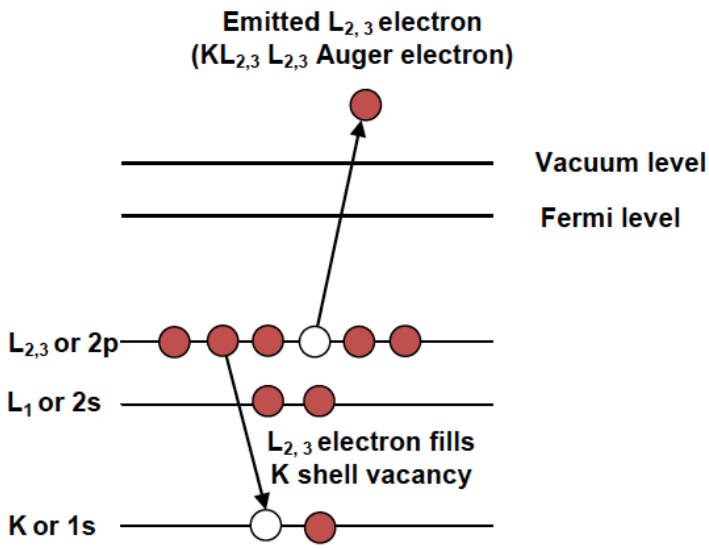

Figure 3.19: Schematic of the emission process of $KL_{23}L_{23}$ Auger electron. This is originated from relaxation of the ionised atom of Figure 3.17.

3.5.2 Low energy electron diffraction (LEED)

Low energy electron diffraction (LEED) is a technique which is used to determine the geometric structure in the surface region of a material. The technique requires an electron beam with energies typically varying between 20 - 500 eV to interact with the sample surface. In this energy range, the electrons have wavelengths within 0.55 Å to 2.74 Å as given by the well known de Broglie relation:

$$\lambda = \frac{h}{p} \approx \sqrt{\frac{150}{E}} \tag{3.5}$$

where λ is the electron wavelength, p is the magnitude of the electron momentum, h is Plank's constant and E is the energy of electron (eV). These wavelengths are

comparable to the lattice spacings of typical material crystal [99]. If the sample surface is a single crystal with a well-ordered surface structure, the electrons will undergo diffraction and form a LEED pattern, an example of which is shown in Figure 3.20. If the sample surface is poorly ordered through roughness or contamination, the pattern generated is diffuse or perhaps even non-existent. Therefore, apart from the determination of the geometrical structure of the surface, LEED can be used to establish if a regular crystal lattice is free from surface impurity, or if an adsorbate over-layer has been successfully applied [88].

Figure 3.20: Photograph of the LEED pattern of Cu(110) surface [88].

The diffraction process conserves both energy and momentum, and can be described in term of *electron wavevectors* and *reciprocal lattice vectors*. The constructive diffraction and high intensity LEED pattern occur only if the wavevector of the incident electron, $\bar{\mathbf{k}}$, and diffracted electron, $\bar{\mathbf{k}}'$, satisfy the Laue condition:

$$\bar{\mathbf{k}}' - \bar{\mathbf{k}} = \bar{\mathbf{G}} \tag{3.6}$$

where $\bar{\mathbf{G}}$ is the reciprocal lattice vector of the surface, which is in the general form:

$$\bar{\mathbf{G}} = h\hat{\mathbf{a}}^* + k\hat{\mathbf{b}}^* + l\hat{\mathbf{c}}^* \tag{3.7}$$

where h, k and l are in general integer numbers and $\hat{\mathbf{a}}^*$, $\hat{\mathbf{b}}^*$ and $\hat{\mathbf{c}}^*$ are the unit reciprocal lattice vectors. Since the electrons in this technique have the elastic mean

free paths in the range of 5 Å to 10 Å, only the first few atomic layers contribute to the diffraction. This means that there is no diffraction condition in the direction perpendicular to the sample surface. Therefore, in this case, Equation 3.6 can be reduced into:

$$\bar{\mathbf{k}}'_{||} - \bar{\mathbf{k}}_{||} = \bar{\mathbf{G}} \tag{3.8}$$

where $\bar{\mathbf{k}}'_{||}$ and $\bar{\mathbf{k}}_{||}$ are the component in parallel to the surface of the incident electron and diffracted electron wave vector. $\bar{\mathbf{G}}$ is reduced into the general form:

$$\bar{\mathbf{G}} = h\hat{\mathbf{a}}^* + k\hat{\mathbf{b}}^* \tag{3.9}$$

The unit reciprocal lattice vectors, $\hat{\mathbf{a}}^*$ and $\hat{\mathbf{b}}^*$, are related to the unit real space lattice vector, $\hat{\mathbf{a}}$ and $\hat{\mathbf{b}}$, in the following way:

$$\hat{\mathbf{a}}^* = \frac{2\pi\hat{\mathbf{b}} \times \hat{\mathbf{n}}}{|\hat{\mathbf{a}} \times \hat{\mathbf{b}}|} \tag{3.10}$$

$$\hat{\mathbf{b}}^* = \frac{2\pi\hat{\mathbf{n}} \times \hat{\mathbf{a}}}{|\hat{\mathbf{a}} \times \hat{\mathbf{b}}|} \tag{3.11}$$

The schematic of a typical LEED apparatus is shown in Figure 3.21. The electron gun is usually a thermally-heated cathode, focussed to produce a well-collimated

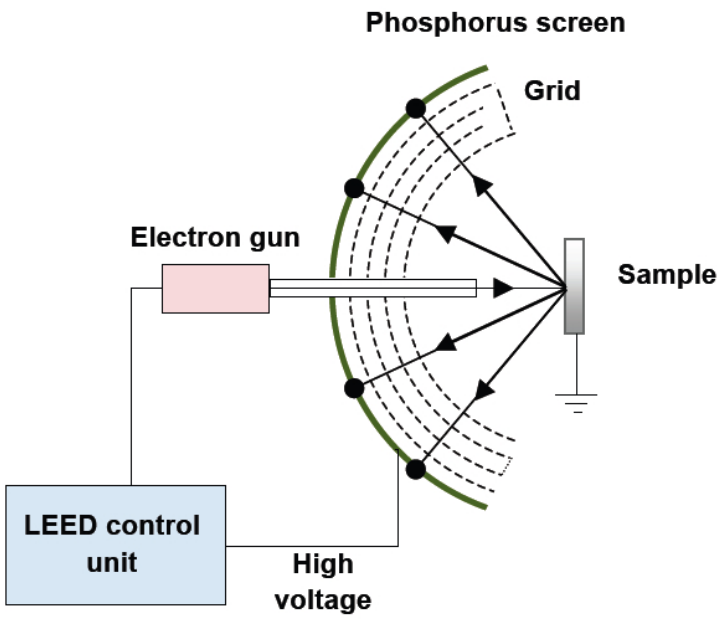

Figure 3.21: Schematic diagram of a LEED apparatus.

electron beam. The electron beam impinges on the sample, and electrons are backscattered. The electron energy may be varied between 20 - 500 eV by changing the potential of the gun relative to the sample, which is kept at ground potential. A number of grids are placed between the sample and the screen, allowing only diffracted electrons above certain energy to pass. This ensures that only elastically-scattered electrons will contribute to the diffraction pattern. Having passed through the grids, the diffracted electrons are accelerated to a fluorescent screen where the diffraction pattern is created. The diffraction pattern can be viewed directly by eye, or recorded by using a camera.

3.5.3 Vacuum chamber

Photographs of the present surface characterisation chamber are shown in Figure 3.22. The chamber is stainless steel, mounted vertically on a rigid frame. The top of the chamber houses a manipulator providing x, y and z translation and rotation about the vertical axis of the sample. The manipulator is equipped with a sample stage which has almost identical design to that in the preparation chamber. This sample stage is connected to an electrical feedthrough providing an electrical contact to the sample for resistive heat cleaning and drain current measurement.

The chamber consists of many standard CF ports arranged in three levels: lower, middle and upper. The middle and upper level ports of the chamber are equipped with surface characterisation hardwares and viewports. To support XPS experiments, the chamber is equipped with a VG MICROTECH twin anode X-ray source, delivering monoenergetic soft X-rays, Al Kα (1486.6 eV) or Mg Kα (1253.6 eV) onto the sample. The emitted photoelectrons are collected and the XPS data are generated using a PSP VACUUM Resolve 120 hemispherical energy analyser. LEED experiments can be performed using an Omicron Specta LEED which incorporates an electron gun with a LaB_6 filament. A photograph of this LEED instrument is shown in Figure 3.23, taken during replacement of the phosphorus screen which was partly damaged, so was replaced. An inert sputter ion source (ISIS3000 from PSP Vacuum Technology) is also installed for sample cleaning by sputtering with Ar^+

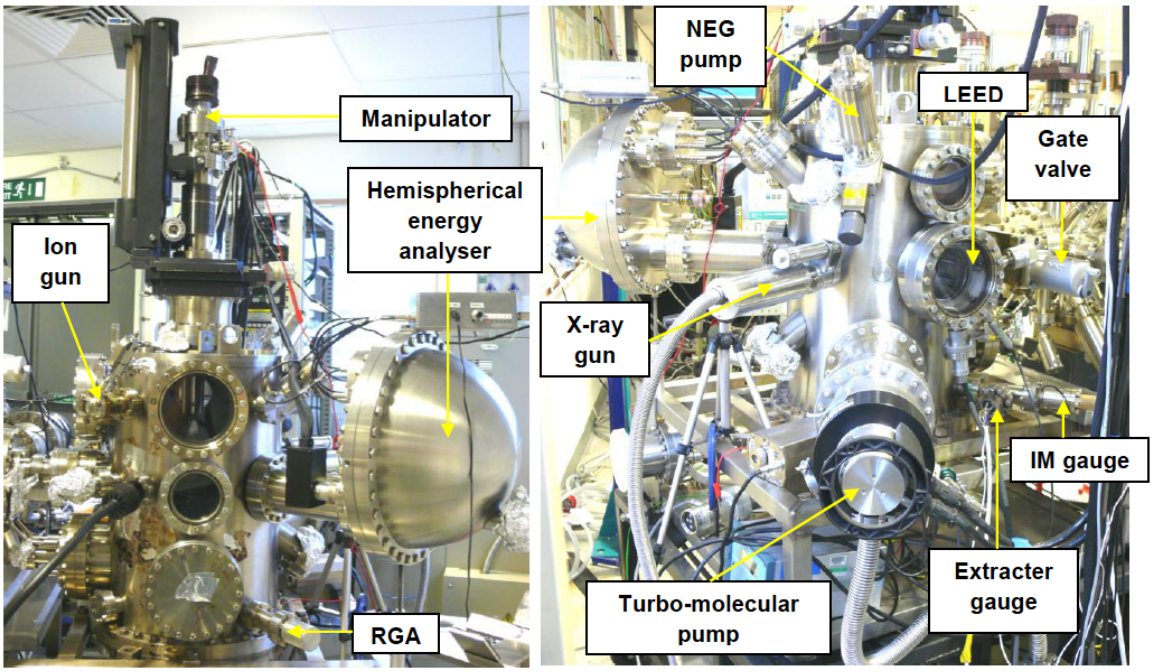

Figure 3.22: Photographs of the surface characterisation chamber as part of this experimental set-up.

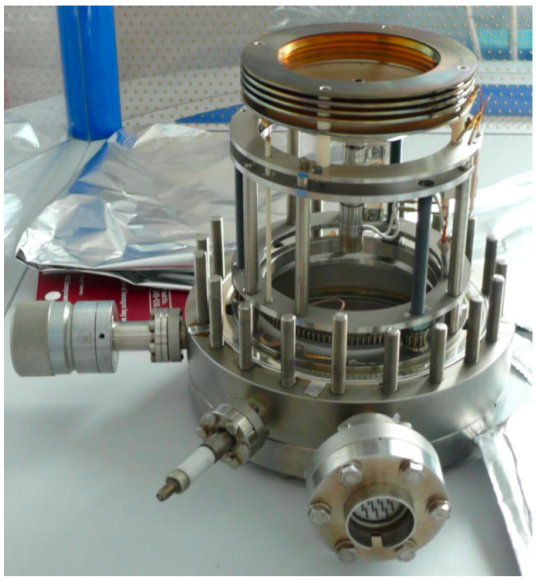

Figure 3.23: Photograph of the LEED optics during re-installation to the surface characterisation chamber.

at an energies up to 2,000 eV. However, since this technique gives rise to physical damage extending hundreds of angstroms into the bulk of GaAs [100], its use is therefore avoided in this experimental programme.

The lower level ports are mainly installed with pumping and pressure monitoring equipments. One 8 inch CF port is connected directly to a 270 $l \cdot s^{-1}$ turbo-molecular pump with magnetic bearing (Turbovac 340 M from Oerlikon Leybold Vacuum). This pump is backed by an oil-free turbo-molecular drag dry pump system (DRYTEL 31 from ACATEL), comprising a turbo-molecular pump backed by a diaphragm pump, operating from atmospheric pressure to 10^{-6} mbar. This pumping system provides most of the pumping capacity required to carry out experiments in an UHV pressure regime. It can pump the chamber down to a pressure below 10^{-8} mbar without bake-out. After a completed bake-out to 150 °C for 2 days, a pressure better than 10^{-10} mbar is achieved. To increase the pumping speed, an additional NEG pump (Capaci-Torr MK5 from SAES Getters) is connected to a 2.75 CF port on the upper level and operated after the bake-out process. The total pressure is monitored by an IM cold cathode gauge (MKS) supported by an extracter gauge (Ionivac IE 514 from Oerlikon Leybold Vacuum). In addition partial pressures of the residual gases are monitored by a residual gas analyser (Thermo VGQ).

Chapter 4

NEA GaAs photocathode preparation aspects

In practice, the NEA state of the GaAs photocathode is obtained through a process referred to as activation. This process requires the preparation of an atomically-clean p-type GaAs surface, free from carbon and oxide contaminants, in an UHV condition. The cleaned surface is then deposited with Cs and oxidant (either O or F) layers, either alternating these two element layers or by co-deposition. The formation of the NEA state and performance of the GaAs photocathode strongly depends on the surface preparation and activation process. The study of these processes for optimal performance NEA GaAs photocathodes has always been and continues to be the most important activity in photocathode development. This chapter presents the experimental studies of the preparation process for the NEA GaAs photocathode in the surface characterisation system. The individual steps of the process were studied with the intention to maximise the QE which is the main parameter of the photocathode in most applications. These studies are supported by experimental evidence from XPS and LEED to demonstrate the processes at the atomic level.

This chapter is oganised as follows. The GaAs sample specification and experimental details used in this experiment are given in section 4.1. Standard activation procedures were firstly studied in order to understand the mechanism of the activation processes and also test the functionality of our surface characterisation system.

The experimental results of the activation process using Cs and O_2 are presented in section 4.2. In addition to O_2, NF_3 is considered as an oxidant gas for the activation process in this experiment. The activation process using NF_3 is presented in section 4.3. Preparation of an atomically-clean GaAs surface is an essential step for obtaining a high QE photocathode. Different surface cleaning techniques for preparing a clean GaAs surface have been investigated in this study. The heat cleaning technique and an effect of the heating temperature are discussed in section 4.4. The wet chemical treatment and the results are presented in section 4.5 and, finally, the atomic hydrogen cleaning technique are described in section 4.6.

4.1 GaAs sample and experimental details

GaAs samples used for all the experiments described in this chapter were a commercial bulk GaAs wafer (from AXT) grown by vertical gradient freeze (VGF) method. It has an active layer thickness of 625±25 μm and heavily-doped p-type with Zn to a level of 5×10^{19} cm^{-3}. Throughout the experiments, the samples were cut into a 1×2 cm^2 square-shape in order to mount on the holder and load into the experimental chambers.

All experiments were carried out in the surface characterisation system as described in the previous chapter. XPS was performed using an Al Kα radiation source ($h\nu$ = 1486.6 eV) without a monochromator. The spectra were mainly collected at an emission angle of 15° with respect to the surface normal. The analyser was in a constant pass energy mode at a pass energy of 50 eV, which yields an overall spectral resolution of 1.0 eV (full width at half-maximum). The pass energy refers to a kinetic energy that an electron must possess in order to pass through the analyser and be detected. The lower the pass energy, the higher the resolution of the spectrum.

The QE measurements were performed under an illumination of a HeNe laser at 632.8 nm with maximum power of 1 mW through a 10% ND bandpass filter. The uncertainty of the measured QE in this chapter is estimated to be 7.2%.

4.2 Activation processes

In the following section, different activation techniques for the NEA GaAs photocathode are studied and discussed in detail.

4.2.1 Experimental preparation and activation techniques

To study the activation processes for the NEA GaAs photocathode, a GaAs wafer was prepared by first degreasing the wafer with a solution of iso-propanol (IPA) and acetone in an ultrasonic bath for 30 minutes. The wafer was then mounted onto the sample holder and loaded into the loading chamber. After introducting to UHV, the sample was transfered into the surface characterisation chamber and heated to 600 °C for 60 minutes to thermally desorb surface contaminants. In order to avoid the thermal stress inside the GaAs wafer, the temperature was ramped up slowly within 20 minutes. During heating of the wafer, the pressure of the chamber was observed to increase up to 10^{-7} mbar range because of thermal desorption of surface contaminants and outgassing from the holder. It was also observed that when the temperature reached to 575 °C, the GaAs wafer began glowing, as shown in Figure 4.1. This red glow is commonly used to roughly estimate the temperature of the GaAs photocathode surface (approximately 575 - 650 °C) during the heating process inside the gun.

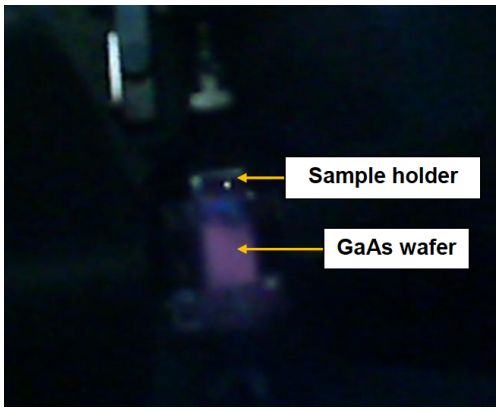

Figure 4.1: Photograph of the GaAs wafer during heating to 600 °C in the surface characterisation chamber.

When the heating process was complete, the wafer was cooled down to room temperature, which took approximately 2 hours. The wafer was then transferred to the preparation chamber and activated to the NEA state.

Activation of the GaAs to the NEA state is performed in most cases by deposition of Cs and O layers onto the surface, as explained in Chapter 2. An optimal deposition procedure is required to achieve the NEA state and high QE. However, this optimal procedure is not fully-developed up to now because the complexity of the Cs and O layers on the GaAs surface, this will be discussed later in section 4.2.3. Up-to-date, the empirically found activation techniques can be separated into two groups [101]. The first group is the so-called Yo-Yo technique [31, 32], in which the Cs and O layers are alternately deposited onto the surface. The second group is the co-deposition technique [71, 72], in which the Cs layers are deposited on the surface followed by simultaneous deposition of Cs and O layers.

The Yo-Yo technique

The Yo-Yo technique has been commonly used since the early development of NEA-devices [102]. It is performed by depositing Cs and O layers alternately. In this technique, the activation is started by exposing the GaAs wafer surface to the Cs dispensers which are activated with an electrical current of approximately 4 A. Cs atoms are generated from the dispensers and then deposit onto the GaAs wafer surface. During the deposition, the GaAs wafer is illuminated by the laser and the generated photocurrent is recorded simultaneously. The photocurrent measurement technique is described in Chapter 3. This photocurrent is used as an indication of the amount of deposited Cs for this activation technique. After deposition for a given amount of time, the photocurrent is registered and increases, as a result of the EA of the GaAs wafer lowering upon Cs deposition. A plot of the evolution of photocurrent and pressure of the chamber during activation is shown in Figure 4.2.

The deposition is continued until the photocurrent reaches the maximum value, 1st peak, and begins to decrease. This decrease in the photocurrent is possibly because a nonequilibrium concentration of Cs deposited on the surface leads to the

depolarisation of the Cs dipole [103]. When the photocurrent drops to approximately 2/3 of the peak value, the Cs deposition is stopped by reducing the current through the dispenser to a value lower than the operational current of 1.5 A. Then, O_2 is immediately admitted into the chamber through the piezo-electric leak valve. In this experiment, the rate of O_2 exposure is controlled so that the total pressure of the chamber does not exceed 5×10^{-9} mbar. The increase of the chamber pressure during this exposure can be seen in Figure 4.2. As exposing to O_2, oxide layers are formed on the GaAs sample surface and it is seen in Figure 4.2 that the photocurrent increases again. The increasing rate of the photocurrent depends on the pressure of O_2 inside the chamber, at a higher pressure the increase in photocurrent is greater. After the photocurrent reaches its peak again and drops to approximately 2/3 of the previous peak value, the piezo-electric leak valve is now closed and the Cs dispensers

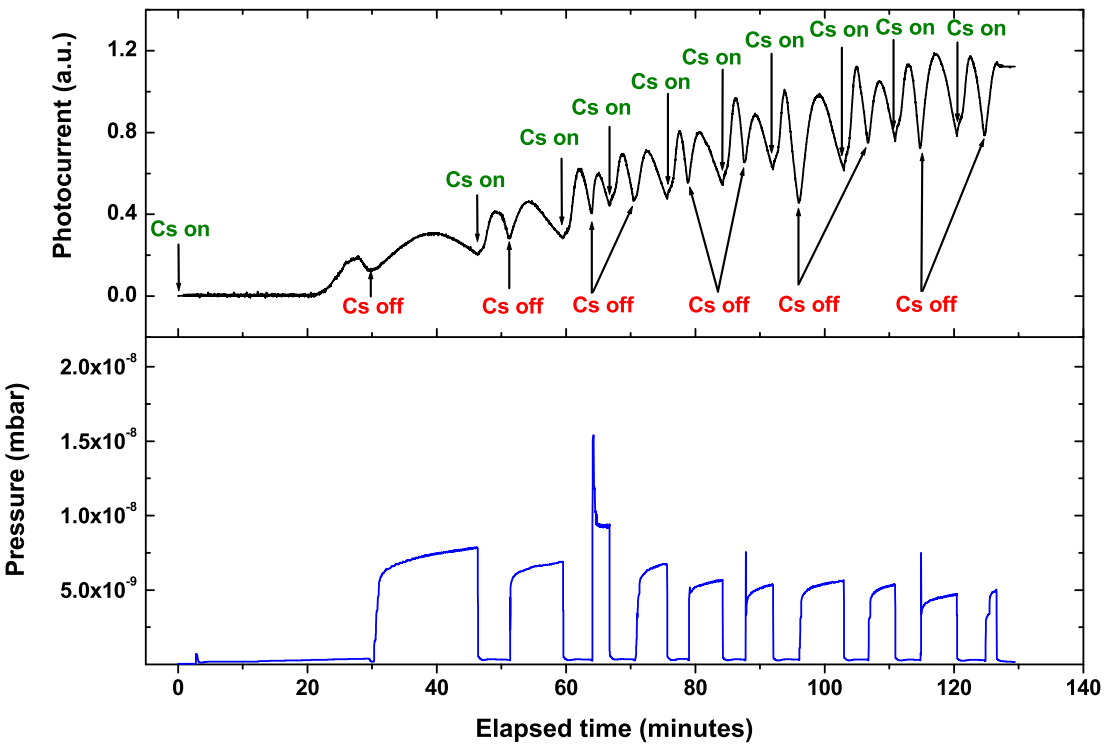

Figure 4.2: A typical plot of the evolution of photocurrent and pressure of the chamber during the activation with the Yo-Yo technique.

are activated, again. This cycle is continuously repeated with the peak values of the photocurrent increases from cycle to cycle. When the peak value increases no further, typically after 10 cycles and within 2 hours as seen in Figure 4.2, the activation process is complete. The maximum achievable photocurrent is the maximum photocurrent obtained from the sample. If the process is continued even further, the peak values begin slowly decrease. This is the so-called over-activation.

The co-deposition technique

An alternative technique is the so-called co-deposition technique. In this technique, the activation is started by depositing Cs on to the surface in similar manner to the Yo-Yo technique. The GaAs wafer is exposed to the Cs dispensers which are activated by an electrical current of 4 A. Simultaneously, the photocurrent is measured and used as a deposition indicator. A plot of the evolution of photocurrent and pressure of the chamber during the activation using the co-deposition technique is shown in Figure 4.3.

It is seen in Figure 4.3 that after Cs is deposited on the GaAs wafer surface for approximately 20 minutes, the photocurrent is registered and gradually increases, similar to the Yo-Yo technique. When the photocurrent reaches its peak and drops to approximately 2/3 of the peak value, O_2 is immediately admitted into the chamber through the piezo-electric leak valve. The total pressure of the chamber is controlled to not exceed 1×10^{-8} mbar. In contrast to the Yo-Yo technique, the Cs deposition continues during O_2 exposure and continues until the activation process is complete. As exposing to O_2, the photocurrent increases again, reaches its peak and begins to decrease. Once the photocurrent decreases to approximately 2/3 of the previous peak value, O_2 exposure is stopped and as can be observed in Figure 4.3, the photocurrent increases again. This cycle is repeated until the peak values became steady, usually after between 6 and 10 cycles within 90 minutes. The activation process is then complete.

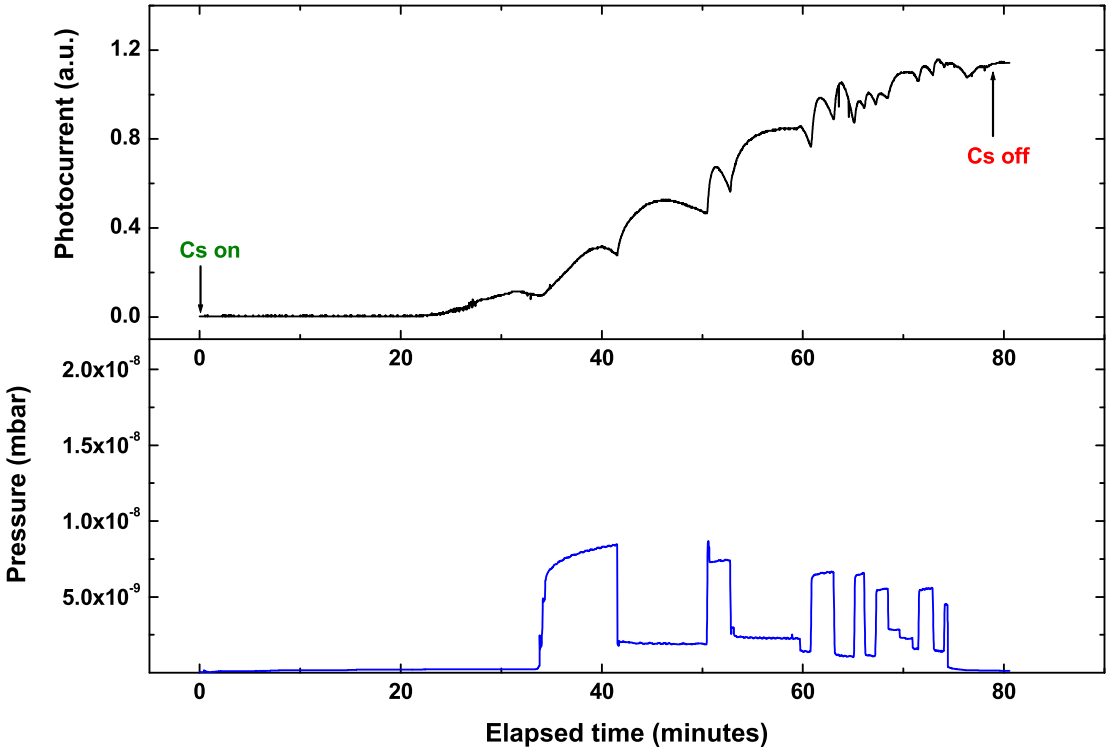

Figure 4.3: A typical plot of the evolution of photocurrent and pressure of the chamber during the activation with the co-deposition technique.

4.2.2 Results and discussion

In this experiment, 10 GaAs wafers were studied: 5 wafers activated using the Yo-Yo technique and 5 wafers activated using the co-deposition technique. The maximum QE obtained from the GaAs wafers activated with both the Yo-Yo and co-deposition technique are shown in Figure 4.4. The maximum QE of between 3.5 - 4.1% and 3.6 - 4.2% were consistently obtained from the GaAs wafers activated by the Yo-Yo technique and co-deposition technique, respectively. From this result, I have not seen a significant difference in the achievable QE obtained between these techniques. However, from the activation point of view, the co-deposition technique uses less time and is easy to control.

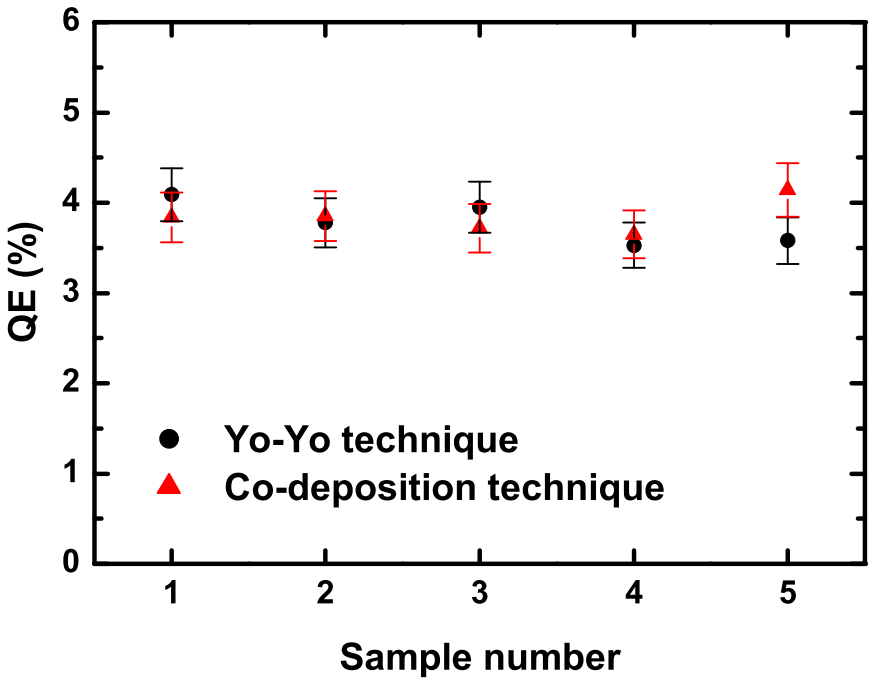

Figure 4.4: The maximum QE obtained from 10 GaAs wafers activated by the Yo-Yo and co-deposition technique.

4.2.3 Characterisation

To study the activation process in more detail, XPS and LEED were carried out after every stage of the preparation and activation processes. Wide range XPS spectra of the as-received GaAs wafer surface, after heating to 600 °C and activation using the Yo-Yo technique are shown in Figure 4.5 and the main Ga and As binding energy peaks observed are summarised again in Table 4.1.

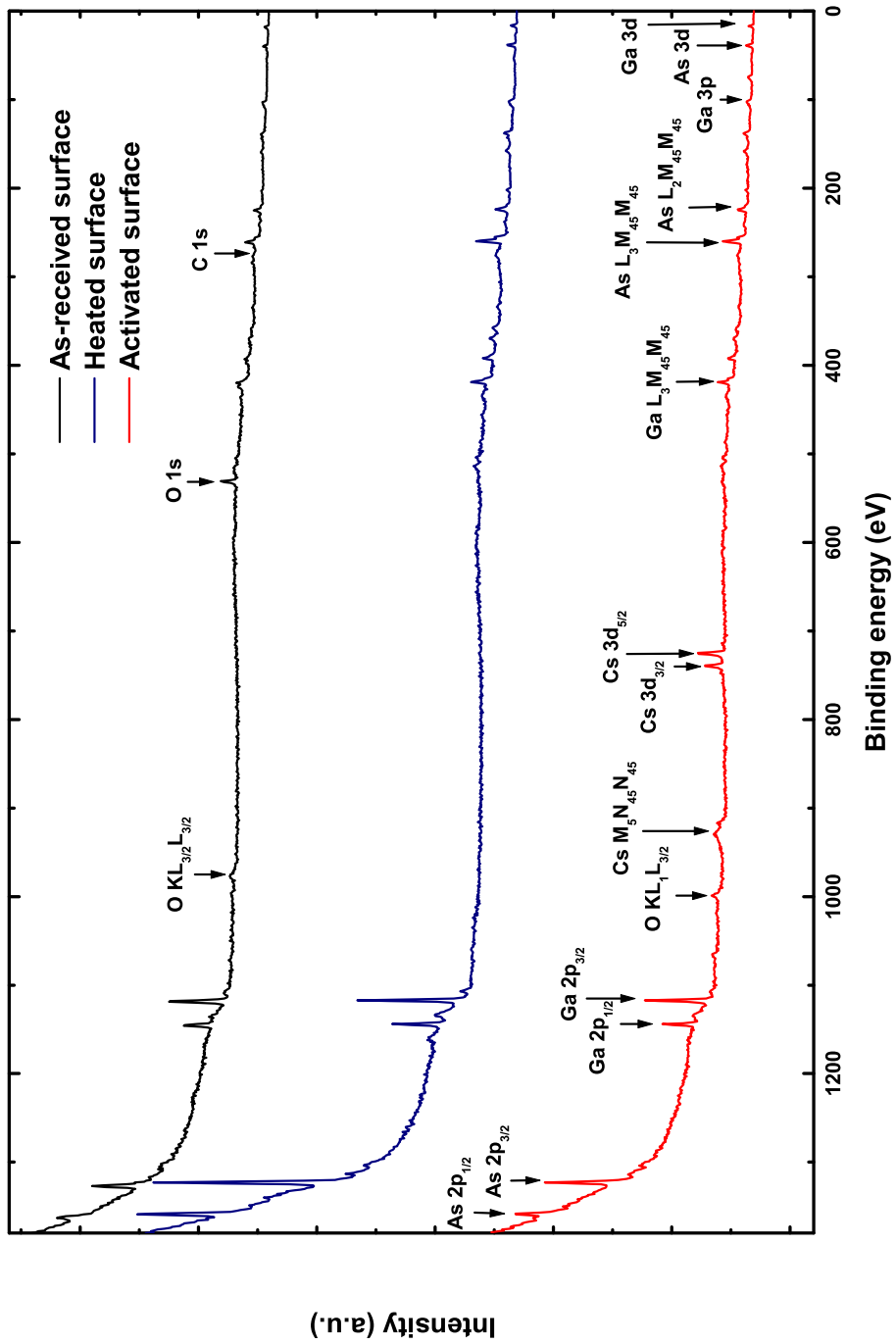

Figure 4.5: Wide range XPS spectra for the as-received GaAs surface, the GaAs surface after heating to 600 °C for 60 minutes, and after activation with Cs and O_2. The arrows mark the main observed Ga, As, O, C and Cs peaks.

Table 4.1: List of the observed main Ga and As binding energy peaks.

Element	Binding energy (eV)			
	As-received surface	Heated surface	Activated surface	Reference [104, 105]
As $2p_{1/2}$	1362	1359	1359	1359
As $2p_{3/2}$	1327	1324	1324	1324
Ga $2p_{1/2}$	1145	1144	1144	1144
Ga $2p_{3/2}$	1118	1117	1117	1117
Ga $L_3M_{45}M_{45}$	419	419	419	419
As $L_3M_{45}M_{45}$	262	262	262	262
Ga $3p_{1/2}$	108	107	107	107
Ga $3p_{3/2}$	104	104	104	104
As 3d	43	40	40	40
Ga 3d	19	18	18	18

For the as-received surface, the shifts of the main Ga and As core binding energy peaks were observed. The Ga $2p_{3/2}$, As $2p_{3/2}$ peaks were found to be shift from their core binding energies of 1117 eV and 1324 eV by 1 eV and 3 eV toward higher binding energy, respectively. These energy shifts indicate the presences of gallium oxide (Ga_2O_3) and arsenic oxides (As_2O_3 and As_2O_5) on the surface. This corresponds to the observation of a large O 1s peak at the binding energy of around 531 eV. The small broadening C 1s peak was also observed around the binding energy of 284 eV, indicating the presence of carbon contaminants on the surface. The XPS spectra in the Ga $2p_{3/2}$, As $2p_{3/2}$, O 1s and C 1s regions are shown in Figure 4.6. The oxides and carbides seem to be the main contaminants on the GaAs surfaces studied in this work. These contaminants have to be removed prior to the deposition of Cs and O layers onto the surface because they prevent Cs atoms forming a strong bond with the GaAs surface. Their presences may also create an interfacial barrier between the activation layer and the GaAs substrate, reducing

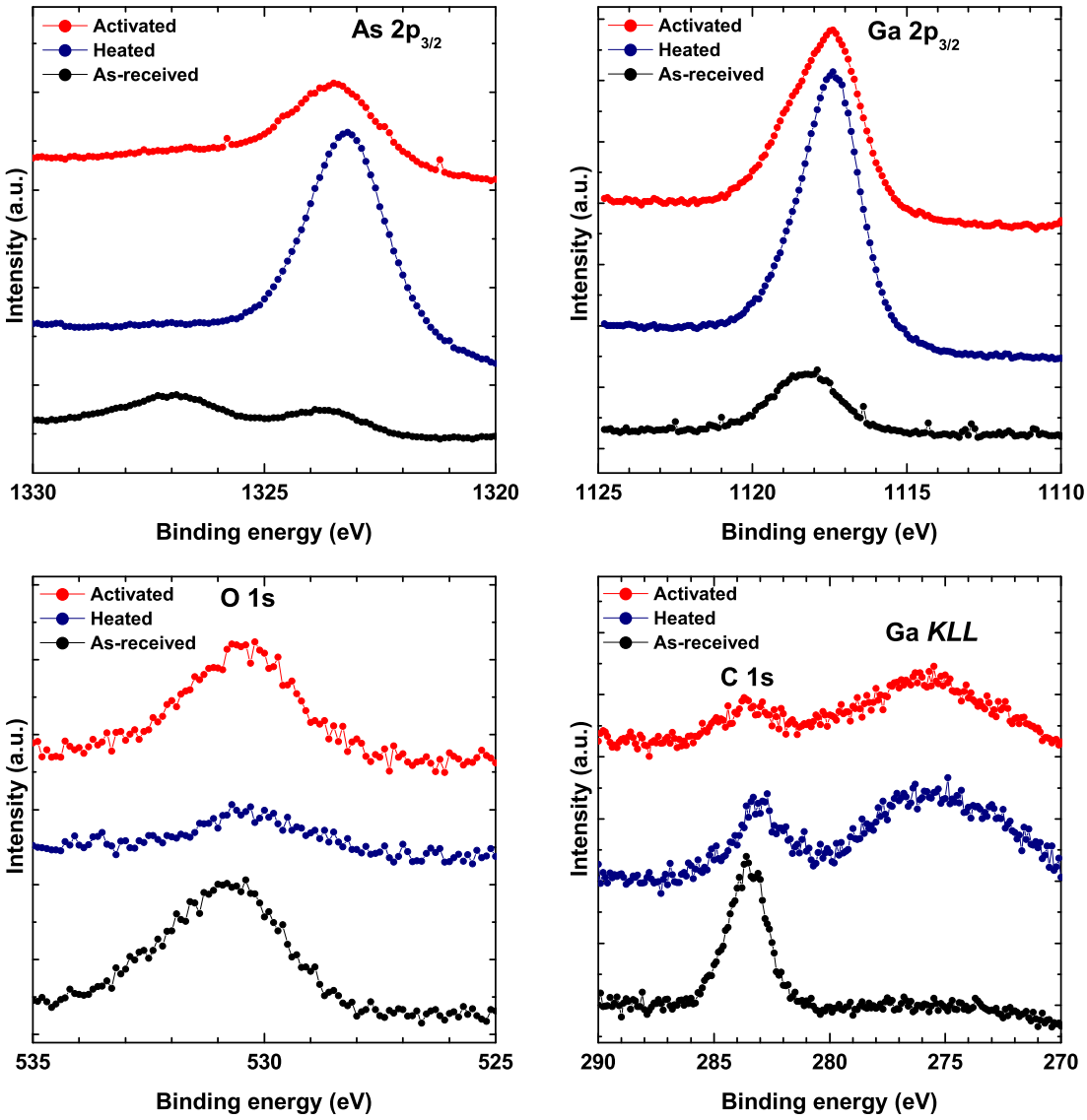

Figure 4.6: The XPS spectra in the Ga $2p_{3/2}$, As $2p_{3/2}$, O 1s and C 1s regions for the as-received GaAs surface, the GaAs surface after heating to 600 °C for 60 minutes, and after activation with Cs and O_2.

the probability for the photo-excited electrons to escape into the vacuum [106].

After heating the GaAs wafer to 600 °C for 60 minutes, it is seen (from Figure 4.5 and Figure 4.6) that the main Ga and As peaks are present at their core binding energies and are in agreement with the reference peaks which are measured for a

cleaned GaAs surface [104]. The Ga $2p_{3/2}$ and As $2p_{3/2}$ peaks are positioned at their core binding energies of 1117 and 1324 eV, respectively. The O 1s peak becomes barely detectable. This result indicates that the oxides or oxygen contaminants are removed from the surface. The Ga and As peaks signals also become stronger due to the removal of the contaminants which screen the Ga and As bulk signals. This result also shows that some surface contaminants such as oxides can be simply desorbed from the GaAs surface by heating to a high temperature up to 600 °C. However, it was found that the intensity of the C 1s peak does not appreciably change after the heating process, as seen in Figure 4.6. The C 1s peak also becomes more complex because of the stronger signal of Ga KLL Auger peak near its position. This peak signal is an superimpose of C 1s and Ga KLL Auger peaks [107]. An exact deconvolution of the peak is required in order to analyse this peak in greater detail. This can be only performed by analysing a Ga KLL spectra from a clean, untreated GaAs surface, e.g., a fresh surface from either a cleaved surface or a newly grown surface [107]. Unfortunately, our system is not capable to perform this experiment.

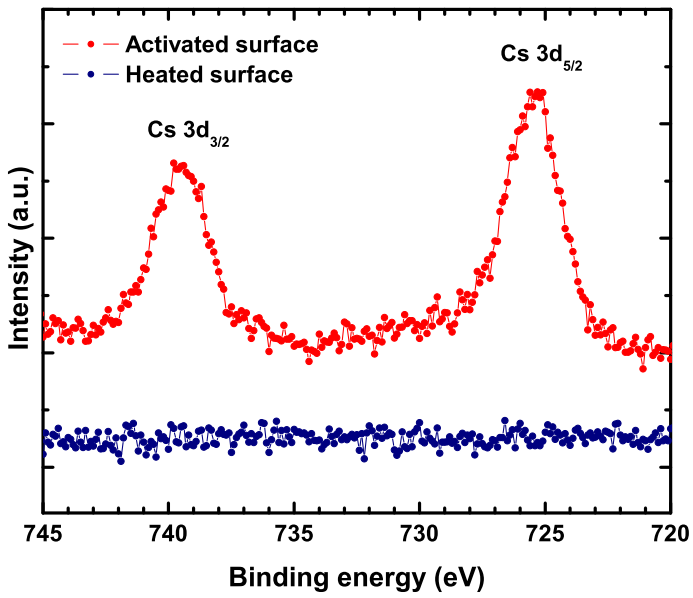

Figure 4.7: The XPS spectrum in the Cs 3d region for the GaAs surface after heating to 600 °C for 60 minutes, and after activation with Cs and O_2.

Nevertheless, the presence of C 1s peak indicates that the carbon contaminants on the GaAs surface cannot be removed by heating the surface up to 600 °C for 60 minutes. The heat cleaning technique and effect of heating temperature will be discussed in more detail in section 4.4.

After activation with Cs and O_2, the Cs $3d_{3/2}$ and Cs $3d_{5/2}$ peaks at binding energies of 739.5 eV are 725.5 eV are clearly observed on the surface, as shown in Figure 4.7. The small signal of O 1s around 531 eV is once again observable, as seen in Figure 4.6. This thus demonstrates that the Cs and O layers are formed on the surface. The intensity of the As and the Ga peaks slightly decrease due to the coverage of Cs and O layers, screening the Ga and As peaks bulk signal. It is interesting that I have not found a shift in the As and Ga peaks from their core binding energies after the deposition, within 1 eV which is the limitation of the instrument. This result suggests that oxygen does not diffuse through the Cs layer and chemically bond with the underlying GaAs wafer. A similar result has been previously reported [108]. Moreover, the difference in the XPS result between the wafer activated by the standard Yo-Yo and co-deposition technique has not been observed in this experiment.

Although the Cs and O layer plays an important role in the achievement of NEA state, the exact stoichiometry of this layer cannot be demonstrated in this experiment and it has not been established up to date. This is because the chemical shifts between Cs metal and Cs oxides are so small, less than 0.5 eV observed in the previous study [108], which is above the limit of our experimental instrument. Moreover, Cs can form a various and complex oxides in the activation layer, for example, the observation of CsO_2, Cs_2O_3, Cs_2O_2, $Cs_{11}O_3$ and Cs_6O in the activation layer were reported [109, 110]. Nevertheless, this experiment has confirmed the existence of Cs and O layers on the activated GaAs surface.

In addition to XPS, LEED was also performed. No pattern was observed on the initial sample surface because of the presence of contaminants such as oxides and carbides on the surface. After heating to 600 °C for 60 minutes, weak LEED spots were observed from the surface. A photograph of LEED spots taken from the GaAs surface after heating to 600 °C for 60 minutes is shown in Figure 4.8. This result

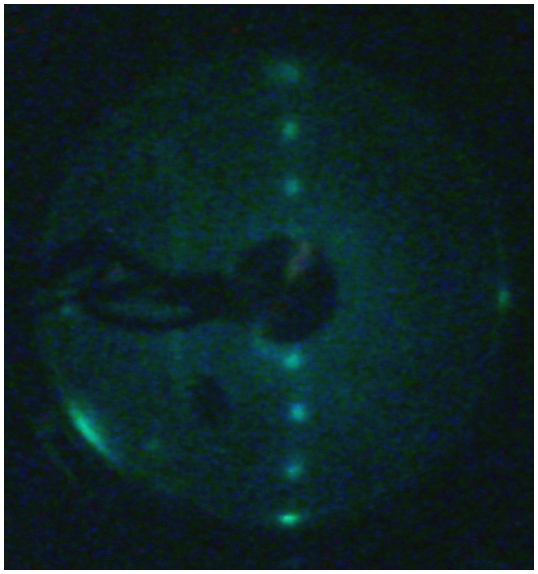

Figure 4.8: Photograph of LEED spots taken from the GaAs surface after heating to 600 °C for 60 minutes with an electron energy, E = 15 eV.

shows that the surface was fairly well-ordered and clean after the heating process, but it was not possible to clearly identify the structure from the observed spots because the spot intensity is too low.

After application of Cs and O layer on the surface, the LEED spots disappeared. This observation suggests that Cs and O_2 deposit in a disordered fashion and form an amorphous layer on the GaAs surface. This result is in agreement with previous studies [100, 111]

It should be addressed here that two main problems were found when I attempted to study the LEED pattern during the course of this thesis. Firstly, the crystalline quality of the GaAs wafers studied in this chapter is low because they were grown using the VGF technique. There are possible structural defects which are generated during the mechanical and chemo-mechanical polishing [112]. As a result, the intensity of LEED signals observed from the GaAs wafters in this work were always low and, therefore, the accuracy and precision of the measurement were far from adequate for real surface analysis. Secondly, in order to record these weak LEED signals, a charge-coupled device (CCD) camera is required for the experiment. Unfortunately, by the time of writing this thesis, the CCD camera has not

been implemented yet. Work toward this is in progress. Hence in this thesis, the LEED technique was only used for verifying the cleanliness and order of the GaAs surfaces.

4.3 NF_3 activation

An alternative to O_2, NF_3 can be used as an oxidant in the activation process. It is believed that F can form a strong ionic bond with Cs and hence create a dipole in the activation layer. As a result, the NEA state can be formed on the GaAs surface in a similar manner to that deposited with Cs and O_2 [113]. In this section, the activation technique for the NEA GaAs photocathode using NF_3 will be studied and discussed in detail.

4.3.1 Preparation and activation

To investigate the activation process using NF_3, a GaAs wafer was prepared in a similar manner to that prepared for the activation process using O_2. The GaAs wafer was degreased with a solution of IPA and acetone in an ultrasonic bath for 30 minutes. Then, it was mounted onto the sample holder and loaded into the system. After introducing to UHV, the sample was transfered to the surface characterisation chamber and heated to 600 °C for 60 minutes. After the heating process, the sample was cooled down to room temperature, transfered to the preparation chamber and ready to be activated.

The activation was performed in the preparation chamber using a technique which is similar to the co-deposition technique. The activation procedure was started with exposure the GaAs wafer to the Cs dispensers which were activated by an electrical current of 4 A. Simultaneously, the photocurrent was measured and used as a deposition indicator. A plot of the evolution of photocurrent and pressure of the chamber during the activation with NF_3 is shown in Figure 4.9.

It is seen in Figure 4.9 that the photocurrent was registered after deposition of Cs for approximately 20 minutes, similar to the activation process with O_2. Then, the photocurrent gradually increased, reached its peak and started decreasing. When

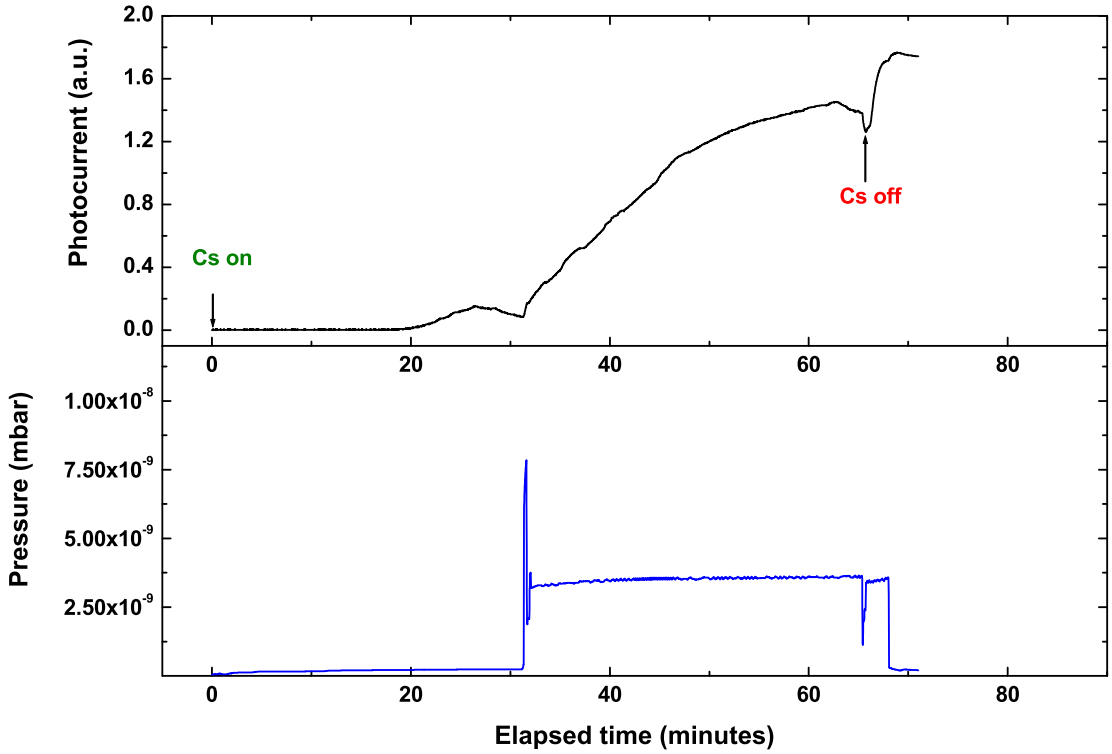

Figure 4.9: A typical plot of the evolution of photocurrent and pressure of the chamber during activation with NF_3.

the photocurrent decreased to approximately 2/3 of the peak value, NF_3 was then admitted into the chamber through the piezo-electric leak valve. The total pressure of the chamber was maintained at approximately 4×10^{-9} mbar during the NF_3 exposure. The photocurrent slowly increased with NF_3 exposure time and reached a peak again. When the photocurrent dropped to approximately 2/3 of the peak value, the Cs dispensers were turned off. The photocurrent immediately increased and reached a peak again. At this point, the NF_3 exposure was stopped and the activation was complete. It is observed in Figure 4.9 that when using NF_3 as an oxidising gas, the photocurrent is almost maximised by the first exposure. This is unlike the activation with O_2 in that a long sequence of alternate O_2 exposures is required to complete the activation. Moreover, the photocurrent is not very sensitive to NF_3 flux. Therefore it is easy to control the activation process.

4.3.2 Results and disscussion

Five GaAs wafers were prepared and activated with NF_3 in this experiment. The maximum QE obtained from the GaAs wafers activated with NF_3 are shown in Figure 4.10. The maximum QE of between 4.2 - 5.5% were obtained. This value is sligthly higher than that obatined from the GaAs wafters activated with O_2. A possible explaination for this slightly higher QE may be because F has a higher electronegativity than O. The electronegativity of F is 3.98, while that of O is 3.44. Therefore, the dipole created from the Cs and F in the activation layer is stronger than the Cs and O dipole, resulting in a lower EA. As a result, the QE of the GaAs wafer activated with NF_3 is slightly higher.

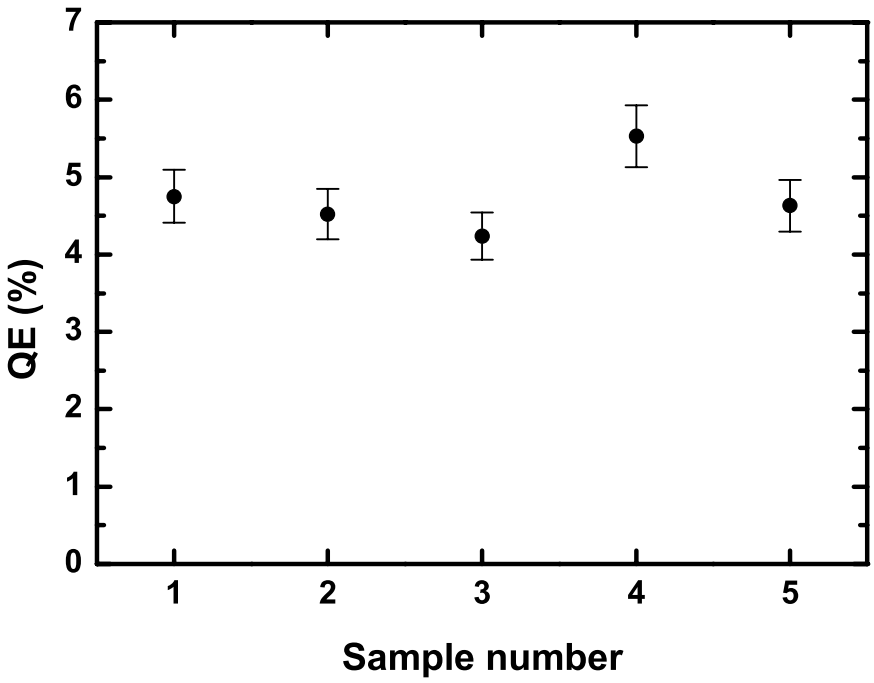

Figure 4.10: The maximum QE obtained from 5 GaAs wafers activated with NF_3

For a further study of the formation mechanism, XPS was carried out to characterise the GaAs surface after heating to 600 °C for 60 minutes and activating with Cs and NF_3. A wide range XPS spectrum and XPS spectra in the Ga $2p_{3/2}$, Cs 3d, F 1s and N 1s regions of the GaAs wafer are shown in Figure 4.11 and Figure 4.12, respectively.

It is seen that after the application of Cs and NF_3 onto the GaAs wafer surface, the Cs $3d_{3/2}$ and Cs $3d_{5/2}$ peaks are clearly observed at peak binding energies of 739.5 eV and 725.5 eV, respectively. A small F 1s peak is observed at a binding energy of 685 eV. Interestingly, no signal of nitrogen is detected around the N 1s peak at a binding energy of 398 eV. This XPS result suggests that only Cs and F forms an activation layer on the GaAs surface.

This experimental result supports the previous assumption that NF_3 acts as a F carrier in the activation process [109, 114]. When NF_3 attaches to the caesiated GaAs surface, it dissociates to provide pure F to form polar Cs and F molecules on the surface. The excess N does not stay in the activation layer because of the strongly-ionic and exclusionary bond formed by Cs and F [113]. This assumption is in agreement with the experimental result as only Cs and F were observed on the surface after the application of Cs and NF_3. However, it is in contrast to the recent photoemission study using synchrotron radiation [113]. In the mentioned study, a significant amount of nitrogen has been observed from the N 1s peak and it was suggested that the nitrogen atoms also bond with the fluorine atoms to form N-F molecules in the activation layer. This disagreement may be because our XPS machine has a lower resolution and surface sensitivity. Therefore, it is not possible for us to observe such a small and sensitive change in the N 1s peak. Nevertheless, a high resolution and surface sensitive XPS experiment is required for a further study this problem in greater detail.

It was also observed that F does not chemically bond with the GaAs substrate, similar to O. As shown in Figure 4.12, no shift in the Ga $2p_{3/2}$ peak at the binding energy of 1117 eV was observed, but its intensity slightly decreases due to the coverage of the activation layer.

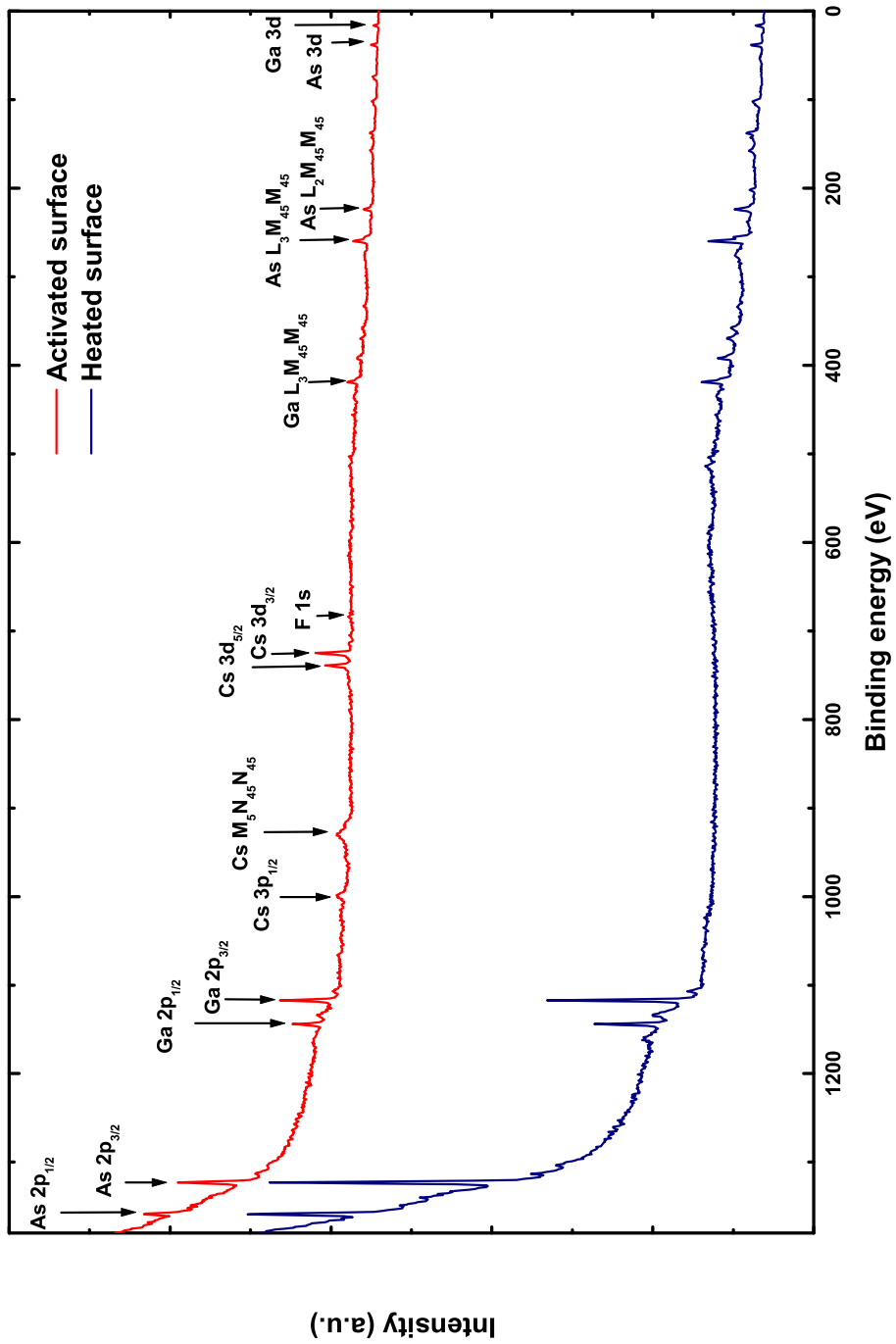

Figure 4.11: Wide range XPS spectra for the GaAs surface after heating at 600 °C for 60 minutes, and after deposition with Cs and NF_3. The arrows mark the main observed Ga, As, F and Cs peaks.

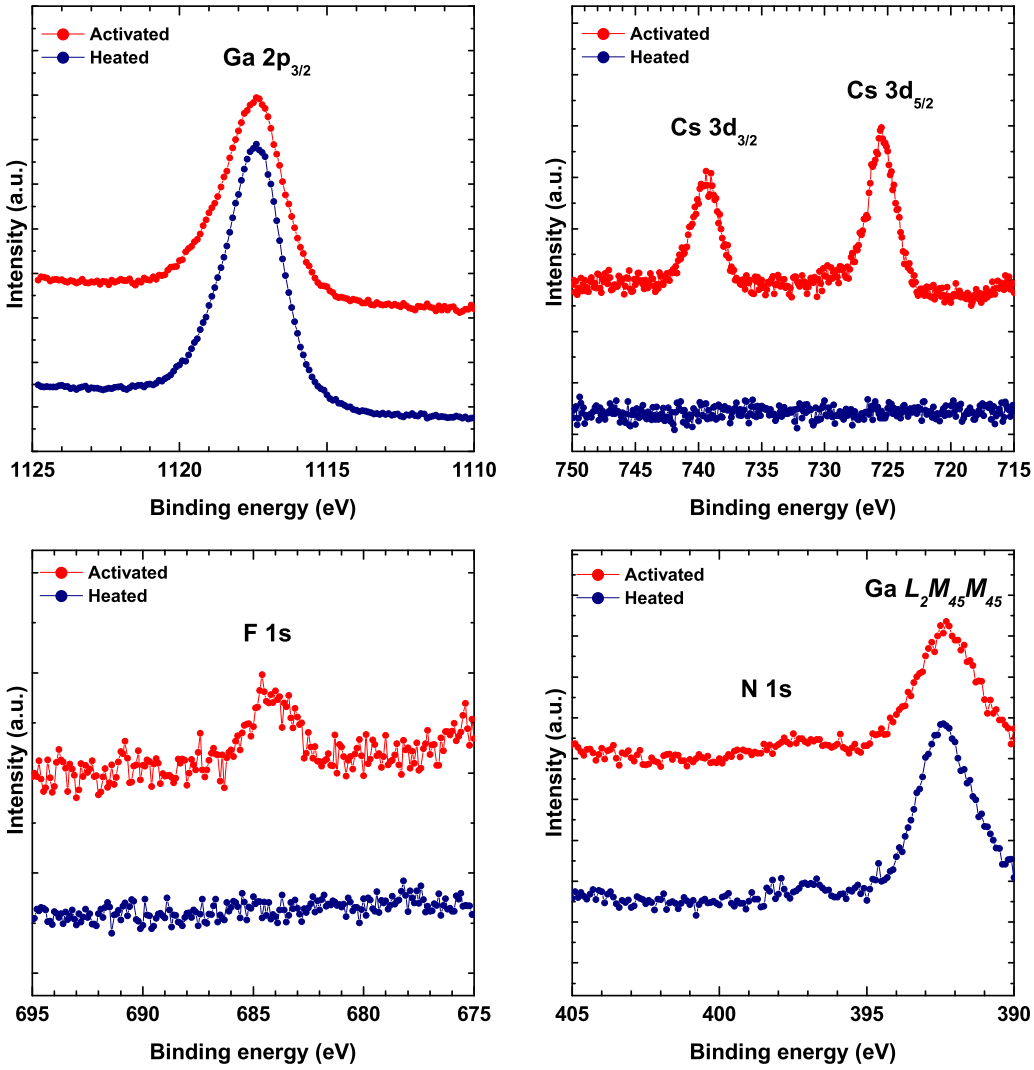

Figure 4.12: The XPS spectra in the Ga $2p_{3/2}$, Cs 3d, F 1s and N 1s regions for the GaAs surface after heating at 600 °C for 60 minutes, and after activation with Cs and NF_3.

In addition to XPS, LEED was carried out to observe a structure of the surface after activation. It was found that LEED spots which had been observed from the cleaned surface disappeared after activation. This result, again, shows that Cs and NF_3 adsorbs in a disordered fashion and form an amorphous layer on the GaAs surface, similar to the activation with O_2.

4.4 Heat cleaning in UHV

It is shown in section 4.2 that some contaminants such as oxides can be thermally desorbed when the GaAs surface is heated to a high temperature up to 600 °C in UHV. Since it is simple and effective, this technique is commonly-used for cleaning the GaAs surface in all laboratories employing a GaAs photocathode in the photoelectron gun. In this section, this technique and effect of the heating temperature on a GaAs surface will be studied and discussed in detail.

4.4.1 Experiments

To study the heat cleaning technique, GaAs wafers were degreased with a solution of IPA and acetone in an ultrasonic bath for 30 minutes. The wafers were then placed onto the sample holders and loaded into the system. After introducing to UHV, the samples were heated separately to five different temperatures; 400, 450, 500, 550, 600 and 625 °C in the surface characterisation chamber. The heating temperature is limited to 625 °C by the congruent evaporation temperature of GaAs(100), which is between 657 to 663 °C [106]. If the GaAs surface is heated above this temperature, As evaporates preferentially as As_2 from the surface, leaving Ga droplets on the surface and generating defects and surface roughening [55].

In all heating experiments, the temperature was slowly increased to the indicated values within 30 minutes to avoid the thermal stress inside the GaAs wafer. The temperature was kept at the temperature for 30 minutes, and then rapidly decreased to room temperature. During the heating process, the temperature of the surface was monitored via an infrared pyrometer with an uncertainty of measurement of ±15 °C.

XPS and LEED were carried out to characterise chemical states and structures of the surface before and after the heat cleaning processes. After each heat cleaning and characterisation, the sample was transfered to the preparation chamber and activated with Cs and O_2 using the standard Yo-Yo technique. The QE measurements were performed with a HeNe laser at 632.8 nm through a 10% ND bandpass filter to evaluate the performance.

4.4.2 Results and discussion

The XPS spectra in As $2p_{3/2}$ and Ga $2p_{3/2}$, O 1s and C 1s regions before and after heating to different temperatures are plotted in Figure 4.13. For the as-received surface, the As $2p_{3/2}$, Ga $2p_{3/2}$ peaks are asymmetrical, broadening and shifts from their core binding energies of 1117 and 1324 eV by 1 eV and 3 eV toward higher energies, respectively. A large O 1s peak is observed at the binding energy of 531 eV. This observation indicates the presence of a gallium oxide (Ga_2O_3) and arsenic oxides (As_2O_3 and As_2O_5) on the surface. Additionally, a broadening C 1s peak is observed around the binding energy of 284 eV, indicating the presence of carbon contaminants on the surface.

After the GaAs surface is heated to 400 °C for 30 minutes, it is seen that the As $2p_{3/2}$ peak at the core binding energy of 1324 eV becomes detectable, while the intensity of the shifted As $2p_{3/2}$ peak at the binding energy of 1327 eV decreases. The shifted As $2p_{3/2}$ peak decreases with the heating temperature and becomes barely detectable when the GaAs surface is heated up to 500 °C for 30 minutes. When the GaAs surface is heated to 550 °C, the change in the shifted Ga $2p_{3/2}$ peak at 1118 eV is observed. The shift in the Ga $2p_{3/2}$ peak decreases and the Ga $2p_{3/2}$ peak is well positioned at its core binding energy of 1117 eV after the GaAs wafer is heated to 600 °C for 30 minutes. It is observed at the same time that the intensity of O 1s gradually decreases when the heating temperature is increased and the O 1s disappears at the heating temperature of 600 °C.

Based on these experimental results, it can be suggested that oxides are thermally desorbed from the GaAs surface in two steps:

1. The arsenic oxides, which are more volatile than the gallium oxide [108], are first desorbed from the surface at the heating temperature between 400 - 500 °C. It is also observed in Figure 5.10 that some arsenic oxides can chemically change into the gallium oxide as the shifted Ga $2p_{3/2}$ peak slightly increases in intensity when the GaAs surface is heated to 500 °C. This is in agreement with the earlier findings [108, 115].

2. The gallium oxide is desorbed at a higher temperature in a narrow range

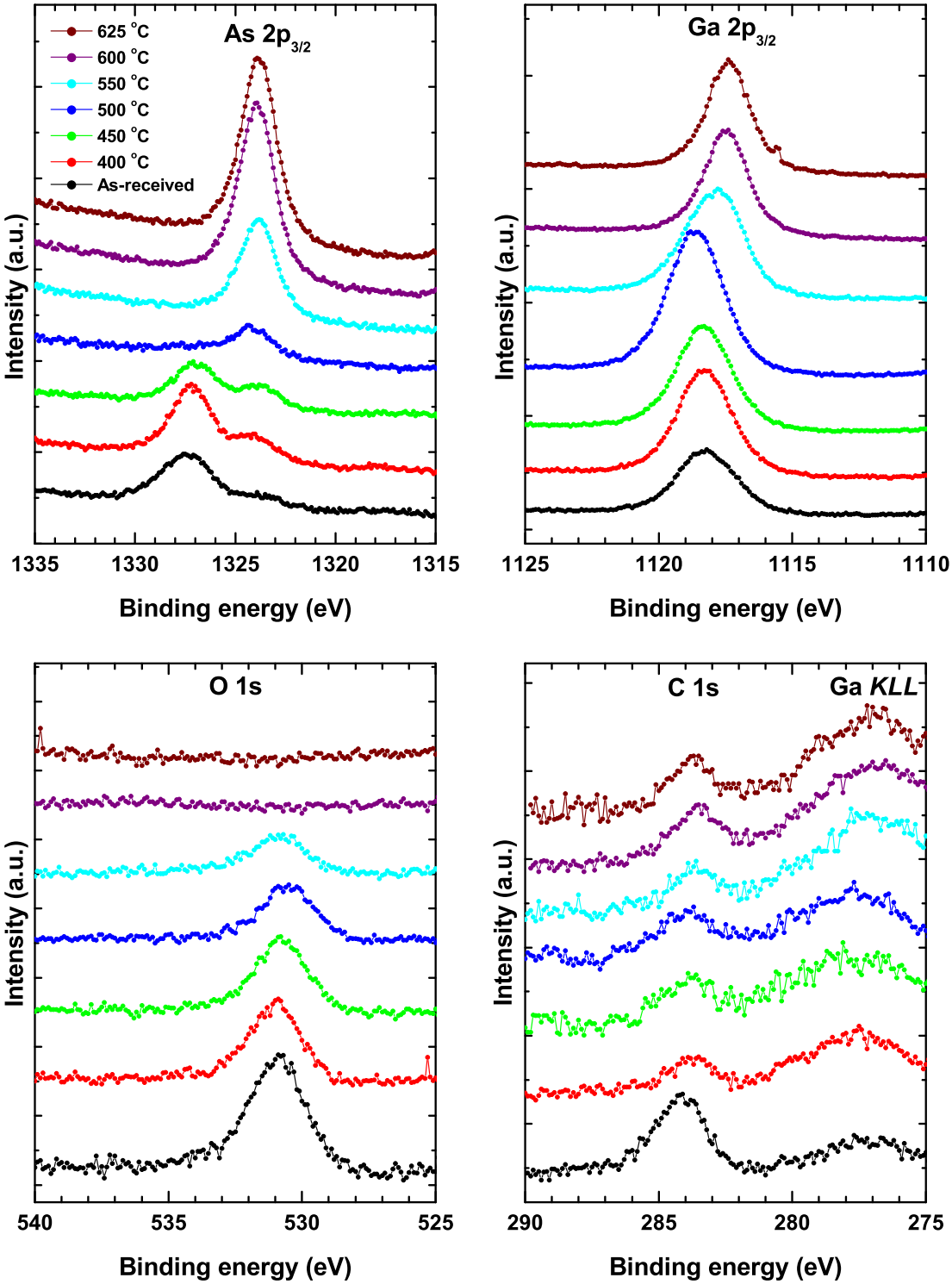

Figure 4.13: The XPS spectra in the Ga $2p_{3/2}$, As $2p_{3/2}$, O 1s and C 1s regions for the as-received GaAs surface, the GaAs surfaces after heating to 400, 450, 500, 550, 600 and 625 °C for 30 minutes.

between 550 - 600 °C and all native oxides on the GaAs surface are removed after heating up to 600 °C.

In contrast to the oxides, it was found that the carbon contaminants cannot be completely removed from the surface after heating the surface up to 625 °C for 30 minutes. As can be seen in Figure 4.13, the C 1s peak slightly decreases with heating temperature and is still dominant after heating the surface up to 625 °C. Thus, the carbon contamination was found to be the main problem for preparing a clean GaAs surface using this technique.

LEED was also carried out to confirm the cleanliness and order of the surfaces after the heating processes. No LEED spots were observed when the sample was heated to a temperature of between 400 - 500 °C. This indicates that the surface is covered with a thick layer of amorphous oxides and carbon contaminants. After heating the surface to 550 °C, weak LEED spots can be seen, indicating a fairly-clean and well-ordered surface. Photographs of LEED spots taken from the GaAs surfaces after heating to 550, 600 and 625 °C are shown in Figure 4.14. It is seen that the LEED spots increase in visibility when the heating temperature increases. However, no clear structure can be determined in the experiment. This result is consistent with the XPS result that all oxides start desorbing from the GaAs surface at a temperature of 550 °C, as a result the LEED spots become visible. After heating to a temperature of between 600 - 625 °C, all oxides are removed from the surface. As a result, the LEED spots becomes brighter and sharper. However, no clear LEED patterns were observed because the small amorphous carbon layers still covered the surface, as seen from the XPS result.

The maximum achievable QE obtained after heating the GaAs wafers to the different temperatures are plotted in Figure 4.15. No photocurrent was detected in this experiment when the GaAs wafer was not heat-cleaned or heated below 450 °C. This is because of the presence of the contaminants on the GaAs surface. The photocurrent became detectable and a QE of 0.84% was obtained when the GaAs was heated to 450 °C for 30 minutes. This result is consistent with the XPS result that the oxide overlayer starts being removed from the surface after heating to a

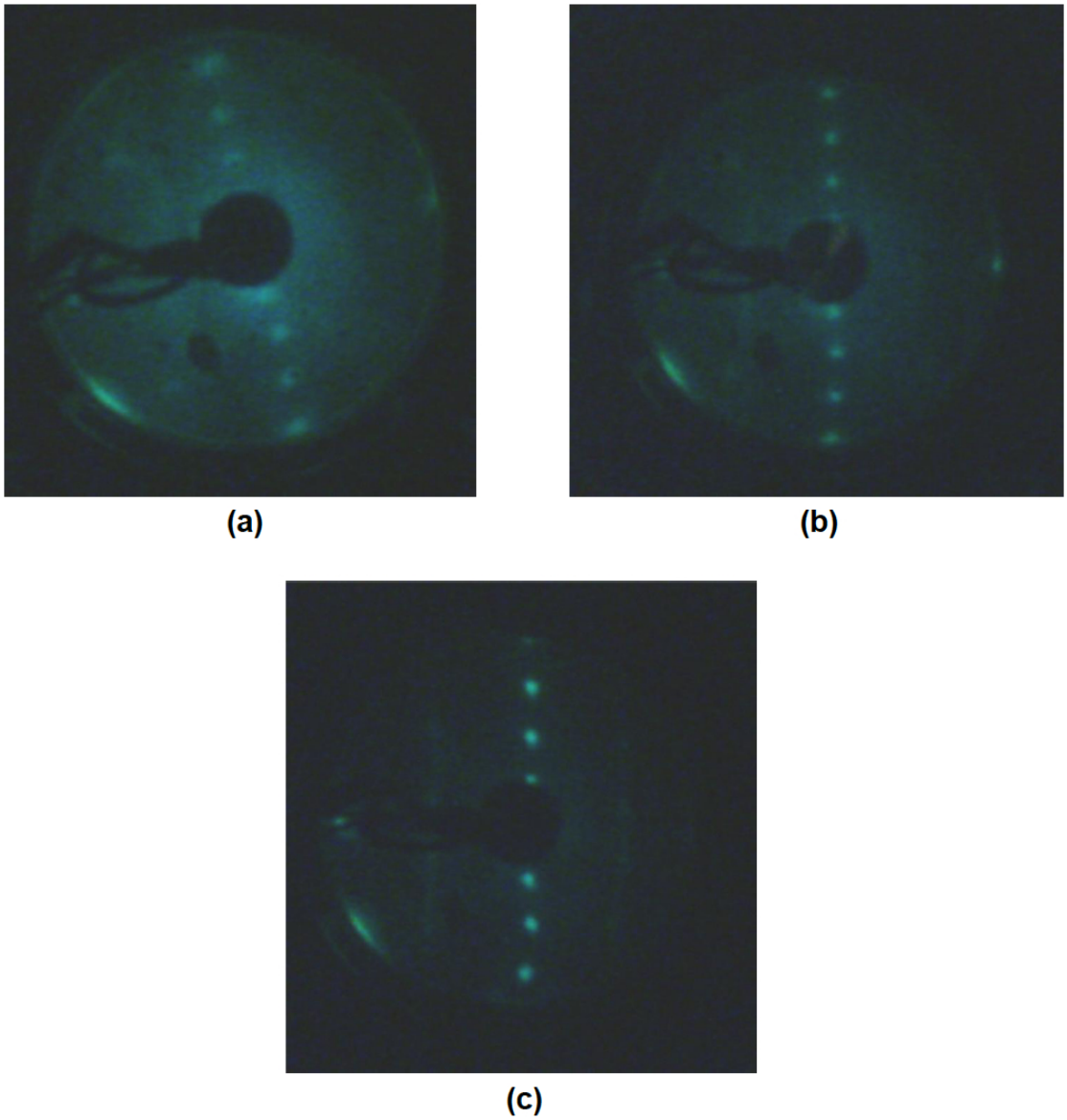

Figure 4.14: Photographs of LEED spots taken from the GaAs surfaces after heating to 550 (a), 600 (b) and 625 °C (c) with an electron energy, E = 15 eV.

temperature of 400 - 450 °C, resulting in a successful activation process. It is seen in Figure 4.15 that the QE increases with the heating temperature and a QE of 4.12% was obtained as a result of heating the sample to 600 °C. This value increases by factor of 2 compared to the result obtained when heating the sample to 500 °C. However, the slight decrease in QE to 3.81% was observed in the GaAs surface after heating to 625 °C.

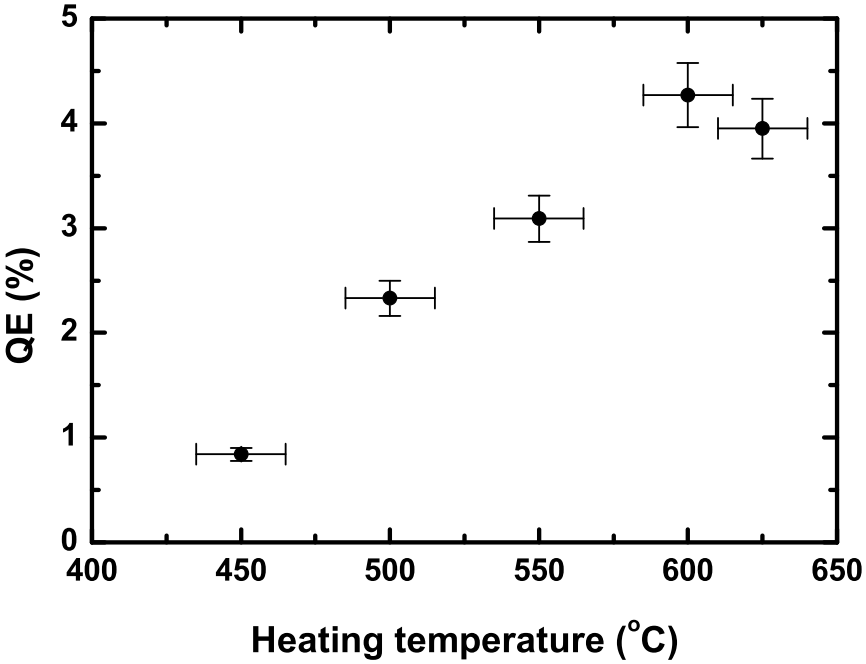

Figure 4.15: The obtained QE as a function of heating temperatures.

The increase in QE with the heating temperature was found to be reproducible and it shows a strong relation between the heating temperature and the achieved QE from the GaAs wafer. This can be explained in terms of surface cleaning as a function of heating temperature. Heating up to 600 °C removes all oxides from the surfaces and therefore, results in the highest acheived QE. However, the slight reduction in the QE at 625 °C observed in this experiment may be because the sample was heated near to the congruent evaporation temperature which might damage the properties of the GaAs and result in a detrimental effect on the achieved QE of the GaAs wafer.

In this section, it has been shown that the maximum achievable QE strongly depends on a degree of cleanliness of the GaAs surface before deposition of Cs and oxidant layers. Heat cleaning in UHV technique was found to be simple, however, it does not provide a carbon-free surface. It has been reported elsewhere [95] that only one monolayer of carbon on the GaAs surface is sufficient to reduce its photoemission to zero. Moreover, a temperature as high as 600 °C is required for removal all

oxides from the GaAs surfaces. At this temperature which is near the congruent evaporation temperature, it can lead to As desorption, generating point defects on the surface [115]. This high temperature also causes the dopant diffusion or loss of doping concentration near the surface. This may have an adverse effect on the QE of the photocathode since the band bending in the photocathode is controlled by the *p*-type doping level [94]. In addition, for an application such as an electron source in an accelerator, a temperature as high as 600 °C may not be attainable and lead to reliability problems for the gun [116]. Therefore, one would like to find a technique which provides a cleaned GaAs surface, free from oxides and carbides, at the lowest temperatures possible.

4.5 Wet-chemical etching

One widely-used technique for preparing a clean GaAs surface at a relatively-low temperature is to etch the surface in a chemical acid followed by heat cleaning in UHV. This etching process minimises the amount of contaminants on the GaAs surface before insertion into the vacuum system. A variety of acid solutions (HCl-based [117, 118], H_2SO_4-based [53], HF-based [119] and NH_4OH_6 [120]) and concentrations can be applied in this etching process. For example, a GaAs photocathode for SLAC [53] had been etched in a 4:1:1 solution of H_2SO_4, H_2O and H_2O_2 and rinsed by H_2O and methanol followed by nitrogen drying. Although this etching technique is effective, the etching rate of the chemical solution is too high for cleaning a delicate structure of thin GaAs photocathode which will be used later for the ALICE PPF.

In this work, I focus on a wet-chemical etching technique with a HCl-based acid solution [117, 118], which was brought my attention by the ISP, Novosibirsk. This technique consists of etching the GaAs photocathode in a dilute solution of HCl in IPA under a clean and non-reactive atmosphere. It has been consistently reported [112, 117, 118] that this technique can remove all gallium and arsenic oxides from the GaAs surface. Moreover, it leaves behind thin elemental arsenic As^0 overlayers of about 1 - 3 monolayers on the surface. The elemental arsenic layers

act as a passivation layer which protects the clean GaAs surface from oxidising and carbon contamination after the chemical etching process, reducing the possibility of contamination during manipulations and transportation to the vacuum system. This As^0 passivation layer can be later removed by heating the surface in UHV at a relatively-low temperature of 400 °C. As a consequence, an atomically-clean GaAs surface is obtained from this technique. Although carbon contaminants cannot be completely removed after this etching process, it was found that the residual carbon contaminants can be easily removed later with the As^0 passivation layer by heating the GaAs surface to 420 °C in vacuum [112, 117]. This is in contrast to the untreated GaAs surfaces where the carbon contaminants cannot be removed even by heating the surface up to 600 °C [112].

Ideally, the etching process has to be performed under a clean and non-reactive atmosphere such as a nitrogen atmosphere. After the cleaning process, it is also necessary to transport the etched GaAs cathode to the vacuum system under the inert gas without exposure to air. This is because a clean GaAs surface is very reactive. Reactive gas species in the air, such as O_2 and CO_2 can adsorb and form the contaminations on the surface. Unfortunately, the surface characterisation system does not have a facility to clean and transport the GaAs wafer under an inert atmosphere. It will be seen later that a nitrogen glove box and transfer vessel have been developed for cleaning and transportation of a GaAs photocathode under the nitrogen atmosphere for the ALICE PPF. Nevertheless, I carried out the experiments in this section in an attempt to see how a GaAs surface is affected by the wet-chemical treatment.

4.5.1 Experiments

The experiment was performed by first degreasing a GaAs wafer with a solution of IPA and acetone in an ultrasonic bath for 30 minutes. After degreasing, the GaAs wafer was etched by following the procedure in references [71, 72]. The GaAs wafer was first dipped in a solution of HCl and IPA with a concentration of 1:60 by volume for 2 minutes, then dipped two times in pure IPA for 1 minute and blown dry with

nitrogen. According to reference [72], all native oxides are completely removed from the surface by etching with this HCl in IPA solution within 10 s. However, a longer etching time period is favorable since it leaves more As^0 passivation layers on the surface.

After the chemical etching, the GaAs wafer was mounted on the sample holder and immediately loaded into the loading chamber. Once the GaAs wafer was introduced to UHV, it was transfered to the surface characterisation chamber and heated to 450 °C for 30 minutes. XPS and LEED were performed before and after heating to characterise the surface. After heating and characterisation, the sample was transfered to the preparation chamber and activated with Cs and O_2 using a co-deposition technique.

4.5.2 Results and discussion

The XPS spectra in the Ga $2p_{3/2}$, As $2p_{3/2}$, O 1s and C 1s regions of the GaAs surface after etching with a 1:60 HCl in IPA solution for 2 minutes and subsequently heating to 450 °C are shown in comparison with the as-received GaAs surface and after heating to 450 °C for 30 minutes in Figure 4.16. It is seen that after etching with a HCl in IPA solution, the intensity of the O 1s peak decreases significantly. Compared to the GaAs surface heated to 450 °C, the level of oxygen is lower by a factor of 2, as judged from the area ratio in Figure 4.16. A strong intense As $2p_{3/2}$ peak at a core binding energy of 1324 eV is observed, whereas only a very weak intensity of the shifted As $2p_{3/2}$ peak, which relates to arsenic oxides, at a binding energy of 1327 eV is detected on the surface. The Ga $2p_{3/2}$ peak is well positioned at a core binding energy of 1117 eV. This result indicates that all gallium and arsenic oxides are nearly removed from the GaAs surface after the etching process. However, a significant amount of carbon contaminants still remains on the surface, as can be seen from a large C 1s peak at a binding energy of 284 eV.

After heating the etched GaAs surface to 450 °C for 30 minutes, further modifications on the surface are observed. The shifted As $2p_{3/2}$ related to arsenic oxides at 1327 eV completely disappears. Both Ga $2p_{3/2}$ and As $2p_{3/2}$ peaks are now po-

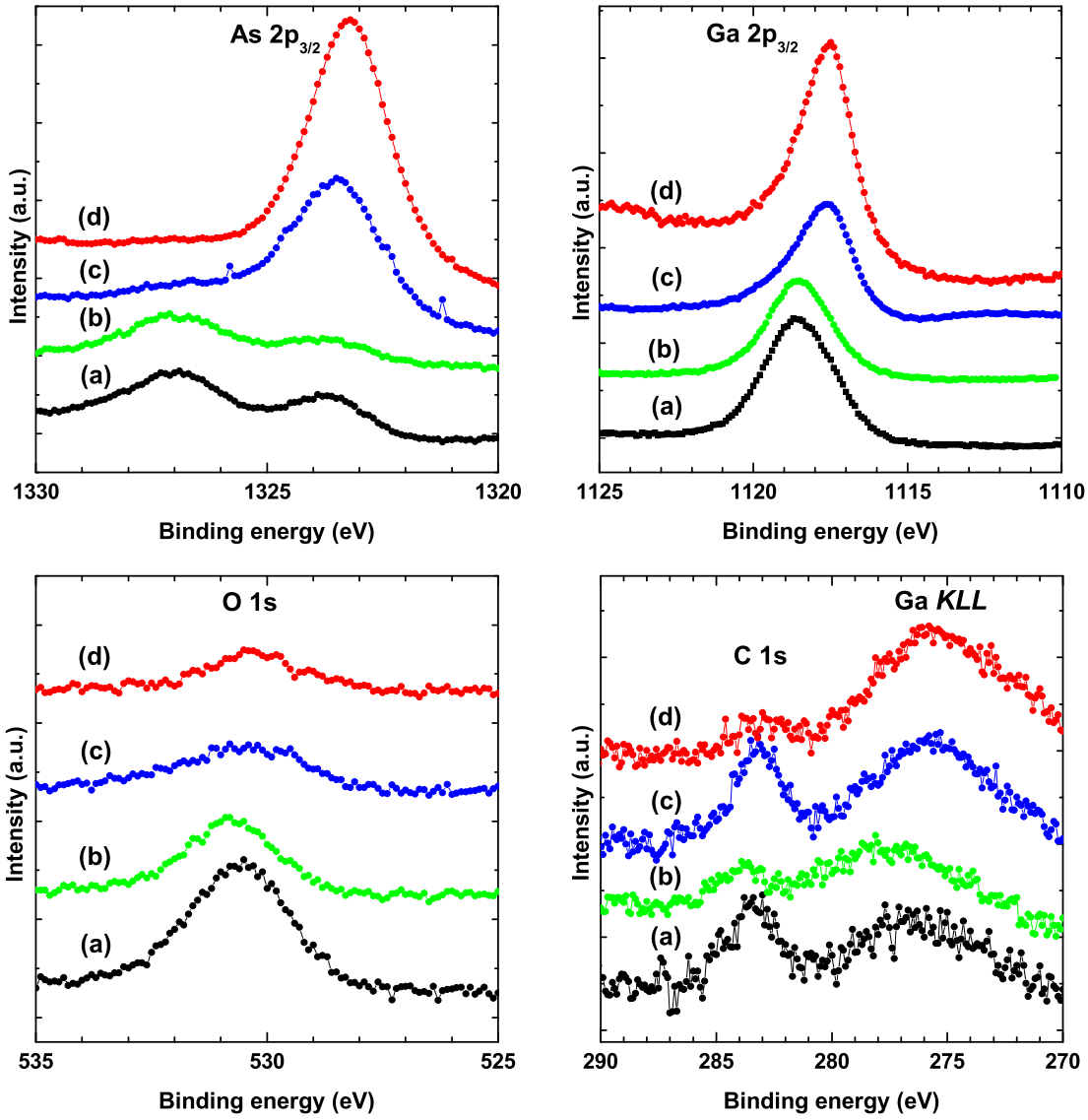

Figure 4.16: The XPS spectra in the Ga $2p_{3/2}$, As $2p_{3/2}$, O 1s and C 1s regions for the as-received GaAs surface (a), the GaAs surfaces after heating to 450 °C for 30 minutes (b), etching with a 1:60 HCl in IPA solution for 2 minutes (c) and etching with a 1:60 HCl in IPA solution for 2 minutes and subsequently heating to 450 °C for 30 minutes (d).

sitioned at their core binding energies and drastically increase in intensity. A very low intensity O 1s peak is detectable, indicating that only a small amount of oxygen still remains on the surface. This residual oxygen is possibly a resilient gallium oxide which is left after the chemical etching and cannot be removed after heating to 450 °C. It is also seen that the C 1s significantly decreases after the heating process. This indicates the removal of carbon contaminants from the GaAs surface.

Figure 4.17 shows photographs of LEED taken from the GaAs surface after etching and consequently heating to 450 °C for 30 minutes. It was found that very low LEED spots were observable after etching in a HCl in IPA solution at an electron energy of 210 eV. After heating to 450 °C, some features of a LEED pattern were seen at an electron energy of 110 eV. Although it is not possible to identify a structure from this pattern because of a low signal intensity, it clearly indicates that a clean and well-ordered GaAs surface is obtained after etching with a HCl in IPA solution followed by heating to a temperature of 450 °C. This is in agreement with the XPS result.

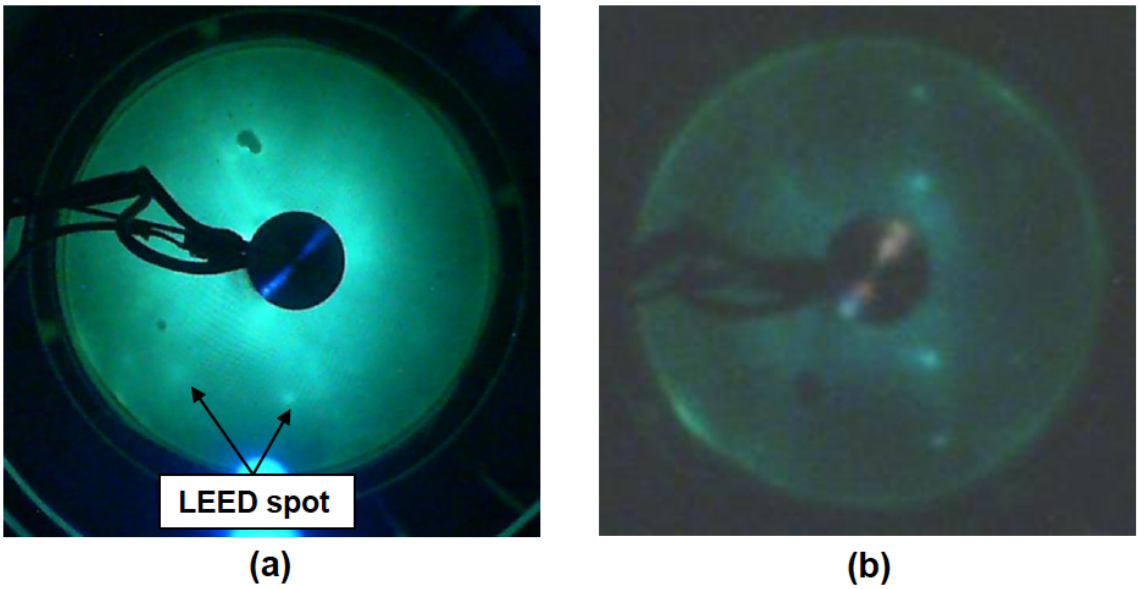

Figure 4.17: Photographs of LEED spots taken from the GaAs surface after etching with a 1:60 HCl in IPA solution for 2 minutes (E = 210 eV) (a) followed by heating to 450 °C for 30 minutes (E = 110 eV) (b).

These experimental results are in good agreement with the effect of the HCl/IPA etching on the GaAs surface, as has been discussed previously [117, 112]. Etching with a solution of HCl in IPA only can remove gallium and arsenic oxides, but cannot remove carbon contaminants from the GaAs surface. However, after the etching process, the residual carbon contaminants are left loosely bound to the GaAs surface and are subsequently desorbed by heating the surface to a low temperature of 450 °C in this experiment. This is in stark contrast to the heat cleaning technique that a temperature as high as 600 °C is required to remove all oxides from the surface. Moreover, the carbon contaminants still remain on the surface even if the surface is heated to 625 °C.

To confirm this result, the GaAs wafers were also cleaned with a 1:60 HCl in IPA solution for 1 minute, 1:30 HCl in IPA solution for 2 minutes and 1:10 HCl in IPA solution for 2 minutes. The XPS spectra in the Ga $2p_{3/2}$, As $2p_{3/2}$, O 1s and C 1s regions of the GaAs wafer surfaces after etching with these chemical solutions are shown in Figure 4.18. It is seen that consistent clean GaAs surfaces were obtained after etching with HCl in IPA solutions and subsequently heating to 450 °C in the vacuum system. Moreover, the cleanliness of the surface increases when the concentration of the chemical solution increases. This result suggests that the etching efficiency increases with the concentration of the chemical solution. After the GaAs wafer was etched with a 1:10 HCl in IPA solution for 2 minutes and subsequently heated to 450 °C for 30 minutes, the O 1s signal disappears and the C 1s signal becomes barely detectable. This indicates that all oxides and carbon contaminants are completely removed from the surface.

However, one has to be careful when increasing the concentration of an acid solution since the etching process does not remove only oxides and carbon contaminants, but also removes an amount of material from the surface. Etching with a high concentration acid solution may remove a significant amount of the GaAs material or dopants from the photocathode and degrades its properties, especially in the case of the thin or strained GaAs photocathodes in which their structures are very delicate. Therefore, in practice, a dilute acid solution is preferential in the etching process to avoid this problem.

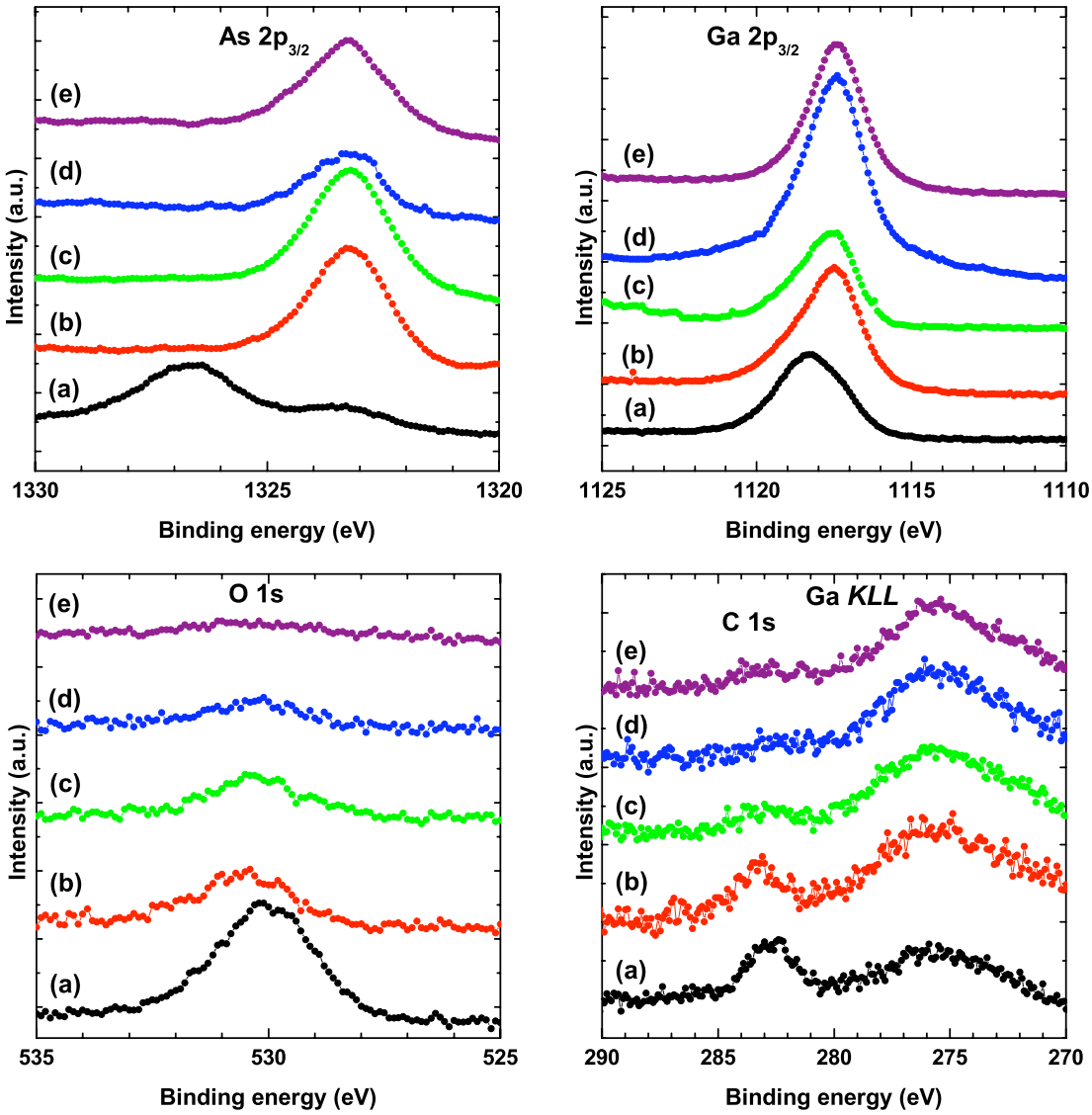

Figure 4.18: The XPS spectra in the Ga $2p_{3/2}$, As $2p_{3/2}$, O 1s and C 1s regions for the as-received GaAs surface (a) after etching with a 1:60 HCl in IPA solution for 1 minute (b), 1:60 HCl in IPA solution for 2 minutes (c), 1:30 HCl in IPA solution for 2 minutes (d) and 1:10 HCl in IPA solution for 2 minutes (e). All etched GaAs surfaces were followed by heating to 450 °C for 30 minutes.

An activation curve for the GaAs wafer after etching with a 1:60 HCl in IPA solution for 2 minutes and subsequently heated to 450 °C for 30 minutes is shown in Figure 4.19. The maximum QE of 4.4% was obtained after the activation. Compared to the maximum QE obtained after only heating to 450 °C, it increases by factor of 4. The maximum QE obtained from the GaAs wafers which were prepared as in Figure 4.18 are also shown in Figure 4.20. It is seen that a consistently high level of QE were obtained from the GaAs wafers prepared by this etching technique. A QE as high as 4.95% was obtained from the GaAs wafer which was etched with the 1:30 HCl in IPA solution for 2 minutes and subsequently heated to 450 °C. This is in good agreement with the XPS results that the cleaned GaAs surfaces were consistently obtained after the etching process.

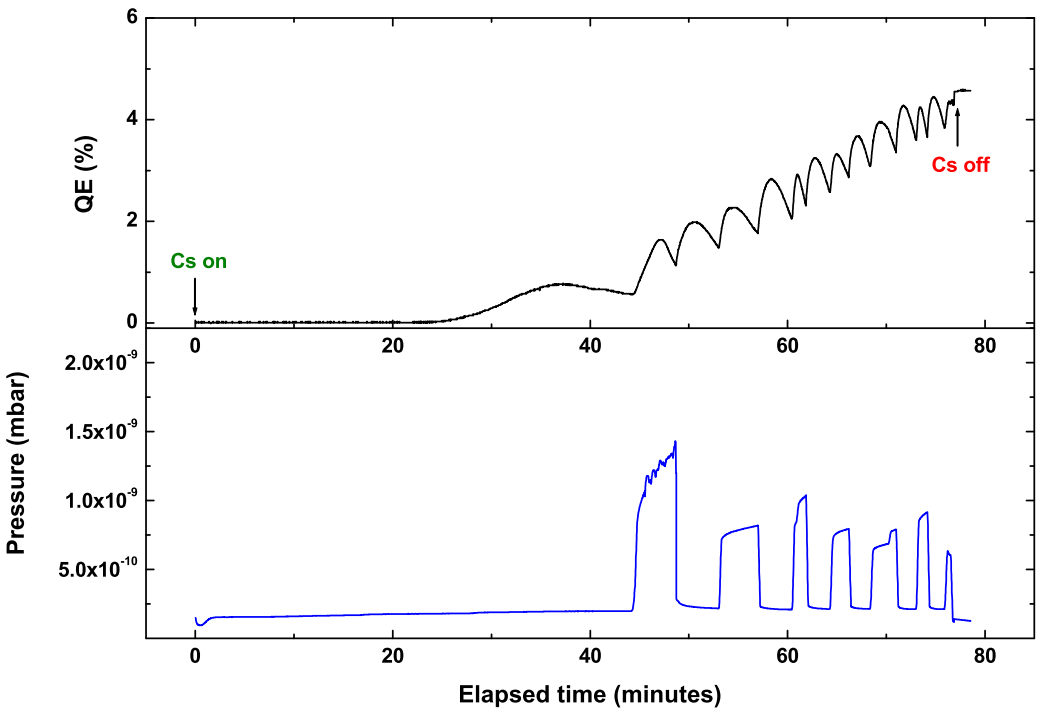

Figure 4.19: A plot of the evolution of photocurrent and pressure of the chamber during the activation of the GaAs wafer etched with a 1:60 HCl in IPA solution for 2 minutes and subsequently heated to 450 °C for 30 minutes.

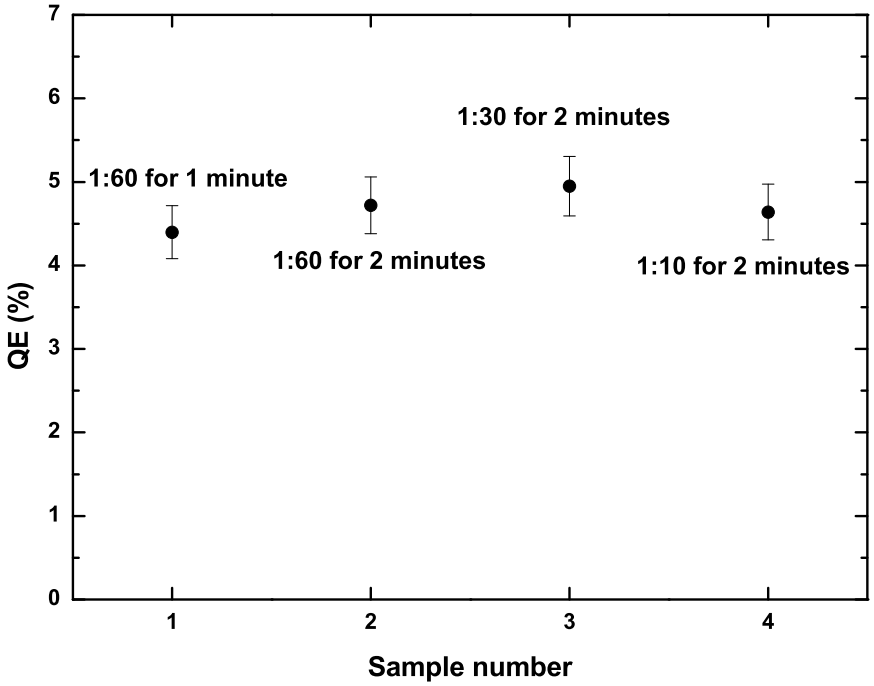

Figure 4.20: The obtained QE from the GaAs wafers etched with a 1:60 HCl in IPA solution for 1 minute (sample 1), 1:60 HCl in IPA solution for 2 minutes (sample 2), 1:30 HCl in IPA solution for 2 minutes (sample 3) and 1:10 HCl in IPA solution for 2 minutes (sample 4) and subsequently heated to 450 °C for 30 minutes.

From this experiment, it is seen that the wet-chemical etching seems to be an effective technique for preparing the NEA GaAs photocathode as it can provide a clean GaAs surface at a relatively low temperature of 450 °C. However, it is a time-consuming process. The GaAs has to be cleaned outside the vacuum and then is transported into the vacuum system. For an operation in a photo-injector, it is not practical to open the vacuum system to atmosphere to regularly clean or repair the GaAs photocathode. It is also difficult to control and avoid the contaminations during cleaning and transportation outside the vacuum. Therefore, another cleaning technique that can be employed inside the vacuum system is desirable.

4.6 Atomic hydrogen cleaning (AHC)

To develop an effective *in-situ* vacuum cleaning technique for the GaAs photocathode, atomic hydrogen cleaning (AHC) was considered. As mentioned in Chapter 3, this technique can provide an atomically-clean GaAs surface, free from oxides and carbon contaminants, at a temperature below 400 °C [95, 96, 97].

The effect of the AHC on the GaAs surface has been previously studied [93, 96, 97, 98, 121]. The mechanism that the atomic hydrogen (H·) reacts and removes oxides are summarised by following equations :

$$2As_2O_x + 4xH\cdot \rightarrow 2xH_2O \uparrow + As_2/(\frac{1}{2}As_4) \uparrow \tag{4.1}$$

$$Ga_2O_3 + 4H\cdot \rightarrow Ga_2O \uparrow + 2H_2O \uparrow \tag{4.2}$$

where $x = 1$, 2, or 5 and represents various arsenic oxides. H· interacts with arsenic oxides and forms molecular arsenic, As_2 or As_4, and H_2O which can be liberated from the surface at room temperature [98, 121]. H· also interacts with non-volatile gallium oxide, Ga_2O_3, and converts to volatile gallium oxide, Ga_2O, and H_2O which are easily desorbed from the GaAs surface at the temperature of approximately 400 °C [97]. In the case of carbon contaminants, they are removed by the formation of various volatile hydrocarbons (CH_2 and CH_3 groups) and subsequent desorption of these compounds from the surface, at room temperature [93, 98].

4.6.1 Experiments

To demonstrate the effectiveness of the AHC, a GaAs wafer was degreased with a solution of IPA and acetone in an ultrasonic bath for 30 minutes. No acid solution was applied to the sample in this experiment. The wafer was mounted onto the sample holder and loaded into the system. After introducing to UHV, the sample was transfered into the surface chracterisation chamber and XPS was carried out on the sample as a reference for further comparison. Following this, the wafer was transfered to the AHC chamber. The GaAs wafer was heated and maintained at the temperature of 450 °C. After heating the GaAs wafer for 20 minutes, the AHC was performed using the hydrogen source cracker. The working principle and design of

this H· source are given in section 3.4. The H· source was switched on and operated with a power of 35 W of the input power. At this stage, the pressure of the chamber increased up to 4.5×10^{-7} mbar due to the outgassing from the sample and the H· source. H_2 was then admitted into the chamber through the H· source and now the heated GaAs wafer was exposed to H·. During the exposure, the total pressure of the chamber was maintained at 2×10^{-6} mbar. Hydrogen with purity of 99.998% pure by volume was used in this experiment. After the sample was exposed to H· for 10 minutes, the H_2 flow was stopped and the hydrogen source cracker was switched off. Following this cleaning, the sample was heated further to 450 °C for 30 minutes. Once the heating was complete and the sample had cooled down to room temperature, it was transfered to the surface characterisation chamber and XPS and LEED were carried out to check the cleanliness of the surface. After characterisation, the GaAs wafer was transfered to the preparation chamber and then activated with Cs and O_2 using the co-deposition technique. The maximum QE was also measured with a HeNe laser at 632.8 nm to evaluate its performance.

4.6.2 Results and discussion

The XPS spectra in the Ga $2p_{3/2}$, As $2p_{3/2}$, O 1s and C 1s regions for the GaAs wafer surface after treating with AHC is shown in comparison with the as-received GaAs surface and after heating to 450 °C for 30 minutes in Figure 4.21. It is observed that the GaAs wafer treated with AHC, both Ga $2p_{3/2}$ and As $2p_{3/2}$ peaks are well positioned at their core binding energies of 1117 and 1324 eV, respectively. No shift in these binding energy peaks is observed. Consistently, the O 1s peak is barely detectable. This result indicates a removal of all oxides from the GaAs surface after cleaning. Moreover, it is observed that the C 1s peak is diminished to a negligible level, indicating a removal of all carbon contaminants from the surface. All these results are in good agreement with the previous studies [93, 96, 97, 98], as has been discussed, that all oxides and carbon contaminants are removed after AHC at a temperature of approximately 450 °C.

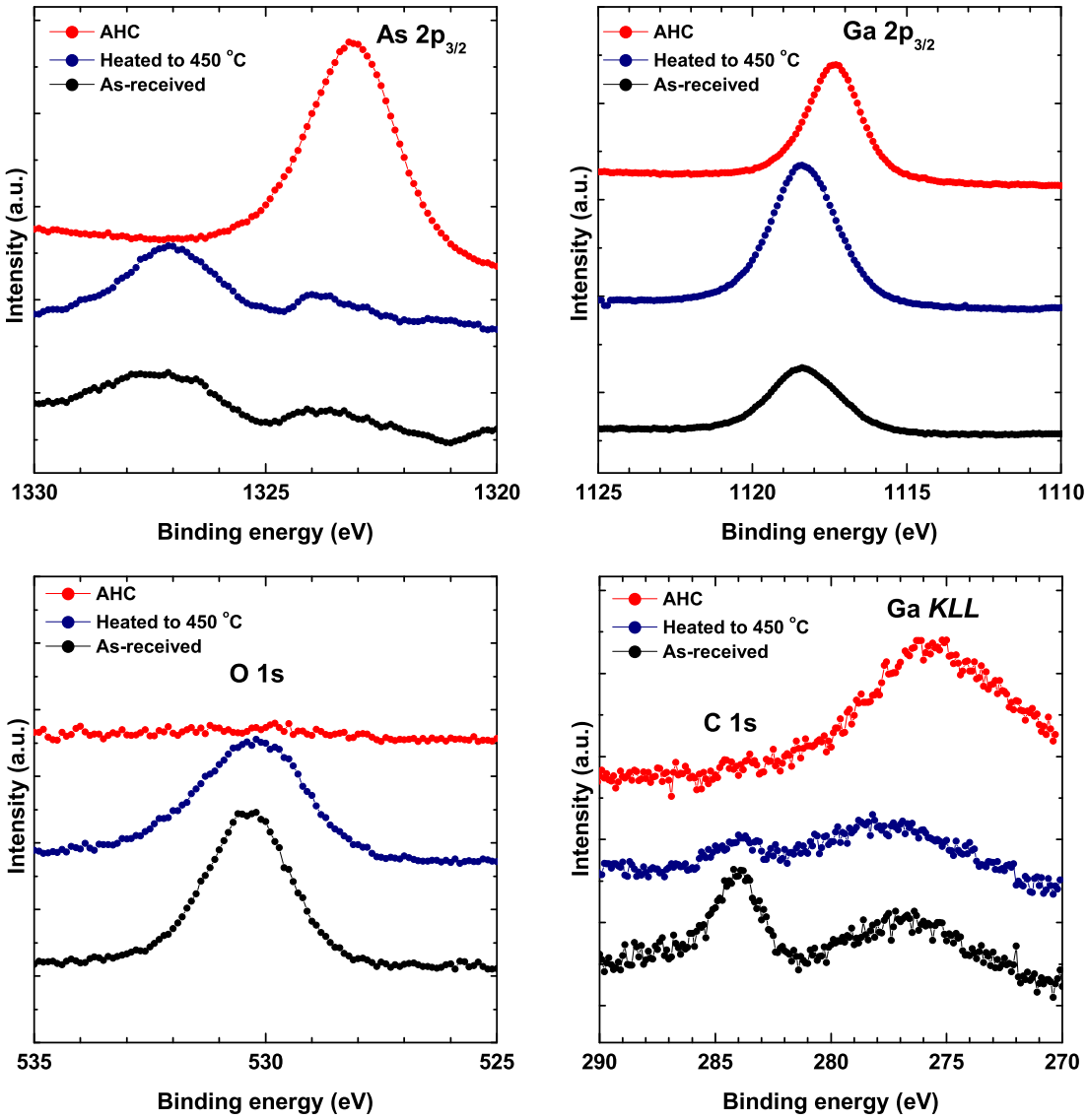

Figure 4.21: The XPS spectra in the Ga $2p_{3/2}$, As $2p_{3/2}$, O 1s and C 1s regions for the GaAs surface as-received, heated at 450 °C for 30 minutes, treated with AHC.

A photograph of the LEED pattern taken from the GaAs after treating with AHC is shown in Figure 4.22. It is seen that a LEED pattern was observed after cleaning at a low electron energy of 20 eV. Although it is not possible to clearly identify, this observed pattern is likely to be a (2×4)/c(2×8) Ga-stabilised pattern which has been observed in a previous study [122]. Nevertheless, this result clearly indicates that the GaAs surface is clean and well-ordered which is consistent with the XPS result.

An activation curve for the GaAs wafer after the atomic hydrogen treatment is shown in Figure 4.23. It is seen that the maximum QE of 4.9% was obtained as a result of cleaning the sample with AHC. This value is the same as that achieved from the cleaned GaAs surface obtained from the wet-chemical etching. This result confirms the effectiveness of this technique.

To further test the AHC, 10 GaAs wafers were prepared, cleaned with the AHC with different powers, exposure times, pressures and heating temperatures. The maximum QE obtained from these GaAs wafers are listed in Table 4.2. It is seen that QE values between 4.72% - 5.12% were obtained after AHC at a pressure between 1.5 - 2.1×10^{-6} mbar and a sample temperature of 450 °C for a variation time of between 10 - 30 minutes. These consistently-high QE's confirm the effectiveness of the AHC. It was also found that the QE increases when the sample temperature during AHC increases. As can be seen from sample 7 and 8, QE's of 5.68% and 5.57% were obtained when the samples were heated to 500 °C during AHC. This result suggests that the heating temperature of 450 °C may be too low for this experiment. When the heating temperature is low, the H· can diffuse into the GaAs surface and forms complexes with shallow acceptors [79]. These complexes result in the increase of the thickness of the band bending region, decreasing the QE obtained from the GaAs wafer.

It is mentioned that XPS and LEED were also performed to check the cleanliness of all sample surfaces in Table 4.2. I have not found any differences in their results. Both XPS and LEED results indicates the clean GaAs surfaces as observed in Figure 4.21 and Figure 4.22 for all samples. Therefore, it is not possible to determine an optimum heating temperature for AHC using XPS and LEED in this

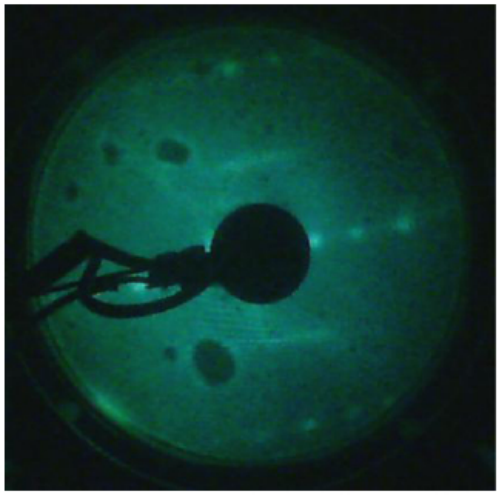

Figure 4.22: Photograph of LEED taken from the GaAs surface after AHC at an electron energy, E = 20 eV .

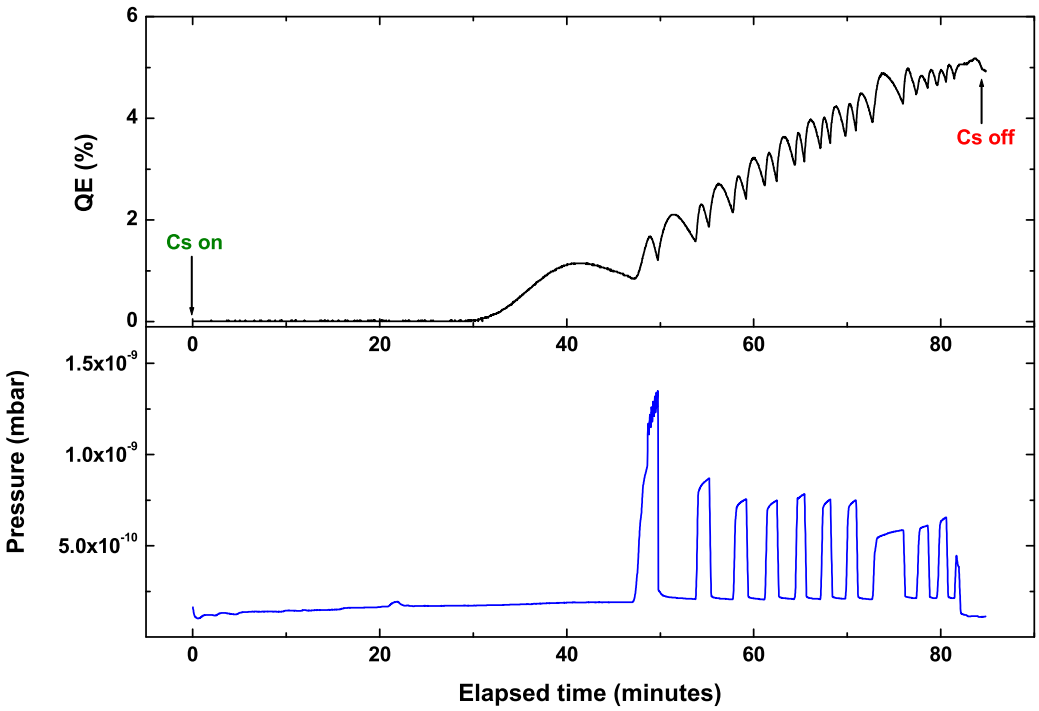

Figure 4.23: A plot of the evolution of photocurrent and pressure of the chamber during the activation of the GaAs wafer treated with AHC.

Table 4.2: The QE obtained from the GaAs wafers after AHC.

Sample number	Power (W)	Exposure time (minutes)	Pressure (mbar)	GaAs temperature (°C)	QE (%)
1	35	10	1.7 - 2.0×10^{-6}	450	4.90
2	35	10	2 - 2.1×10^{-6}	450	4.65
3	35	20	1.8 - 2.0×10^{-6}	450	4.83
4	35	30	1.8 - 1.9×10^{-6}	450	5.16
5	25	10	1.5 - 2×10^{-6}	450	4.85
6	45	10	1.5 - 2×10^{-6}	450	4.72
7	35	10	1.8 - 2.0×10^{-6}	500	5.68
8	35	10	1.8 - 1.9×10^{-6}	500	5.57
9	35	15	5×10^{-5}	450	3.82
10	45	35	6.5 - 8.5×10^{-6}	450	2.87

experiment. The only way to find the optimum heating temperature is to clean, subsequently activate the photocathode and measure the QE [79].

In the case of sample 9, the sample was exposed to H· at a pressure of 5×10^{-5} mbar for 15 minutes. A QE of 3.82% was obtained after the cleaning process. This sample represents a result of an excessive exposure to H· which shows a deleterious effect on a QE of a sample. A similar result was observed on sample 10. It is suggested by [79] that when the flux of H· increases, the probability of the recombination of hydrogen atoms increases. As a consequence, hydrogen molecules can easily form in the vicinity of the GaAs surface and may influence the QE of photocathode surface [79].

This experiment clearly shows the effectiveness of AHC. A clean and well-ordered GaAs surface is obtained by this technique, resulting in a successful activation and high QE. However, results of the AHC process depend on the surface temperature during the process as well as the degree of exposure to H·. These parameters need to be carefully optimised in order to achieve the optimum performance.

In summary, this chapter has shown that the NEA GaAs photocathode can be prepared by deposition of Cs and O_2 or NF_3 onto a clean GaAs surface under UHV conditions. The formation of the NEA state and performance of the photocathode strongly depend on the cleanliness of the GaAs surface before the deposition process. Several techniques can be applied in the cleaning process. A chemical etching with a solution of HCl in IPA and subsequently heating in UHV has been demonstrated to be an effective technique as it provides a clean GaAs, free from oxides and carbon contaminations at a relatively-low temperature of 450 °C. This results in a successful activation and high QE obtained from the GaAs photocathode. This technique will be mainly used in the PPF and the results will be presented in Chapter 6. However, as the chemical etching has to be performed outside the vacuum, it is, therefore, a time consuming process and may not be practical for an operation in a photo-injector. The atomic hydrogen cleaning was also considered in this experiment. This technique can be operated inside the gun vacuum and provides a clean GaAs surface, free from oxides and carbon contaminants, at a temperature below 400 °C. However, the surface temperature and degree of H· exposure during the cleaning process have to be carefully optimise as it can change the GaAs surface properties, resulting in a low QE obtained from the photocathode.

Chapter 5

The ALICE photocathode preparation facility

This chapter presents the development of the ALICE PPF. It is organised as follows. The designs of the new GaAs/AlGaAs hetero-structure photocathodes developed in collaboration with the ISP, Novosibirsk are presented and discussed in section 5.1. In section 5.2, the design and construction of the PPF which consists of three UHV/XHV chambers: a loading chamber (LC), an atomic hydrogen cleaning chamber (AHCC) and a preparation chamber (PC) are described in detail, followed in section 5.3 by the operation of the facility. Finally, the design of the new gun vessel which is presently under construction and the transfer mechanism between the PPF and cathode ball are described in section 5.4.

5.1 The design of GaAs photocathodes

The current ALICE photocathode is a single crystal GaAs wafer grown by VGF (purchased from MaTecK[1] and AXT[2]). The wafer has a diameter of 31 mm and thickness of 500 μm. It was heavily-doped p-type with Zn at a concentration of 5×10^{19} cm^{-3}. One side has a polished face that was cut at $\pm0.25°$ off the 100 axis towards the (111)A plane.

[1]MaTecK GmbH, Juelich, Germany

[2]AXT semiconductor, Geo Semiconductor Ltd, UK

It is well known and experimentally observed [79, 98] that the GaAs photocathode grown by epitaxial technique provides much higher QE than the bulk GaAs photocathode. This is possibly due to the fact that the epitaxial growth provides a better quality of GaAs crystal [79].

According to this observation, two different types of epitaxial grown GaAs photocathodes have been designed and manufactured by the ISP (Novosibirsk) for the gun upgrade and ALICE PPF. One is designed for front-side illumination, and is the so-called *reflection mode* (RM) photocathode. This type of photocathode is technologically easier to fabricate and is consequently in widespread used. Another one is designed for back-side illumination, and is the so-called *transmission mode* (TM) photocathode.

5.1.1 Reflection mode (RM) photocathode

The design of the RM photocathode and the semiconductor structure is shown in Figure 5.1. The semiconductor structure is a GaAs/AlGaAs hetero-structure with an active working area of 10 mm in diameter. The working area was designed to be smaller than that of the current ALICE photocathode which is 25 mm in diameter in order to reduce the emitted dark current. As the laser-illuminated area is only around 4 mm in diameter in the operation, parasite electrons are also emitted from the surface outside the illumination area due to the application of high voltage and cause the problem, as discussed in Chapter 1.

The semiconductor structure is bonded to 1.4 mm pedestal on the bottom of an upturned 2 mm thick molybdenum dish with a diameter of 19 mm and a height of 6.5 mm, as shown in Figure 5.1. Molybdenum was chosen for the base because it is UHV compatible and has an acceptable thermal conductivity. It can also withstand various chemicals used during the photocathode preparation procedures. The hollow, which is seen on the side wall of the base is used in fixing the photocathode within the photocathode holder. The detail of the photocathode holder will be described in section 5.2.2. The semiconductor structure and the molybdenum base are soldered together by a thin ($\sim$1 μm thick) indium layer to eliminate any problems

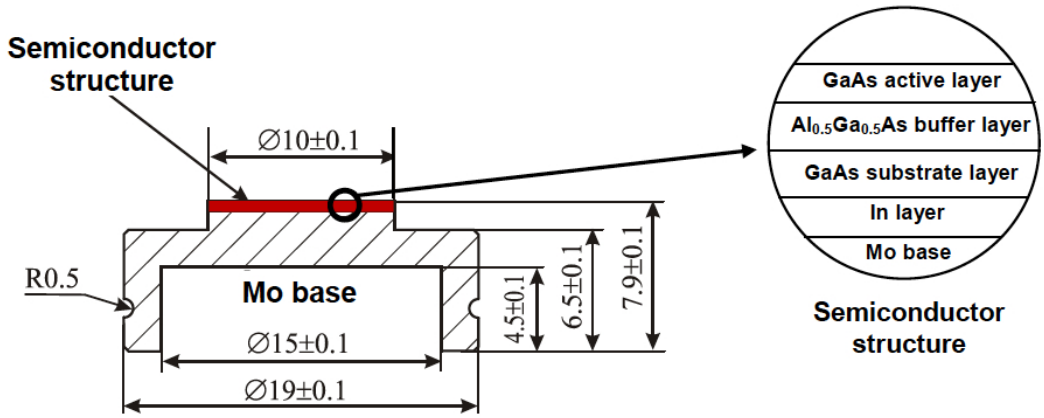

Figure 5.1: Design of the RM photocathode and the semiconductor structure.

with the matching of the thermal expansion coefficients of semiconductor and of metal.

The semiconductor structure of the RM photocathode consists of three layers: the substrate layer, the buffer layer and the active layer. The substrate layer is a bulk GaAs crystal, heavily doped p-type with Zn, with a thickness of between 400 - 500 μm. This layer is a supporting structure for the photocathode which prevents bending and other structural deformations in the semiconductor structure. The buffer and active layers were grown on the substrate by means of metal organic chemical vapour deposition (MOCVD). The buffer layer acts as a transition layer between the substrate and active layers. It is a grown layer of $Al_{0.5}Ga_{0.5}As$ with a thickness of between 0.3 - 0.5 μm, and is doped p-type with Zn at a hole concentration of approximately 5×10^{17} cm^{-3}. The bandgap of the buffer layer is larger than the bandgap of the active layer in order to ensure that it does not contribute electrons to the photoemission process, and that it will block any electron exited in the active layer from diffusing into the substrate. In addition, the buffer layer has the same crystal lattice constant as the active layer, so avoids any strain between the two layers. The active layer is the layer where photoelectrons are generated. It is a grown layer of GaAs and is heavily doped p-type with Zn at a hole concentration of between 1 - 3×10^{19} cm^{-3}. Two different thicknesses for the active layers were mainly used and studied in this work: 2.0 μm and 0.3 μm.

The "thick" active layer of 2.0 μm is designed to fully absorbs the laser power, providing a high QE after activation. The "thin" active layer of 0.3 μm is designed to achieve a fast response time of approximately $\sim$20 ps [59]. As discussed in Chapter 2, the response time of the photocathode depends on the thickness of the active layer and it has been shown that the response time below 2 ps can be obtained from the photocathode with the layer thickness below 0.3 μm. However, the use of the thin active layer of 0.3 μm leads to a decrease in the maximum achievable QE obtained from the photocathode. This is because of an incomplete absorption of the incident laser power when illuminating the photocathode at a photon energy which slightly exceeds the energy gap of photocathode. It is observed in Figure 2.5 that the optical absorption coefficient of p-doped GaAs with holes concentration of 1×10^{19} cm^{-3} at a photon energy of 1.5 eV is approximately 9,300 cm^{-1}. Using Equation 2.2, it can be roughly estimated that only approximately 24% of the incident light power will be absorbed within the 0.3 μm thick active layer. Therefore, the maximum achievable QE of only 24% of that obtained from the thick active layer photocathode that can fully absorb the laser power is expected.

One solution to increase the absorption coefficient of the photocathode is to increase the energy of the illuminating laser (i.e., shorter wavelength). It is seen in Figure 2.5 that the absorption coefficient increases up to 8×10^{4} cm^{-1} when the photon energy increases to 2.3 eV. This level of absorption coefficient is sufficient to absorb 90% of incident laser power within a thickness of $\sim$0.3 μm. However, an increase in the illuminated photon energy leads to an increase in the number of high energy photo-excited electrons in the conduction band. Therefore, a broad range of the high energy electrons are emitted into the vacuum and contribute to the photoemission, causing an increase in electron energy spread of the photoelectrons generated.

5.1.2 Transmission mode (TM) photocathode

The design of the TM photocathode and the semiconductor structure is shown in Figure 5.2. The total geometry of the TM photocathode is similar to the RM photocathode. The semiconductor structure is a two layer GaAs/AlGaAs heterostructure, consisting of a buffer layer and an active layer. The active layer is a grown layer of GaAs with a thickness of 2.4 μm. It is heavily doped p-type with Zn at a hole concentration of between 1 - 3×10^{19} cm^{-3}. The buffer layer is a grown layer of $Al_{0.5}Ga_{0.5}As$ with a thickness of approximately 0.02 μm and doped p-type with a hole concentration of approximately 5×10^{17} cm^{-3}. The small thickness of the buffer layer is needed to reduce the light absorption at photon energies above ~2 eV. The thickness of the active layer is of ~2.4 μm. The anti-reflection layer, made of SiO with a thickness of approximately 65 nm, is deposited on the surface of the buffer layer in order to suppress the reflection of illuminated light from approximately 30% to 5 - 7%. The semiconductor structure is thermally bonded to a disc shape glass base with a diameter of 19 mm and a height of 6.5 mm. This glass base is transparent, permitting illumination of the photocathode from the back-side. It has nearly the same thermal expansion factor as GaAs, reducing the thermal stress during heating processes. The outer rim of the structure layer and the radial surface of the glass carrier are covered with a 1 mm thick layer of Ti/Cr to provide an

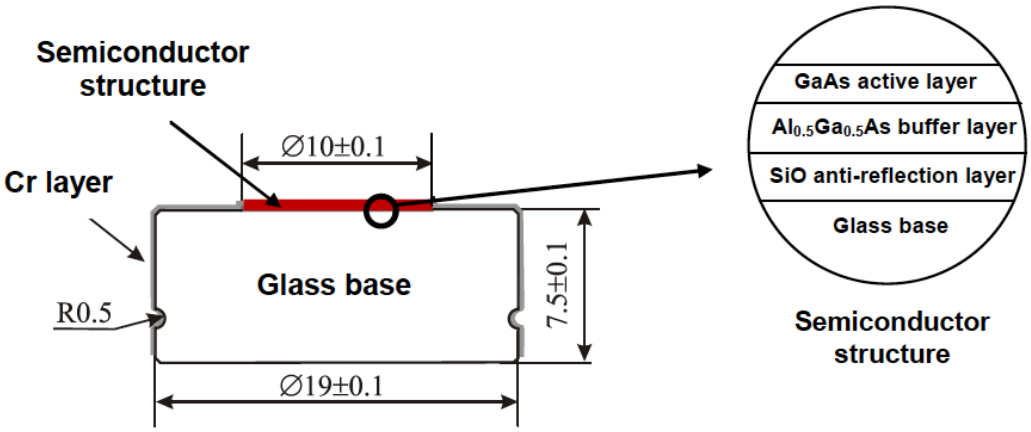

Figure 5.2: Design of the TM photocathode and the semiconductor structure.

electrical contact between the semiconductor structure and the photocathode holder.

The TM photocathode offers several advantages over the RM photocathode. With the TM photocathode, it is possible to illuminate the thin active layer thickness (0.2 - 0.3 μm) to obtain a QE of between 15 - 20% with a high photon energy of 2.3 eV without increasing the electron energy spread. This is because most photoelectrons are excited near the back-side where the photocathode is illuminated, but emits into the vacuum on the front-side. Since the thickness of the active layer is nearly comparable to the thermalisation length, these electrons will undergo scattering, lose their excess energy and eventually become thermalised before reaching the emitting surface, as already discussed in Chapter 2. The energy of the photoelectrons are concentrated in the energy scale within the $\sim k_B T$ energy interval above the conduction band minimum and they are not significantly spread when increasing the illuminated laser energy. The TM photocathode also has an advantage from its illumination geometry. It is easier to design the laser beam transport system and diagnostics when illuminating the photocathode from the back-side. This is in contrast to the illumination from the front-side that it has to avoid clashes between the incident laser beam and internal components of the gun chamber, such as the anode plate and ion-back bombardment suppression electrode etc.

5.2 The design of the ALICE PPF

The design of the ALICE PPF and the photograph of the completed set-up are shown in Figure 5.3. The facility consists of three separate chambers: the loading chamber (LC), the atomic hydrogen cleaning chamber (AHCC) and the preparation chamber (PC). The LC is used to introduce photocathodes into the UHV system. The AHCC is permanently equipped with an atomic hydrogen source for cleaning and rejuvenating used photocathodes. The PC is where the photocathodes are activated, and stored before operation in the gun. These chambers are isolated from each others by two manually-operated UHV gate valves. The photocathodes are transfered between these chambers using a magnetic linear transfer arm, attached to the LC as indicated in Figure 5.3. A second magnetic linear transfer arm is

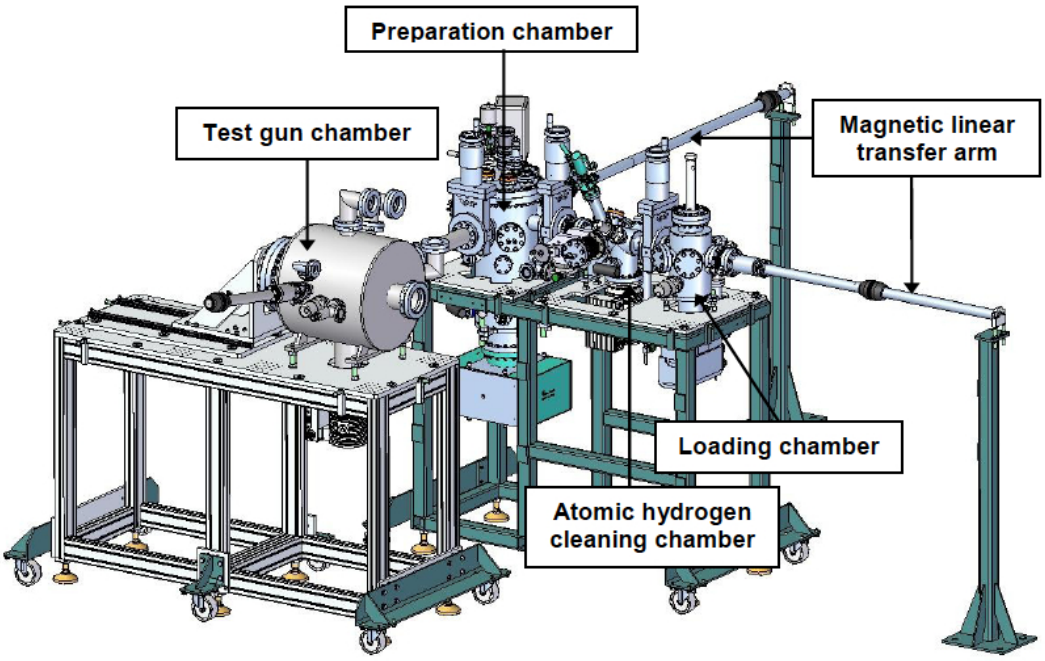

(a)

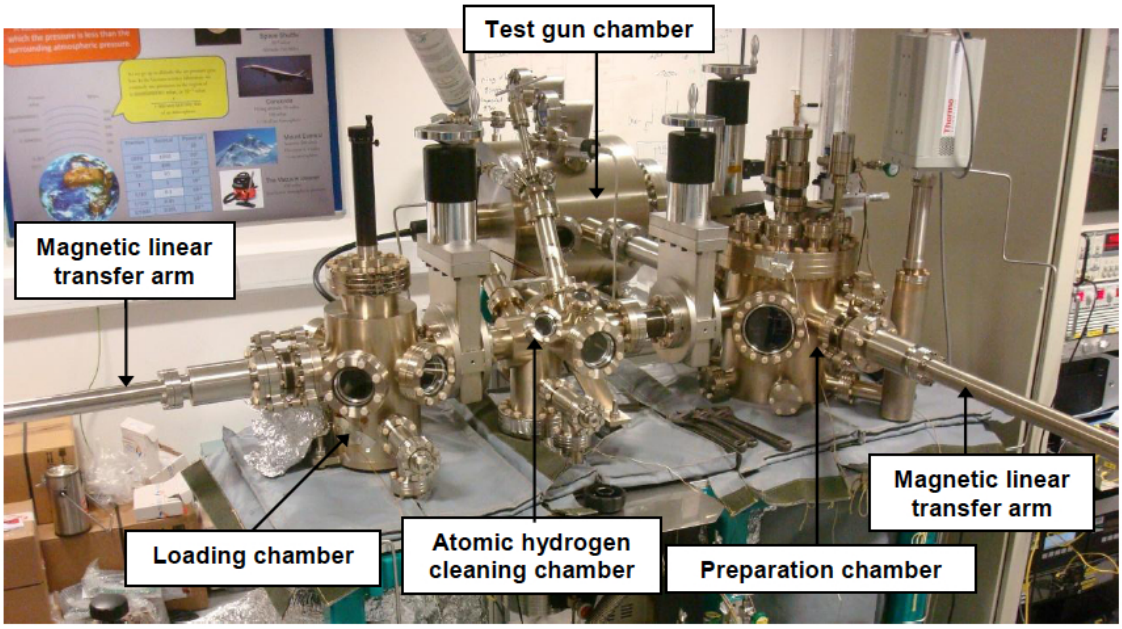

(b)

Figure 5.3: Schematic (a) and a photograph (b) of the ALICE PPF.

attached to the PC and is used to move photocathodes between the PC and the gun. In addition to these chambers, the facility includes a nitrogen purge glove box for preliminary chemical treatment of the photocathodes before their introduction into the set-up.

5.2.1 Construction and assembly

The ALICE PPF were designed and constructed by ASTeC and I made a major contribution at the commissioning stage. The construction and assembly were adhered strictly to the highest levels of UHV/XHV practice as written in the ASTeC vacuum specifications [89]. Only UHV compatible materials that could be baked to at least 250 °C were used. All chamber walls and flanges were fabricated from non-magnetic austenitic 316L stainless steel because this type of stainless steel has a low level of carbon and provides sufficient strength for flange joints exposed to vacuum-firing procedures (typically 900 °C in the UHV range). All flanges are Conflat type with a knife edge style using silver-plated copper gaskets as a sealing medium. In order to reduce virtual leaks, component sizes and shapes were designed to remove all possible trapped volumes, and all welds were full penetration on the vacuum chambers. All stainless steel and titanium components were vacuum fired at 1025 °C for 2 hours to deplete the hydrogen reservoir from the bulk of materials. This ultimately reduces the hydrogen outgassing rate when the vessel is under vacuum. A high degree of cleanliness was observed at all stages of production of all vacuum components to provide an acceptably low outgassing rate. The installation and assembly of all components were carried out in a class 100,000 ISO5 clean room which is "particulate free" under controlled conditions. This is necessary because the photocathode facility will eventually be an integral part of the ALICE photo-injector. Particulates can act as field emitters, and thus, limit the high voltage performance of the photo-injector and superconducting accelerating structures. Once the installation was complete and high vacuum was established, a standard vacuum bake followed at 250 °C for approximately 14 days.

5.2.2 Photocathode holder

The design of the photocathode holder is illustrated in Figure 5.4 a. This holder enables a photocathode to be transported inside and installed in the various different mounting positions for photocathode cleaning and activation within the vacuum system. It consists of three main parts: a titanuim base plate, a flexible ring, and a handle. The base plate allows the photocathode to be placed into the mounting slots present in the transfer vessel, the carousel in the PC and the cathode ball in the gun chamber. The design of these mounting slots is shown in Figure 5.4 b. It can be seen that this mounting slot works like a fork fitting with the base plate. The flexible ring is used to fix the photocathode by pressing on the side wall of the photocathode base, which also provides the electrical path to the GaAs layer. It also has a very low thermal conductivity insulating the base plate and platform during thermal cleaning of the photocathode. The handle has a coarse screw thread which can engage with the end of the magnetic linear transfer arm, as shown in Figure 5.4 c, allowing the holder to be picked up and transported within the vacuum system.

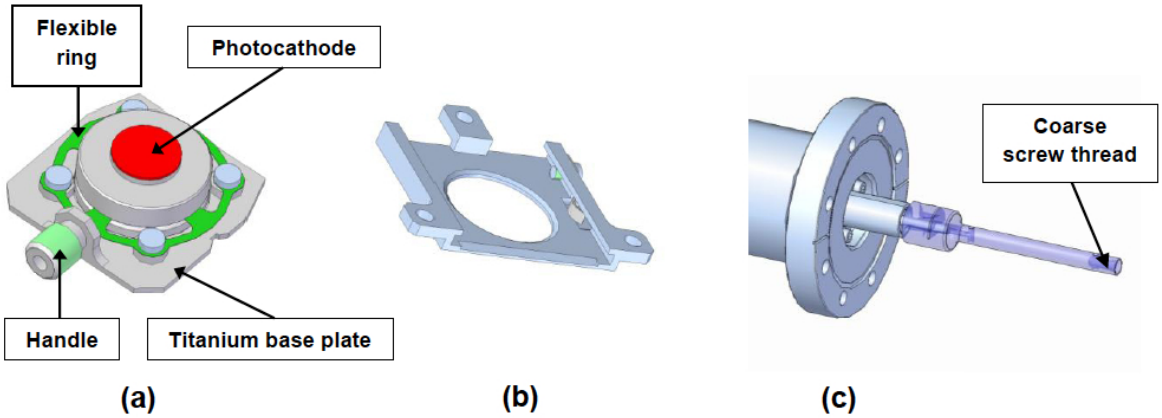

Figure 5.4: Schematic drawing of the holder with a photocathode (a). The holder and photocathode can be slid into the Kovar cathode mounting plate (b) which is installed in various different positions within the PPF system and gun. The end of transfer arm (c) has a coarse screw thread for engaging with the handle of the holder shown in (a).

5.2.3 Loading chamber (LC)

A section through of the LC is shown in Figure 5.5 a. The top of the chamber houses a removable transfer vessel that is used for transportation of cleaned photocathodes from the nitrogen glove box to the chamber. The design of the removable transfer vessel is shown in Figure 5.5 b. It consists of a z-translation stage which carries four mounting slots, and thus allows the transfer of up to four photocathodes at any one time. The translational movement of this stage is provided by the rotation of a "driving cup", and when closed the vessel is sealed by a viton seal.

The chamber is pumped down by a 210 $\mathrm{l{\cdot}s^{-1}}$ turbo-molecular drag pumping station (TSU 261 from Pfeiffer Vacuum). When the pressure reaches the 10^{-7} mbar range a 150 $\mathrm{l{\cdot}s^{-1}}$ ion pump (Noble diode ion pump from Gamma Vacuum) takes

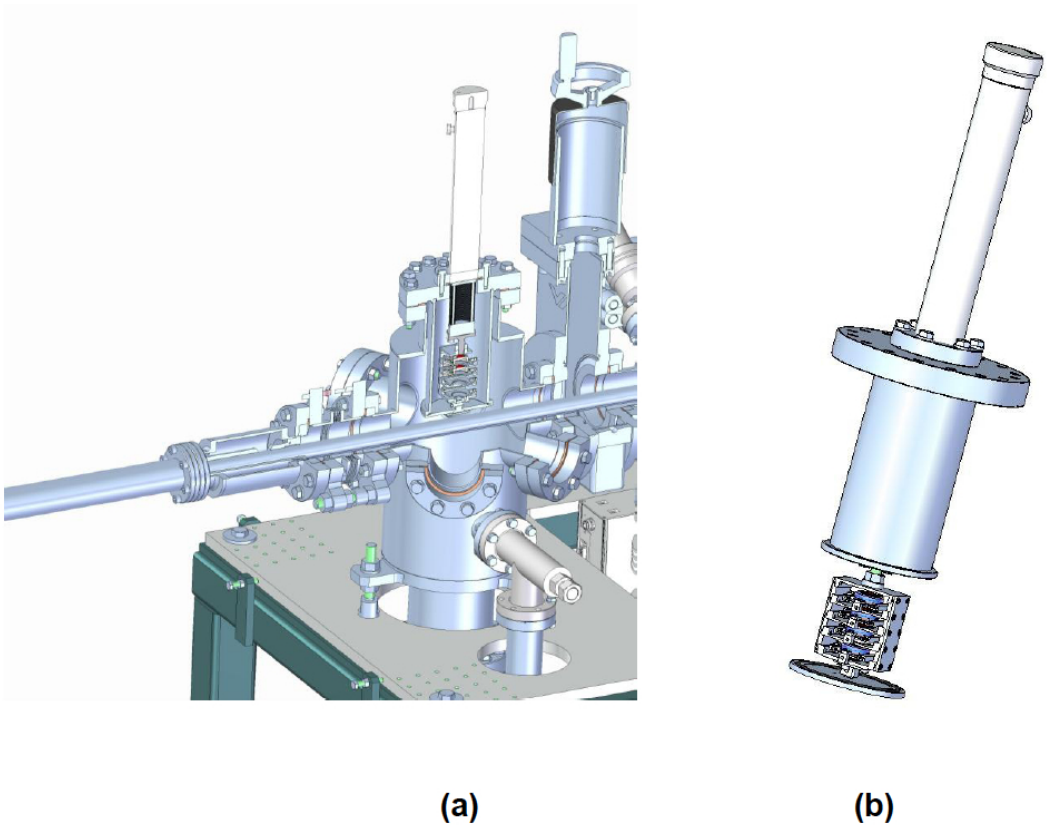

Figure 5.5: Schematic drawing showing a section through of the loading chamber (a) and the removable transfer vessel (b).

over the pumping, providing a final pressure in this chamber in the 10^{-9} mbar range (without bake-out). The pressure is monitored by a pirani gauge (MKS) which operates from atmosphere (10^3 mbar) to 10^{-3} mbar, and an IM cold cathode gauge (MKS) which operates for pressure below 10^{-3} mbar.

5.2.4 Atomic hydrogen cleaning chamber (AHCC)

Figure 5.6 a shows a section through the AHCC. The chamber is installed with a commercial capillary cracking ion-free source (TGC-H Thermal gas cracker from SPECS Scientific Instruments, Inc) for atomic hydrogen cleaning. The flow of hydrogen is controlled by a fine leak valve and monitored by a pirani gauge (MKS). To increase hydrogen purity, a hot palladium membrane filter is installed at the inlet of the source. During the atomic hydrogen cleaning process, the photocathode is held

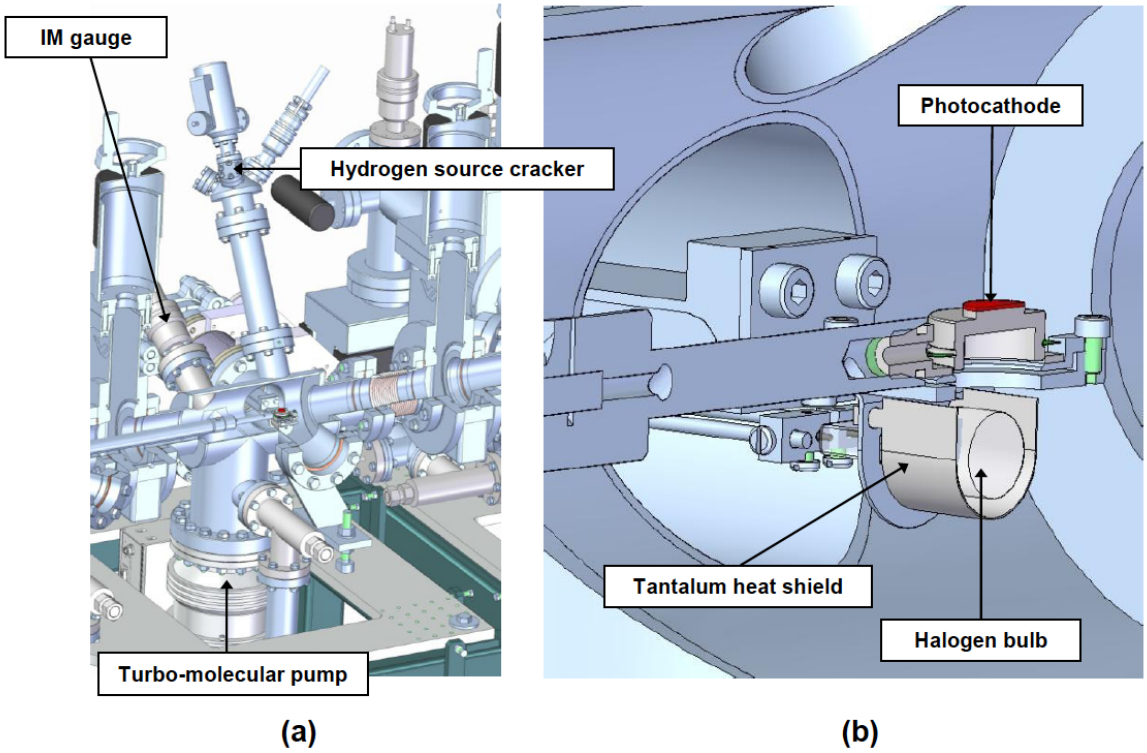

Figure 5.6: Schematic drawing showing a section through of the atomic hydrogen cleaning chamber (a) and the position for atomic hydrogen cleaning (b) inside the chamber.

with the manipulator, as shown in Figure 5.6 b, and can be radiatively heated from the back-side using a 250 W halogen bulb, applied power up to 25 W (maximum). The halogen bulb is shielded by tantalum and installed as close to the photocathode as possible to avoid any radiative heating of other components, whilst focussing the radiated heat onto the photocathode. This assembly is also mounted on a z-stage and can be retracted from the centre of the chamber when transferring the photocathode to the PC.

The chamber is pumped by a 400 $\mathrm{l{\cdot}s^{-1}}$ turbo-molecular pump with a magnetic bearing (Mag W300 from Oerlikon Leybold Vacuum), providing a base pressure of $1{\times}10^{-10}$ mbar in the chamber after bake-out. The pressure is measured only by an IM cold cathode gauge (MKS).

5.2.5 Preparation chamber (PC)

Figure 5.7 shows a schematic drawing (a) and section through (b) of the preparation chamber. The PC houses a rotary carousel with a capability to hold up to six photocathodes. This carousel is located in the center of the upper flange of the chamber as shown in Figure 5.8. It can be moved up/down and rotated to a number of positions for the various processes performed in the PC. The maximum angle of the rotation is restricted within 360° by means of a mechanical stop. The design of the rotary carousel is shown in Figure 5.9. The carousel is made of a 2 mm thick Ti-plate because of the thermal properties. A large slot in the middle of the carousel allows the photocathode to be transferred to the gun using the magnetic linear transfer arm. Radial slots were designed to limit in-plate heat conduction to neighbouring photocathodes during heat cleaning. From the engineering calculations, the nearest neighbour should not exceed 100 °C, whilst the heated photocathode can reach 600 °C at equilibrium steady state condition. The carousel is electrically isolated from the ground with a ceramic insulator. Electrical contact with the carousel is provided via a feedthrough which is connected to the carousel with a flexible (spring-like) wire.

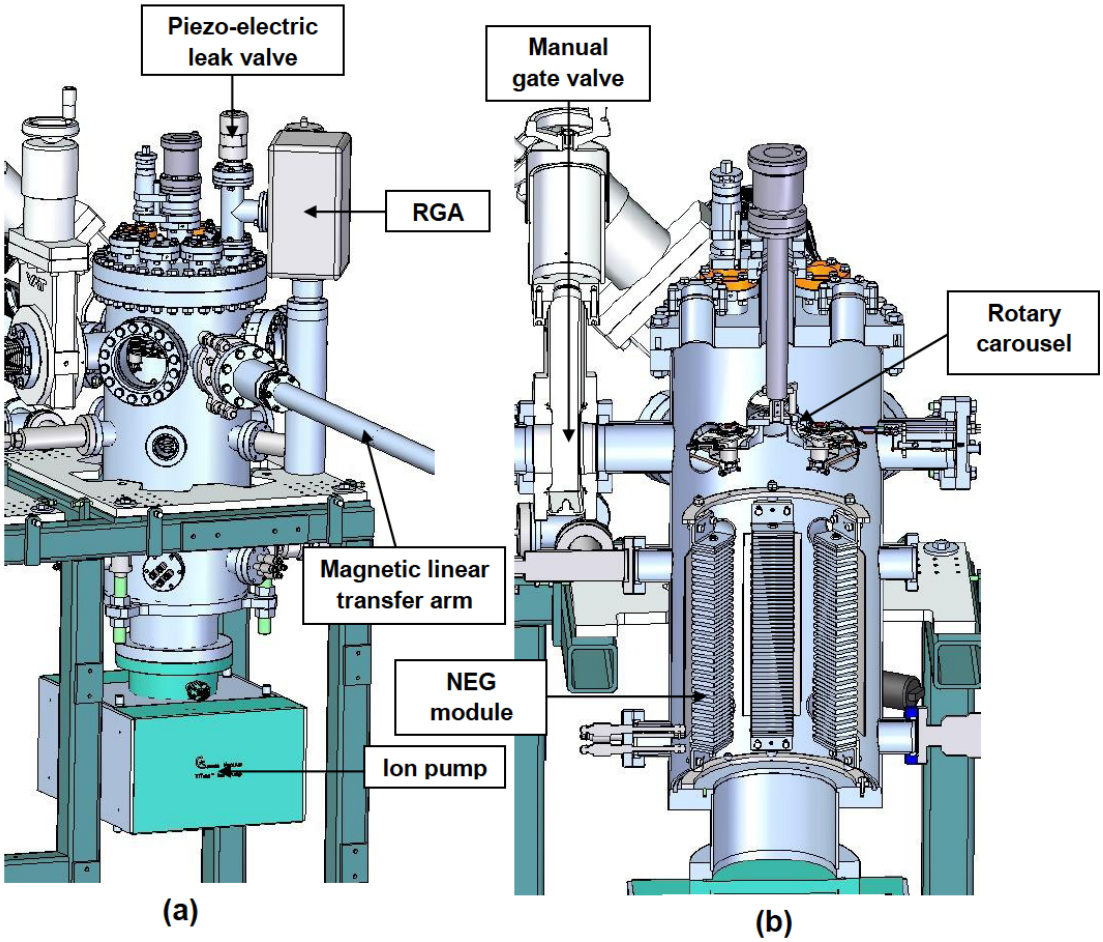

Figure 5.7: Schematic drawing (a) and a section through of the preparation chamber (b).

There are two possible heating positions, each using 250 W halogen bulbs, applied power up to a maximum of 25 W and heating the photocathode up to 600 °C from the back-side. These heater positions are shown in Figure 5.10. The halogen bulbs are shielded by tantalum to reduce radiative heating of other components whilst focussing the heat onto the photocathode. These assemblies are mechanically attached to electrical feedthroughs which allow application of electrical current to the bulbs.

An activation of a photocathode to the NEA state is carried out at the activation position. Four Cs dispensers (Alkali Metal Dispensers (AMDs) from SAES) are spot-weld together in series (2 pairs, effectively) and placed symmetrically above the

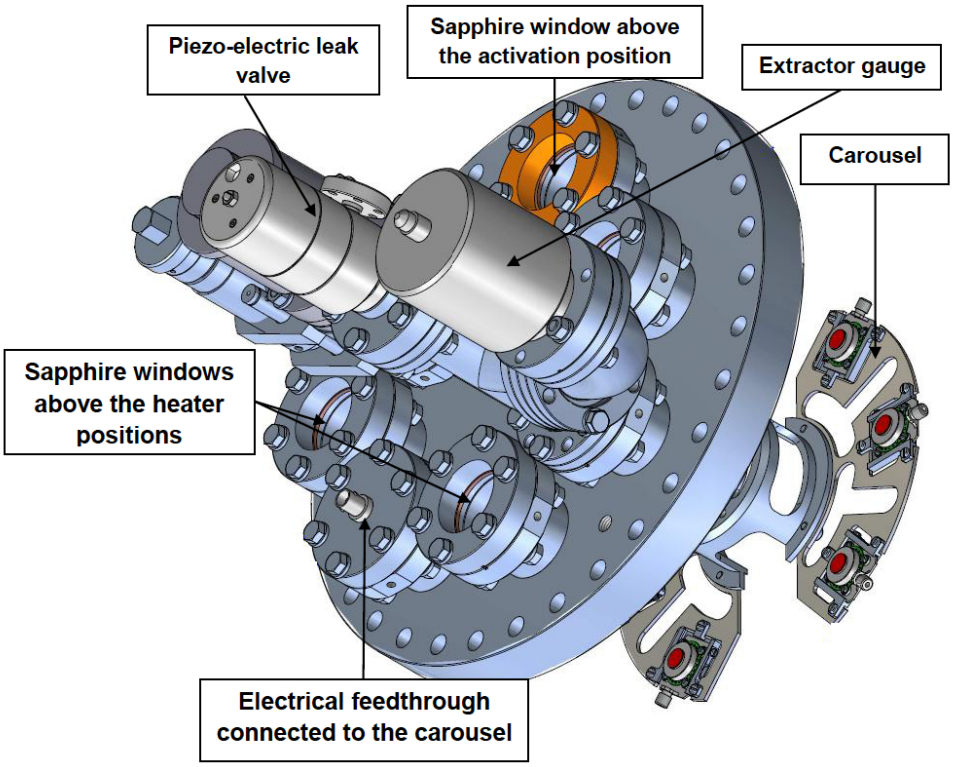

Figure 5.8: Schematic drawing of the upper flange of the preparation chamber.

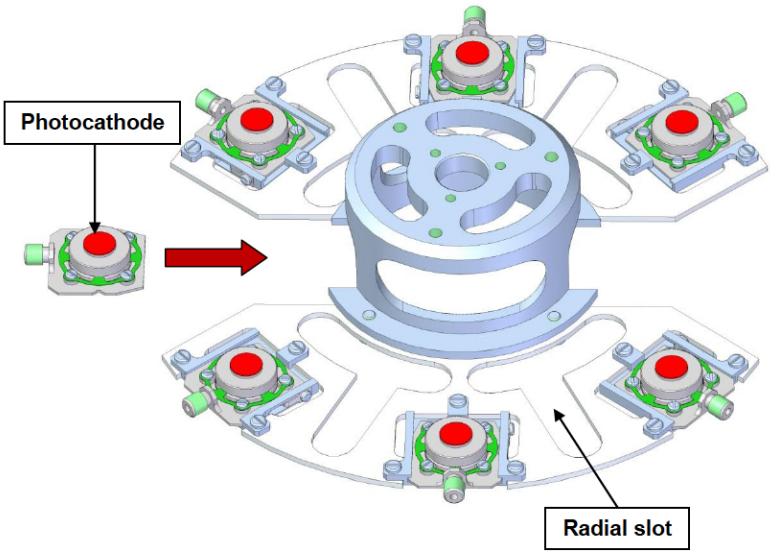

Figure 5.9: Design of the rotary carousel which can accommodate up to six photocathodes, shown with six Kovar cathode mounting plates.

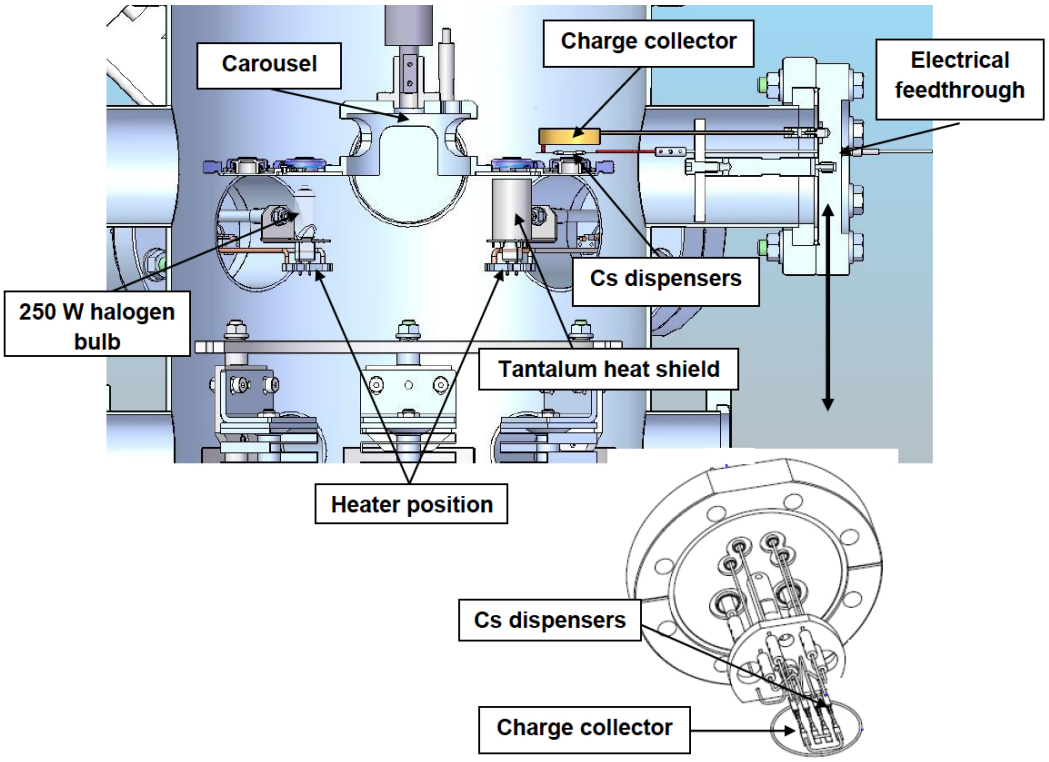

Figure 5.10: Section view of the preparation chamber showing the heater and activation positions.

photocathode surface. The Cs dispensers are mounted on an electrical feedthrough which also provides mechanical support for the dispenser assembly. A charge collector is for "partial" yield measurements, and for collimating the emitted electron beam in a high current experiment with a higher laser power. We usually work in total yield mode by using the connection to the carousel, and so measuring all emitted electrons. It is isolated from both the carousel and the chamber wall and grounded through the electrical feedthrough when not in use. The O_2 or NF_3 leak rate into the system is precisely controlled via a piezo-electric leak valve (PLV 1000 from Oxford Applied Research). Three sapphire windows are positioned exactly above the heater and activation positions. These windows are necessary for temperature measurement with a pyrometer during the heating process, and photocurrent generation during the activation process.

The chamber is pumped-down by a 300 l·s^{-1} ion pump (Noble diode ion pump from Gamma Vacuum) in combination with 6 ST-707 type NEG modules. These NEG modules were made from SAES NEG Getters, model number WP 1200 and installed in the lower half of the chamber. The getter modules are activated by passing a large DC current through them which generates ohmic heating and raises the NEG modules to temperatures up to around 500 °C. This current is carried through the 3 high current feedthroughs in the lower half of chamber. The total pressure is monitored by an IM cold cathode gauge (MKS) and extractor guage (IONIVAC IE514 from Leybold). The residual gas composition is monitored by a quadrupole mass spectrometer (VGQ RGA 200D). The total pressure of the chamber after careful baking at 250 °C for 14 days is in the 10^{-12} mbar range and the residual gas composition is shown in Figure 5.11. It can be seen that the dominant residual gas is H_2 in the 10^{-12} mbar while the reactive gases such as water vapour, O_2 and CO_2 (whose molecular masses are 18, 32 and 44 respectively) have partial pressures lower than 10^{-12} mbar. It will be shown in Chapter 6 that this level of vacuum provides a dark-life time for the photocathode in excess of 6,800 hours.

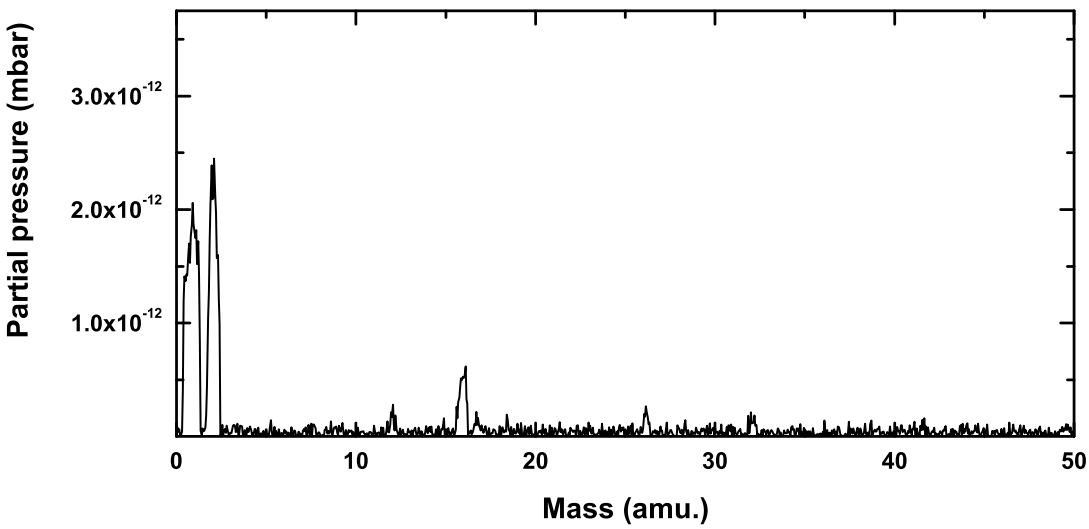

Figure 5.11: A typical spectrum of the the residual gas composition in the PC.

5.2.6 The photocurrent measurement system

The schematic diagram of the experimental set-up for the photocurrent measurements is shown in Figure 5.12. The photocurrent is measured whilst illuminating of the photocathode from the front-side with red light generated by a 635 nm Acculase laser diode. This laser is clamped in a laser mount which is installed exactly above the activation position. The mechanical design of this laser mount is shown in Figure 5.13. The laser mount allows the laser spot to be moved across the photocathode surface with a high degree of precision in order to scan the uniformity of QE. Before the laser beam reaches the photocathode surface, it is split into two beams of approximately equal power by a 50/50 beamsplitter. One beam is directed to a calibrated photo-diode in order to measure the laser power for the QE calculation. The other

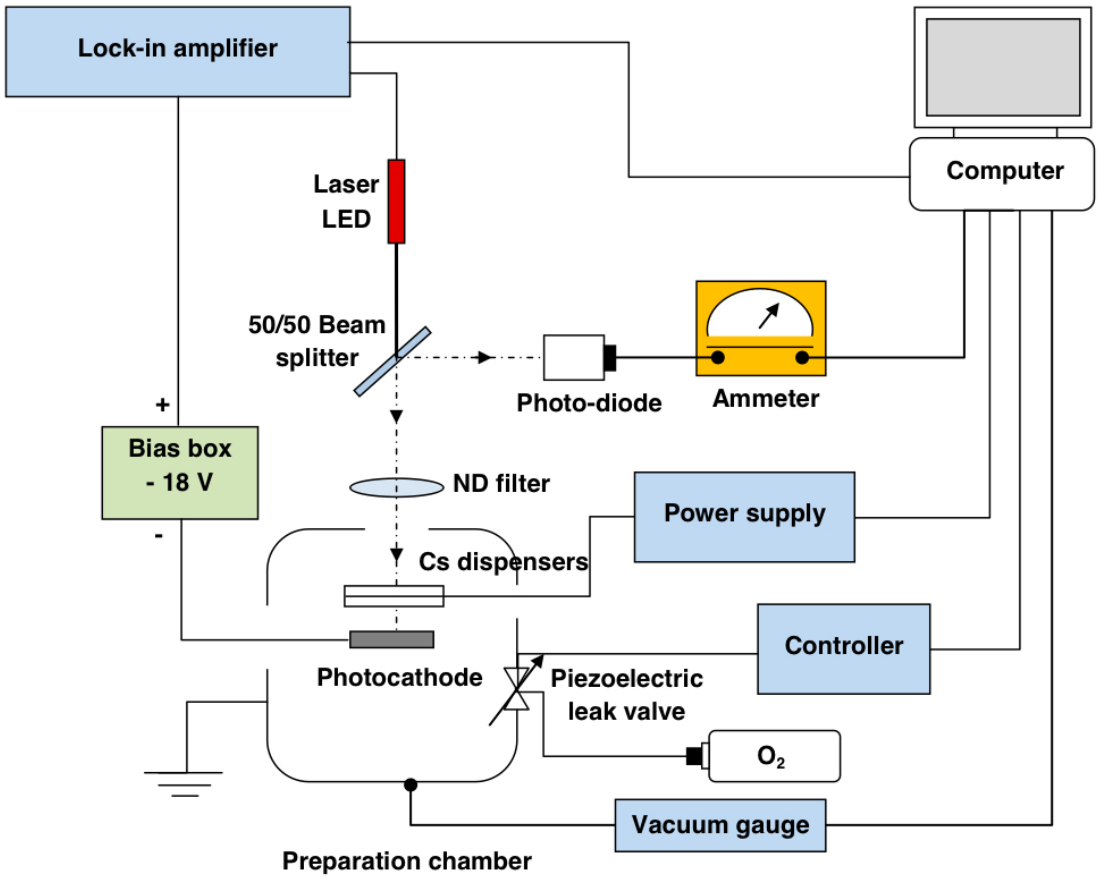

Figure 5.12: Schematic diagram of the total yield QE measurement system.

beam is transmitted onto the photocathode through a ND bandpass filter. This ND filter is used to lower the delivered laser intensity into the micro-watt range in order to avoid pressure rise due to electron-induced desorption from the surrounding metal surfaces, and also to limit the photocurrent to a level compatible with a lock-in amplifier input channel. To prevent noise contribution from other light sources, such as the filament of an ion gauge, the laser is modulated at frequency of 3 kHz using the clock signal from the lock-in amplifier and the photocurrent measurement is carried out using phase sensitive detection. To facilitate photocurrent measurement, the photocathode is negatively biased to 18 V with respect to the walls of the chamber using the battery bias box. This negative bias is applied to the carousel which has electric contact with the photocathode holder, allowing the total electron yield to be measured. A software package developed using LabVIEW is used to display and record the photocurrent and chamber pressure during the activation. This software allows control of the piezo-electric leak valve and the Cs power supply. A screenshot of our developed software is shown in Figure 5.14. The whole activation process can be manually controlled from the computer, and this will expanded in the near future to support automatic control by the software itself.

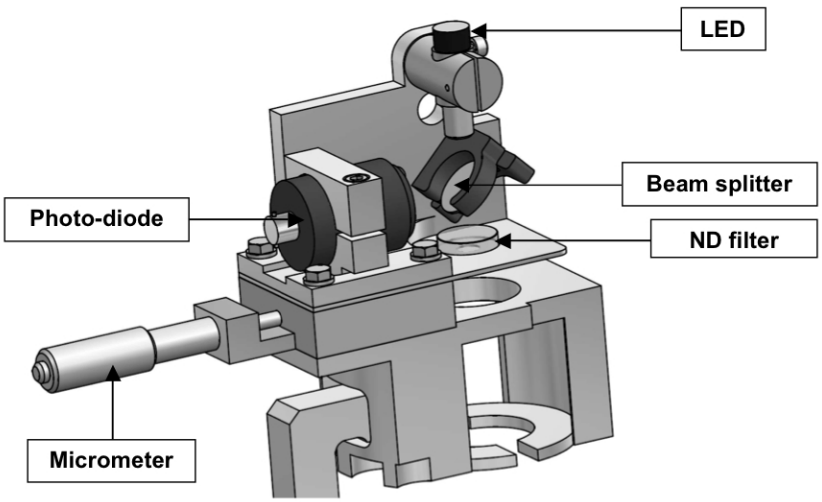

Figure 5.13: Design of the laser mount incorporating with a beamsplitter and photodiode to monitor delivered laser power.

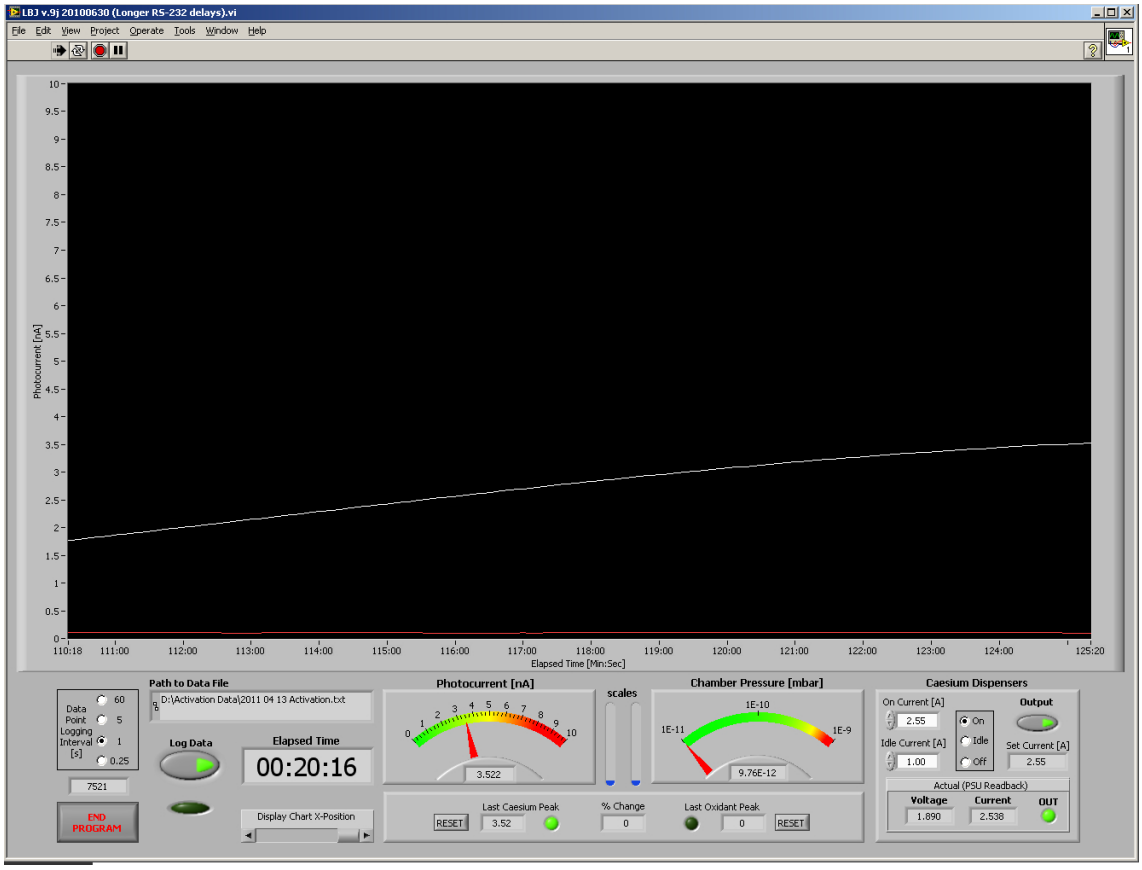

Figure 5.14: Screenshort of the software developed in LabVIEW used for the preparation process.

5.3 Photocathode preparation procedure and operation of the facility

The procedure for the preparation of a GaAs photocathode and operation of the ALICE PPF have been proposed as the following steps. The GaAs photocathode is first cleaned with a chemical solution in the glove box under dry nitrogen conditions, yielding an estimated oxygen concentration 400 times lower than in the ambient atmosphere. After the chemical treatment, the photocathode is mounted in a photocathode holder and installed into the transfer vessel. Using the transfer vessel, the photocathode is stored in a leak tight nitrogen environment and transported to the loading chamber without exposure to the air. The transfer vessel is bolted to the loading chamber and the chamber is roughly pumped down by the

turbo-molecular pumping station. When the pressure reaches 10^{-3} mbar range, the transfer vessel is opened and the chamber is pumped-down further to the pressure of 10^{-9} mbar range. In this way, the cleaned photocathode is not polluted with the contaminations from the residual air. This photocathode transport technique was introduced by Prof. A.S. Terekhov [52, 72, 79]

After introduction to the UHV environment, the photocathode is extracted from the transfer vessel and transferred to the AHCC by means of the magnetic linear transfer arm. Here, the photocathode is heated to approximately 300 °C for 30 minutes to desorb the chemical residues from the glove box treatment which may contaminate the preparation and the gun chambers. During the heating process, the temperature is increased slowly over approximately 20 minutes to avoid thermal stress inside the photocathode. As soon as the process is complete, the photocathode is transfered and mounted onto the carousel in the preparation chamber. The final cleaning is carried out by heating the photocathode from the back-side up to 450 °C for 30 minutes for a new photocathode. From my study and according to [123], this temperature is sufficient to provide an atomically-clean GaAs surface after cleaning with a HCl in IPA solution. The temperature is ramped up slowly over 30 minutes. Once the photocathode cools down to room temperature (approximately 3 hours), it is rotated to the activation position, beneath a set of Cs dispensers.

The activation process can be performed following either the standard Yo-Yo, or co-deposition technique as our study has shown no significant difference in the final activation results between the two techniques (as described in Chapter 4). The Cs deposition is controlled by the electrical current delivered through the dispensers. The operational current is approximately 2.5 - 3 A. It is suggested that prior to the activation, the dispensers should be carefully degassed at 1.5 A to improve the purity of the evaporated Cs. Research grade O_2 is admitted to the chamber through the piezo-electric leak valve. The pressure for each O_2 exposure is normally between 2.5 - 5×10^{-10} mbar. The purity of O_2 is verified using the RGA. During the activation, the photocurrent and the pressure inside the chamber are monitored using the circuit and software described in section 5.2.6. The activation can be manually controlled at present, but will be fully computer-controlled in the future.

When the activation process is complete, the photocathode is ready for use, and can transferred to the operational position in the gun chamber. While operating one photocathode in the gun, another (new) photocathode can be prepared and stored in the preparation chamber. Once the QE of the photocathode in the gun degrades to the point where the required bunch charge cannot be achieved any longer, it will need to be exchanged. The operational photocathode can be replaced immediately with the new prepared photocathode, and the gun can continue in operation. The degraded photocathode can be restored by heat cleaning and re-activation in the preparation chamber, ready for the further usage. After several cycles, the QE of the photocathode will degrade until it is not possible to fully recover the QE simply through heat cleaning and re-activation. This photocathode needs to be completely cleaned again. This can be done by either chemical treatment in the nitrogen glove box, or through atomic hydrogen cleaning in the AHCC. However, the use of atomic hydrogen cleaning is preferable because the photocathode is kept in a "closed cycle" without exposure to the laboratory atmosphere, thus avoiding further contamination.

5.4 The design of the new gun vessel and transportation mechanism

The design and the section through view of the new gun vessel is shown in Figure 5.15. The gun is designed with side-loading geometry for transportation of the photocathodes. A photocathode can be introduced from the PPF through the flange **(1)** in Figure 5.15. The photocathode is illuminated through a vacuum window under the Brewster angle conditions in reflection geometry, and the generated photoelectrons emerge from the beam line, passing through the flange **(2)**. The gun has a Pierce electrode structure which consists of an earthed anode and GaAs photocathode mounted on the face of a spherical high voltage cathode ball. The design and operational parameters of the modified cathode ball are similar to those of the current ALICE gun. The cathode ball assembly is mechanically supported and electrically

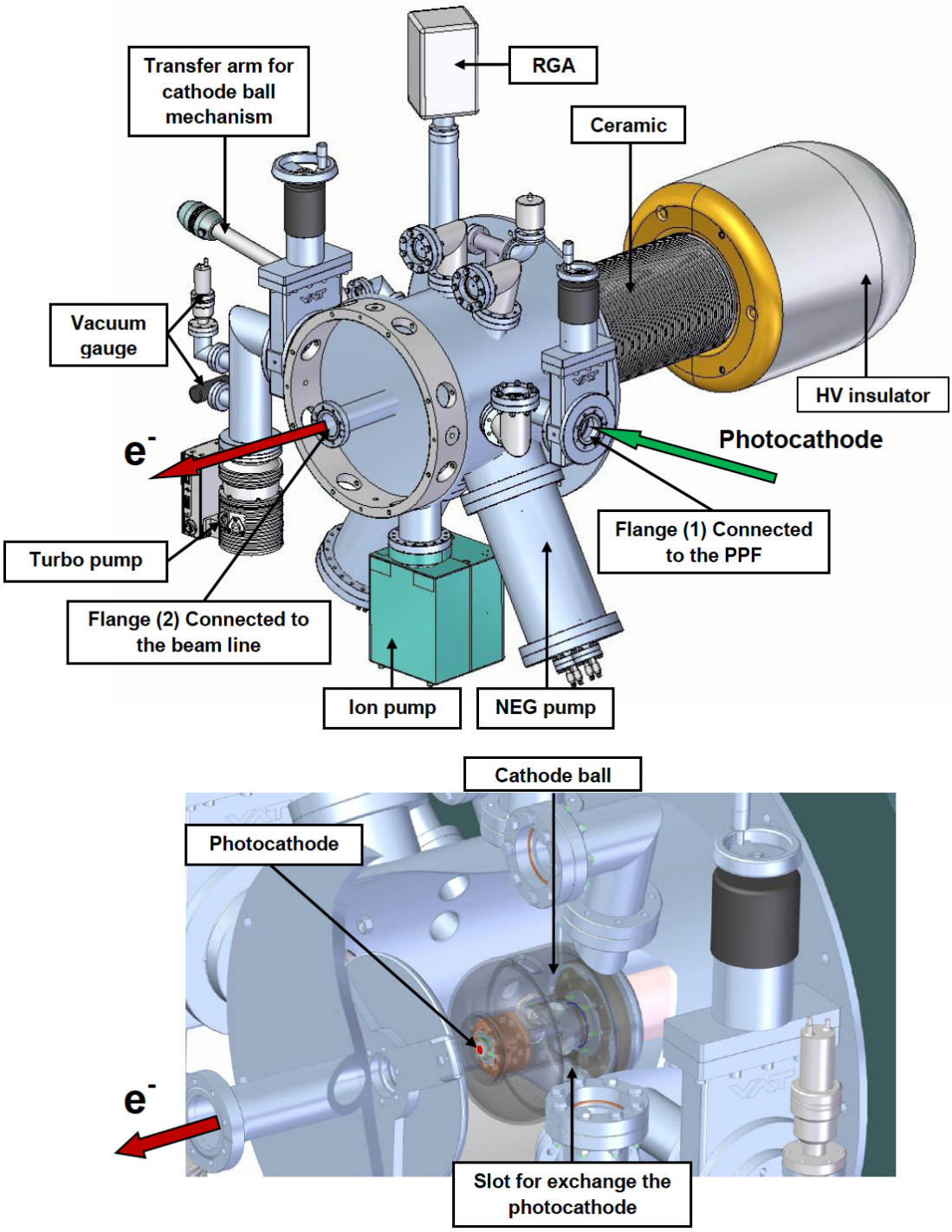

Figure 5.15: Schematic drawing and a section through of the new gun vessel.

isolated by a large ceramic insulator. The ceramic and electrode structure are physically large to reduce the peak electric fields. This HV section is surrounded with sulphur hexaflouride (SF_6) to prevent any electrical breakdowns occurring outside the vacuum chamber.

To improve the vacuum, the gun vessel will be fabricated from stainless steel 316L. The chamber walls will be vacuum-fired up to 1025 °C to decrease the hydrogen load in the bulk material. During the bake-out process, the gun chamber will be roughly pumped by a turbo-molecular pump, through an all-metal gate valve. XHV within the gun chamber is maintained using a Noble diode ion pump combined with two NEG pump modules, as shown in Figure 5.15. The vacuum diagnostics consists of a quadrupole RGA with electron multiplier, and an extractor gauge.

The principle of the photocathode transportation is shown in Figure 5.16. The prepared photocathode is extracted from the carousel in the PPF and transported into the gun vessel trough the flange **(1)** using the magnetic linear transfer arm. The photocathode is inserted into the cathode ball through a side slot which is positioned on the flat part of the ball surface in order to minimise HV field distortion, see Figure 5.16. The cathode ball has a mechanism based on a bevel gear for winding the cathode forwards and backwards. This mechanism is driven by a magnetic transfer arm which will engage with the small joystick shown in Figure 5.16 and through rotation of the joystick the photocathode can be moved forward to the operational position. Once in position the activated photocathode is ready for use as an electron source.

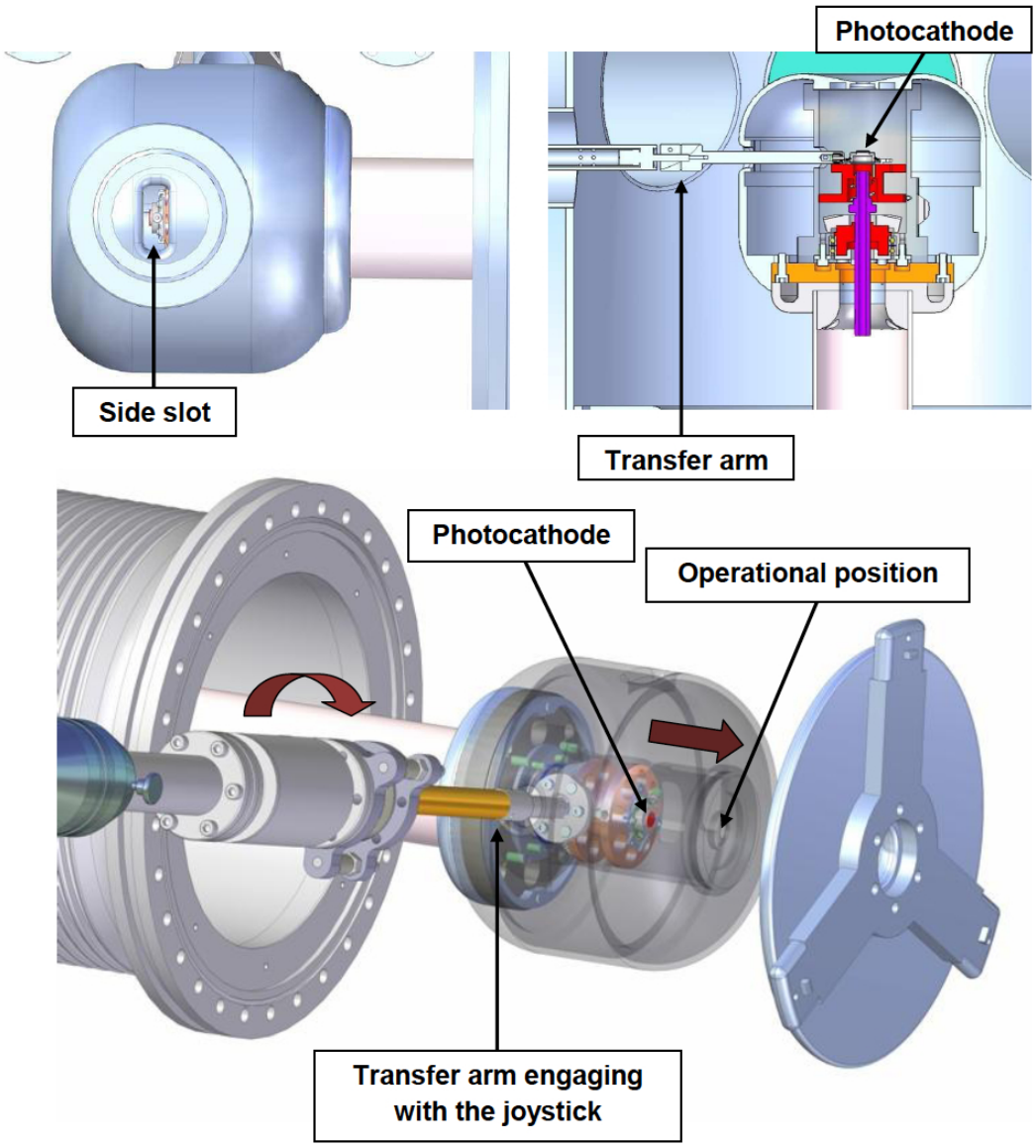

Figure 5.16: Principle of the photocathode transportation between the PC and the gun vessel.

Chapter 6

Results from the ALICE PPF

This chapter presents the results obtained from the ALICE PPF during the commissioning phase in the stand-alone mode. The major experiments and results can be summarised as follows. Once fully-constructed, initial operations were carried out to test the performance and functionality of the facility. The details of this first operation and experimental results are presented in the section 6.1. To further study and optimise the photocathode preparation procedure for the ALICE PPF, a number of experiments were completed with the TM GaAs photocathodes. Together with the experience and knowledge gained from Chapter 4, a QE of between 12 - 19% with long dark lifetimes of approximately 6,800 hours could be obtained from the photocathodes in a reproducible way. This result shows the high performance and usefulness of the PPF for a photo-electron gun. The preparation procedure for TM GaAs photocathodes and their results are presented and discussed in section 6.2.

After this success, the preparation procedure was applied to and tested on the RM GaAs photocathodes which are planned for use in the upgraded gun. The result is consistent with the TM GaAs photocathode as a QE of between 15 - 19% was achieved. The experimental procedure and the results from the RM GaAs photocathodes are presented in section 6.3.

In addition to those new photocathode types, experiments were also carried out on the ALICE GaAs photocathodes in the PPF. The result shows an improvement in their performance compared to that achieved when activating cathodes in the current

ALICE photo-injector, due to the much more controllable preparation process in the PPF. The experimental procedure and results are discussed in section 6.4. One main problem of using the current ALICE GaAs photocathode is the emission of dark current since the photocathode has an active area of 25 mm in diameter, while it is illuminated only over an area of 4 mm in diameter. To minimise this problem, the surface of the photocathode has been anodised, leaving only a small un-anodised active area for activation and operation. The anodising procedure and results are presented in section 6.5.

6.1 First operation and results

The first operation of the ALICE PPF was performed at the Cockcroft Institute in Spring 2009 [60]. The RM GaAs photocathodes with active layer thicknesses of 0.4 and 1.5 μm were used in this first test. Note that these active layer thicknesses were only used for the first operation. A photograph of the photocathode is shown in Figure 6.1.

For an ideal photocathode preparation procedure, the first step is to chemically clean the photocathode surface in the glove box under a pure nitrogen atmosphere and then transfer the photocathode to the LC via the nitrogen-filled transfer vessel,

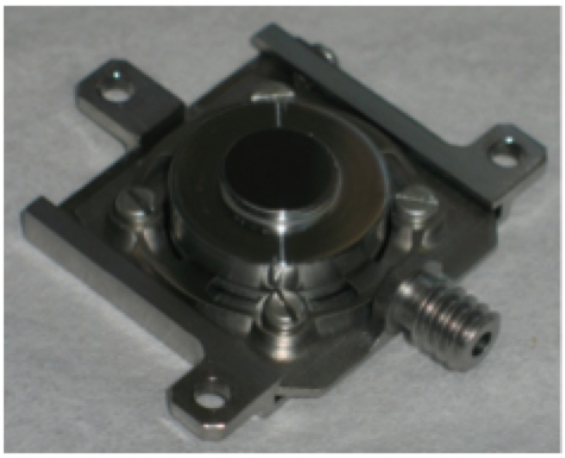

Figure 6.1: Photograph of the RM GaAs photocathode mounting on the photocathode holder.

as described in section 5.3. However, at the time the first operation was performed, the glove box facility had not been implemented. Consequently, the first experiment was carried out by placing the photocathode into the transfer vessel *as delivered* without any chemical treatment. After the transfer vessel was mounted on the LC, and the chamber was pumped-down to 10^{-8} mbar range, the photocathode was transfered to the AHCC for exposure to atomic hydrogen. Although, the atomic hydrogen cleaning was originally implemented for the *restoration* of degraded photocathodes, in this experiment it was used for *initial* photocathode cleaning. The cleaning process was performed by first heating the photocathode to a temperature of 450 °C. The photocathode was then exposed to atomic hydrogen at the total pressure of 2×10^{-6} mbar for 15 minutes, then allowed to cool. Following the atomic hydrogen cleaning, the photocathode was transferred into the PC where it was further heated to 600 °C for 1 - 2 hours to remove hydrogen adsorbed on the photocathode surface during the cleaning process. This high cleaning temperature was set (in the first operation) because the photocathode had not been chemically etched to remove oxides. It will be seen later that the heat-cleaning temperature for an etched photocathode is reduced to 450 °C. After the final heating process, the photocathode was activated to the NEA state using the co-deposition technique. During the activation, Cs was evaporated from the dispensers which were powered constantly at 2.5 A. The photocathode was illuminated by a 635 nm laser modulated at 3 kHz, and the photocurrent was monitored with a picoammeter. O_2 was admitted into the chamber alternately through the piezo-electric leak valve. The base pressure in the PC was 1.2×10^{-11} mbar, though during O_2 injection the pressure rose to 5×10^{-10} mbar. The activation procedure was halted when the photocurrent reached its saturation level, and an activation curve is shown in Figure 6.2. The preparation and activation shown in Figure 6.2 were performed by H.E. Scheibler, ISP (Novosibirsk), at the Cockcroft institute [60].

As can be seen from Figure 6.2, a QE as high as 15% was obtained in the first operation. This result demonstrates both the performance of the ALICE PPF, and also the benefit of using atomic hydrogen cleaning. However, the operational and photocathode preparation procedure need to be further studied and optimised. One

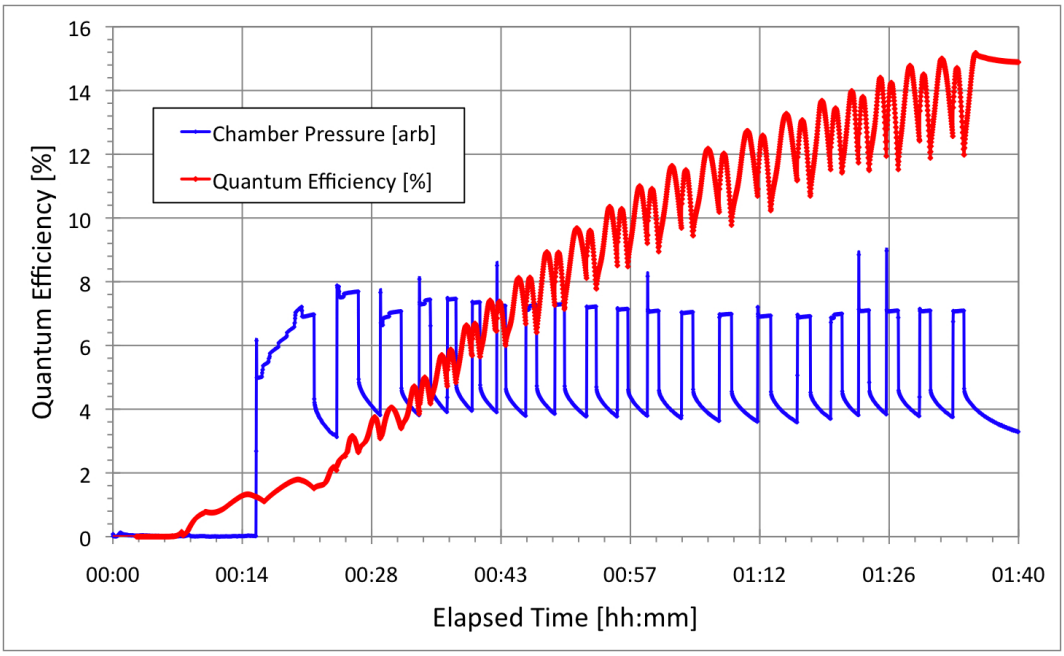

Figure 6.2: The activation curve for the RM GaAs photocathode in the first operation of the PPF using the co-deposition technique, performed by H.E. Scheibler, ISP (Novosibirsk), at the Cockcroft Institute [60].

outstanding issue was the optimisation of the chemical cleaning procedure for the GaAs photocathode which will be discussed shortly.

6.2 Transmission mode GaAs photocathode

The design and semiconductor structure of the TM GaAs photocathode are described in section 5.1.2. Photographs of the TM GaAs photocathode are shown in Figure 6.3. Emphasis again that the TM GaAs photocathodes used in this experiment have active layer thicknesses of 2.4 μm and can completely absorb the laser power when illuminated at a photon energy which slightly exceeds the band gap of the photocathode.

Initially, this type of photocathode was intended to study the possibility of operating a TM GaAs photocathode in the upgraded ALICE gun. However, due to their cost and structure which is easy to prepare and, in general, similar to the RM GaAs photocathodes which will be actually used in the upgraded gun, this type of

(a) (b)

Figure 6.3: Photographs of the TM GaAs photocathode as grown on a glass substrate, showing the front side (a) and the back side (b).

photocathode was used mainly in this work for the study and optimisation of the photocathode preparation procedure.

6.2.1 Photocathode preparation

The best result with the TM photocathode was achieved when the photocathode was prepared in the following way. The photocathode was first chemically cleaned in the nitrogen glove box with the oxygen level below 200 ppm. The chemical treatment involved etching in a solution of HCl in IPA (1:10 by volume) for one minute. The photocathode was then etched two times in pure IPA for one minute and blown dry with flowing nitrogen. The hydrochloric acid S.G. 1.18 (∼36%) with laboratory reagent grade was used in this experiment. The etched photocathode was then mounted in a holder which had previously been heated inside the vacuum system and transfered to the glove box without exposure to the air. It was found that this procedure increases the ultimate QE because it reduces photocathode exposure to contaminants released from the holder during the heating process.

After mounting in the holder, the photocathode was placed into the transfer vessel while still inside the glove box. The transfer vessel was closed and moved to the LC under the nitrogen atmosphere, without exposure to the air. Once the photocathode had been introduced to the LC and UHV, it was transfered to the AHCC

and heated to a temperature of approximately 300 °C for 30 minutes in order to remove any chemical residual which may contaminate the preparation chamber. During the heating process, the temperature was increased slowly over approximately 20 minutes to avoid thermal stress inside the photocathode and the maximum pressure rise observed was 3×10^{-8} mbar. As soon as the process was complete and when the pressure had recovered to the 10^{-9} mbar range, the photocathode was transfered and placed onto the carousel in the preparation chamber. The final cleaning was carried out by heating the photocathode from the back-side to approximately 450 °C for 30 minutes. Once the photocathode cooled down to room temperature, approximately 3 hours, the activation process was performed following either the Yo-Yo or co-deposition technique. This work has shown no significant difference in the final activation level between the two techniques. However, the co-deposition technique is preferential because it takes less time and is easier to control. A typical activation curve using the co-deposition technique is shown in Figure 6.4. The Cs deposition rate was controlled by the electrical current (approximately 2.5 A) delivered through the dispensers. The dispensers should be carefully degassed prior to the activation in order to improve the purity of evaporated Cs, this is achieved by operating them at 1.5 A for 2 minutes. O_2 was admitted into the chamber at a typical pressure between 2.5 - 5×10^{-10} mbar.

6.2.2 Results and discussion

This cleaning procedure and activation has been shown to be repeatable and a QE of 10 - 12% is typically obtained from the TM GaAs photocathode in the first activation. After the first activation, the photocathode is heated to 450 °C for 30 minutes in the PC and then activated again. A QE of between 12 - 16% is obtained in this second activation and it was found in this work that this is the maximum achievable QE obtained from the photocathode. A plot between the number of chemical clean and activation cycles and the QE obtained from one of the TM photocathode is shown in Figure 6.5.

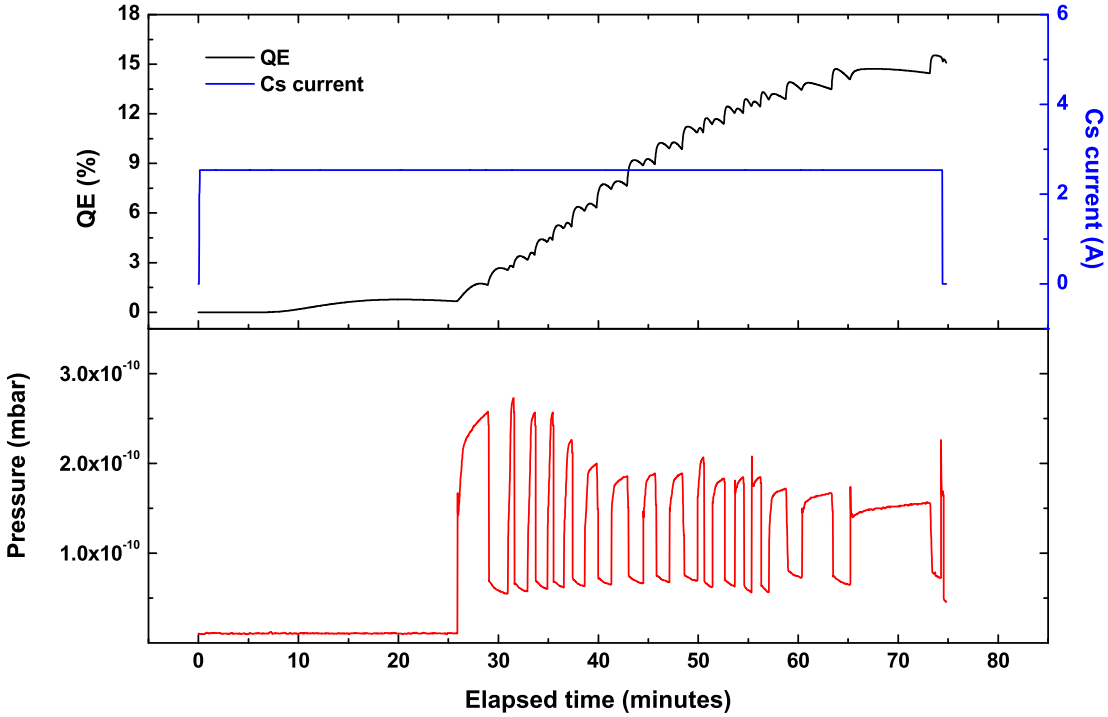

Figure 6.4: A typical activation curve for the TM GaAs photocathode using the co-deposition technique with O_2.

However, after the second activation, it was found that the QE of the photocathode degrades with the number of heat clean and activation cycles. A comparison between QE and the number of heat clean and activation cycles is shown in Figure 6.6. From this plot, it can be seen that the ultimate QE drops to approximately 4% in the fifth activation. This behaviour from the hetero-structure GaAs photocathode grown by metal organic chemical vapour deposition (MOCVD) has also been observed in the other studies [71, 72, 124].

A QE lifetime plot for an activated TM GaAs photocathode is shown in Figure 6.7. A dark lifetime of approximately 6,800 hours is consistently measured for a well-prepared TM GaAs photocathode in the preparation chamber which has a base pressure of approximately 1.5×10^{-11} mbar.

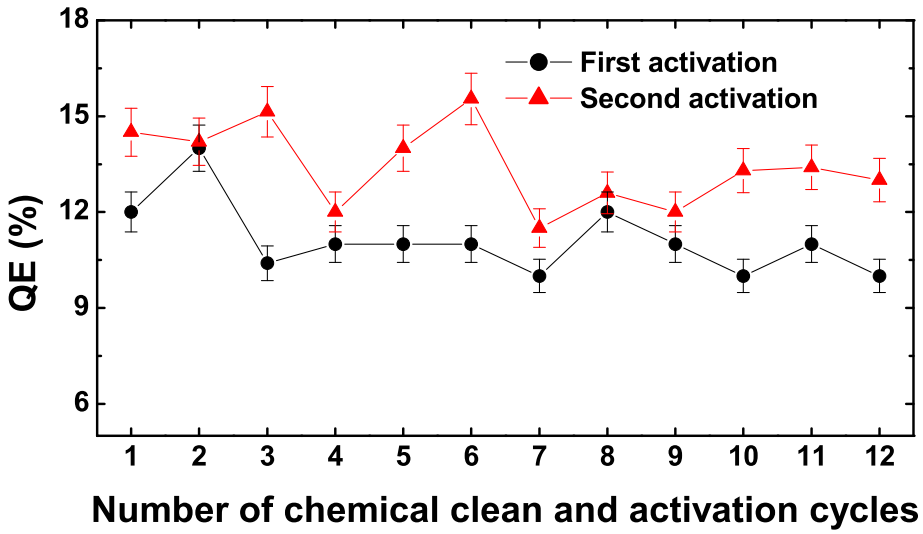

Figure 6.5: Plot showing the achieved QE against the number of chemical clean and activation cycles with O_2 for the TM GaAs photocathode

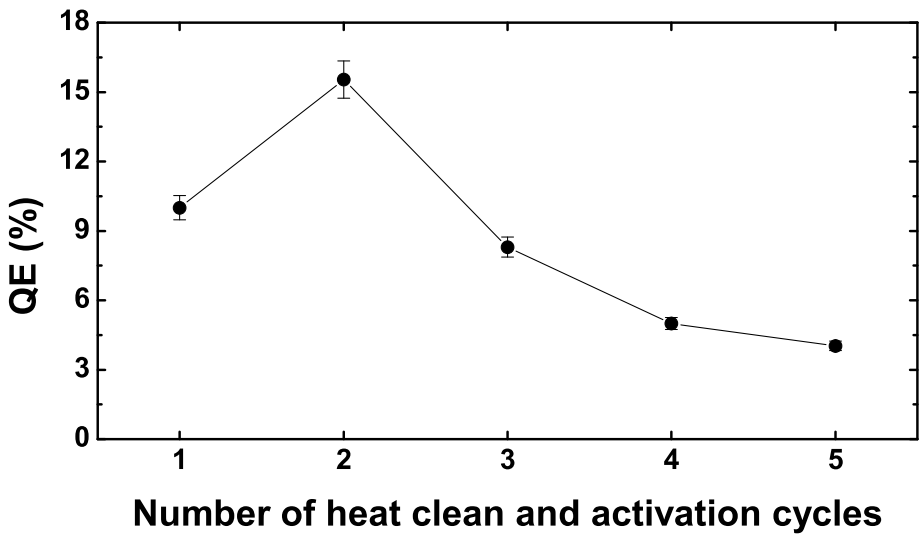

Figure 6.6: Plot showing the achieved QE against the number of heat clean and activation cycles with O_2 for the TM GaAs photocathode

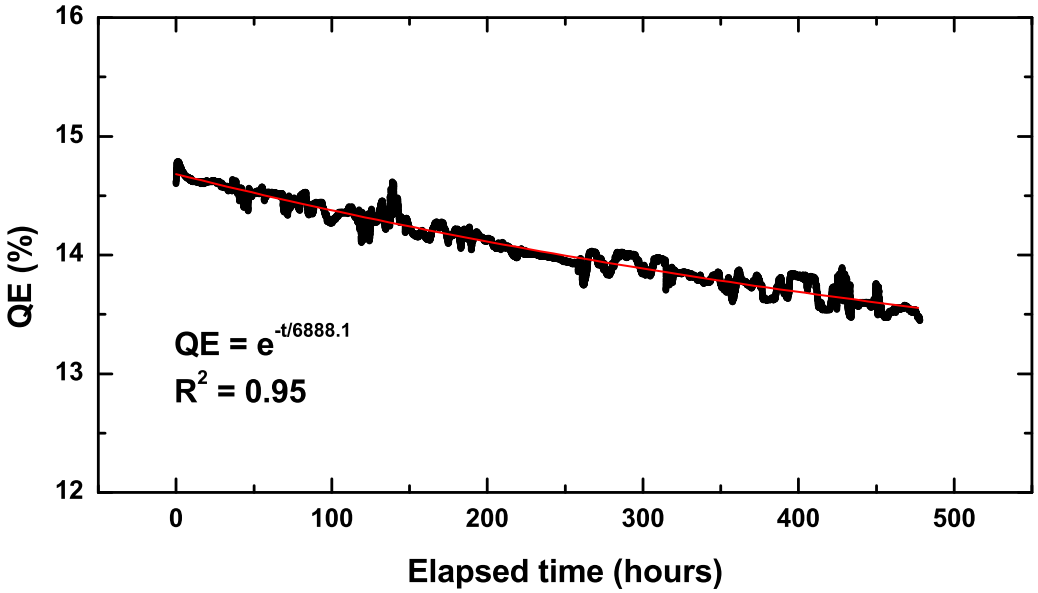

Figure 6.7: QE dark lifetime plot for the activated TM GaAs photocathode, showing the lifetime approaching 7,000 hours.

A possible explanation for the increase in the QE in the second activation might be that the Cs atoms are not completely removed from the photocathode after heating to 450 °C for 30 minutes. At this heating temperature, only weakly-bonded Cs atoms are desorbed from the surface, while some strongly-bonded Cs atoms still remain. These Cs atoms can diffuse and find a favorable reconstruction on the surface during the heating process, resulting in the higher QE obtained in the second activation. However, oxygen is also left on the surface after the activation and heating process as the heating temperature is not high enough. This residual oxygen is accumulated and contaminates the photocathode surface after each cleaning and activation. As a result, the achieved QE of the photocathode decreases with the number of heat clean and activation cycles after the second activation.

To verify this assumption, I carried out the experiment separately in the surface characterisation system. The bulk VGF GaAs wafer with the specification described in section 4.1 was used in this experiment. The GaAs wafer was prepared

and activated with O_2 using the co-deposition technique following the procedure described in section 4.2. After the activation, the GaAs wafer was heated to 450 °C for 30 minutes. XPS was performed before and after the heating process. The XPS spectra in the Cs 3d and O 1s regions for the GaAs surface after activating with O_2 and consequently heating to 450 °C for 30 minutes are shown in Figure 6.8.

It is observed in Figure 6.8 that the Cs $3d_{3/2}$ and Cs $3d_{5/2}$ peaks at binding energies of 739.5 eV and 725.5 eV are still detectable after heating the surface to 450 °C for 30 minutes. This indicates that a small amount of Cs remains on the surface. The intensity of the O 1s peak at a binding energy of 531 eV slightly decreases after the heating process, indicating that oxygen is not completely removed from the surface. These XPS results are in a good agreement with the assumption.

It is emphasised again that heating the photocathode surface to a temperature near or slightly above 600 °C may allow the removal of surface oxides, but it is avoided in this work as it degrades the photocathode properties due to diffusion of

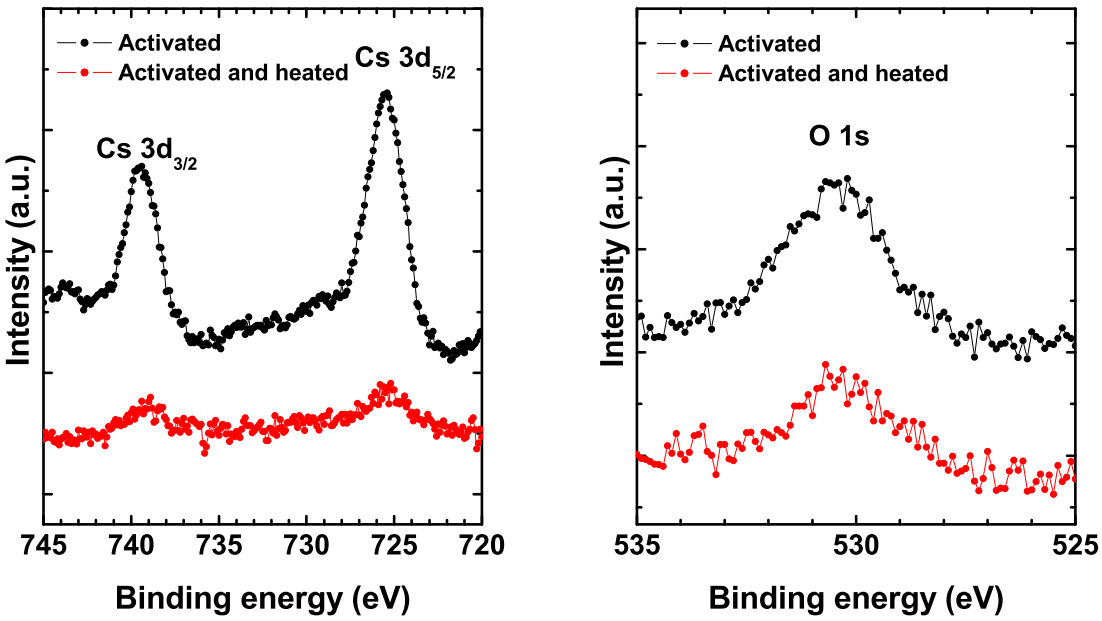

Figure 6.8: The XPS spectra in the Cs 3d and O 1s regions for the GaAs surface after activating with O_2 and consequently heating to 450 °C for 30 minutes.

dopants and the preferential evaporation of As atoms from the lattice, generating As vacancies in the vicinity of the emitting surface. Moreover, in the case of our photocathodes, there are a mechanical strain between the semiconductor structure and the base plate due to differing thermal expansion coefficients, and a strain in the semiconductor multilayer structure due to a small difference in lattice constants [124]. These strains may create a dislocation network within the photocathode active layer during exposure to high temperature. Dislocations, which are highly-efficient recombination centres, cause a decrease in the photoelectron diffusion length and thereby of the QE [124].

6.2.3 NF_3 activation

To overcome the problem of QE degradation with the number of heat clean and activation cycles, I proposed to use of NF_3 instead of O_2 in the activation process. To test this premise, the TM photocathode was prepared using the same procedure as for the O_2 activation. The photocathode was first etched in a solution of HCl/IPA (1:10 by volume) for one minute, then etched in pure IPA for one minute and then blown-dry with pure nitrogen. These were performed in the nitrogen-purged glove box with an oxygen level below 200 ppm. After chemical treatment, the photocathode was mounted in the holder, placed in the transfer vessel and then transported to the LC without exposure to the air. Once the photocathode was under UHV, it was transfered to the AHCC and heated to a temperature of approximately 300 °C for 30 minutes. When the process was complete, the photocathode was transfered onto the carousel in the preparation chamber. The final cleaning was carried out by heating the photocathode from the back-side to 450 °C for 30 minutes. Once the photocathode had cooled down to room temperature, the activation process was performed. During the activation process, Cs dispensers were powered constantly at 2.5 A. After the photocurrent reached its peak and dropped to approximately 20% of the first peak, NF_3 was admitted into the chamber at a pressure between 2.5 - 3×10^{-9} mbar. A typical activation curve for the TM GaAs photocathode with NF_3 is shown in Figure 6.9.

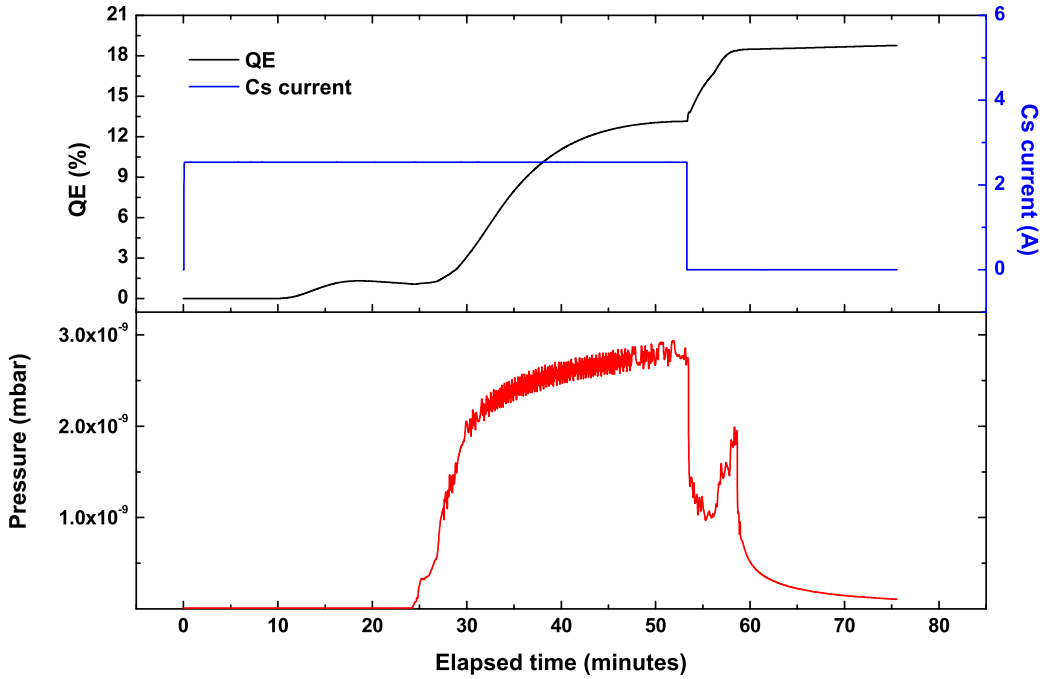

Figure 6.9: A typical activation curve for the TM GaAs photocathode with NF_3.

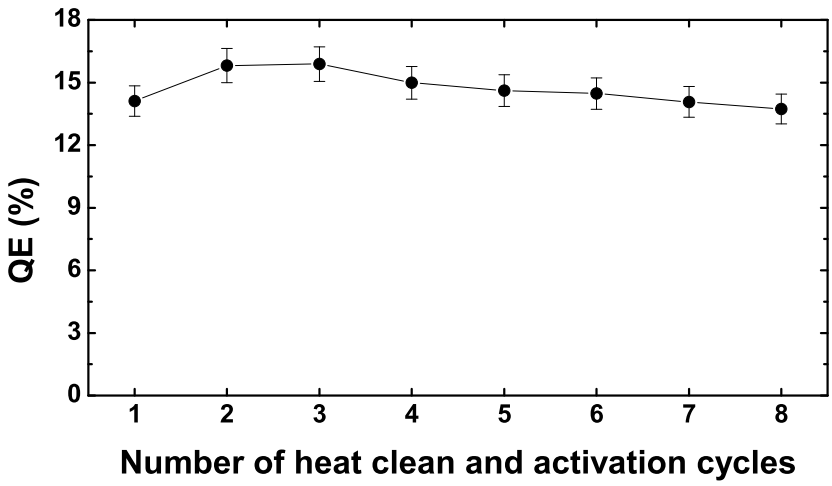

Figure 6.10: Plot showing the achieved QE against the number of heat clean and activation cycles with NF_3 for the TM GaAs photocathode.

Using NF_3 as the oxidant, a QE of between 12 - 15% is typically obtained in the first activation which is higher than that obtained using O_2. After the first activation, the photocathode is heated to 450 °C for 30 minutes, and then activated again. A QE as high as 15 - 19% is achieved in this second activation. This is the highest value obtained from the TM photocathode.

A plot showing QE versus the number of heat and activation cycles using NF_3 is shown in Figure 6.10. It can be observed that the QE of the photocathode still degrades after the second activation, however, the level of degradation is very low compared to activation using O_2. A QE as high as 13.7% can still be obtained after the eighth activation. This performance factor makes NF_3 a good choice of oxidiser when activating a GaAs photocathode to the NEA state in the experiments.

6.3 Reflection mode GaAs photocathode

The design and structure of the RM GaAs photocathodes are described in section 5.2.1. The RM GaAs photocathodes with two different active layer thicknesses were used in this experiment: One design with an active layer of 2.0 μm can completely absorb the incident laser when illuminating the photocathode with a photon energy which slightly exceeds the band gap of photocathode. Another design with a thin active layer of 0.3 μm is optimised for a fast response time.

6.3.1 Photocathode preparation

The RM photocathode was prepared in the following way. The photocathode was first chemically cleaned in the nitrogen-purged glove box with an oxygen level below 200 ppm. The chemical treatment involved rinsing with a solution of HCl/IPA (1:10 by volume) for one minute. The photocathode was then rinsed two times in pure IPA for one minute and blown-dry with flowing nitrogen. The rinsing technique was used instead of the etching technique because the RM photocathode structure contains an indium layer. This layer can be dissolved in the acid solution and thus pollutes the photocathode during the etching process. After mounting on the holder, the photocathode was placed into the transfer vessel and transported to

the LC under a nitrogen atmosphere. Once the photocathode was introduced into UHV, it was transfered to the AHCC and heated to a temperature of 300 °C for 30 minutes. When the process was complete and the pressure had recovered to the 10^{-9} mbar range, the photocathode was transfered and placed onto the carousel in the PC. The final cleaning was carried out by heating the photocathode to 450 °C for 30 minutes. Once the photocathode cooled down to room temperature (within approximately 3 hours), it was then activated to the NEA state. The activation was carried out using NF_3 as an oxidant because it exhibited a QE advantage over O_2, as shown in our previous study with the TM GaAs photocathode. During the activation process, the Cs dispensers were powered constantly at 2.5 A. After the photocurrent reached its peak and dropped to approximately 20% of the first peak level, NF_3 was admitted into the chamber at a pressure between 2.5 - 5×10^{-9} mbar.

6.3.2 Results and discussion

The "thick" active layer photocathode: 2.0 μm

A typical activation curve for the thick active layer RM GaAs photocathode using NF_3 is shown in Figure 6.11. A QE of between 15 - 16% was obtained in the first activation. After the first activation, the photocathode was heated to 450 °C for 30 minutes and then activated again. A QE of between 16 - 18% was achieved in this second activation. After the second activation, the photocathode can be heated to 450 °C for 30 minutes and then activated many times with only a small QE degradation. A plot showing QE versus the number of heat and activation cycles using NF_3 for the thick RM photocathode is shown in Figure 6.12. This result is consistent with the result from the TM GaAs photocathode and confirms the reproducibilty of my preparation procedure.

The "thin" active layer photocathode: 0.3 μm

For the thin RM GaAs photocathode, a lower level of QE was expected compared to the thick photocahode because of its reduced ability to absorb the laser power, as discussed in section 5.1.1. Using the absorption coefficient in Figure 2.5 (approx-

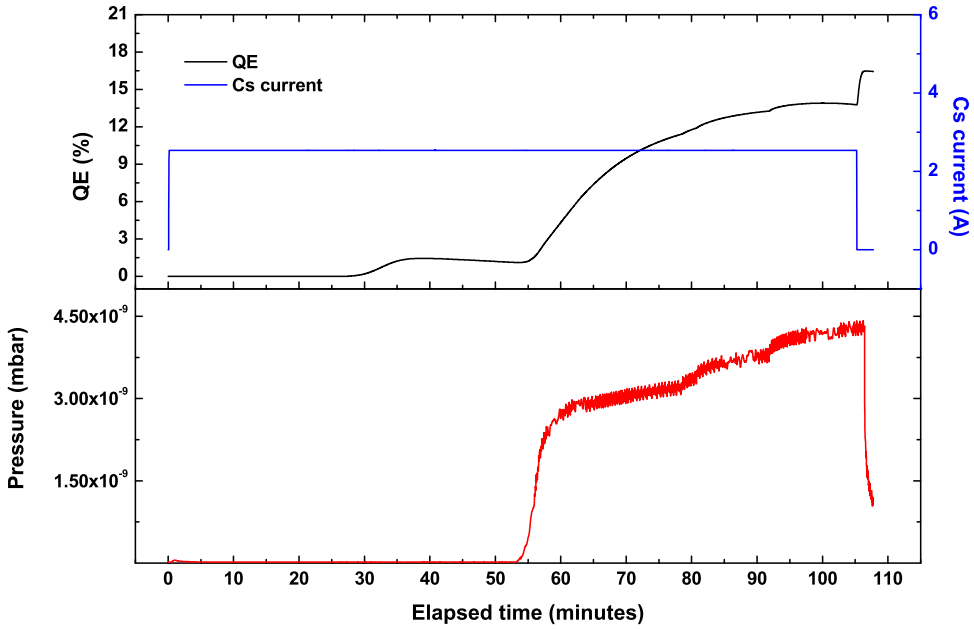

Figure 6.11: An activation curve for the thick RM GaAs photocathode: 2.0 μm with NF_3.

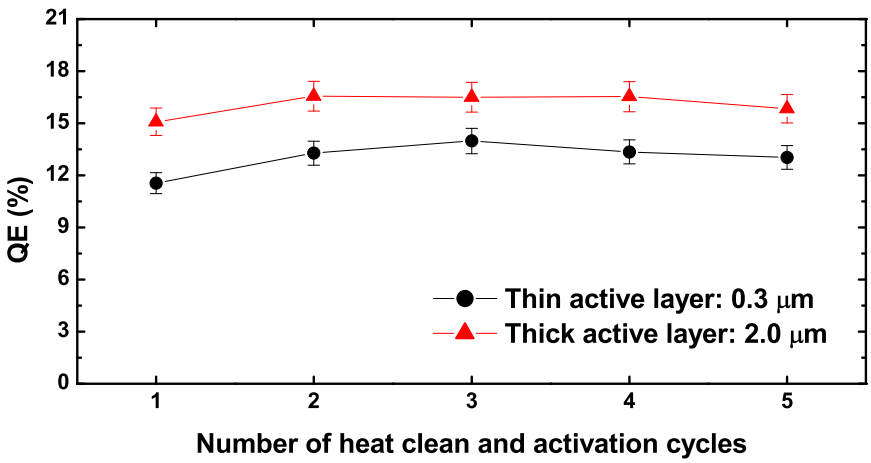

Figure 6.12: Plot showing the achieved QE against the number of heat clean and activation cycles with NF_3 for a thick active layer: 2.0 μm and thin active layer 0.3 μm RM GaAs photocathode.

imately 4×10^4 cm^{-1} at the photon energy of 1.95 eV), it can be estimated that only 70% of the incident laser power is absorbed by the 0.3 μm active thickness layer. When compared to the result obtained from the thick photocathode that can fully absorb the incident laser light (an average QE of approximately 16.1% in Figure 6.12), an average QE of approximately 11.3% was expected from the thin active layer RM photocathode. A typical activation curve for the thin active layer RM GaAs photocathode using NF_3 is shown in Figure 6.13. From the experiment, a QE of between 10 - 11.5% was obtained in the first activation. After the first activation, the photocathode was heated to 450 °C for 30 minutes and then activated again. A QE of 13% was achieved in the second activation. A plot showing QE versus the number of heat and activation cycles using NF_3 for the thin RM photocathode is also shown in Figure 6.12. From the figure, it is observed that the average QE obtained from the thin active layer is approximately 80% of that obtained from

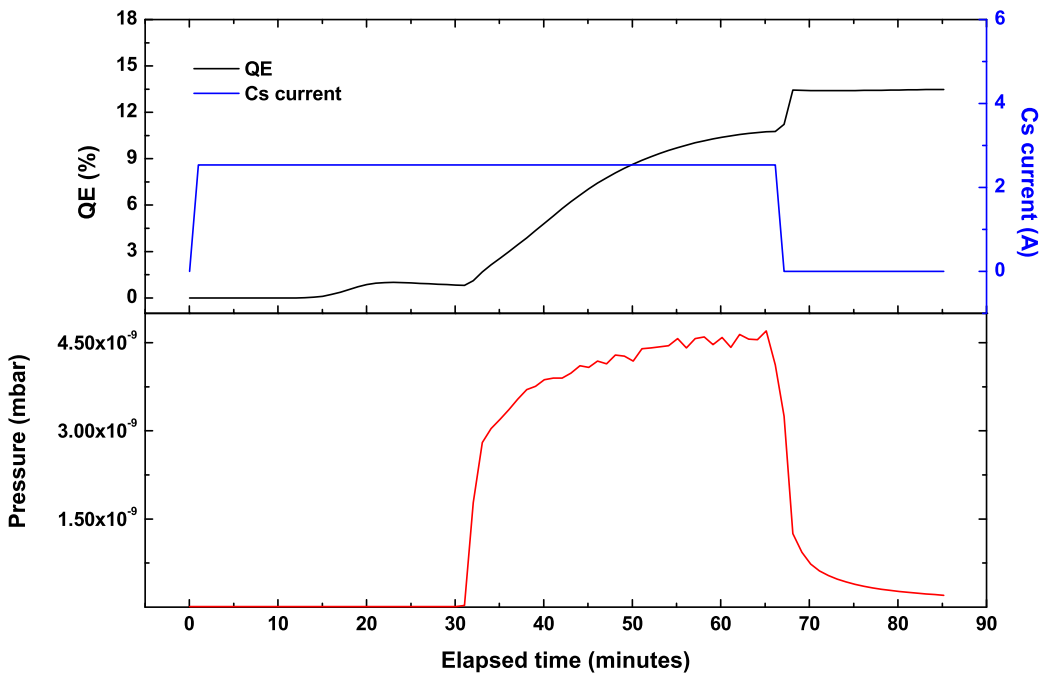

Figure 6.13: An activation curve for the thin RM GaAs photocathode: 0.3 μm with NF_3.

the thick active layer RM photocathode. This result is slightly different from the expectated value.

6.4 The ALICE photocathode

As discussed in Chapter 5, the ALICE photocathode differs significantly from those made by the ISP. It is a single crystal GaAs wafer grown by VGF with a diameter of 31 mm and thickness of 500 μm. In order to load the ALICE GaAs photocathode into the PPF, the GaAs wafer has to be mounted on a molybdenum "puck", as displayed in Figure 6.14. The wafer was retained in position with a tantalum cap with circular cutout in the centre, leaving the centre portion of the wafer exposed to 27.30 mm diameter. An indium foil was also placed between the GaAs wafer and the puck to increase the thermal conductivity. This foil is melted in the first heating, and consequently becomes a soldered joint between the wafer and the puck.

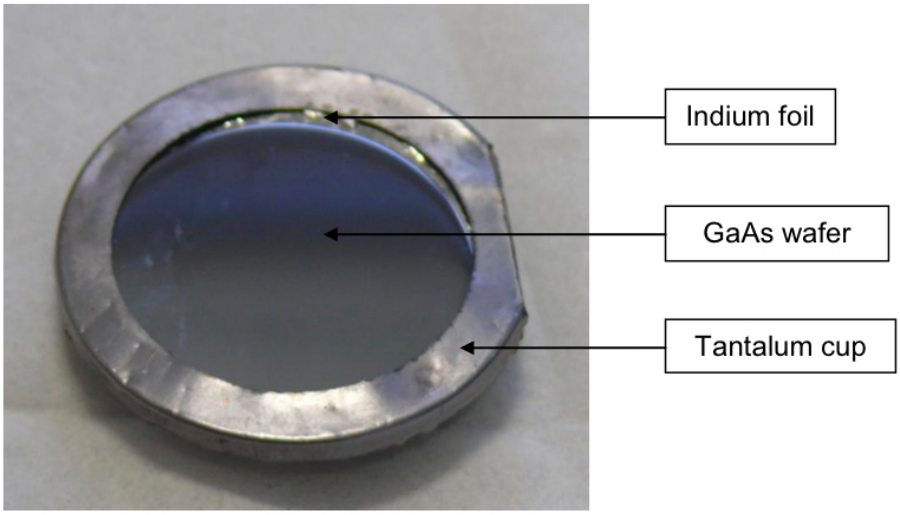

Figure 6.14: Photograph of the ALICE GaAs photocathode mounted on the molybdenum puck for use in the PPF

6.4.1 Photocathode preparation

Our initial experiments with the ALICE GaAs photocathode were done to compare the PPF results with the typical photocathode performance when activated *in-situ* in the ALICE photo-electron gun. The ALICE photocathode was prepared by first degreasing the GaAs wafer in pure IPA. It should be emphasised that no acid treatment was carried out on the photocathode. The wafer was then mounted on the puck, placed into the transfer vessel and loaded into the loading chamber. After the LC was pumped-down to the 10^{-8} mbar range, the photocathode was transfered to the AHCC and heated to approximately 550 °C for 30 minutes. The temperature was increased slowly over 30 minutes during the heating process in order to maintain the pressure inside the chamber and avoid thermal stress inside the wafer. After the heating cycle was completed and the pressure of the AHCC recovered to the 10^{-9} mbar range, the photocathode was transfered to the PC and placed onto the carousel. The photocathode was then heated again to 600 °C for 30 minutes, and again the temperature was increased slowly over 30 minutes during the process. Once the photocathode had cooled down to the room temperature (approximately 4 - 5 hours for the ALICE photocathode), the activation was carried out using a co-deposition technique. The Cs dispensers were powered constantly at 2.7 A during the activation. After the photocurrent reached its peak and dropped to approximately 20% of the first peak, O_2 was admitted into the chamber at a pressure between 3 - 6×10^{-10} mbar. A typical activation curve is shown in Figure 6.15.

6.4.2 Results and discussion

A QE of approximately 4% was obtained from the fresh ALICE GaAs photocathode by preparing the photocathode in this manner. Following the activation, the photocathode was heated to approximately 600 °C for 30 minutes in the PC and then activated to the NEA state many times. A plot showing the obtained QE and the activation number is shown in Figure 6.16. It can be seen that the QE of the photocathode increases over successive reheating and activation cycles, reaching approximately 8% by the eighth activation. After that, a QE of between 8 - 9%

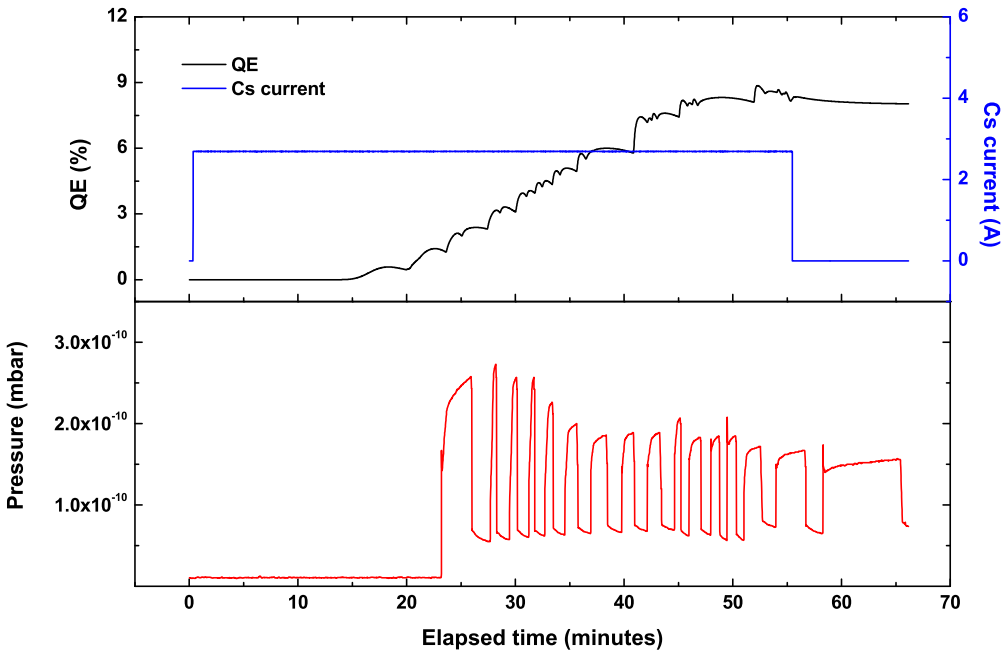

Figure 6.15: A typical activation curve for the ALICE GaAs photocathode using the co-deposition technique with O_2 in the PPF.

is routinely obtained from the ALICE photocathode at a wavelength of 635 nm. This level of QE is higher than that obtained in both the surface characterisation system, and following *in-situ* activation in the ALICE photo-injector, normally 3%. It should be noted that the QE of the current ALICE photocathode is measured at a wavelength of 532 nm. At this shorter wavelength, the measured QE of the GaAs photocathode is slightly enhanced and a measurement at 635 nm in ALICE would return an even smaller QE level. The reason for the increase in QE with the activation number is not yet clear. However, I believe that this increase in QE is as a result of the improved surface cleanliness since the photocathode was heated to 600 °C prior to activation many times. This temperature is high enough to remove the residual oxides from the activation process which is in contrast to the TM GaAs photocathode, where the photocathode was heated to 450 °C.

The QE lifetime plot for the activated ALICE photocathode is shown in Figure 6.17. The dark lifetime of the ALICE photocathode was quite consistent, a small variation

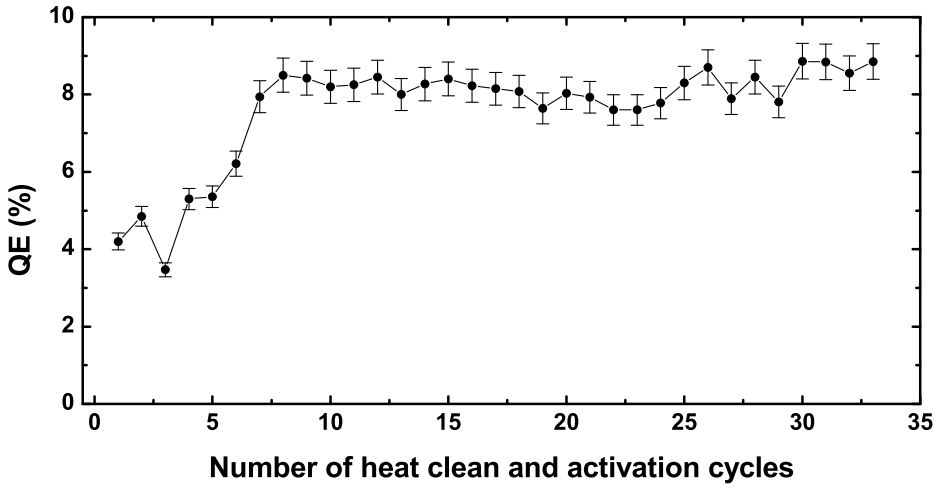

Figure 6.16: Plot showing the achieved QE and the activation number for the ALICE GaAs photocathode in the PPF.

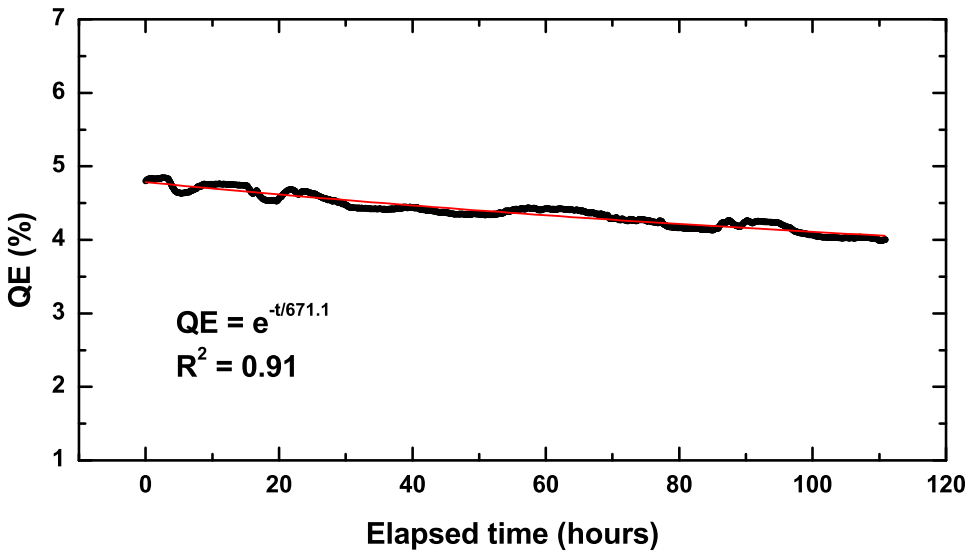

Figure 6.17: QE dark lifetime plot for the activated ALICE GaAs photocathode, showing a dark lifetime approaching 700 hours.

due to the small pressure fluctuations in the vacuum system of the PC. Lifetimes of between 600 - 700 hours were usually measured under illumination by a CW laser delivering 0.45 mW with the beam splitter and the ND filter modulated at 3 kHz.

6.5 Anodised GaAs photocathode

After activation to the NEA state, the entire circular active area of the ALICE GaAs photocathode, approximately 25 mm in diameter, becomes an efficient electron emission surface. As a consequence, parasitic electrons can be easily emitted from the surface outside the 4 mm in diameter illumination area, due to the application of high voltage, and cause the problems discussed in Chapter 1. To overcome this problem, one effective solution is to grow a thick oxide layer over the surface of the photocathode, leaving only a small area for later activation. The oxidised surface outside the active area cannot be activated into the NEA state and also presents itself as a rough surface that has poor electron emission properties, leading to suppression of electron emission in this region [125]. This is the so-called anodisation process.

6.5.1 Experimental set-up

Anodisation can be carried out by masking a specific area of the cathode surface for activation, whilst exposing the remainder of the front surface to an acid to create the oxide layer. The process is driven by the application of a voltage to the cathode of +50 V during the anodisation.

In this experiment, the anodised GaAs photocathode was prepared based on the TJNAF procedure [125]. An anodising fixture has been constructed to aid the anodising process. The assembly view of the anodising fixture is shown in Figure 6.18. It consists of front and back plates bolted to the anodiser body, sealed with large o-rings. The photocathode is seated on an o-ring on the back spacer that prevents anodisation of the back of the photocathode, thus retaining its thermal and electrical properties when it is soldered to the photocathode support stem. The front spacer locates the masking o-ring with an inner diameter of approximately 6 mm to preserve the un-anodised area for later activation. This o-ring inner diameter defines

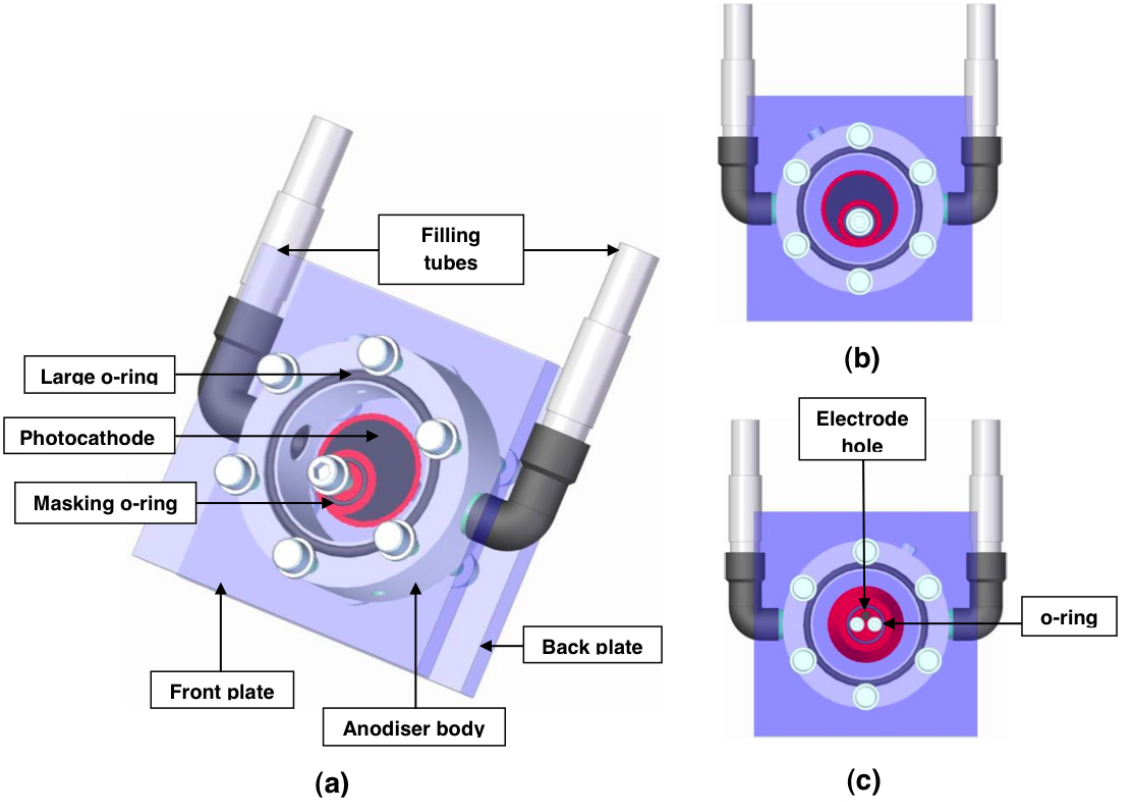

Figure 6.18: Schematic overview of the anodising fixture (a). Front view of the anodising fixture (b), the photocathode is shown as the dark blue circle in the centre with the masking o-ring held on the cathode by the front spacer. Back view of the anodising fixture (c), showing the +50 V electrode hole through which electrical contact is made with the photocathode during anodising.

the ultimate active area of the photocathode after the anodisation, approximately 6 mm in this experiment.

6.5.2 Photocathode anodising procedure

The anodised photocathode was prepared by first degreasing the GaAs wafer in pure IPA. All equipment described in the previous section was cleaned by rinsing in an ultrasonic bath with IPA, then methanol, finishing with DI water. After all cleaning processes, the anodiser was carefully assembled and the cathode to be anodised was installed. The anodising fixture with a photocathode installed is shown

in Figure 6.19. During anodisation, a dilute phosphoric acid solution, prepared by adding 4 drops of 85 % Phosphoric acid to the 200 ml of DI water, was filled into the anodiser body through the tubes either side of the fixture. An electrical potential of +50 V DC was applied to the photocathode for 5 to 10 s. The electrical connections are made to both the aluminium anodiser body (negative) and directly to the back of the cathode (positive) through the electrode hole. After applying the voltage, a colour change in the anodised (i.e., non-masked) area of the photocathode was observed and the anodisng process was complete.

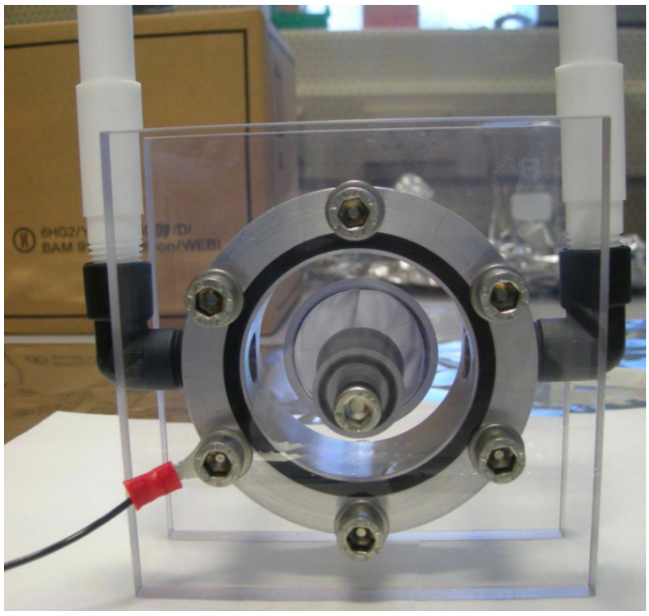

Figure 6.19: Photograph of the anodising fixture with a photocathode installed.

6.5.3 Results and discussion

Using the experimental set-up and procedure described above, the ALICE GaAs photocathode was successfully anodised. A photograph of the anodised photocathode is shown in Figure 6.20. The photocathode shows a blue/purple finish in the outermost part of the wafer which was exposed to the acid, leaving an unexposed portion between 5 - 6 mm in diameter which was masked by an o-ring for later activation.

Figure 6.20: Photograph of the ALICE GaAs photocathode after the anodising process, clearly showing the blue anodised surface with a small active area preserved.

To test its performance, the anodised photocathode was prepared and activated in a similar way to the ALICE photocathode. The photocathode was first degreased in pure IPA and mounted on the puck. It should be emphasised that any acid treatment cannot be applied to the photocathode surface after anodisation as it will remove the oxide layer and damage the anodised surface. After mounting on the puck, the photocathode was placed to the transfer vessel, then loaded into the loading chamber. The first heat cleaning cycle was performed by heating the photocathode to 550 °C for 30 minutes in the AHCC. After the heating process was complete and the photocathode transfered to the PC, the final heat cleaning cycle was carried out by heating to 600 °C for 30 minutes. Once the photocathode had cooled to room temperature, activation was carried out using a co-deposition procedure. The Cs source was powered constantly at 2.7 A during the activation. After the photocurrent reached its peak and dropped to approximately 20% of the first peak, O_2 was admitted into the chamber within the pressure range between 3 - 6×10^{-10} mbar.

The resulting activation curve is shown in Figure 6.21. A QE of only 2.9% was obtained in the first activation. However, after heating to 600 °C for 30 minutes, the photocathode was activated again. An improvement in QE was observed, yielding a QE of 7.8% after the fifth activation. The result is consistent with the earlier result

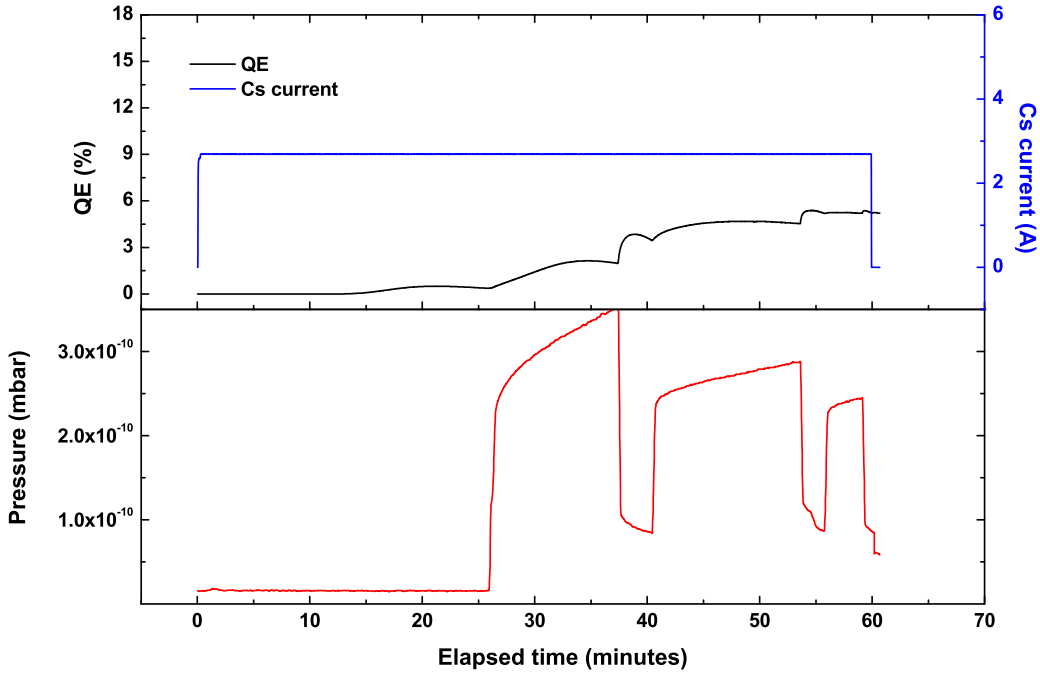

Figure 6.21: An activation curve for the anodised ALICE GaAs photocathode using the co-deposition technique with O_2.

for the un-anodised ALICE GaAs photocathode. A plot showing the achieved QE versus the number of heat and activation cycles for the anodised photocathode is shown in Figure 6.22.

To demonstrate the difference between the active and anodised areas, the QE's were measured at several positions on the photocathode surface. This was done by rotating the carousel (θ) in conjunction with translating the laser position (r) across the photocathode surface, as illustrated in Figure 6.23. The carousel was rotated in 1° steps and the laser position was translated in 0.25 mm steps. The photocurrent was measured under the illumination of a 635 nm diode laser with the laser spot size of approximately 1.2 mm at the photocathode surface. The QE surface scan result is displayed in Figure 6.24.

From Figure 6.24, it is observed at $\theta = 14$ that the QE starts being registered only from $r = 5$ to 12.5 mm. This result shows that only a small area of the

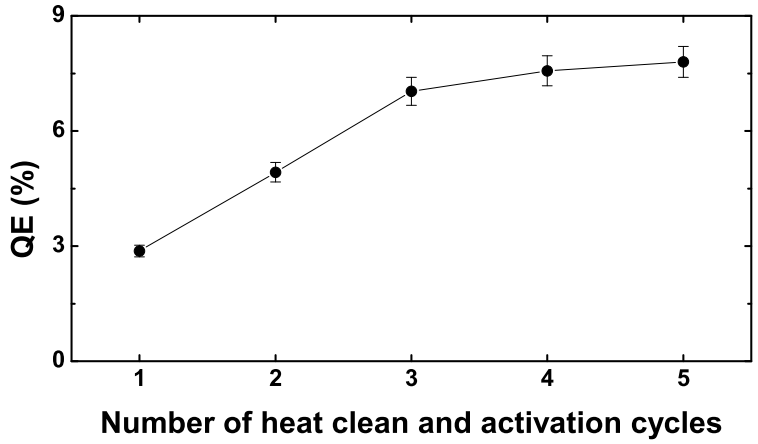

Figure 6.22: Plot showing the achieved QE against the number of heat clean and activation cycles for the anodised ALICE GaAs photocathode.

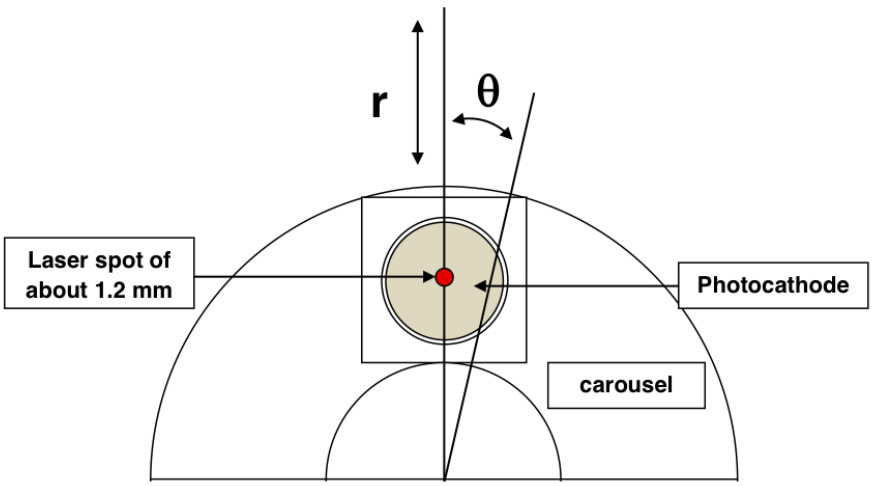

Figure 6.23: Schematic showing the QE profile measurement across the anodised GaAs photocathode surface.

photocathode surface, approximately 6 mm in diameter was activated to the NEA state, resulting in the measured photocurrent and QE observed in Figure 6.24, whilst no photocurrent was detected outside this area. It is not clear if the variation of QE in the active area is the result of the quality of the photocathode surface

itself, or the preparation process. Further studies needs to be carried out with a precise QE surface scan, however, it is clearly shown in this experiment that the active area of the GaAs photocathode can be reduced by anodising the edge of the photocathode. This technique is very simple and effective for reducing the active area and consequent dark current for a NEA GaAs which has a relative large emitting surface.

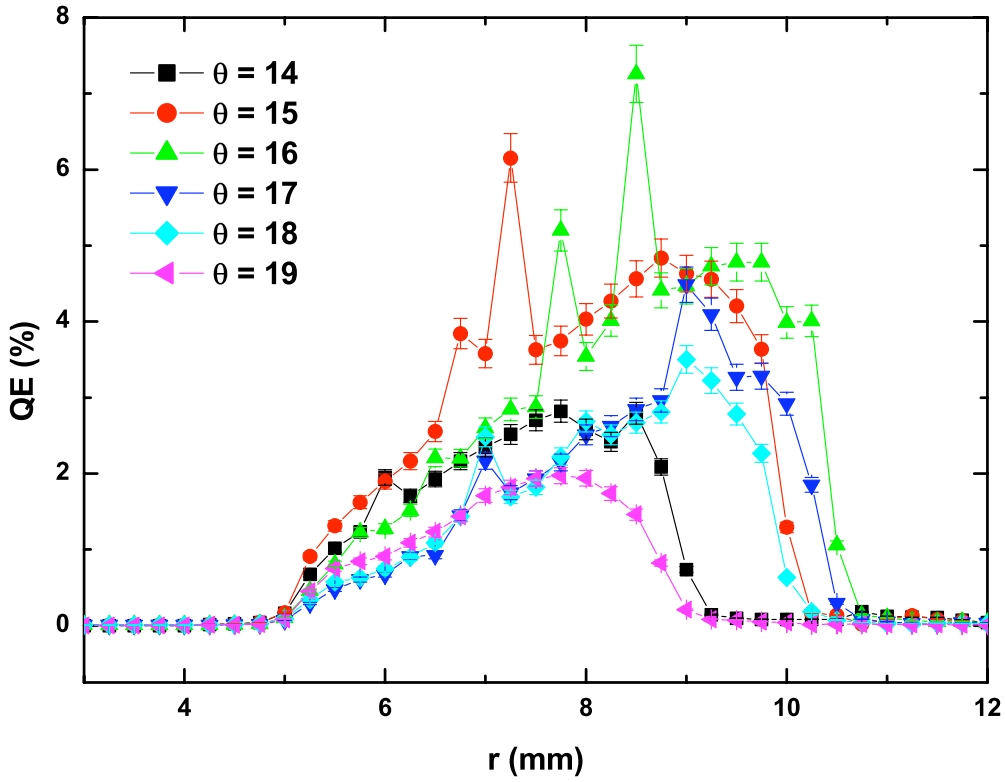

Figure 6.24: The QE surface scan for an activated anodised ALICE GaAs photocathode. The measurement was performed by rotating the carousel (θ) in 1° steps in conjunction with translating the laser position (r) in 0.25 mm steps across the photocathode surface. The photocathode was illuminated with a 635 nm diode laser with the laser spot size of approximately 1.2 mm at the photocathode surface.

In summary, the results presented in this chapter clearly demonstrate the success and performance of the ALICE PPF. The NEA GaAs photocathode with a QE as high as between 12 - 19 % at a wavelength of 635 nm and a lifetime of approximately 6,800 hours can be prepared and delivered from the PPF in a reproducible way. Having prepared the NEA GaAs photocathode in a reproducible way, the influence of the residual gas species on the QE lifetime of the photocathode will be studied in the next chapter.

A remark should also be made about the degradation of the achievable QE from the photocathode with the number of heat clean and activation cycles when the photocathode is activated with Cs and O_2. This degradation problem was also found in other laboratories [71, 72, 124]. In this chapter, It has been shown that this problem can be simply avoided by using NF_3 as an oxidant. Only a small level of the degradation of the achievable QE with the number of heat clean and activation cycles was observed in this experiment. This result may help to map the strategy for the future development of photo-injector employing the GaAs photocathode.

Chapter 7

QE lifetime studies

QE lifetime is a very important parameter for a NEA GaAs photocathode and its practical use. It is clearly shown in Chapter 1 (Figure 1.11) that the QE of the NEA GaAs photocathode degrades with time, even if it is not subjected to high current operation. This degradation is predominantly caused by the adsorption of residual gas species inside the gun vacuum. It is thus crucial to investigate this degradation process in order to improve the performance of the photocathode.

This chapter presents my experimental study on the influence of the residual gas species on the QE lifetime of a GaAs photocathode. Using the ALICE PPF, I had prepared and activated GaAs photocathodes following the previously explained procedures to produce a consistent level of cathode performance, then I measured the QE lifetime of the photocathodes under various gas species exposures. This is the first time demonstration of the influence of the residual gas species on the QE lifetime of a NEA GaAs photocathode at a base pressure in the 10^{-11} mbar range where the influence of the background residual gas can be minimised.

This chapter is organised as follows. I first carried out the experiment on the NEA GaAs photocathode activated with O_2. The experimental results and discussion are presented in section 7.1. To compare the results with the NEA GaAs photocathode activated with O_2, a series of experiments were also carried out on the NEA GaAs photocathode activated with NF_3. These experimental results and discussion are presented in section 7.2.

7.1 NEA GaAs photocathodes activated with O_2

7.1.1 Experiments

Two different types of photocathodes with different levels of achievable QE were used in the experiment: the TM GaAs photocathodes with a QE of between 11 - 15% and the ALICE GaAs photocathode with a QE of between 7 - 8%. Each experiment was performed separately by preparing and activating the photocathode following the procedures described in sections 6.2.1 and 6.4.1. The actual QE lifetime measurements were performed after the activation when the pressure of the PC recovered to approximately 1.5×10^{-11} mbar. At this point, it is seen that the photocurrent becomes steady and only a very small degradation of the QE over time was observed. The tested gas was then carefully injected into the chamber through the piezo-electric leak valve. During the injection, the total pressure of the chamber was increased slowly, and maintained at a constant value of approximately 1.5×10^{-10} mbar. The purity of the injected test gas was monitored using the RGA, and its quality assured by not permitting a background partial pressure more than 5% for any residual oxidiser present relative to the gas under test. Gas exposures were quoted in Langmuirs (L), where 1 L = 1.33×10^{-6} mbar·s, and calculated as the integral of the total pressure rise over the injection time. The uncertainty of the pressure measurement and the gas exposure is 5%, based on the uncertainty of the vacuum gauge. The QE was measured under the illumination of a 635 nm diode laser with a small power of 0.45 mW transmitted through a 20% ND filter. The uncertainty of all QE data sets is estimated to be 5.2%.

Six gas species were tested, selected because they are the main residual gases found in the vacuum system of a typical photo-injector: H_2, CH_4, N_2, O_2, CO_2 and CO. These gas species were provided from laboratory gas research grade (99.998% pure by volume). For all of the experiments, only freshly-activated photocathodes were used to avoid the historic effects of the photocathode QE documented earlier.

7.1.2 Experimental results

Gas exposures

The QE lifetime of the TM and the ALICE GaAs photocathode during exposures to H_2, CH_4, N_2, CO, CO_2 and O_2 at a total pressure of 1.5×10^{-10} mbar for approximately 30 minutes are shown in Figure 7.1 and Figure 7.2. The total amount of exposure is approximately 0.2 L for each gas exposure. It is clearly seen that no changes in the QE's were observed during the H_2, CH_4 and N_2 exposures for both the TM and the ALICE GaAs photocathodes. This result clearly shows that H_2, CH_4 and N_2 have no effect on the QE lifetime of the NEA GaAs photocathode. On the other hand, significant degradation of the QE were clearly seen during the CO_2 and O_2 exposures, with only a slight degradation during CO exposure.

Comparisons of the QE degradation under different gas exposures in Langmuir (L) units for the TM and ALICE GaAs photocathodes are shown in Figure 7.3 and Figure 7.4, respectively. It is clearly seen from these plots again that H_2, CH_4 and N_2 have no effect on the QE of the photocathodes. CO has only a small effect on the photocathode and can reduce the QE to only 90% of the initial value after the exposure of approximately 0.125 L for both the TM and ALICE GaAs photocathodes. CO_2 has a severe effect on the photocathode, resulting in the degradation of the QE to 10% of the initial value after an exposure of approximately 0.08 L and 0.21 L for the TM and ALICE GaAs photocathodes, respectively. O_2 shows the strongest effect since it can degrade the QE to 10% of the initial value after an exposure of only 0.025 L for both the TM and ALICE GaAs photocathodes. Interestingly, this level of O_2 exposure is in agreement with the result reported by Pastuszka *et al.*[126] which was approximately 0.021 L.

The most interesting result is the observed effect of the CO exposure on the QE lifetime of the photocathode. This result is in stark contrast to the previous study by Wada et al. [127]. Wada studied the influence of CO, CO_2 and H_2O on the stability of GaAs photocathodes and found no effect under CO exposure up to 100 L. This contradictory result may be due to the fact that their experiment was performed in the vacuum chamber which has a base pressure in the mid to high

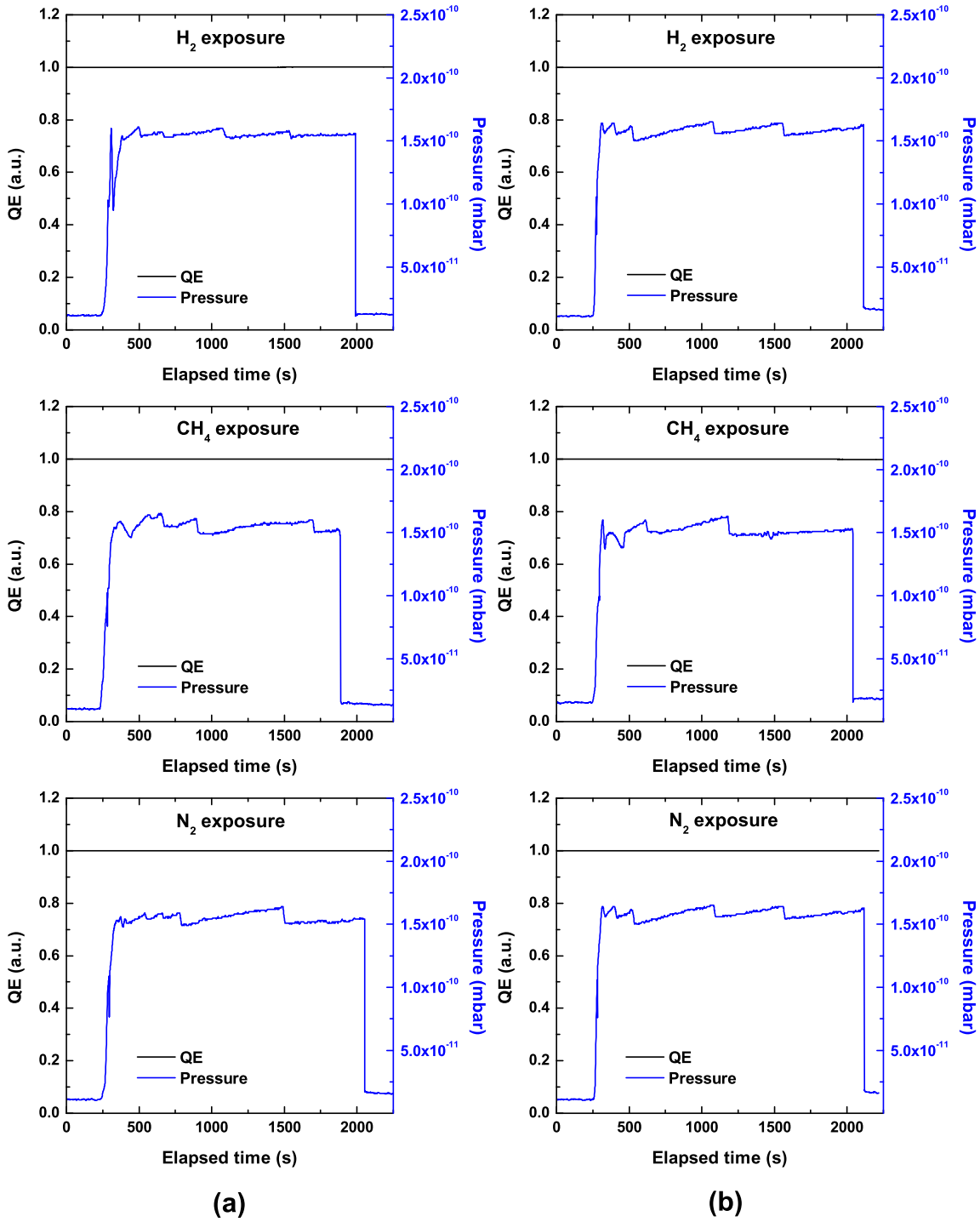

Figure 7.1: The QE lifetime of the TM GaAs photocathodes (a) and the ALICE GaAs photocathode (b) during exposures to H_2, CH_4 and N_2 at a pressure of 1.5×10^{-10} mbar.

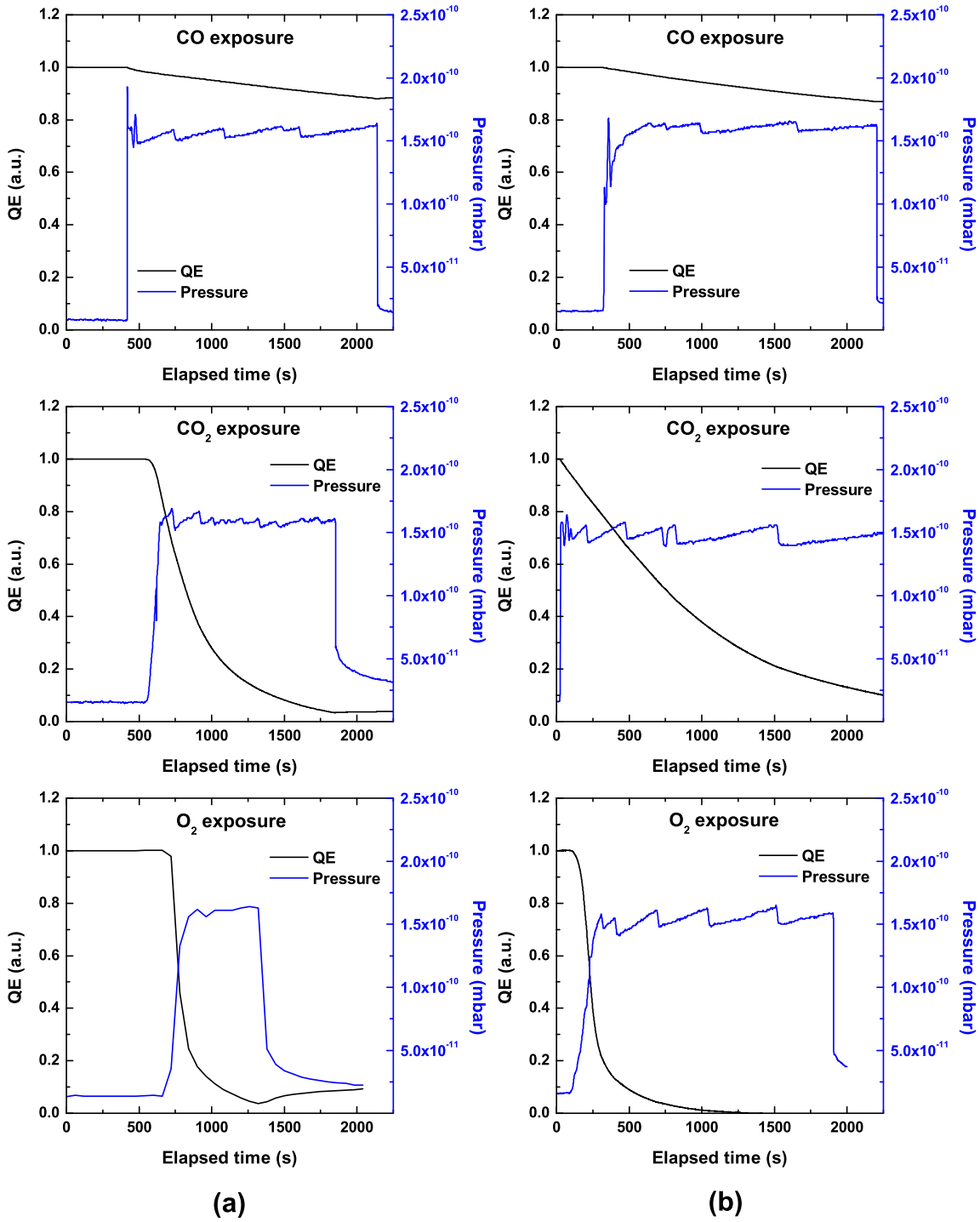

Figure 7.2: The QE lifetime of the TM GaAs photocathodes (a) and the ALICE GaAs photocathode (b) during exposures to CO, CO_2 and O_2 at a pressure of 1.5×10^{-10} mbar.

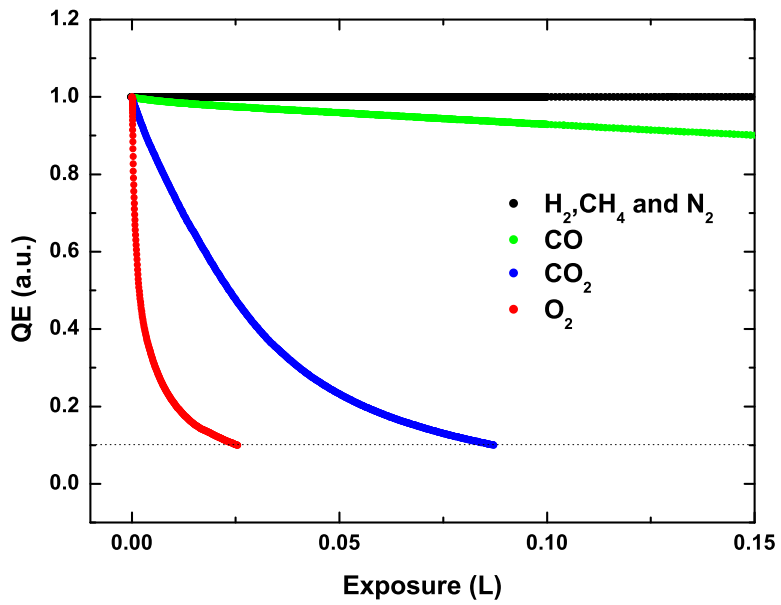

Figure 7.3: Comparison of the QE degradation for the TM GaAs photocathode during different gas exposures at a pressure of 1.5×10^{-10} mbar.

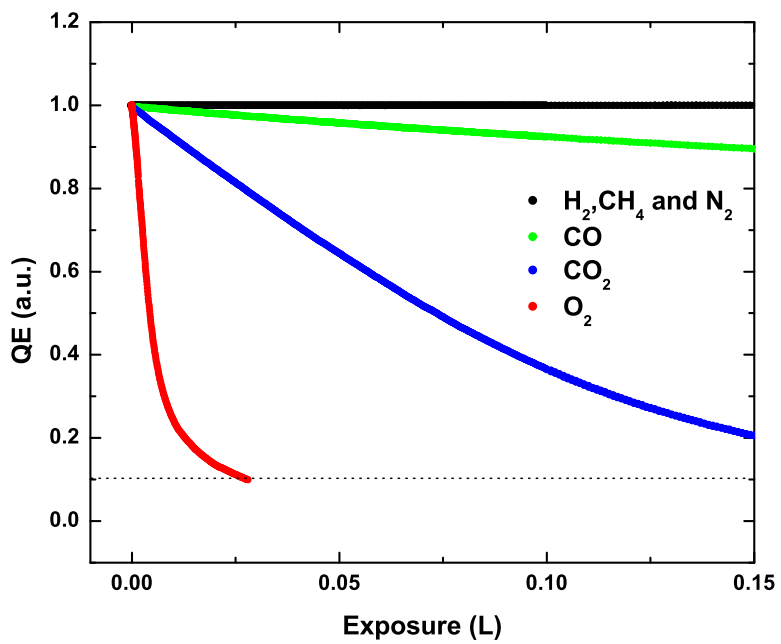

Figure 7.4: Comparison of the QE degradation for the ALICE GaAs photocathode during different gas exposures at a pressure of 1.5×10^{-10} mbar.

10^{-10} mbar range [127]. At that level of pressure, the QE of the photocathode will be degraded gradually due to the residual gases inside the chamber without any additional gas exposure. Therefore, it would not have been possible to observe the small degradation during CO exposure in that experiment.

To further validate these results, I have repeated the experiments with different exposure levels. The photocathodes were exposed to H_2, CH_4 and N_2 at exposures up to 1 L and no changes in QE were observed. The effects of CO and O_2 and degradation rates with exposure level (L) were repeatedly observed at all injection pressures for both the TM and ALICE GaAs photocathodes. A plot of QE lifetime of the ALICE GaAs photocathode during O_2 exposures at different injection pressures is shown in Figure 7.5. However, I have found a discrepancy of the degradation rates when exposing both the TM and ALICE GaAs photocathodes to CO_2 at different injection pressures. A plot of QE lifetime of the ALICE GaAs photocathode during CO_2 exposures at different injection pressures is shown in Figure 7.6. It is seen in that the degradation rate varies during CO_2 exposures, depending on the injection pressures and the level of CO_2 exposure that degrades the QE to 10% of the initial value varies between 0.15 and 0.27 L for the ALICE GaAs photocathode.

Rejuvenation

Another interesting result found in this experiment is the possibility to restore QE after degradation. It is well known [71, 72] that the QE of NEA GaAs photocathodes can be recovered by adding Cs layers to a degraded surface, or the so-called "re-caesiation", and it is widely used to prolong the operational lifetime of the NEA GaAs photocathode. To investigate the effect of the gas exposures after degradation, the experiment was carried out by adding Cs onto the photocathodes after the degradation.

The evolution of the QE during the application of Cs to the degraded TM GaAs photocathodes after O_2, CO_2 and CO exposures are shown in Figure 7.7 to Figure 7.9. Note that as the QE degradation during CO exposure is very slow, the photocathode was thus exposed to CO at a pressure up to 2×10^{-10} mbar. From the experimental results, it is seen that after adding Cs onto the surface, the QE

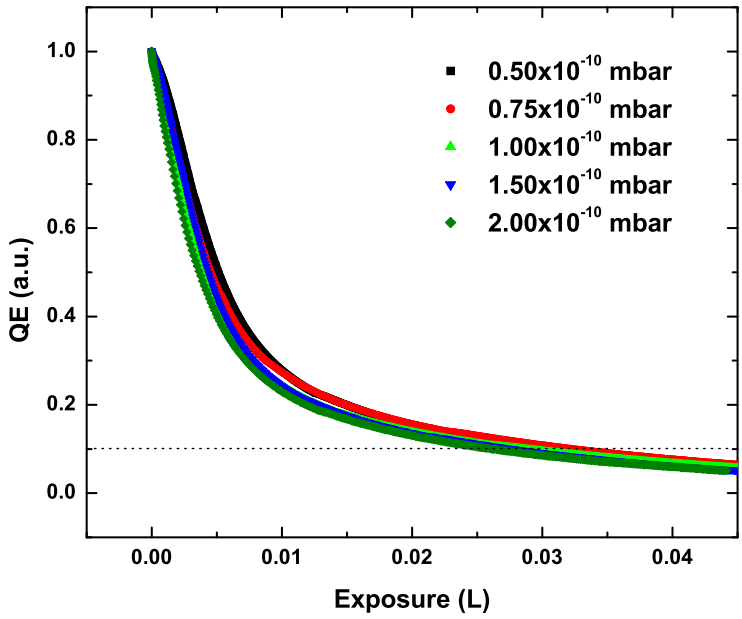

Figure 7.5: Comparison of the QE degradation for the ALICE GaAs photocathode during O_2 exposures at different injection pressures.

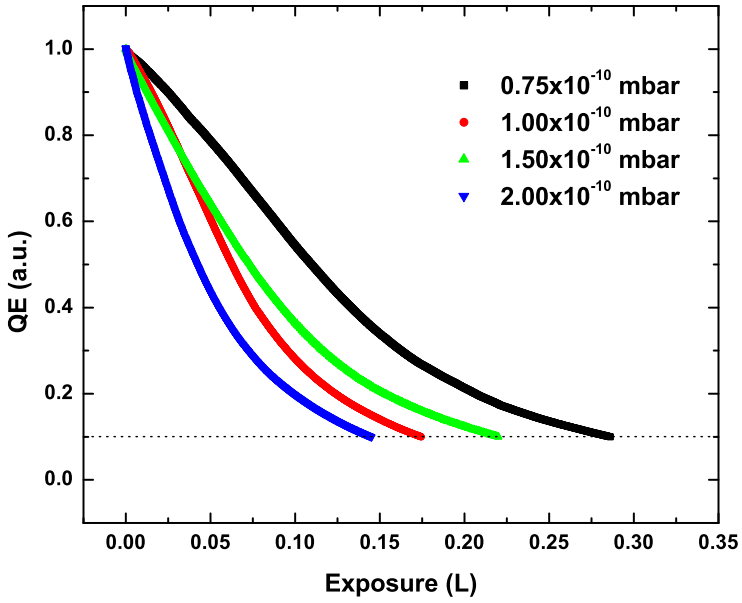

Figure 7.6: Comparison of the QE degradation for the ALICE GaAs photocathode during CO_2 exposures at different injection pressures.

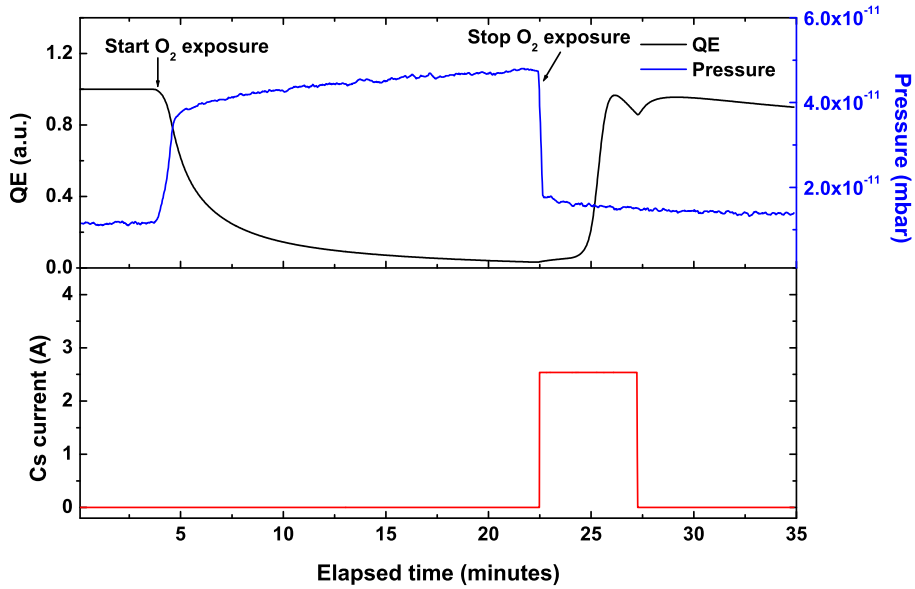

Figure 7.7: Evolution of the QE of the TM GaAs photocathode during exposure to O_2 followed by re-caesiation. Cs exposure for approximately 5 minutes restored QE to 95% of the initial level.

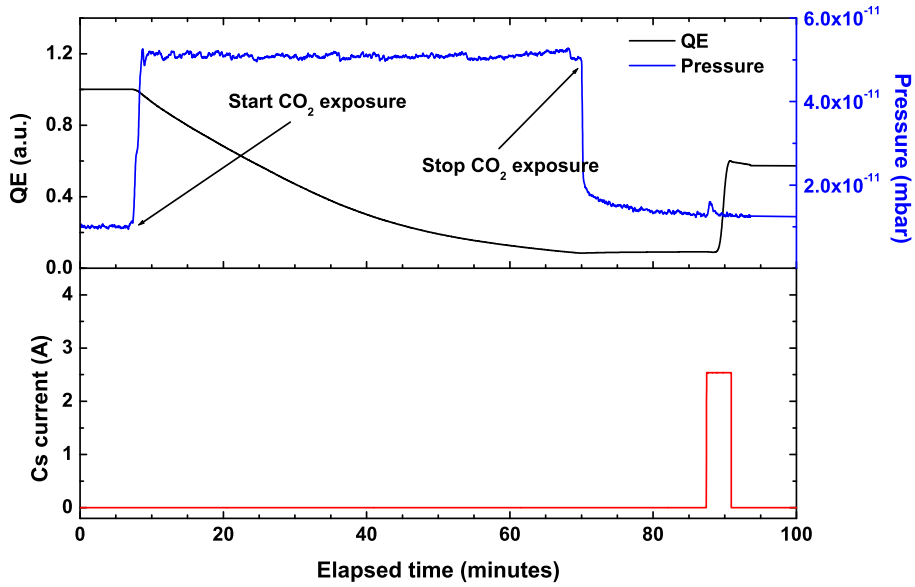

Figure 7.8: Evolution of the QE of the TM GaAs photocathode during exposure to CO_2 followed by re-caesiation. Cs exposure for approximately 5 minutes restored QE to 60% of the initial level.

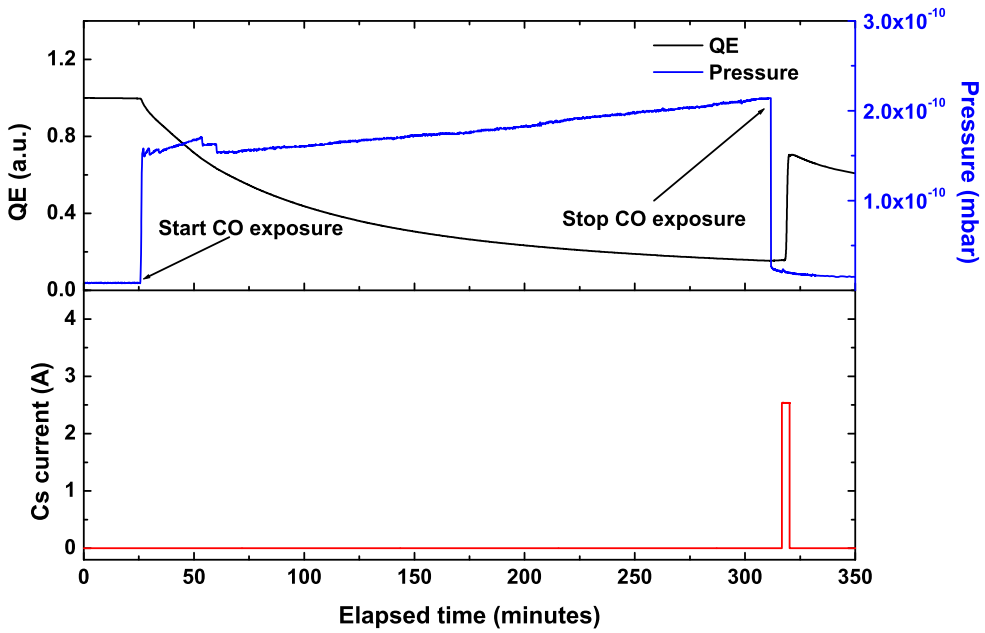

Figure 7.9: Evolution of the QE of the TM GaAs photocathode during exposure to CO followed by re-caesiation. Cs exposure for approximately 5 minutes restored QE to 70% of the initial level.

can be restored to 95% of the initial value in the case of O_2 exposure, whereas the QE can recover only to 60% and 70 % of the initial value in the case of CO_2 and CO exposures, respectively.

7.1.3 Discussion

The results described above clearly show the influence of the residual gas species on the QE of a NEA GaAs photocathode. The NEA GaAs photocathode degrades predominantly due to the adsorption of oxygen or oxygen-containing gas species, CO_2 and CO. All these results can be explained by the double-dipole model [69, 70], which is based on the dipole model described in Chapter 2.

A schematic energy band diagram of the double-dipole model is shown in Figure 7.10. In this model, the surface potential barrier consists of two regions with different slopes: **(1)** and **(2)** in Figure 7.10. The barrier **(1)** is created by a GaAs/Cs dipole

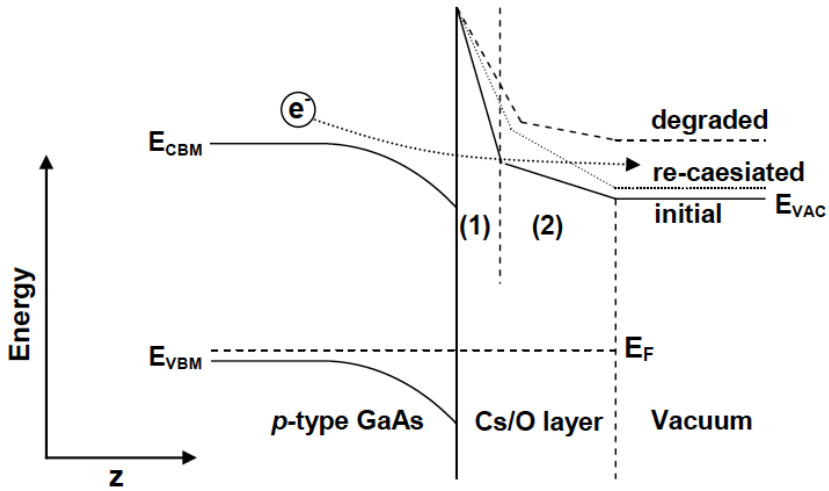

Figure 7.10: Schematic energy diagram showing the surface potential for the NEA GaAs photocathode when first activation ("initial") is degraded by exposure to contaminants, then re-caesiated.

at the GaAs surface, while the barrier **(2)** is created by a Cs/O dipole in the activation layer.

When oxygens (as atoms, molecular oxygen, or part of some other species) attach to the NEA GaAs photocathode surface, they accept electrons from Cs atoms and are chemisorbed inside the activation layer. I propose that this changes the chemistry of the Cs/O layers and weakens the dipole in the activation layer region. As a result, the height of the surface potential barrier in region **(2)** and the vacuum level increase. Moreover, the adsorbed oxygens can effectively penetrate the activation layer and directly interact with the GaAs substrate, thus forming substrate oxides as has been reported [128]. Consequently, the width of barrier region **(1)** increases and the barrier profile for a degraded photocathode will evolve as a dashed line as shown in Figure 7.10. It has been mentioned in reference [128] that the specific barrier profile, such as barrier width and height, can be obtained from the fit of spectral response data with the QE equation.

As seen in Figure 7.10, the change in the barrier profile reduces the escape probability of photoelectrons, especially in the case of the NEA GaAs photocathode where most photoelectrons are thermalised electrons which have low energies. This

also suggests that GaAs photocathodes with a high level of NEA (high QE) are likely to be unstable compared to those with a low level of NEA (low QE). This is in further agreement with the results that the ALICE GaAs photocathode with a QE of around 8% was observed to be slightly more stable than the TM GaAs photocathodes with a QE of around 15%.

The dipole in region **(2)** can be restored by the re-caesiation process. The additional Cs atoms on the degraded photocathode surface strengthen the Cs/O dipole in the activation layer, so that the vacuum level will be reduced again as shown by the dotted line in Figure 7.10. However, the re-caesiation process has little influence on the barrier region **(1)**. In other words, the substrate oxides formed during the degradation process cannot be removed by the re-caesiation process. Therefore, the QE of the degraded photocathode cannot be fully recovered to its initial value in this way.

From my experimental results, O_2 has the strongest effect on the QE of the photocathode because it directly reacts with the Cs/O layer and weakens the dipole in the activation layer. On the other hand, CO was found to have little effect on the QE. It has been suggested by Wada [127] that this may be related to the fact that CO does not react with pure Cs clusters. Moreover, CO would rather be molecularly adsorbed on the activation layer than dissociate and provides oxygens to the surface because of its high dissociation energy of 11.10 eV [127]. Therefore, there is only a small change in the chemistry of the Cs/O layer which weakens the dipole in the activation layer, resulting in a small degradation observed.

For the case of CO_2, because the dissociation energy of CO_2 into CO and O is low, 5.44 eV [127], it is hence expected to dissociate and provide oxygen and CO to the activation layer. Therefore, the QE degrades much faster than when exposed to CO alone, but slower than that exposed to O_2. This also explains the variation in the QE degradation rate found during exposures to CO_2 at different injection pressures, in Figure 7.6. This is because CO_2 can also be dissociated by our experimental instruments inside the vacuum chamber such as the ion pump and the filaments of the ionisation guages before attaching to the photocathode surface. Therefore, the QE degradation rate under CO_2 also depends on the experimental

conditions such as the operation of the vacuum diagnostics. The increase in the gas injection rate (partial pressure of CO_2 during injection) also increases the degree of dissociation, as it is seen that the QE degradation rate increases when the partial pressure of CO_2 during exposure increases.

My experimental results on the recovery of QE after degradation are also in good agreement with the double-dipole model. Oxygen can penetrate the activation layer and directly interact with the GaAs substrate. This results in an increase of the region barrier width **(1)**. Therefore, the QE of the photocathode can be restored to only 95% of the initial value after the O_2 exposure. This is similar to the result obtained after CO exposure as CO is adsorbed molecularly, it penetrates the activation layer and directly interacts with the GaAs substrate [128]. As a result, the restored QE of only 70% was obtained after the re-caesiation process. The lower restored QE in the case of CO exposure suggests that the interaction of CO causes a greater increase in the width of barrier region **(1)** compared to oxygen. In the case of CO_2 exposure, CO_2 is dissociated to CO and O which both can penetrate the activation layer and interact with the GaAs substrate. Therefore, the restored QE of only 60% was obtained after the re-caesiation process.

7.2 NEA GaAs photocathodes activated with NF_3

I also carried out the experiments on the NEA GaAs photocathode activated with NF_3. As mentioned in Chapter 4, F has a very high electron negativity, higher than O and owing to its high electronegativity, it is believed that the activation layer is more stable than that obtained from a Cs and O activation [114]. Therefore, the photocathode has a longer QE lifetime and an increase in lifetime by a factor of 20 as observed by one group [129]. However, this has been a controversial result and has not been proven conclusively. In this section, the comparison of the QE lifetime between the GaAs photocathode activated with NF_3 and O_2 is presented for the first time.

7.2.1 Experiments

The experiments were carried out with the TM GaAs photocathodes in a similar manner to those in section 7.1.1. The photocathodes were prepared and activated to the NEA state using NF_3. QE lifetime measurements were performed after activation when the pressure of the PC had recovered to approximately 1.5×10^{-11} mbar. The test gas was carefully injected into the chamber through the piezo-electric leak valve. During the injection, the total pressure of the chamber was increased slowly and maintained at a constant level of approximately 1.5×10^{-10} mbar. The QE lifetime was measured under the illumination of a 635 nm diode laser with a small power of 0.45 mW transmitted through a 20% ND filter. The uncertainty of the pressure measurement and the gas exposure is 5% and the uncertainty of all QE data sets is estimated to be 5.2%. The test gases in this experiment were H_2, CH_4, N_2, O_2, CO_2 and CO and each experiment was performed separately on a freshly-activated photocathode.

7.2.2 Experimental results and discussion

The experimental results during the H_2, CH_4, N_2, CO, CO_2 and O_2 exposures at a total pressures of 1.5×10^{-10} mbar for 30 minutes are shown in Figure 7.11. The total amount of exposure is approximately 0.2 L for each gas exposure. It is clearly seen that no changes in the QE's were observed during the H_2, CH_4 and N_2 exposures. CO has a very small effect, while CO_2 and O_2 have a severe effect on the QE of the photocathodes. These results are similar to that obtained from the photocathode activated with O_2.

What is perhaps surprising is that N_2 has no effect on the photocathode, despite it being recently reported from synchrotron radiation photoelectron spectroscopy (SR-PES) experiments [113] that nitrogen is also present in the activation layer of the photocathode activated with NF_3 and it may play an important role in the dipole layer and consequently the NEA state of the photocathode. It was expected that exposure to N_2 may affect the chemical composition of the activation layer, resulting in a change in the QE. Contrary to the expectation, no change in QE was

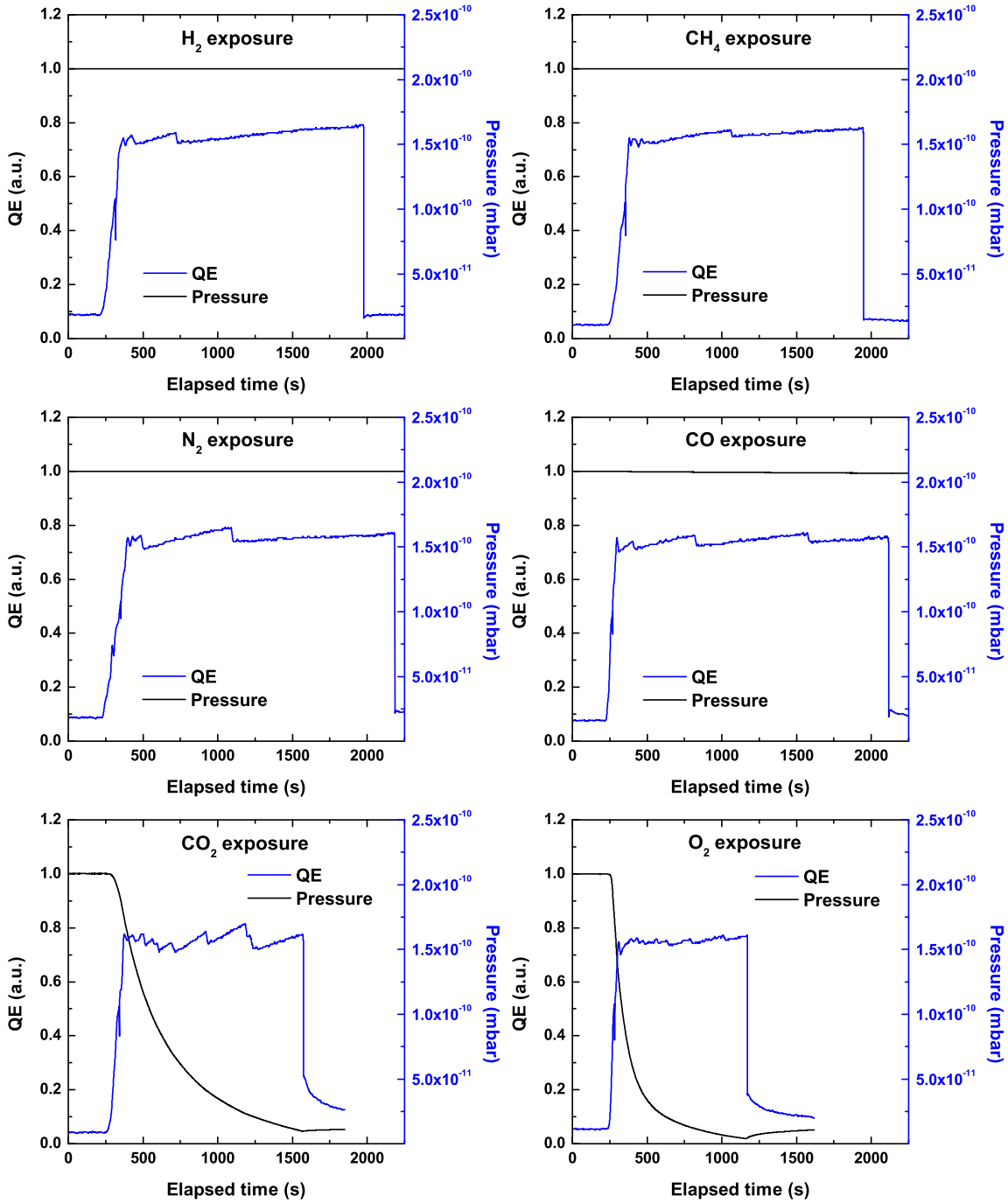

Figure 7.11: The QE lifetime of the TM GaAs photocathodes activated with NF_3 during exposures to H_2, CH_4, N_2, CO, CO_2 and O_2 at a pressure of 1.5×10^{-10} mbar.

observed. To confirm this result, the photocathode was exposed to approximately 1 L of N_2 but there was no change observed in the QE of the photocathode. This result implies that nitrogen does not play any role in the dipole layer of the NEA GaAs photocathode activated with NF_3.

A comparison of the QE degradation under different gas exposures in Langmuire units for the TM GaAs photocathodes activated with NF_3 are shown in Figure 7.12. Similar to a photocathode activated with O_2, the injection of O_2 still has the strongest effect on the QE of the photocathode. CO_2 also has a severe effect on the photocathode, while CO clearly has a very small effect. A comparison of the QE degradation under O_2, CO_2 and CO exposures for the photocathode activated with O_2 and NF_3 is shown in Figure 7.13. Stability is improved for a photocathode activated with NF_3, and the amount of O_2 needed to reduce the QE of the photocathode to 10% of the initial value was found to be 0.03 L which is in quantitative agreement with the previous study [126]. However, I found a discrepancy in the result under CO exposure. It is interesting that the photocathode activated with NF_3 shows much more resilience to CO than that activated with O_2. The reason for this is not clear, and to the best of my knowledge, no study of CO adsorption on the Cs/O and Cs/NF_3 layers has yet been reported. However, my experimental result indicates that the Cs/O activation layer can more easily chemically adsorb CO than the Cs/NF_3, thus having a greater impact on the dipole in the activation layer, and therefore degrading QE of a Cs/O photocathode faster.

The possibility of restoring the QE of a photocathode activated with NF_3 after degradation due to O_2, CO_2 and CO exposures are shown in Figure 7.14 to Figure 7.16, respectively. In the case of CO, the photocathode was exposed at a pressure up to 2.3×10^{-8}mbar because CO has a very small effect on the QE of the NEA GaAs photocathode activated with NF_3. It is seen that the QE loss due to O_2 exposure can be restored nearly to the initial value, 95% of the initial value, while the degraded QE due to CO_2 and CO can be partly recovered, only to 60% and 72% of the initial value, respectively.

The results of my investigation show that in general H_2, CH_4, N_2, CO, CO_2 and O_2 affect the photocathode activated with NF_3 in similar way to that activated

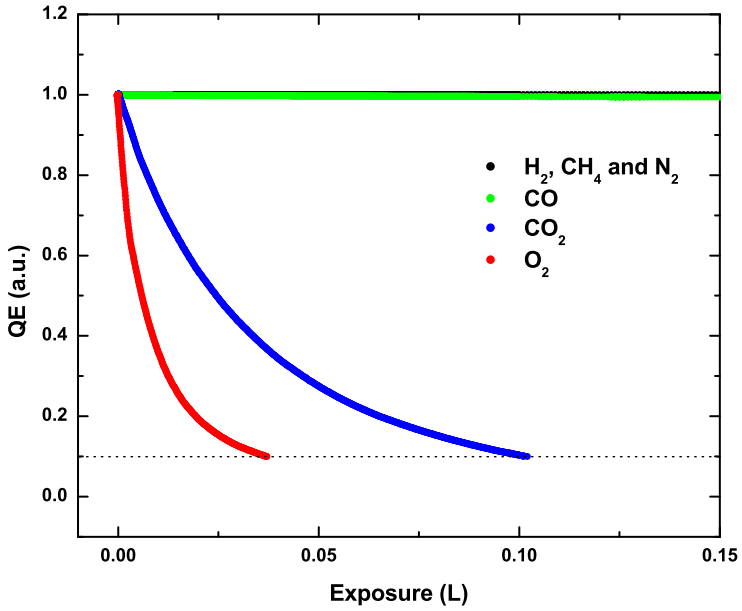

Figure 7.12: Comparison of the QE degradation for the TM GaAs photocathode activated with NF_3 during different gas exposures at a pressure of 1.5×10^{-10} mbar.

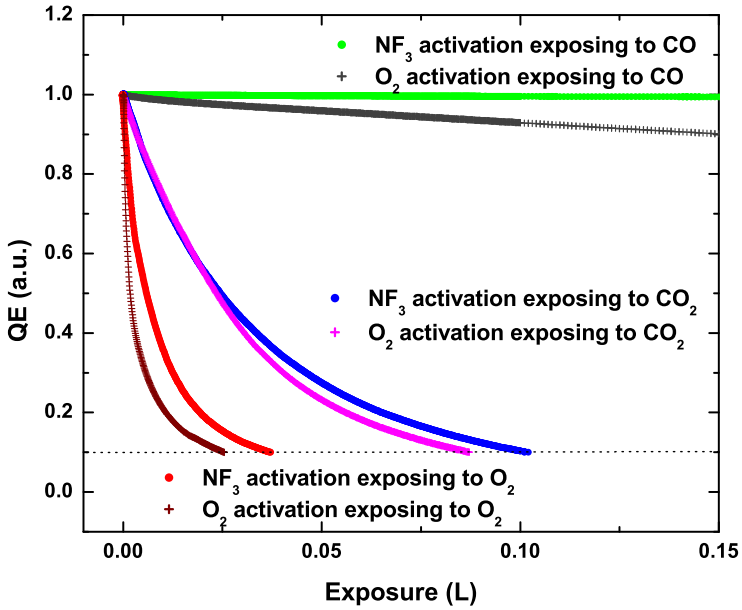

Figure 7.13: Plot of the QE degradation for the TM GaAs photocathode activated with NF_3 during CO, CO_2 and O_2 exposures compared with those activated with O_2.

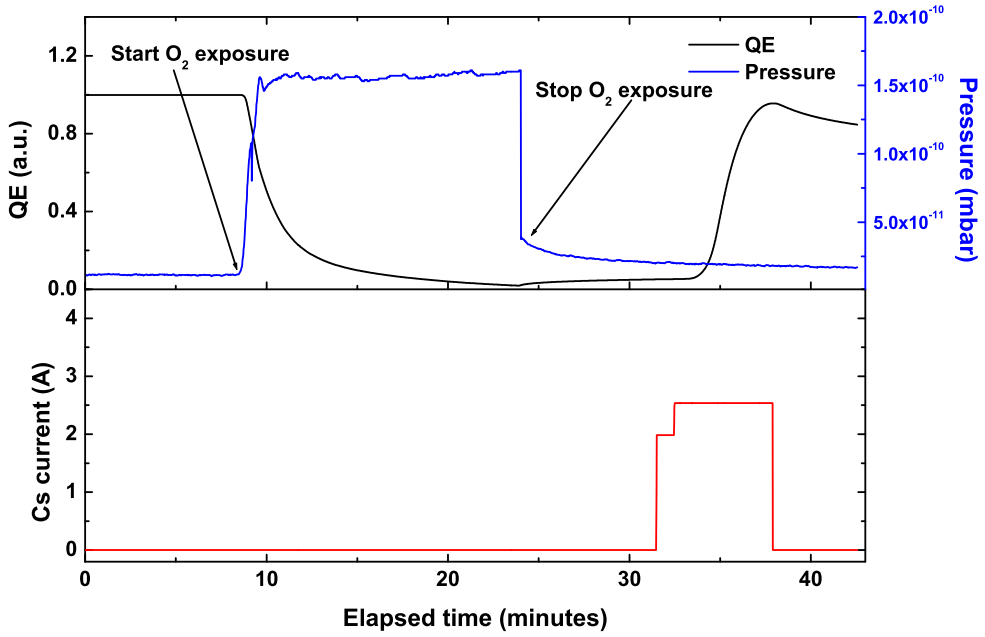

Figure 7.14: Evolution of the QE of the TM GaAs photocathode activated with NF_3 during exposure to O_2 followed by re-caesiation.

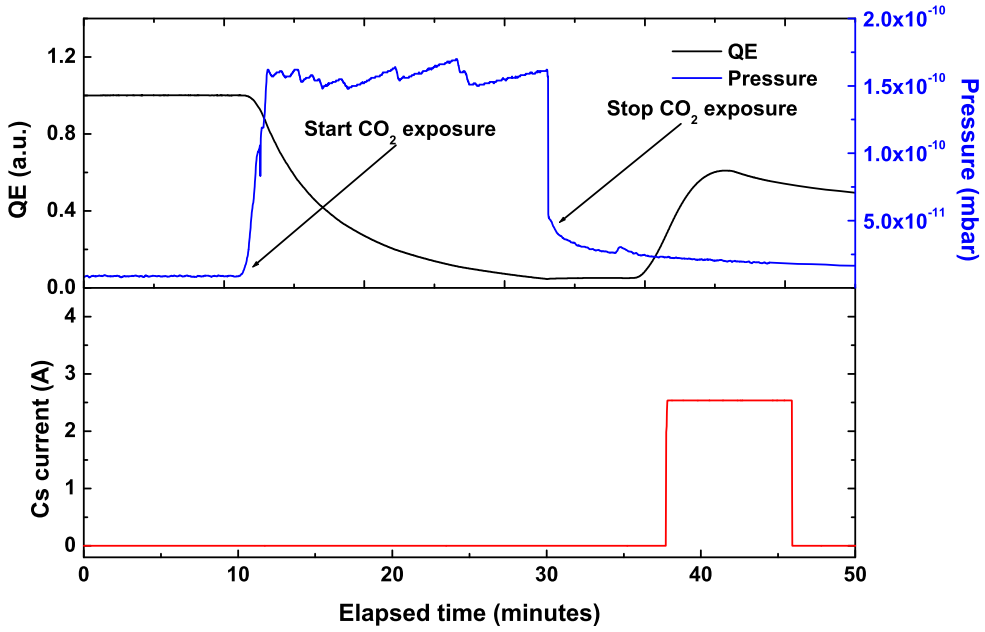

Figure 7.15: Evolution of the QE of the TM GaAs photocathode activated with NF_3 during exposure to CO_2 followed by re-caesiation.

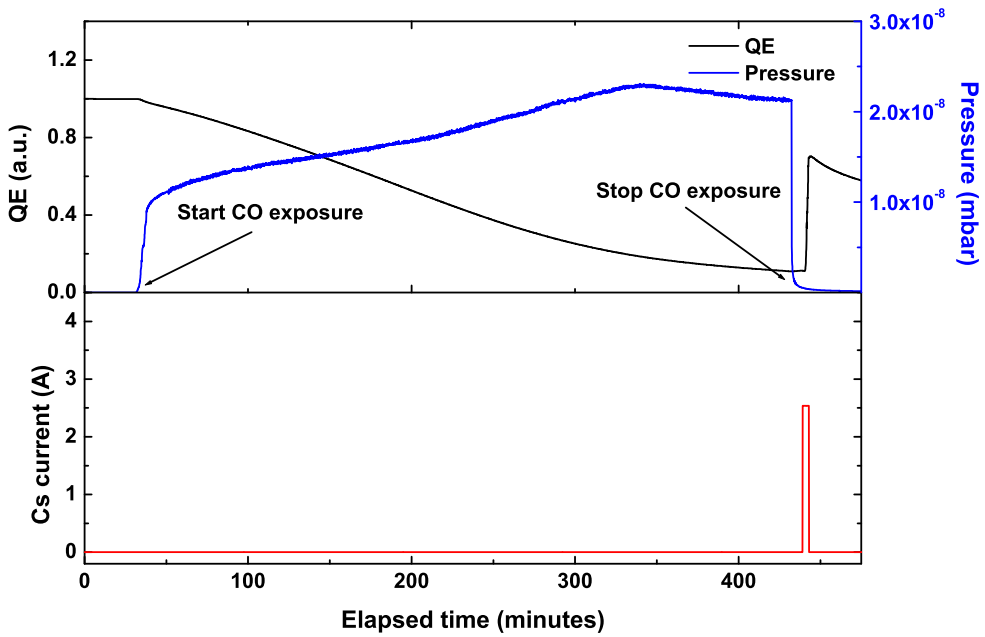

Figure 7.16: Evolution of the QE of the TM GaAs photocathode activated with NF_3 during exposure to CO followed by re-caesiation.

with O_2, which can be explained using the double-dipole model discussed in the previous section.The observed effect for CO exposure suggests that the NEA GaAs photocathode activated with NF_3 is indeed more stable than that activated with O_2. Additional studies are required in order to fully understand the nature of the activation layer. Nevertheless, the effect of the residual gases on the NEA GaAs photocathode is clearly demonstrated in this experiment.

In summary, this chapter represents the first time study of the influence of H_2, CH_4, N_2, CO, CO_2 and O_2 on the QE lifetime NEA GaAs photocathode in the vacuum system which has a base in the 10^{-11} mbar range. It was clearly demonstrated that H_2, CH_4 and N_2 have no effect on the photocathodes lifetime, whilst substantial reductions of the QE have been observed during the exposures to O_2, CO_2 and CO. CO_2 and CO have a severe effect on the stability of NEA GaAs photocathodes as the degraded QE can be partly restored to only 60 - 70% of the initial value by re-caesiation. It was also first demonstrated that the NEA GaAs photocathode

activated with Cs and NF_3 is more stable than the photocathode activated with Cs and O_2. These experimental results help uncover the degradation mechanism for the NEA GaAs photocathodes, and will be a great benefit to the development of photocathode and photo-injector.

Chapter 8

Conclusions

GaAs photocathods have been widely used as electron sources in several high average current accelerators and light sources. A high level of QE in photoemission over the entire spectrum of visible light is obtained only when the photocathode is activated to the NEA state by deposition of Cs and oxidant layers onto its atomically-clean surface. However, the major disadvantage with the use of NEA GaAs photocathodes is their short lifetime, both the operational lifetime and dark lifetime. While their operational lifetime is limited mainly by the ion back-bombardment, the dark lifetime of the NEA GaAs photocathode is limited by the adsorption of residual gas species inside the vacuum system. UHV conditions of at least 10^{-10} mbar are required for their operation, ideally XHV conditions in the order of 10^{-12} mbar are preferred.

For the ALICE accelerator, its current photo-electron gun employs only a single NEA GaAs photocathode, delivering a QE of approximately 3% under laser illumination with a wavelength of 532 nm. Under high voltage and high illumination power, the photocathode decays with time and may be damaged irreversibly, degrading the performance of the accelerator. Replacement of the photocathode requires a full vacuum bake-out to re-estrablish the optimum gun conditions, which can take up to three weeks.

This thesis reports on the development of a photocathode preparation facility (PPF) with a load-lock system as part of an upgrade to the ALICE photo-injector.

The preparation facility consists of three UHV/XHV chambers. It has ability to take GaAs photocathodes from the laboratory environment, clean, activate them to the NEA state and transfer to the gun, while maintaining the integrity of the gun vacuum system. This facility also offers several potential advantages which can be summarised as follows:

- It provides a rapid and reliable way to exchange the photocathode.
- It has a capability to prepare photocathodes in a controllable and reproducible way, resulting in high performance photocathodes, essentially high QE and long lifetime.
- It protects the gun from risks which may result from the preparation and activation process for the photocathodes.
- It will provide opportunities and flexibility for the gun to operate with new different types of the photocathode.

The PPF was successfully commissioned in the "stand-alone" mode, i.e., not connected to the gun. The transfer mechanism for photocathodes between the PPF and a gun vessel was demonstrated at both atmospheric pressure and under UHV using a mock-up of the cathode ball and gun.

In order to find the optimal preparation procedures for NEA GaAs photocathodes, I also developed a photocathode preparation and surface characterisation system which permits NEA GaAs photocathode preparation in conjunction with the application of several surface science techniques within the same vacuum system. The preparation techniques including vacuum heat cleaning, chemical treatment, atomic hydrogen cleaning and activations, and the physics behind were studied through the material properties such as surface chemistry and bulk crystallinity.

Using the developed preparation procedures in the PPF, an excellent QE as high as 19 % at a wavelength of 635 nm with long dark lifetimes in the order of 6,800 hours is obtained in a reproducible way from the GaAs/AlGaAs hetero-structure photocathodes designed and developed in collaboration with the ISP, Novosibirsk.

This result demonstrates the achievement of the PPF and the development in the photocathode technology for accelerators.

Having prepared the NEA GaAs photocathode in a reproducible way, I used the PPF to investigate the degradation of the QE of NEA GaAs photocathodes during exposures to gases typically present in the gun vacuum system, namely O_2, CO_2, CO, H_2, CH_4 and N_2. The effects of these gases on the NEA GaAs photocathodes have been demonstrated for the first time in a vacuum setup with a base pressure below 10^{-11} mbar. It was found that H_2, CH_4 and N_2 have no effect on the photocathodes lifetime, whilst substantial reductions of the QE have been observed during the exposures to O_2, CO_2 and CO. CO_2 and CO have a severe effect on the stability of NEA GaAs photocathodes as the degraded QE cannot be fully restored (only 60 - 70% of the initial value in this experiment) by re-caesiation. This degradation behaviour is similar for photocathodes activated with both Cs/O_2 and Cs/NF_3. However, the photocathodes activated with Cs/NF_3 were found to be more stable than those activated with Cs/O_2 during CO and CO_2 exposures. These experimental results have contributed to the understand of the degradation mechanism for the NEA GaAs photocathodes. Moreover, it can help to develop the vacuum system design for future photoelectron-guns in order to prolong the lifetime of NEA GaAs photocathodes.

The success of the PPF should provide further motivation to study several important issues in photocathode technology. Together with the surface characterisation system, a number of interesting experiments can be performed to further the understanding of GaAs photocathodes. Some of these include:

- The chemical change on the NEA GaAs surface after degradation due to residual gases.
- The possibility of using other oxidants for the activation process to improve the lifetime of the photocathode.
- The possibility of adding a second alkali such as Li and Na to the Cs and NF_3 activation process, it was demonstrated by G.A. Mulhollan and J.C. Bierman [130] that it increases the stability of GaAs photocathode.

- The degradation in QE after a number of atomic hydrogen cleaning cycles, as was demonstrated by D. A. Orlov, *et al.*. [124] that for liquid-phase epitaxy (LPE) GaAs photocathodes, the QE is stable at approximately 20% over a large number of cleaning cycles.

- The change in the energy distribution of the NEA photocathodes after degradation of the photocathode.

It is hoped that the experiments mentioned above would be of benefit to the future development of photocathode and accelerator technology.

References

[1] The International Linear Collider. ILC reference design report. Available: http://lcdev.kek.jp/RDR/(ISBN 978-92-9083-300-0) [Accessed May 2010].

[2] ASTeC. ALICE. Available: http://www.astec.ac.uk/project/alice.html [Accessed May 2010].

[3] The 4GLS Design Team. 4GLS conceptual design report. Available: http://www.4gls.ac.uk/ERLP.htm [Accessed May 2010].

[4] The LCLS Design Group. Linac coherent light source (LCLS) conceptual design report(CDR). *SLAC-R-593* (2002).

[5] P.R. Boltona, *et al.*. Photoinjector design for the LCLS. *Nucl. Instr. and Meth. A* **483**, 296 (2002).

[6] C. Travier. Rf guns : bright injectors for FEL. *Nucl. Instr. and Meth. A* **304**, 285 (1991).

[7] F. Hannon. Overview of high Brightness, high average current electron guns. *ERLP-INJ-GUN-RPT-002* (2004).

[8] M. Borland. A high-brightness thermionic microwave electron gun. *SLAC-R-402* (1991).

[9] N. Nishimori, *et al.*. A thermionic electron gun system for the JAERI superconducting FEL. *Proceedings of European Particle Accelerator Conference 2000 (EPAC 2000)* (2000).

[10] SCSS X-FEL, R&D Group. SCSS X-FEL conceptual design report. Available: http://www-xfel.spring8.or.jp [Accessed May 2010].

[11] A.V. Aleksandrov, *et al.*. Experimental study of the response time of GaAs as a photoemitter. *Phys. Rev. E* **51**(2), 1449 (1995).

[12] D.A. Engwall. High-brightness electron beams from a DC, High-voltage, GaAs photoemission gun. Ph.D. thesis, University of Illinois (1998).

[13] S.H. Kong, *et al.*. Performance of cesium telluride photocathodes as an electron source for the Los Alamos FELA. *Proceedings of 16th International Free Electron Laser Conference 1994* (1994).

[14] J. Rosenzweig, *et al.*. Initial measurements of the UCLA rf photoinjector. *Nucl. Instr. and Meth. A* **341**, 379 (1994).

[15] C.K. Sinclair, *et al.*. Development of a high average current polarized electron source with long cathode operational lifetime. *Phys. Rev. ST Accel. Beams* **10**, 23501 (2007).

[16] D. Sertore, *et al.*. First operation of cesium telluride photocathodes in the TTF injector RF gun. *Nucl. Instr. and Meth. A* **445**, 422 (2000).

[17] N. Nishimori, *et al.*. Development of an electron gun for the ERL light source in Japan. *International Workshop on Energy Recovery Linacs 2007 (ERL2007)* (2007).

[18] A. Todd. State-of-the-art electron guns and injector designs for energy recovery linacs (ERL). *Nucl. Instr. and Meth. A* **557**, 36 (2006).

[19] S.J. Russell. Overview of high-brightness, high-average-current photoinjectors for FELs. *Nucl. Instr. and Meth. A* **507**, 304 (2003).

[20] T. Siggins, *et al.*. Performance of a DC GaAs photocathode gun for the Jefferson Lab FEL. *Nucl. Instr. and Meth. A* **475**, 549 (2001).

[21] I. Ben-Zvia and I.V. Bazarov. Summary, Working group 1: Electron guns and injector designs. *Nucl. Instr. and Meth. A* **557**, 337 (2006).

[22] K. Batchelor, *et al.*. Performance of the Brookhaven photocathode RF gun. *Nucl. Instr. and Meth. A* **318**, 372 (1992).

[23] D.H. Dowell, *et al.*. The status of normal conducting RF (NCRF) guns, A summary of the ERL 2005 workshop. *SLAC-PUB-11754* (2005).

[24] D. Sertore, *et al.*. High QE photocathode at FLASH. *Proceedings of European Particle Accelerator Conference 2006 (EPAC 2006)* (2006).

[25] H.H. Braun, *et al.*. The photo-injector option for CLIC: Past experiments and future development. *Proceedings of 2001 Particle Accelerator Conference (PAC 2001)* (2001).

[26] C. Pagani, *et al.*. High brightness, long pulse, electron beam production with SC photo-injectors. *Nucl. Instr. and Meth. A* **340**, 17 (1994).

[27] D. Janssen, *et al.*. Technology challenges for SRF guns as ERL sources in view of Rossendorf work. *Nucl. Instr. and Meth. A* **557**, 80 (2006).

[28] A. Burrill, *et al.*. BNL superconducting RF guns technology challenges as ERL sources. *Nucl. Instr. and Meth. A* **557**, 75 (2006).

[29] S.L. Bennett. Cathode for high brightness electron sources for 4GLS. *ERLP-INJ-CATH-RPT-001* (2003).

[30] K.L. Jensen, *et al.*. A photoemission model for low work function coated metal surfaces and its experimental validation. *J. Appl. Phys.* **99**, 124905 (2006).

[31] W.E. Spicer. Negative affinity 3-5 photocathodes: Their physics and technology. *Appl. Phys.* **12**, 115 (1977).

[32] W.E. Spicer and R.L. Bell. The III-V photocathode: A major detector development. *Pub. Astron. Soc.* **84** 110 (1972).

[33] W.E. Spicer. Modern theory of photoemission and its applications to practical photocathodes. *SLAC-R-432* (1993).

[34] T. Rao, *et al.*. Photocathodes for the energy recovery linacs. *Nucl. Instr. and Meth. A* **557**, 124 (2006).

[35] M. Conde, *et al.*. The ARGONNE wakefield accelerator high current photocathode gun and drive laser. *Proceedings of 1995 Particle Accelerator Conference (PAC 1995)* (1995).

[36] T. Srinivasan-Rao, *et al.*. Photoemission studies on metals using picosecond ultraviolet laser pulses. *J. Appl. Phys.* **69**(5), 3291 (1991).

[37] W.J. Brown, *et al.*. A high gradient 17 GHz RF gun for the production of high brightness electron beams. *Proceedings of 1999 Particle Accelerator Conference (PAC 1999)* (1999).

[38] X.J. Wang, *et al.*. Mg cathode and its thermal emittance. *Proceedings of 21st Linear Accelerator Conference (LINAC 2002)* (2002).

[39] H. Iijima, *et al.*. High charge Mg photocathode RF gun in S-band LINAC at University of Tokyo. *Proceedings of European Particle Accelerator Conference 2002 (EPAC 2002)* (2002).

[40] S.H. Kong, *et al.*. Photocathodes for free electron lasers. *Nucl. Instr. and Meth. A* **358**, 272 (1995).

[41] Q. Zhao, *et al.*. Test of niobium cathode for the superconducting radio frequency gun. *Proceedings of 2003 Particle Accelerator Conference (PAC 2003)* (2003).

[42] D. Sertore, *et al.*. First operation of cesium telluride photocathodes in the TTF injector RF gun. *Nucl. Instr. and Meth. A* **445**, 422 (2000).

[43] J.-P. Carneiro, *et al.*. First results of the Fermilab high-brightness RF photoinjector. *Proceedings of 1999 Particle Accelerator Conference (PAC 1999)* (1999).

[44] K. Masao, *et al.*. Electron emission characteristic of CsTe photo-cathode in RF gun. *Proceedings of the 1st Annual Meeting of Particle Accelerator Society of Japan and the 29th Linear Accelerator Meeting in Japan 2004* (2004).

[45] D. Bisero, *et al.*. High efficiency photoemission from Cs-K-Te. *Appl. Phys. Lett.* **70**(12), 1491 (1997).

[46] D. Bisero, *et al.*. K-Te photocathodes: A new electron source for photoinjectors. *J. Appl. Phys.* **82**(3), 1384 (1997).

[47] P. Michelato. Photocathodes for RF photoinjectors. *Nucl. Instr. and Meth. A* **393**, 445 (1997).

[48] U. Weigel, *et al.*. Cold intense electron beams from LN2-cooled GaAs-photocathodes. *Nucl. Instr. and Meth. A* **536**, 323 (2005).

[49] D.H. Dowel, *et al.*. Cathode R&D for future light sources. *SLAC-PUB-14002* (2010).

[50] J. Smedley, *et al.*. Lead photocathodes. *Phys. Rev. ST Accel. Beams* **11**, 013502 (2008).

[51] J. Smedley, *et al.*. Progress on lead photocathodes for superconducting injectors. *Proceedings of 2005 Particle Accelerator Conference (PAC 2005)* (2005).

[52] C. Travier. An introduction to photo-injector design. *Nucl. Instr. and Meth. A* **340**, 26 (1994).

[53] R. Alley, *et al.*. The Stanford linear accelerator polarized electron source. *Nucl. Instr. and Meth. A* **365**, 1 (1995).

[54] R.A. Mair, *et al.*. Anisotropies in strain and quantum efficiency of strained GaAs grown on GaAsP. *Phys. Lett. A* **212**, 231 (1996).

[55] D.T. Pierce *et al.*. GaAs spin polarized electron source. *Rev. Sci. Instrum.* **51**(4), 478 (1980).

[56] H. Sonnenberg. Low work function surfaces for negative electron affinity photoemitters. *Appl. Phys. Lett.* **14**(9), 289 (1969).

[57] D.T. Pierce, *et al.*. Negative electron affinity GaAs. *Appl. Phys. Lett.* **26**(12), 670 (1975).

[58] R. Alley, *et al.*. The design for the LCLS RF photoinjector. *Nucl. Instr. and Meth. A* **429**, 324 (1999).

[59] B.L. Militsyn, *et al.*. Desing of an upgrade to the ALICE photocathode electron gun. *Proceedings of 2008 European Particle Accelerator Conference (EPAC 2008)* (2008).

[60] B.L. Militsyn, *et al.*. First result from the III-V photocathode preparation facility for the ALICE ERL photoinjector. *Proceedings of 1st International Particle Accelerator Conference (IPAC 2010)* (2010).

[61] J.S. Blakemore. Semiconducting and other major properties of gallium arsenide. *J. Appl. Phys.* **53**(10), R123 (1982).

[62] D.T. Pierce and F. Meier. Photoemission of spin-polarised electrons from GaAs. *Phys. Rev. B* **13**(12), 5454 (1976).

[63] V.V. Bakin, *et al.*. Semiconductor surfaces with negative electron affinity. *e-J. Surf. Sci. Nanotech.* **5**, 80 (2007).

[64] S. Adachi. Handbook on physical properties of semiconductors. Kluwer Academic Publishers, Boston (2004).

[65] S.S. Li. Semiconductor physical electronics. Plenum, New York (2006).

[66] U.K. Mishra and J. Singh. Semiconductor device physics and design. Springer-Verlag, Dordrecht (2008).

[67] R.L. Bell. Negative electron affinity devices. Oxford University Press, London (1978).

[68] P.J. Sez. Polarization and charge limit studies of strained GaAs photocathodes. *SLAC-R-501* (1997).

[69] D.G. Fisher, *et al.*. Photoelectron surface escape probability of (Ga,ln)As : Cs-O in the 0.9 to ∼1.6 μm range. *J. Appl. Phys.* **43**(9), 3815 (1972).

[70] C.Y. Su, *et al.*. Photoelectron spectroscopic determination of the structure of (Cs,O) activated GaAs(110) surfaces. *J. Appl. Phys.* **54**(3), 1413 (1983).

[71] M. Hoppe. Differential energy analysis of electron beams: A study of photoemission from NEA-GaAs. Ph.D. thesis, University at Heidelberg (2001).

[72] U. Weigel. Cold intense electron beams from gallium arsenide photocathodes, Ph.D. thesis, University at Heidelberg (2003).

[73] V.L. Alperovich, *et al.*. Domination of adatom-induced over defect-induced surface states on p-type GaAs (Cs,O) at room temperature. *Phys. Rev. B* **50**, 5480 (1994).

[74] V.L. Alperovich, *et al.*. Unpinned behavior of the electronic properties of a p-GaAs(Cs,O) surface at room temperature. *Surf. Sci.* **331-333**, 1250 (1995).

[75] H.-J. Drouhin, *et al.*. Photoemission from activated gallium arsenide: I. Very-high-resolution energy distribution curves. *Phys. Rev. B* **31**, 3859 (1985).

[76] J. Clendenin and G.A. Mullhollan. High quantum yield, low emittance electron sources. *SLAC-PUB-7760* (1998).

[77] X. Du and B. Chang. Angle-dependent XPS study of the mechanisms of "high-low temperature" activation of GaAs photocathode. *Appl. Surf. Sci.* **251**, 267 (2005).

[78] F. Machuca, *et al.*. Oxygen species in Cs/O activated gallium nitride GaN negative electron affinity photocathodes. *J. Vac. Sci. Technol. B* **21**(4), 1863 (2003).

[79] A.S. Terekhov. Conceptual design report of the photocathodes and a system for their preparation for the 4GLS injector and recommendations for design of the high average current photocathode gun. (2007).

[80] J.I. Pankov. Optical processes in semiconductors, Academic Press, New York (1975).

[81] K. Aulenbacher, *et al.*. Pulse response of thin III/V semiconductor photocathodes. *J. Appl. Phys.* **92**(12), 7536 (2002).

[82] A.V. Aleksandrov, *et al.*. A prototype of RF photogun with GaAs photocathode for injector of VEPP-5. *Proceedings of European Particle Accelerator Conference 1996 (EPAC 1996)* (1996).

[83] P. Hartmann, *et al.*. A diffusion model for picosecond electron bunches from negative electron affinity GaAs photocathodes. *J. Appl. Phys.* **86**(9), 2245 (1999).

[84] A. Herrera-Gmóez and W.E. Spicer. Physics of high intensity nanosecond electron source. *SLAC-PUB-6307* (1993).

[85] M. Woods, *et al.*. Observation of a charge limit for semiconductor photocathodes. *J. Appl. Phys.* **73**(12), 8531 (1993).

[86] G.A. Mulhollan, *et al.*. Photovoltage effects in photoemission from thin GaAs layers. *Phys. Lett. A* **282**, 309 (2001).

[87] K. Togawa, *et al.*. Surface charge limit in NEA superlattice photocathodes of polarized electron source. *Nucl. Instr. and Meth. A* **414**, 431 (1998).

[88] L.B. Jones. An investigation into the effect of a chiral adsorbate on surface magnetism using spin-resolved electron spectroscopy: Tartaric Acid on Ni(110). Ph.D. thesis, University of Liverpool (2006).

[89] R.J. Reid. General specification for the design, construction and handling of ultra high vacuum vessels, components and assemblies for ASTeC. *ASTEC-VAC-QCD-spc-002* (2003).

[90] J. Grames. Using the congruent (frosting) temperature of GaAs to calibrate the load lock gun thermocouple. *JLab-TN-04-005* (2004).

[91] K.G. Tschersich and V. von Bonin. Formation of an atomic hydrogen beam by a hot capillary. *J. Appl. Phys.* **84**(8), 4065 (1998).

[92] I. Suemune, *et al.*. Incidence angle effect of a hydrogen piasma beam for the cleaning of semiconductor surfaces. *Appl. Phys. Lett.* **55**(8), 760 (1989).

[93] G.R. Bell, *et al.*. Atomic hydrogen cleaning of polar III-V semiconductor surfaces. *Surf. Sci.* **401**, 125 (1998).

[94] T. Maruyama, *et al.*. Atomic hydrogen cleaning of polarized GaAs photocathodes. *Appl. Phys. Lett.* **82**(23), 4184 (2003).

[95] K.A. Elamrawi and H.E. Elsayed-Alia. Preparation and operation of hydrogen cleaned GaAs(100) negative electron affinity photocathodes. *J. Vac. Sci. Technol. A* **17**(3), 823 (1999).

[96] E.J. Petit, *et al.*. Interaction of an atomic hydrogen with native oxides on GaAs(100). *J. Vac. Sci. Technol. A* **10**(4), 2172 (1992).

[97] Y. Ide and M. Yamada. Role of Ga_2O in the removal of GaAs surface oxides induced by atomic hydrogen. *J. Vac. Sci. Technol. A* **12**(4), 1858 (1994).

[98] M. Baylac, *et al.*. Effects of atomic hydrogen and deuterium exposure on high polarization GaAs photocathodes. *Phys. Rev. ST Accel. Beams* **8**, 123501 (2005).

[99] L.J. Clarke. Surface crystallography, An introduction to low energy electron diffraction. Wiley, Chichester (1985).

[100] B.J. Stocker. AES and LEED study of the activation of GaAs-Cs-O negative electron affinity surfaces. *Surf. Sci.* **47**, 501 (1975).

[101] V.V. Bakin, *et al.*. Semiconductor surfaces with negative electron affinity. *e-J. Surf. Sci. Nanotech.* **5**, 80 (2007).

[102] R.L. Bell. Negative electron affinity devices. Clarendon Press. Oxford (1973).

[103] T. Balasubramanian, *et al.*. X-ray photoemission spectroscopy studies of cesium and oxygen on GaAs(100). *J. Vac. Sci. Technol. A* **10**(5), 3158 (1992).

[104] J.F. Moulder, *et al.*. Handbook of X-ray photoelectron spectroscopy. ULVAC-PHI, Inc. Japan (1995).

[105] Z.H. Lu, *et al.*. A surface analytical study of GaAs(100) cleaning procedures. *J. Vac. Sci. Technol. A* **7**(3), 646 (1989).

[106] K.A. Elamrawi and H.E. Elsayed-Ali. GaAs photocathode cleaning by atomic hydrogen from a plasma source *J. Phys. D: Appl. Phys.* **32**, 251 (1999).

[107] N. Razek, *et al.*. GaAs surface cleaning by low energy hydrogen ion beam treatment. *J. Vac. Sci. Technol.* **20**(4), 1492 (2002).

[108] Q.-B. Lu, *et al.*. Optimum (Cs,O)/GaAs interface of negative-electron-affinity GaAs photocathodes. *J. Appl. Phys.* **68**(2), 634 (1990).

[109] E. Weissman and Y. Shapira. Photoemission efficiency and persistence of (Cs, F) and (Cs, O) activated GaAs(110). *Vacuum* **41**(2-4), 1006 (1990).

[110] T. Wada, *et al.*. A thermal desorption analysis for the adsorption of CO_2 on GaAs photocathodes. *Surf. Sci.* **285**, 188 (1993).

[111] A.J. van Bommel, *et al.*. LEED, AES and photoemission measurements of epitaxially grown GaAs(100), (111)A and $(\bar{1}\bar{1}\bar{1})$B surfaces and their behaviour upon Cs adsorption. *Surf. Sci.* **72**, 95 (1978).

[112] V.L. Alperovich, *et al.*. Surface passivation and morphology of GaAs(100) treated in HCl-isopropanol solution. *Appl. Surf. Sci.* **253**, 249 (2004).

[113] Z. Liu, *et al.*. Photoemission study of Cs-NF_3 activated GaAs(100) negative electron affinity photocathodes. *Appl. Phys. Lett.* **92**, 241107 (2008).

[114] F. Ciccacci and G. Chiaia. Comparative study of the preparation of negative electron affinity GaAs photocathodes with O_2 and with NF_3. *J. Vac. Sci. Technol. A* **9**(6), 2991 (1991).

[115] H. Morota and S. Adachi. Properties of GaAs(001) surfaces thermally annealed in vacuum. *J. Appl. Phys.* **105**(4), 43508 (2009).

[116] C.K. Sinclair, *et al.*. Atomic hydrogen cleaning of semiconductor photocathodes. *Proceedings of Particle Accelerator Conference 1997 (PAC 1997)* (1997).

[117] O.E. Tereshchenko, *et al.*. Atomic structure and electronic properties of HCl-isopropanol treated and vacuum annealed GaAs(100) surface. *Appl. Surf. Sci.* **142**, 75 (1999).

[118] O.E. Tereshchenko, *et al.*. Composition and structure of HCl-isopropanol treated and vacuum annealed GaAs(100) surfaces. *J. Vac. Sci. Technol. A* **17**, 2665 (1999).

[119] G. Mulhollan, *et al.*. Preparation of GaAs photocathodes at low temperature. *SLAC-PUB-7345* (1996).

[120] M.V. Lebedev, *et al.*. Synchrotron photoemission spectroscopy study of ammonium hydroxide etching to prepare well-ordered GaAs(100) surfaces. *Appl. Surf. Sci.* **229**, 226 (2004).

[121] M. Yamada and Y. Ide. Direct observation of species liberated from GaAs native oxides during atomic hydrogen cleaning. *Jap. J. Appl. Phys.* **33**(5), L671 (1994).

[122] K.V. Toropetsky, *et al.*. New reconstruction-stoichiometry correlation for GaAs(001) surface treated by atomic hydrogen. *Appl. Surf. Sci.* **254**, 8041 (2008).

[123] S. Pastuszka, *et al.*. Preparation and performance of transmission-mode GaAs photocathodes as sources for cold dc electron beams. *J. Appl. Phys.* **88**(11), 6788 (2000).

[124] D.A. Orlov, *et al.*. Long term operation of high quantum efficiency GaAs(Cs,O) photocathodes using multiple recleaning by atomic hydrogen. *J. Appl. Phys.* **106**, 54907 (2009).

[125] M. Stutzman. Photocathode anodization, Standard Operating Procedure (SOP). *A-09-002-SOP* (2009).

[126] S. Pastuszka, *et al.*. Stable to unstable transition in the (Cs,O) activation layer on GaAs (100) surfaces with negative electron affinity in extremely high vacuum. *Appl. Surf. Sci.* **99**, 361 (1996).

[127] T. Wada, *et al.*. Influence of exposure to CO, CO_2 and H_2O on the stability of GaAs photocathodes. *Jap. J. Appl. Phys.* **29**(10), 2087 (1990).

[128] J. Zou, *et al.*. Stability and photoemission characteristics for GaAs photocathodes in a demountable vacuum system. *Appl. Phys. Lett.* **92**, 172102 (2008).

[129] G.D. Cates, *et al.*. The BATES polarized electron source. *Nucl. Instr. and Meth. A* **278**, 293 (1989).

[130] G.A. Mulhollan and J.C. Bierman. Enhanced chemical immunity for negative electron affinity GaAs photoemitters. *J. Vac. Sci. Technol. A* **26**(5), 1195 (2008).